Picobiophotonics for the investigation of pigment-pigment and pigment-protein interactions in photosynthetic complexes

vorgelegt von

Diplom-Physiker

Franz-Josef Schmitt

geboren in Marburg/ Lahn

von der Fakultät II - Mathematik und Naturwissenschaften
der Technischen Universität Berlin

zur Erlangung des akademischen Grades

Doktor der Naturwissenschaften

Promotionsausschuss:

Vorsitzender: Prof. Dr. Mario Dähne

Berichter/Gutachter: Prof. Dr. Hans Joachim Eichler

Berichter/Gutachter: Prof. Dr. Gernot Renger

Berichter/Gutachter: Prof. Dr. Thomas Renger

Tag der wissenschaftlichen Aussprache: 15.08.2011

Berlin 2011

D 83

ABSTRACT

Franz-Josef Schmitt

Picobiophotonics for the investigation of pigment-pigment and pigment-protein interactions in photosynthetic complexes

Excitation energy transfer (EET) processes in different photosynthetic pigment-protein-complexes were analysed by time- and wavelength correlated single photon counting (TWCSPC). A new mobile 16-channel photomultiplier with flexible fiber optics, exchangeable light sources and temperature regulator (10 K – 350 K) was built up for the spectroscopy of samples in cuvettes, on surfaces or of whole leaves in vivo. The system represents a mobile setup of the powerful TCSPC technique with high optical throughput up to 10^6 counts/sec.

The theoretical description of the excited state dynamics in systems with pigment-pigment and pigment-protein interaction was performed by using rate equations that were applied on structures with increasing hierarchical complexity. The study started with a system consisting of two excitonically coupled Chl molecules in a tetrameric protein environment represented by the recombinant water soluble Chl binding protein (WSCP) of type IIa and it was completed with a study of the photosystem II (PSII) dynamics in whole leaves of the higher plant *Arabidopsis thaliana*. In this way a quantification of dissipative excited state relaxation processes as a function of increasing excitation light intensity was achieved. For parameter adaption in the corresponding systems of linear differential equations a highly efficient algorithm was developed that allows the variation of parameters used to fit the time resolved optical data under any constraints on the coefficient matrix (e.g. invariance of the symmetry). The approach permits the determination of selected parameter values, their probability and stability in any dynamical system. A way to calculate thermodynamic quantities (e.g. entropy) under nonequilibrium conditions from rate equations is proposed.

The excited state dynamics observed in WSCP were explained by assuming an excitonically coupled Chl dimer that is modulated by the protein environment on different time scales. The dominating fluorescence decay component increases from 4.8 ns or 5.2 ns for Chl *b* or Chl *a* homodimers, respectively, at room temperature, to 7.0 or 6.2 ns, respectively, at 10 K. This temperature dependency is most probably caused by the pigment-pigment- interaction and the energies of the triplet states of the Chl molecules. A modulation of the electronic states of the coupled Chl dimer by the protein environment with a typical time constant of 100 ps at 10 K is inferred to be responsible for a fast and strongly temperature dependent fluorescence component. This idea is qualitatively in line with refined theoretical models and results of complementary studies of hole burning and fluorescence line narrowing spectroscopy.

In the phycobiliprotein (PBP) antenna of the cyanobacterium *Acaryochloris marina* EET occurs with characteristic time constants of 400 fs, 3-5 ps and 14 ps inside trimeric phycocyanin (PC), from PC to allophycocyanin (APC) and from APC to the terminal emitter (TE) of the PBP antenna, respectively. The TWCSPC spectra of whole cells and preparations of isolated PBP complexes exhibit a 20 ps component each that indicates the intact EET from PC to the TE in agreement with the results of transient fs absorption spectroscopy. The EET from the PBP antenna to the Chl *d* containing core antenna complexes of PS II represents an additional limiting transfer step of about 30-40 ps which leads to a time constant of the EET from PBP to Chl *d* in the range of 70 ps.

Coupled and temperature switch-able hybrid systems of surface treated CdSe/ZnS quantum dots (QDs) with 530 nm emission wavelength and the isolated PBP antenna complexes from *A.marina* were formed in aqueous solution by electrostatic self assembly. Based on the theory of Förster Resonance Energy Transfer (FRET) an average value of 3.2-3.5 nm was obtained for the distance between the neighbouring transition dipole moments in the QDs and the PBP antenna. It was shown that the functional coupling between QDs and PBP complexes is interrupted at temperatures below 0°C. This effect enables the construction of switch-able molecular sensors, photosensibilisators or light harvesting devices with various applications in biochemistry, biomedicine and photovoltaics.

KURZZUSAMMENFASSUNG

Franz-Josef Schmitt

Pikobiophotonik zur Untersuchung der Pigment-Pigment und Pigment-Protein Wechselwirkungen in photosynthetischen Komplexen

Anregungsenergietransfer-(EET)-prozesse wurden in verschiedenen photosynthetischen Pigment-Protein-Komplexen mit zeit- und wellenlängenkorrelierter Einzelphotonenspektroskopie (TWCSPC) analysiert. Ein neuer mobiler 16-Kanal Photomultiplier mit flexibler Faseroptik, austauschbaren Lichtquellen und einem Kryostaten (10 K – 350 K) wurde für die Spektroskopie von Proben in Küvetten, auf Oberflächen oder von ganzen Blättern in vivo aufgebaut. Das System stellt einen mobilen Messplatz auf Grundlage der leistungsfähigen TCSPC Technik mit hohem Lichtdurchsatz bis zu 10^6 Photonen/ Sekunde dar.

Die theoretische Beschreibung der Anregungszustandsdynamik unter Berücksichtigung von Pigment-Pigment und Pigment-Protein Wechselwirkung erfolgte über Ratengleichungen, die auf Systeme mit hierarchisch steigender Komplexität angewendet wurden. Die Untersuchung startete an einer Anordnung von zwei exzitonisch gekoppelten Chl Molekülen in einer tetrameren Proteinumgebung wie sie in rekombinantem wasserlöslichen Chlorophyll bindenden Protein (WSCP) des Typs IIa vorliegt und wurde mit einer Untersuchung der Photosystem II (PSII) Dynamik in ganzen Blättern der höheren Pflanze *Arabidopsis thaliana* abgeschlossen. Auf diese Weise wurde z.B. die Quantifizierung dissipativer Relaxationsprozesse der Anregungszustände bei ansteigender Intensität des Anregungslichtes ermöglicht. Für die Parameteranpassung in den entsprechenden Systemen linearer Differentialgleichungen wurde ein effizienter Algorithmus entwickelt, der die Variation von Parametern zur Anpassung der zeitaufgelösten optischen Daten unter beliebigen Randbedingungen an die Koeffizientenmatrix (z.B. Invarianz der Symmetrie) ermöglicht. Der Zugang erlaubt die Bestimmung ausgewählter Parameterwerte, ihre Wahrscheinlichkeit und Stabilität in einem beliebigen dynamischen System. Ein Weg zur Berechnung thermodynamischer Größen (z.B. Entropie) aus Ratengleichungen unter Nichtgleichgewichtsbedingungen wird vorgeschlagen.

Die Anregungszustandsdynamik in WSCP wurde durch die Annahme eines gekoppelten Chl Dimers, das durch die Proteinumgebung auf verschiedenen Zeitskalen moduliert wird, erklärt. Die dominierende Komponente der Fluoreszenzkinetik steigt von 4,8 bzw. 5,2 ns für Chl *b* bzw. Chl *a* Homodimere bei Raumtemperatur auf 7,0 bzw. 6,2 ns bei 10 K an. Diese Temperaturabhängigkeit wird höchstwahrscheinlich durch die Pigment-Pigment Wechselwirkung und die energetische Lage der Triplettzustände der Chl Moleküle bestimmt. Eine Modulation der elektronischen Zustände durch die Proteinumgebung mit einer typischen Zeitkonstante von 100 ps bei 10 K ist sehr wahrscheinlich für eine schnelle und stark temperaturabhängige Fluoreszenzkomponente verantwortlich, die qualitativ mit weiterentwickelten theoretischen Modellen und Ergebnissen komplementärer Studien mittels Lochbrenn- und Fluoreszenz line narrowing Spektroskopie übereinstimmt.

In der Phycobiliprotein (PBP) Antenne des Cyanobakteriums *Acaryochloris marina* findet der EET mit charakteristischen Zeitkonstanten von 400 fs, 3-5 ps bzw. 14 ps innerhalb des trimeren Phycocyanins (PC), vom PC zum Allophycocyanin (APC) bzw. vom APC zum terminalen Emitter (TE) der PBP Antenne statt. Die TWCSPC Spektren ganzer Zellen und Präparationen von isolierten PBP Komplexen zeigen jeweils eine 20 ps Komponente, die dem Anregungsenergietransfer vom PC zum TE entspricht, in Übereinstimmung mit Ergebnissen aus transienten fs absorptionsspektroskopischen Untersuchungen. Der EET von der PBP Antenne zu den Chl *d* haltigen Komplexen der Core Antenne von PS II weist einen zusätzlichen limitierenden Transferschritt von 30-40 ps auf, der zu einer Zeitkonstante für den gesamten EET vom PBP zum Chl *d* in der Größenordnung von 70 ps führt.

Gekoppelte und temperaturschaltbare Hybridsysteme aus oberflächenbehandelten CdSe/ZnS Quantenpunkte (QDs) mit 530 nm Emissionswellenlänge und isolierten PBP Komplexen aus *A.marina* wurden in wässriger Lösung durch elektrostatische Selbstorganisation gebildet. Nach der Theorie des Förster Resonanz Energietransfers (FRET) wurde der Abstand der benachbarten Übergangsdipolmomente in den QDs und der PBP Antenne zu 3,2-3,5 nm berechnet. Es wurde gezeigt, dass die funktionelle Kopplung von QDs und PBP Komplexen bei Temperaturen unterhalb von 0°C unterbrochen wird. Dies ermöglicht die Konstruktion von schaltbaren molekularer Sonden, Photosensibilisatoren oder Lichtsammelsystemen mit vielfältigen Anwendungsfeldern in der Biochemie, Biomedizin und Photovoltaik.

INDEX

PREFACE **7**

INTRODUCTION **10**

1. BIOLOGICAL BACKGROUND **15**

1.1 Structures and organisation of photosynthesis **15**

1.2 Fluorescence emission as a tool for monitoring PS II function **22**

1.3 Antenna complexes in photosynthesis **23**
  1.3.1 The light harvesting complex of PS II (LHCII) of higher plants 24
  1.3.2 The LH1 and LH2 of purple bacteria 31
  1.3.3 The Fenna-Matthews-Olson (FMO) complex of green sulfur bacteria 33
  1.3.4 Phycobilisomes (PBS) of cyanobacteria 35
  1.3.5 Phycobiliprotein (PBP) antenna of A.marina 40

1.4 Core complex of PS II **43**

1.5 Water soluble chlorophyll binding protein (WSCP) **46**

2 EXPERIMENTAL SETUP AND DATA ANALYSIS **50**

2.1 Setup for time- and wavelength correlated single photon counting (TWCSPC) **50**

2.2 Data analysis **56**
  2.2.1 Data acquisition and fit routine 56
  2.2.2 Optimal χ^2 and size of the parameter space 63

3. THEORY, FORMALISM AND RELATED EXPERIMENTS **66**

3.1 Light and matter **66**
  3.1.1 Description of short laser pulses 66
  3.1.2 Interaction between light and matter 72
  3.1.3 The plasmon resonance of gold nanoparticles 74
  3.1.4 Quantum mechanical description of molecule complexes 78

3.2 Rate equation formalism **84**
  3.2.1 Axiomatic motivation 84
  3.2.2 Absorption and emission of light 87
  3.2.3 Relaxation processes and fluorescence dynamics 89
  3.2.4 Rate equations in photosynthesis and an efficient algorithm for the solution 93
  3.2.5 Simulated decay associated spectra 97

3.3 Transition probabilities in coupled pigments **102**
  3.3.1 Excited states in coupled pigments 102
  3.3.2 Förster Resonance Energy Transfer (FRET) 104

3.4 The optical spectra of coupled pigments in pigment-protein complexes **113**

3.5 Thermodynamic aspects of photosynthesis **117**
  3.5.1 Gibbs free energy and entropy 117
  3.5.2 The entropy in the ensemble of coupled pigments 122

4 EXCITED STATE DYNAMICS IN WSCP 127

4.1 The electronic structure of Chl dimers bound to class IIa WSCP 127

4.2 Fluorescence spectroscopic studies on WSCP 130
  4.2.1 Time integrated fluorescence spectra at room temperature 130
  4.2.2 Time integrated fluorescence spectra at cryostatic temperatures 133
  4.2.3 Lifetimes of excited singlet states in homo- and hetero-dimers of class IIa WSCP 138

4.3 Simulation of the temperature dependent DAS of Chl dimers bound to WSCP 143
  4.3.1 Double well potential for different configuration states of the protein 143
  4.3.2 Pigment-protein coupling in WSCP 145
  4.3.3 Pigment-pigment coupling in WSCP 151

4.4 Concluding remarks to WSCP and future perspectives 156

5 PHYCOBILIPROTEIN ANTENNA RODS AND WHOLE CELLS OF *A.MARINA* 158

5.1 Excitation energy transfer and electron transfer in whole cells of *Synechocystis* and *A.marina* 158

5.2 Excited state dynamics inside the PBP antenna of *A.marina* 161
  5.2.1 Fluorescence measurements 163
  5.2.2 Transient absorption measurements 167

5.3 Simulation of the excited state dynamics in *A.marina* 172

5.4 Summary excitation energy transfer 175

6 HYBRID COMPLEXES OF PBP ANTENNA COMPLEXES AND CDSE/ZNS NANOPARTICLES 177

6.1 Time integrated Fluorescence emission of CdSe/ZnS-530-QD - PBP hybrid complexes 178

6.2 Time resolved fluorescence of CdSe/ZnS QD - PBP hybrid complexes 180

6.3 EET between CdSe/ZnS-530-QDs and the primary acceptor in the PBP antenna 182

6.4 Applications of hybrid structures containing photosynthetic light harvesting complexes. 185

7 THE PS II OF WHOLE LEAVES OF *A.THALIANA* 190

7.1 Single Flash induced transient fluorescence yield measurement data 190

7.2 PS II model based on rate equations 192

7.3 Results for energy- and electron transfer processes in *A.thaliana* 195

7.4 Conclusion on dissipative processes in whole leaves of *A.thaliana* 198

8 Summary 200

ABBREVIATIONS 204

REFERENCES 206

ACKNOWLEDGMENTS 223

CURRICULUM VITAE AND PUBLICATIONS 225

PREFACE

Mein Hang zum philosophischen Nachdenken beruht auf der einfachen Grundlage, dass ich über das kleinste Stück Natur irgendwelcher Art in höchste Verwunderung geraten kann.
Christian Morgenstern, (1871 - 1914), German author, journalist and translator

The secrets of nature that are hidden behind a “world” of molecules and atoms are definitely different from the imagination of “nature” Christian Morgenstern had when he talked about “the smallest piece of nature”. I agree with his opinion, identifying this smallest piece of nature with an elementary particle or – in line with my work presented here – with a single molecule in its environment. Up today it is not possible to understand the existence and nature of elementary particles in full detail. Beyond that we are far from a basic theory that is able to explain the existence of living matter [1].

It is an interesting fact that the smallest structures change on the fastest time scales. This general behaviour follows Heisenberg´s relation of uncertainty denoting that any quantum state which is confined to a small spacial region Δx exhibits an uncertainty of momentum in the order of $\Delta p_x \geq \hbar/(2\Delta x)$.

Therefore quantum states of electrons confined to molecular orbitals with $\Delta x < 10^{-9}\,m$ exhibit velocities up to $\Delta v_x = \Delta p_x / m_{el.}$ which is $\Delta v_x \geq 75\,km/s$. The probability of presence of the electrons spreads Δx in a typical time of $t \approx \Delta x / \Delta v_x < 1.32 \cdot 10^{-14}\,s \approx 10\,fs$.

The investigation of such processes on the picometer-scale, e.g. electronic transitions in molecules, therefore requires shortest light pulses on the fs-time scale generated by fs-laser systems.

The measurement of transient absorption changes in the fs time domain is one of the most prominent techniques used in the field of ultrafast spectroscopy [2] of fs-dynamics. Also light pulses, scattered light or fluorescence light is analysed with fs-resolution (generally by correlation measurements performed as wave mixing, e.g. by fluorescence up-conversion [3]).

Progress in long term stabilisitaion of the experimental setups and the generation of well defined samples combined with mathematical signal processing enabled the analysis of dynamics down to the sub ps-timescale with ps-fluorescence spectroscopy performed with pulsed diode lasers or fs-laser systems with low pulse energies [4]-[6]. The advantages of ps fluorescence spectroscopy in comparison to nonlinear fs techniques are mainly low cost and easy handling of the ps laser diode modules. Lower pulse energies are needed for this technique and the demand on the optical properties of the sample material is much lower compared to time resolved transient absorption spectroscopy. This is a big advantage because the fluorescence measurements can be performed directly *in vivo* (e.g. in living cells which are suspended in buffer solution, directly on whole plant leaves) which is shown by the time resolved investigations on whole cells of the cyanobacterium *Acaryochloris marina*, the green algae *chlorella pyrenoidosa chick* and on whole living plants of *Arabidopsis thaliana*. This technique is sensitive to the sample but virtually insensitive to the optical properties of the sample. It can also be performed in strongly scattering and inhomogeneous media.

In the mode of time and wavelength correlated single photon counting (TWCSPC) fluorescence spectroscopy is performed with pulse energies down to 10^{-15} Joule/pulse or less. This is especially necessary when light driven dynamics like photosythetic processes are to be observed without being influenced by the experimental setup.

The field of highly resolved structural and dynamical analyses has undergone a boost in the last decades. The main reasons for the boom are i) progress in sample preparation and crystallization techniques (e.g. growing of crystals of photosynthetic complexes for x-ray diffraction [7]) ii) the development and improvement of many different experimental techniques like nonlinear polarisation spectroscopy in the frequency domain [8], photon-echo spectroscopy [9], hole burning spectroscopy [10], total internal reflection fluorescence microscopy (TIRF), fluorescence lifetime imaging nanoscopy (FLIN) [11], atomic force microscopy (AFM) (just to mention a few ones) accompanied by progress in generating ultrashort laser pulses and iii) significant progress in high resolved fluorescence microscopy and theoretical studies leading to a break of the diffraction limit of resolution in the optical far field. As a consequence new methods were developed like stimulated excited state depletion (STED) microscopy and photo activation localization microscopy (PALM). These techniques appear to exhibit quite high resolution if the gathered information is not limited or a suitable amount of “a priori information” exists [12-18]. The achievable principal resolution limits look very promising in obtaining further progress in the coming years [19]. The theoretical limit of microscopic techniques is not longer given by the experimental setup but by the Heisenberg uncertainty of the states themselves [20]. The highest occupied molecular orbital of a pentacen molecule in the ground state has been visualised with AFM [21]. The picture appears blurred due to the limited localisation of the electronic orbital and not longer due to the resolution limit of the AFM. Is it just a question of time until the molecular orbitals can be seen in the light microscope ? Can we also expect such highest resolution for time constants of molecular interaction processes ?

High resolution techniques need to shift the measurement uncertainity to a “currency” that is available without limitation of the achievable resolution [18]. For TWCSPC one available “currency” is the measuring time. Monitoring over several hours and averaging the results of many measurements show that the remaining resolution limit is given by the reproducibility of the preparation of the sample and the intrinsic uncertainty of the sample. A numerical simulation of the decay associated spectra (DAS) suggests that TWCSPC performed on living cells of *A.marina* reached this limitation with the data presented here.

The combination of different techniques is of high interest for future studies and promises success. This might help to shift nanobiophotonics to picobiophotonics and femtobiophotonics not in the time scale and also regarding the spatial resolution. One example is the combination of AFM and time resolved fluorescence spectroscopy [22–26].

On the other hand one can not expect that one setup will show an infinite resolution of a biological sample. The scientist has to be careful in selecting the suitable methodology, keeping in mind that certain questions might be inaccessible by a chosen technique. In that case the scientist might get an arbitrary answer to his question. Even if the amount of information that can be collected would tend to highest values, there are unbreakable limitations of physical resolution. The limited information content of a system, as it can e.g. be derived from the so called “Bekenstein limit”, proves that no infinite resolution can be achieved [19, 27-30].

It might be useful to introduce the concept of information and some kind of cellular automata that process such information as discussed in [31], rather than working with concepts of energy or states or any other typical physical observable. The progress of solid state physics is partially based on the possibility to approximate the solid state by a periodic grating that can be treated quantum mechanically. This approach cannot be simply transformed to biophysics. Erwin Schrödinger called the living system a nonperiodic solid state [32].

This thesis presents mainly experimental data and in addition an attempt to achieve a theoretical description on the basis of rate equation models. These models might appear to be very simple but will be shown to present principally the whole information content that is experimentally accessible and they enable approaches to derive thermodynamic quantities as entropy in a nonequilibrium condition. The master equations represent a complete description. Approximations in this approach are helpful to answer questions on the basis of the experimental observables. The Fockker-Planck equation of diffusion and convection can be derived from the master equations as a 2nd order approximation.

In fact the concept of rate equations is strongly related to the concept of information because the master equations handle with probability vectors representing the possible outcome of experiments [33-36].

Theoretical physics achieved great progress in understanding the effects determining experimental observations of the properties of electronically excited states in pigment-protein complexes of plants [37-42]. These results are promising in expecting further exciting insights into this type of systems.

INTRODUCTION

The properties of chlorophyll molecules in photosynthetic complexes are tuned by binding to specific protein environments. This principle has developed evolutionarily in the biosphere and resulted in pigment-protein structures with highest efficiency in light harvesting, transfer of electronically excited states and transformation of light into electrochemical free energy.

Until today it is not possible to assemble a nanomachine of comparable complexity, stability and regulatory control. A full understanding of the functional relevance of molecular interactions in photosynthetic pigment-protein-complexes (PPCs) might be helpful in many areas of application.

Artificially designed PPC could work as nanoscaled tunable antenna systems for photovoltaics in form of light harvesting complexes with high exciton diffusion coefficients thus rising and/ or regulating the light absorption cross section. Other applications might be switchable PPCs which undergo state transitions from an inactive to an active state when illuminated or when in contact to certain environments. Such PPCs could be applicable e.g. in the photodynamic diagnostics and therapy of diseases like skin cancer by reducing the toxicology of the applied photodynamic dyes.

Nanobiophotonics comprises investigations of nanoscaled spatial structures and dynamics in living matter with light. Mainly fluorescence techniques are applied as a result of recent progress in high resolution fluorescence nanoscopy [12-15]. During the last years of work on this thesis different techniques of time- and wavelength-correlated single photon counting (TWCSPC) were mainly performed on

1) preparations of the phycobiliprotein (PBP) antenna from *A.marina* [43, 44],
2) different solubilized and aggregated LHCII trimers from spinach [45],
3) the water soluble chlorophyll binding protein (WSCP) that was genetically expressed in *E.coli* and reconstituted with Chl *a*, Chl *b* or mixtures of Chl *a* and Chl *b* [46-49],
4) artificial PPCs formed from eosin as chromophores bound to proteins [50],
5) semiconductor-pigment-protein-hybrid-complexes [51]-[53],
6) whole cells of different cyanobacteria, especially *A.marina* [43, 44, 54-56],
7) whole cells of the green algae *Chlorella pyrenodoisa chick* [57] and whole leaves of the higher plant *Arabidopsis thaliana* [58].

The results of this thesis are presented starting with WSCP as a model system (chap. 4). After that the fluorescence dynamics in the PBP complexes of *A.marina* and of whole cells of *A.marina* are analysed (chap. 5). Then it is shown how excitation energy transfer (EET) occurs in more complex systems containing semiconductor-pigment-protein-hybrid-complexes (chap. 6) and finally how the Photosystem II fluorescence dynamics of higher plants (chap. 7) observed during 8 orders of magnitude in time can be described with the formalism of rate equations that was used for the description of all samples. Regarding the omitted topics (LHCII trimers and aggregates (2), artificial

PPCs (4) and whole cells of *Chlorella pyrenodoisa chick* (7)) the reader is referred to the cited publications.

The main focus was the analysis of time resolved EET and electron transfer (ET) steps on the temporal scale of picoseconds but not the spatial structure and dynamics of traceable fluorophores.
In the following a short overview on phycobiliprotein (PBP) antenna preparations of *A.marina* and WSCP as a model system for the investigation of pigment-pigment and pigment-protein interactions is presented.

A. marina was discovered in 1996 and is until today the only known organism which mainly contains Chl *d* instead of Chl *a* in the membrane intrinsic Chl antenna and reaction centers [59]. In whole living cells of *A.marina* the EET between the uniquely structured and rod shaped phycobiliprotein (PBP) antenna and the Chl *d* containing membrane intrinsic antenna complex was found to occur with an overall time constant of 70-80 ps. This value is 3 times faster than in other cyanobacteria containing pycobilisomes (PBS) assembled from several PBP rod structures and Chl *a* containing membrane intrinsic antenna complexes [44, 60-64].
The EET from phycocyanin (PC) and allophycocyanin (APC) containing hexamers of the membrane extrinsic PBP antenna to spectrally red shifted APC was resolved to occur within 20 ($^{+}$/- 10) ps in *A.marina*. The red shifted APC is most probable located in the linker protein representing the so called terminal emitter (TE). Further elucidation of the fast equilibration processes in the PBP antenna of *A.marina* is not easily possible with TWCSPC as can also be shown by numerical simulations of the expected time resolved spectra. Measurements of flash induced transient absorption changes performed in the fs-ps time domain by C.Theiss on isolated PBP complexes showed fast energy equilibration between different phycocyanine (PC) molecules (equilibration time < 1 ps) which are bound to a hexameric protein structure in the PBP of *A.marina* and in PBS. The equilibration between the PC and the APC containing hexamers occurs with a time constant of 3-5 ps [44]. Complementary techniques like hole burning spectroscopy and transmission electron microscopy (TEM) completed the picture of the measurement results of transient fluorescence and absorption changes.

Simulations of the exciton diffusion inside the rod shaped structures of *A.marina* were performed. These simulations showed that the EET rate depends critically on entropy effects caused by the small distance of the energetic states of the coupled PC chromophores. Therefore the exciton diffusion is slower inside the PBS containing more than 300 PBP chromophores [65] coupled to Chl *a*, in contrast to the PBP complexes of *A.marina* containing 63 PC and 6 APC chromophores coupled to Chl *d*. The geometry and small size of the *A.marina* antenna in contact to Chl *d* leads to faster energy transfer in comparison to the structure of the much larger PBS.

In *A.marina* the site energies of the different chromophores in the PBP and membrane intrinsic Chl *d* containing antenna are tuned by the protein environment to achieve high EET rates and to adapt to the external light conditions. This enables *A.marina* to live in a coexistence with Chl *a* containing prokaryotes like *Prochloron didemni*.

The distance between the terminal APC-emitter of the PBP antenna in *A.marina* and the nearest Chl *d* molecule in the membrane intrinsic antenne was determined to 2.7 ($^+$/- 0.3) nm according to the theory of Förster resonance energy transfer (FRET) [52]. This distance rises at 0°C as a result of decoupling of the PBP antenna from the membrane intrinsic Chl *d* antenna [43]. Similar effects were also observed in artificial FRET-systems constructed from charged CdSe-quantum dots in contact with PBP complexes isolated from *A.marina* [51]. The mechanism could help to construct switch-able light harvesting systems.

The mathematical model that is used for the numerical simulation of EET and ET processes in this thesis is constructed from rate equations. It implements a concept of coupled linear differential equations 1st order that is suitable to describe any system that can be analysed in terms of "states" that undergo dynamical transitions and therefore exhibit occupation probabilities evolving in time. This formalism was used to describe intensity dependent fluorescence quantum yield changes along eight orders of magnitude of the time scale from 100 ns up to a value of 10 seconds [57, 58].

A very interesting natural PPC is the water soluble chlorophyll binding protein (WSCP) which exhibits an unusually high photostability of the chlorophyll dimers bound to the protein matrix. The reason for this photostability is not yet clear in full detail [66-68]. In agreement with current literature it is assumed that the protein environment forms a diffusive barrier for oxygen and therefore prevents the reaction between Chl triplet states and oxygen in its triplet ground state to highly reactive singlet oxygen [46, 69, 70]. Such a protective protein, especially if the protein barrier might be photoswitch-able, is of highest interest for biomedical applications of pigments in photodynamic cancer diagnostics and therapy.

The transient absorption change and fluorescence dynamics of WSCP can be explained by a combination of pigment-pigment and pigment-protein interactions [47]. Two strongly coupled chlorophyll molecules are modulated by the protein environment which leads to retarded wavelength shifts of the fluorescence or effects of spectral diffusion.

Based on the proposal of an "open sandwich" dimer motif for this pigment array for recombinant class IIa WSCP from *cauliflower* [69] T. Renger et al. used a microscopic theory of the spectra and available data of linear absorption at 77 K and 298 K and circular dichroism at 298 K to characterize the pigment-pigment interaction [38]. They calculated that the angle between the planes of the two Chl

molecules in this configuration is about 30° in contrast to the value of about 60° gathered from the original calculations [69] employing a more simple Gaussian band fitting procedure (see also [48]).
T. Renger et al. calculated the center-to-center distance of the transition dipole moments of the two coupled Chl molecules to be 0.74 nm. The authors explained the data of femtosecond absorption spectroscopy [2, 46] that suggests about 400 fs for the exciton relaxation in Chl *a*/Chl *b* heterodimers bound to class II a WSCP. The predicted 30° angle between the transition dipoles of the Chl molecules was later confirmed by the X ray crystallography structure of class IIb WSCP of *Lepidium virginicum* [70] at a resolution of 2.0 Å. This similarity between reconstituted recombinant class IIa from *cauliflower* and the native class IIb WSCP from *Lepidium virginicum* may be indicative of a general mode of pigment array in class II WSCPs. WSCP therefore turned out to be an excellent model system for systematic experimental and theoretical studies on strongly coupled Chl molecules and the functionalizing of Chls by the protein matrix. It opens the way for further detailed analyses on a deeper understanding of the properties of pigment-protein complexes.

The newest findings deliver information on temporal sub-ps dynamics and sub-nm structural organisation. Therefore we suppose that the termini “picobiophotonics” or even “femtobiophotonics” seem to be suitable to describe the biophysical research at the edge of achievable resolution. These termini are therefore introduced in the work presented here.

The investigation of the temporal resolution limit of TWCSPC showed that fluorescence spectroscopy is a tool for the study of ps and even sub-ps-processes with pulses down to 100 ps in full width of half maximum if - and only if - the system and the sample are sufficiently stable and the investigated sample consists of a sufficient small number of coupled states. In this case the resolution is rising with the total energy used for the measurement (and therefore with measurement time if a constant energy per pulse is used during the experiment). In some cases the principal resolution limits allow a much better resolution than achieved up today [19, 27, 30]. It seems possible in principle to analyse the spatial distribution of the probability of presence of an electron down to the pico-meter regime employing an optical wide field fluorescence microscope [12-15]. But this method is very time consuming and/or needs high intensities of the employed laser beams.
In marked contrast to the finding that resolution is still far away from the best achievable values it was shown that a unique analysis of ultrafast single energy transfer steps is not always possible. In the PBP antenna of *A.marina* for example the equilibration between PC and APC molecules can still be resolved with a time constant of 20 ($^{+}$/- 10) ps [43]. The information of faster equilibration processes simply can not be found in the fluorescence dynamics observed by TWCSPC. In that case it is intrinsically impossible to extract information oabout the accurate values of the single energy transfer steps as the dynamics of different coupled states take place in the same time domain between spectrally strongly overlapping chromophores. The states of the systems can mix in a way that makes

it impossible to separate the processes even if the experimental resolution is high enough. This fact mostly limits the available information content [57]. TWCSPC is limited by the amount of accessible information as shown with theoretical approaches regarding single molecule fluorescence microscopy [71,72]. The desired goal of the scientist should be to extract all experimentally accessible information to have the general possibility to prove any predicted effect of an applied theory. The experimenter is not able to accumulate an infinite amount of information and it would be efficient to choose the exact amount. Therefore the experimenter has to take care that the accumulated information represents the accessible information [71].

An improvement can only be achieved by a study of the decomposed sample or by the employment of complementary experimental techniques which localise the observed state. But in both cases the experimental results might depend on the special configuration of the sample and the measurement setup. It is therefore necessary to investigate the influence of the sample preparation and experimental manipulation onto the experimental results. In the case of the investigation of PBP and WSCP combined results of TWCSPC, time- and wavelength resolved fs- absorption changes, ground state absorption spectroscopy, hole burning spectroscopy, transmission electron microscopy and theoretical analysis [37], sometimes based on additional experiments (e.g. CD or LD spectroscopy [38]) were used to complete the picture. Other complexes (LHC aggregates) were studied with atomic force microscopy (AFM) [45].

It might be useful to accomplish a kind of methodical statistics of the experimental techniques. Then the scientist can shift systematic aberrations to statistical uncertainties to a certain amount. For this purpose the researcher has additionaly to be able to reproduce the sample often enough without any variation.

In most cases the principal resolution is not limited by the setup but by the heterogeneity of the sample or even the uncertainty of the observed states. Doing high resolved fluorescence nanoscopy we shift the uncertainty from the optical wavelength representing our measurement setup to the observed states [20], which is an ultimate resolution limit.

This thesis starts with a short introduction of the structure and organisation of the investigated samples (chap. 1) and explains the experimental setup of TWCSPC and the techniques of data analysis (chap. 2). Chapter 3 presents an overview of the existing theoretical concepts and introduces the formalism of rate equations used to simulate the time course of the fluorescence emission (chap. 3.2). The light driven dynamics of excitons is investigated in the WSCP complex (chap. 4), in the isolated PBP antenna and whole cells of *A.marina* (chap. 5) and in complex composed hybrid systems consisting of semiconductor nanoparticles and the PBP antenna of *A.marina* (chap. 6). Finally the full PS II dynamics of EET and ET transfer steps in whole living organisms (whole leaves of the higher plant *Arabidopsis thaliana*) (chap. 7) are discussed. In the latter case the formalism of rate equations is used to cover 15 orders of magnitude in time (fs- processes to changes in the time domain of seconds).

1. BIOLOGICAL BACKGROUND

Träumen wir uns für einen Moment in einen zukünftigen Zustand der Naturwissenschaft, in dem die Biologie ebenso vollständig mit Physik und Chemie verschmolzen sein wird, wie in der heutigen Quantenmechanik Physik und Chemie miteinander verschmolzen sind. Glaubst du, dass die Naturgesetze in dieser gesamten Wissenschaft dann einfach die Gesetze der Quantenmechanik sein werden, denen man noch biologische Begriffe zugeordnet hat, so wie man den Gesetzen der Newtonschen Mechanik noch statistische Begriffe wie Temperatur und Entropie zuordnen kann; oder meinst du, in dieser einheitlichen Naturwissenschaft gelten dann umfassendere Naturgesetze, von denen aus die Quantenmechanik nur als ein spezieller Grenzfall erscheint, so wie die Newtonsche Mechanik als Grenzfall der Quantenmechanik betrachtet werden kann ?

Werner Heisenberg (1901 – 1976), German physicist (see [1])

1.1 Structures and organisation of photosynthesis

Photosynthesis appears to be the biosphere´s most important process in solar energy exploitation [73]. It can be described as the light induced chemical reaction of water with carbondioxide to glucose (see Figure 1):

$$12\,H_2O + 6\,CO_2 \overset{h\cdot\nu}{\rightarrow} C_6H_{12}O_6 + 6\,O_2 + 6\,H_2O \quad \text{chemical equation 1}$$

The photosynthetic reaction summarized by chemical equation 1 is highly endergonic and driven by Gibbs free energy of solar radiation on earth that is absorbed by green plants (for more detailed thermodynamic considerations see chap. 3.5).

The dynamics and structural organisation of photosynthetic organisms covers more than 10 orders of magnitude in space, ranging from the pm-dimension of electronic orbitals up to tens of meters sized plants and up to 26 orders of magnitude in time, from the fs dynamics of light absorption to the life time of trees covering thousands of years.

Figure 1 presents a schematic overview on the hierarchic organisation of structures that form a photosynthetic organism (e.g. a photosynthetic tree of 10 m) which is a sum of its cells (typically 10-100 µm). The photosynthesis takes place inside the leaves which are formed by an inhomogeneous 3-dim. array of cells on the µm-scale. The single cell is the smallest organized form that is still named “living system”. It is a whole organism and all higher individual organisms are formed by a symbiotic biosystem of such cells [74, 75].

In eukaryotic organisms the cells contain chloroplasts of very different sizes and geometries (see e.g. [76]) where photosynthesis takes place inside the thylakoid membrane.

The cells contain the endoplasmatic reticulum that connects ribosomes and the cell organells, i.e. mitochondria, chloroplasts, the nucleus and the vacuole. Additional minor components like hormones, proteins, free DNA and RNA and a number of different small molecules are not shown in Figure 1. The chloroplasts have their own DNA, lipid droplets, starch, ribosomes and contain the Grana stacks of the thylakoid membrane. The thylakoid membrane is formed by a lipid bilayer with hydrophilic surface. Inside the thylakoid membrane the lipophilic environment contains the membrane proteins. They are hydrophobic and therefore bound to the membrane (membrane intrinsic proteins).

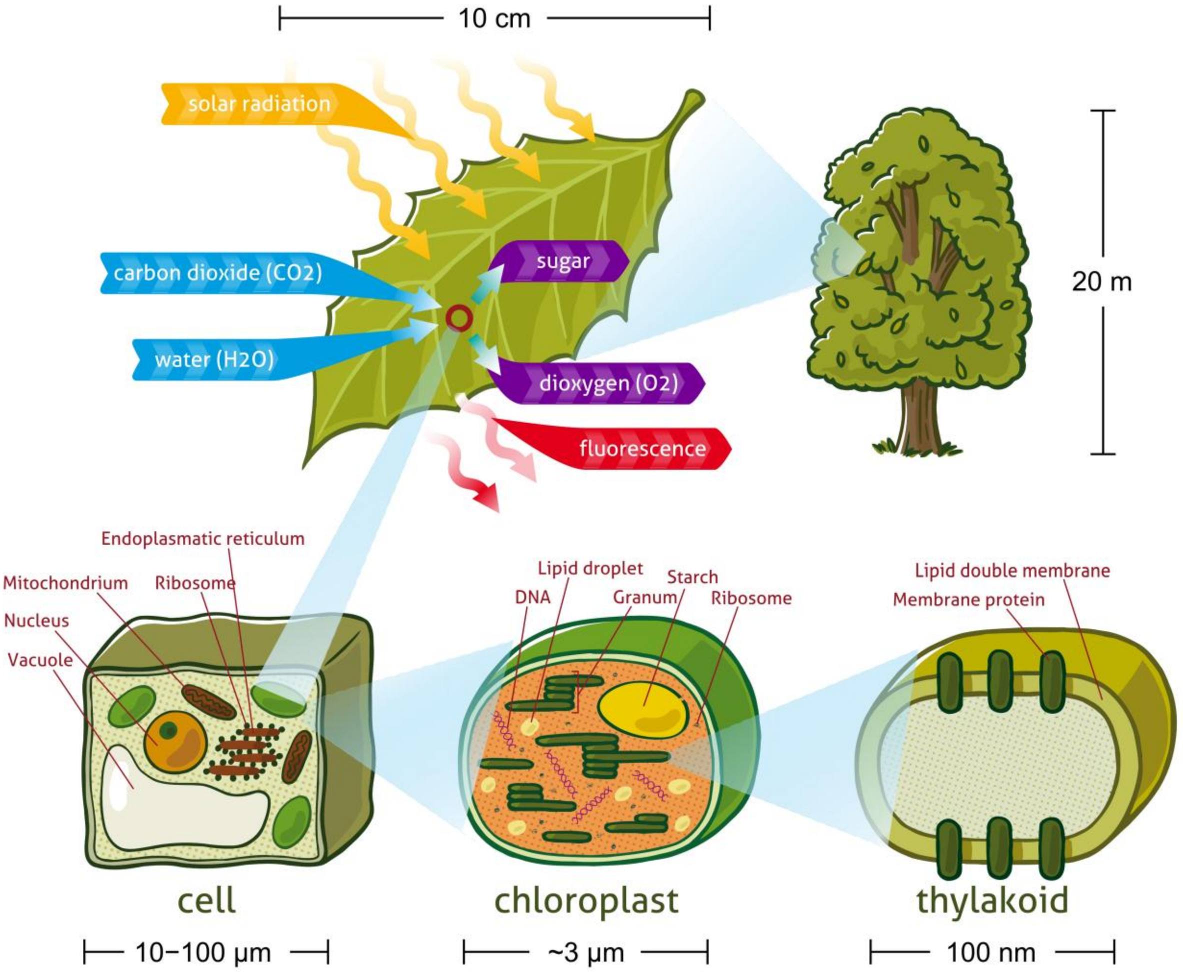

Figure 1: Hirarchic structures of green plants. The chloroplasts contain the Grana stacks of the thylakoid membrane where photosynthesis takes place. Figure provided by Florian Schmitt (Florian Schmitt Illustration)

Figure 2 shows schematically the substructure of the chloroplasts containing the thylakoid membrane where the photosynthetic pigment-protein-complexes are located as membrane intrinsic proteins.

The dynamics of the thyalkoid membrane is assumed to have impact on the transient changes of the quantum yield of photochemical light transformation.

The photosynthetic reactions leading to CO_2-fixation comprise the light driven reactions which take place inside the thyalkoid membrane, and the “dark” reactions which take place inside the chloroplast stroma (indicated as a red cycle process in Figure 2).

The thylakoid membrane divides the aqueous phase of the chloroplasts into the thylakoid lumen and the chloroplast stroma. Protons released into the thylakoid lumen and protons transferred from the stroma into the lumen form a transmembrane electrochemical potential difference. This drives the adenosine triphosphate (ATP) synthase that phosphorylates adenosine diphosphate into the energy rich ATP compound required as free energy source in the dark reaction for carbon reduction.

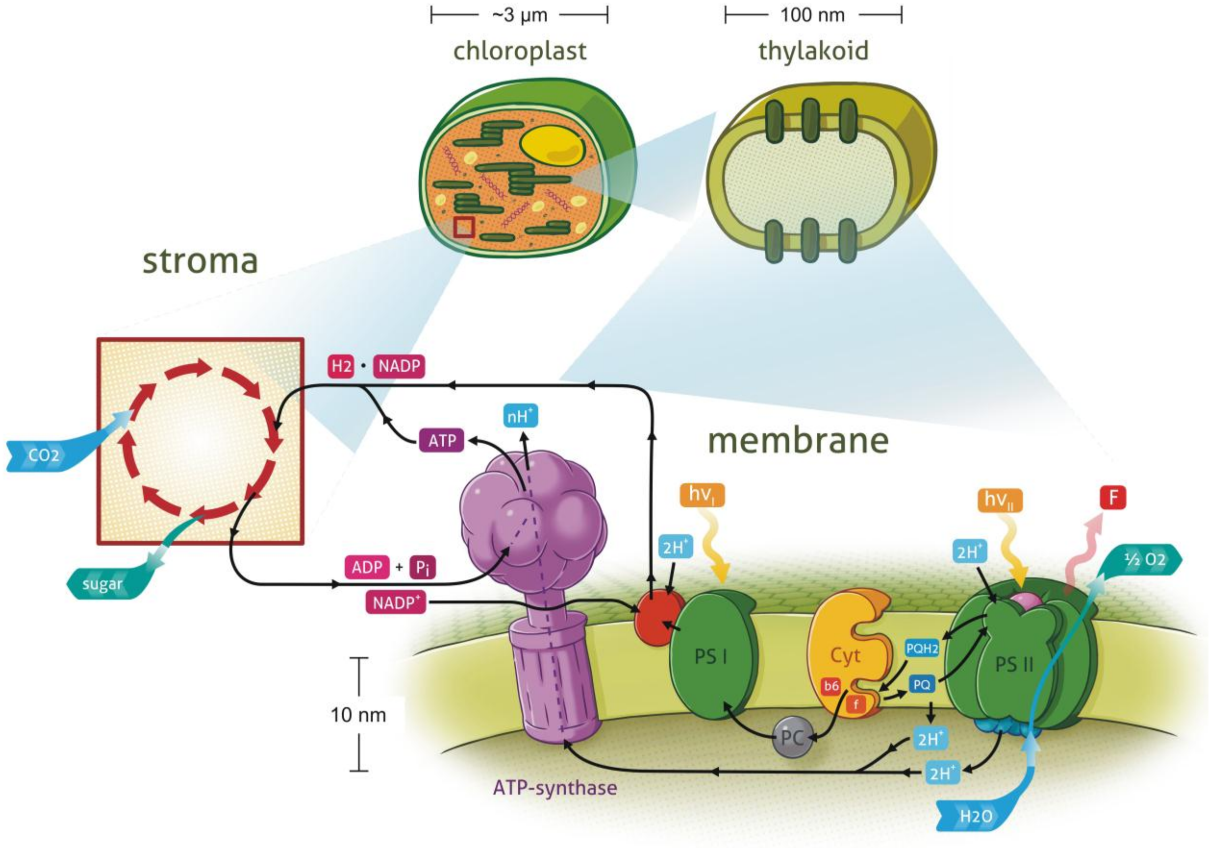

Figure 2: Membrane proteins inside the lipid double membrane of the thylakoids. Figure provided by Florian Schmitt (Florian Schmitt Illustration). For further details see text.

The “light” reaction performs the exploitation of solar energy by highly functionalized PPCs. Solar energy represents the unique Gibbs free energy source of earth´s biosphere. The Gibbs free energy is converted into high energy chemical compounds via the process of photosynthesis. This is achieved perfectly by incorporation of suitable chromophores into protein matrices. The PPCs are optimized to energy absorption and transfer producing the high energetic compounds ATP and NADPH.

Two classes of pigment-protein complexes have evolved with distinctly different functions: antenna systems and reaction centers (RCs) (see [77]). These operational units perform the light driven processes of photosynthesis in a controlled and highly efficient manner: The pigments of the antenna complexes (for reviews, see [73, 78]) absorb light and transfer the electronic excitation energy via radiationless EET to the photochemically active pigment(s) of the RCs. There they are transformed into electrochemical free energy (for a review, see [79]).

The photochemically active chlorophyll containing photosynthetic PPCs are classified into the PS I and the PS II (Figure 2). Electrons flow from PS II to PS I. Light absorption changes the redox properties of a single electron in each photosystem. The nomenclature has developed historically denoting the “first” PS as PS II which delivers electrons to the PS I [80].

It should be mentioned that in contrast to the simplified schemes shown in Figure 1 and Figure 2 the distribution of different pigment-protein complexes with different optical properties is not homogeneous along the thylakoid membrane (PS I and PS II [81] or PS II complexes with different antenna sizes, so called alpha centers and beta centers [82], are inhomogeneously distributed along the thylakoid membrane).

The light energy is absorbed by chromophores bound to the photosynthetic complexes of PS I and PS II. These chromophores are mainly chlorophyll and carotenoid molecules. The redox chemistry of PS I is not a topic of this thesis and therefore a detailed description of this system is not presented here. The reader is referred to the existing literature of the light harvesting complex and RC of PS I (see [80] and references therein).

The electronically excited singlet states formed by light absorption of the Chl molecules are not completely transformed into Gibbs free energy. A fraction is emitted as red fluorescence and the dynamics of the fluorescence emission of all samples containing PS I and PS II is mainly determined by the properties (organisation and coupling) of the photosynthetic pigment-protein complexes of PS II (see [83]).

Structure, electrochemistry and function of the PS II

While the light harvesting systems of the PS II exhibit strong variations between different photosynthetic organisms (e.g. cyanobacteria and higher plants) the architecture of the so called core complex containing the RC is very similar among all oxygenic photosynthetic organisms. The RC consists of the D1 and D2 core protein (in anoxygenic purple bacteria the analogous proteins are named L and M, respectively) binding 6 Chl molecules and the CP 43 and CP 47 core antennae (see Figure 3) that contain 13 and 16 Chl molecules, respectively. After light absorption inside the PS II an excited singlet state of the chlorophyll finally localizes inside the RC. The molecular identities of the excited state $^1P680^*$, from where the electron transfer starts, and the state $P680^{+\bullet}$, where the hole stabilizes, are different [84]. Together with the strongly coupled Chl dimer P_{D1}/P_{D2} called “special pair” the two Chl molecules Chl_{D1} and Chl_{D2} and two pheophytin molecules which have different site energies form a flat energetic “trap” represented by the reaction center in comparison to the excited

states in the Chl antenna and the two Chl molecules Chl_{zD1} and Chl_{zD2}. (for further details see [84] and references therein).
PS II and PS I are functionally connected by the $Cytb_6f$ complex where plastoquinol PQH_2 formed at PS II is oxidized and the electrons are transferred to PS I via plastocyanin (PC) as mobile carrier (see Figure 2). This process is coupled with proton transport from the stroma to the lumen thus increasing the proton concentration in the lumen. At PS I the light driven reaction finally leads to the reduction of $NADP^+$ to NADPH. The proton gradient provides the driving force for the ATP synthase where ATP is formed from ADP + P. NADPH is used in the dark reactions for CO_2 reduction to produce glucose inside the chloroplast stroma.

The spatial separation between lumen and stroma and the oriented arrangement of PS I, PS II and $Cytb_6f$ enables a directional electron flow coupled with the formation of a transmembrane electrochemical potential difference. This way the absorbed Gibbs free energy of the photons is partially and transiently “stored”. For further thermodynamic considerations of the initial processes of photosynthesis, see chap. 3.5.

The antenna complexes permit a very efficient adaptation of anoxygenic photosynthetic bacteria [85], cyanobacteria [86] and plants [87] to different and widely varying illumination conditions. At low light intensities the few excited singlet states are funnelled with high efficiency to the photochemically active pigment of the RCs. There the photochemical charge separation takes place [84, 88 - 92] An opposite effect is induced under strong illumination: The radiationless decay of the superfluous excited singlet states is stimulated by opening dissipative channels. In addition (bacterio) chlorophyll triplets formed via intersystem crossing are effectively quenched by carotenoids (Cars) [93].
In contrast to the reactions in the antenna, only the excited states in RCs, PS I and PS II are transformed into electrochemical Gibbs free energy via electron transfer thus giving rise to formation of the primary cation-anion radical pairs, followed by stabilization steps under the participation of secondary acceptor components (for reviews, see refs [84, 88 - 92] and references therein). In plants both of these types of pigment-protein complexes (antennas and photosystems) are highly hydrophobic. Therefore they are located inside the lipophilic intrinsic part of the thylakoid membrane as integral proteins.

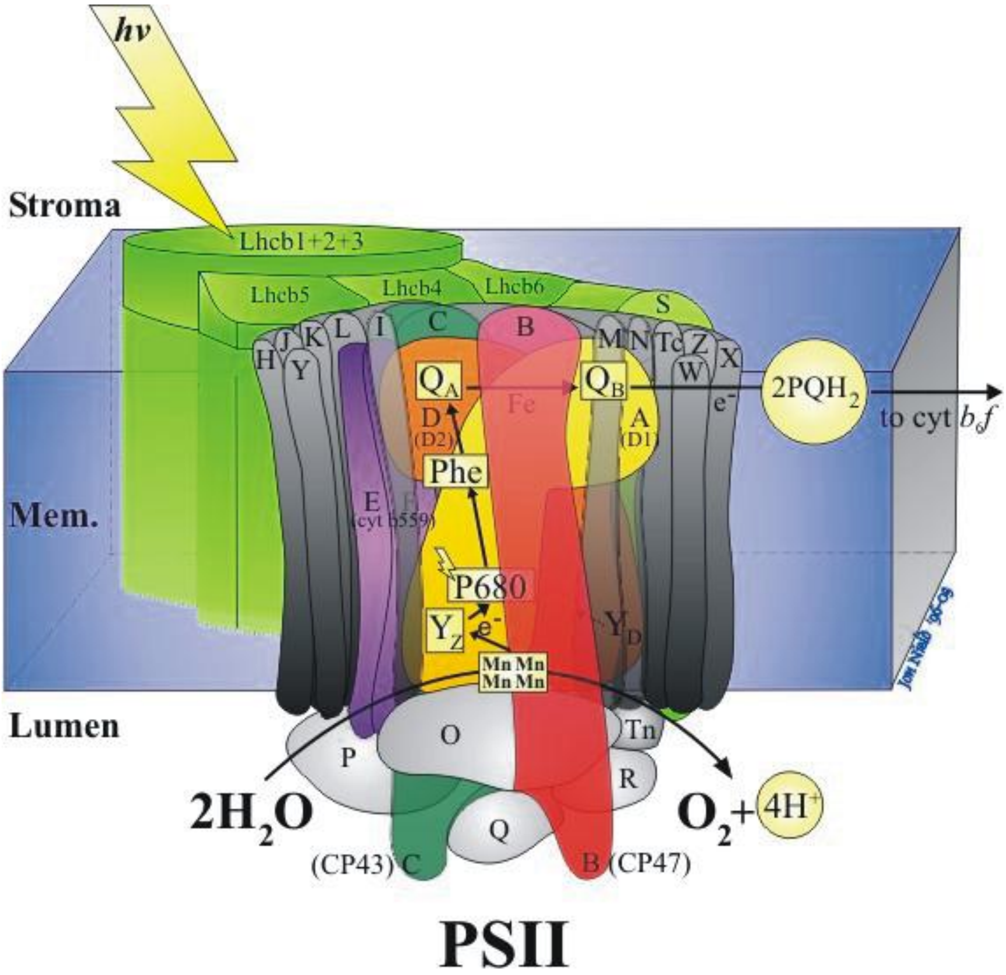

Figure 3: Subunits of the PS II of higher plants including the LHC b complexes as light harvesting system and the core complex [94] (for details see text).

Figure 3 presents a schematic overview of the protein and pigment protein complexes which form the PS II. The electron flow/ pathways between the cofactors shown in Figure 3 are indicated as black arrows.

The PS II light harvesting complex (LHCII) in higher plants contains the pigments Chl *a*, Chl *b* and carotenoids (see [73],[95] and chap. 1.3.1). The pigment-pigment and pigment-protein interaction leads to a complex energetic surface of the excited Chl states (see [96]). Next to the Chl containing core antenna the LHCII complexes are also in contact to protein structures (shown in black in Figure 3) surrounding the core complex and containing nearly no pigments. These proteins most likely stabilize the structure of the core complex. Like the protein complex S they work as linker proteins which seem to be very important for the energy transfer processes. The exact function of these linker proteins is still not clearified in full detail [97]. The core complex of the PS II (see chap. 1.4) consists of the reaction center (D1, donor side, yellow and D2, acceptor side, orange in Figure 3) and the Chl containing core proteins CP 43 (dark green in Figure 3, containing 13 Chl molecules) and CP 47 (red in Figure 3, containing 16 Chl molecules) which form the core antenna. As mentioned above this core complex exhibits a common architecture among all oxygenic photosynthetic organisms (and is also very similar in anoxygenic photosynthetic bacteria). It remained nearly unchanged during evolution. Differences are found in the oligomeric macrostructure of the core complex that leads to dimeric or tetrameric supercomplexes as found in several species, e.g. the cyanobacteria *Prochloron didemni* and *A.marina* [98], [99].

In marked contrast the antenna complexes of cyanbacteria, green sulphur bacteria, purple bacteria and higher plants (just to mention a few examples) are very different in composition and/or architecture. An overview on different light harvesting systems is presented in chap. 1.3. ff.

The substrate water (H_2O) interacts with the water oxidising complex (WOC) containing four manganese ions (see Figure 3). The interaction between H_2O and the WOC elevates the energetic state of the H_2O molecule. The interaction process activates the release of two electrons per molecule H_2O to an intermediate acceptor Y_Z which fullfills the role of an electron donator for $P680^+$. P680 is the lower excitonic state of the two Chl *a* molecules forming the „special pair“ P_{D1}/P_{D2} inside the RC [100].

The oxidation of P680 is possible via the interaction with pheophetin (Pheo). The formation of the first radical ion pair $P680^+Pheo^-$ is the primary charge separation. The energy of this radical pair strongly depends on the state of the environment. After formation of the primary radical pair the environment relaxes and shifts the energy level of $P680^+Pheo^-$ to a lower value [101].

Due to the strong interaction between $P680^+$ and $Pheo^-$ the recombination rate of $P680^+Pheo^-$ is comperatively high. The charge separation is more stable after the relaxation of the environment and the subsequent “charge stabilization” process, when $Pheo^-$ releases an electron to the plastochinone Q_A (see chemical equation 2). Strongly coupled molecules with partial excitonical coupling and EET fast in comparison to the resolution limit of TWCSPC are indicated with a double arrow ($\Leftrightarrow$), while localised electron transitions are indicated with simple arrows for reactions that occur in both directions ($\underset{\leftarrow}{\longrightarrow}$). The index N in chemical equation 2 indicates that a high number of Chl molecules (N = 100 – 400) are coupled inside and in between the PS II subunits. The electronically excited complexes are marked with an asterix (*).

$$\left((Chl)_N \Leftrightarrow P680\right)^* \, Pheo\ Q_A \underset{\leftarrow}{\longrightarrow} (Chl)_N P680^+\ Pheo^-\ Q_A \longrightarrow (Chl)_N P680^+ Pheo Q_A^-$$

chemical equation 2: most important steps of the charge separation in the reaction center after absorption of light energy in the antenna which interacts strongly with the *P680* inside the reaction center. The electron is released towards pheophetin and (*Pheo*) and plastochinone (Q_A).

The primary donor P680 and the primary acceptor Pheo are bound to the D1 protein as shown in Figure 3. D1 is the donor side of the reaction center. Q_A is located inside the D2 protein on the acceptor side. From there the electron is transferred towards the plastoquinone molecule at the Q_B site. This mobile plastochinone electron carrier binds protons and diffuses through the membrane as Q_BH_2. Therefore electrons are transferred towards the PS I via the cytochrome complex.

1.2 Fluorescence emission as a tool for monitoring PS II function

As mentioned in [57, 58] the radiative emission from Chl *a* offers an invaluable tool to study the dynamics and the efficiencies of the primary processes of photosynthesis [65, 81, 83, 102-125]. Important information can be gathered from various techniques of fluorescence measurements depending on the mode of excitation and detection.

Information on excitation energy transfer among antenna pigments, trapping, charge separation and charge stabilisation within the reaction centers (according to chemical equation 2), forming of channels for nonphotochemical quenching, pigment–pigment or pigment-protein coupling can be gathered from analyses of the time decay and wavelength dependence of the emitted fluorescence [65]. Often short (typical ps) light pulses are used [115, 116]. This technique of time resolved analysis of prompt fluorescence decay after excitation is often performed in the mode of TCSPC as done in the thesis presented here.

A different technique is the monitoring of light induced transients of fluorescence quantum yield, often referred to as fluorescence induction. A great variety of methods is applied for monitoring fluorescence induction curves: samples are excited either by continuous light at different intensities [102, 103, 112, 117] or by light pulses of different duration and intensities [81, 104, 118-120], with or without a background of continuous light.

In general, the prompt fluorescence decay and the transient changes of the fluorescence yield are complicated functions depending on many parameters. Therefore model-based data analysis is required to deconvolute both, the fluorescence decay [83, 107, 109] and the transient changes of the fluorescence emission [112, 114] into a set of parameters for individual reactions.

Numerous models which simulate the experimentally determined fluorescence curves have been developed. One essential feature for data analysis is the finding that fluorescence emission of oxygen-evolving photosynthetic organisms is dominated by processes connected with photosystem II (PS II) (see [57, 112]).

It has been shown that the prompt fluorescence decay is mostly determined by the kinetics of EET in antenna complexes, charge separation and charge stabilisation as shown in chemical equation 2 [83], [107, 109].

A much greater variety of models exists for simulations of the transient fluorescence change from ns – s range, because these are monitored under quite different excitation conditions. They depend on very different processes which take place on different time scales. The models typically cover a time range of up to about 10 s. At time periods longer than 500 ms, formation and decay of an electric potential and the pH difference across the thylakoid membrane have to be taken into account for an accurate description of transient fluorescence changes [57, 58, 105, 110, 121-125].

1.3 Antenna complexes in photosynthesis

The enhancement of the absorption cross section of the photosystems is only one function of photosynthetic antenna complexes. In addition they have regulatory functions like the dissipation of excess energy to avoid the generation of singlet oxygen at high light conditions (see [76] for an overview).

The structural arrangement of the pigments and the fine tuning of the Chl molecules by the environment leads to a directed energy transfer from the antenna to the photochemically active reaction center (RC). The absorbed light energy is able to bridge distances of 30 nm to the RC with up to 99 % quantum efficiency [76].

In contrast to the common architecture of the RC the antenna structures are found to vary in different photosynthetic organisms. The exact pigment composition of the antennae is not completely determined for a certain species but depends on the growth condition, light intensity and light quality during growth. The latter effect is known as chromatic adaption.

Therefore a short outline of some selected antenna systems of anoxygenic bacteria, oxygenic bacteria and higher plants is presented in the following subsections. A detailed overview on the different complexes is found in ref. [76].

Anoxygenic photosynthetic bacteria contain bacteriochlorophyll (BChl) in the antenna complexes and reaction centers. BChl *a* is e.g. found in the light harvesting antennae (LH1, LH2) of purple bacteria as presented in chap. 1.3.2 and the Fenna-Matthews-Olson (FMO) complex of green sulphur bacteria (chap. 1.3.3).

In contrast to anoxygenic bacteria the oxygenic photosynthetic organisms contain two separated photosystems (PS I and PS II). Both PS have own reaction centers and antenna complexes. The major membrane extrinsic light harvesting antenna of cyanobacteria are phycocyanobilin containing protein structures that are mostly associated with PS II but are also found to undergo so called “state transitions” between PS II and PS I. The PBPs organize in different forms as huge phycobilisomes in most cyanobacteria (chap. 1.3.4) or minor rod shaped PBP antennae in the cyanobacterium *A.marina* (chap. 1.3.5). Cyanobacteria contain several additional pcb complexes (recently also named “chlorophyll binding proteins” CBP) surrounding the reaction center and core proteins (see chap. 1.4 and [98], [99]).

In higher plants the trimeric major light-harvesting complex II (LHCII) is found which is located inside the thylakoid membrane present in ratios of four or even more trimers per PS II core dimer (see Figure 3 and chap. 1.3.1 and [128]). The LHCII is one of the most prevalent proteins found on earth.

In addition oxygenic photosynthetic organisms contain further Chl binding proteins that are associated with the PS II core complex (see Figure 3 chap. 1.4). Next to the core proteins CP 43 and CP 47 containing 13 and 16 Chl molecules, respectively, further minor complexes, the CP 24, CP 26 and CP 29 are found in higher plants which take over regulatory functions (see [76], [79] for more details).

1.3.1 The light harvesting complex of PS II (LHCII) of higher plants

In the photosynthetic membrane an array of several antenna units is functionally connected with one reaction center complex, so that energy transfer between the antenna complexes and from the antenna to the RC occurs.

Four or even more (six in Figure 3) trimeric LHCII structures are connected with one reaction center. It is outlined in ref. [45] that the PSII-LHCII super-complexes can be arranged in large ordered domains in the granal thylakoids [129]. Ordered LHCII domains with a diameter of hundreds of nanometers have been observed [130], [131]. These physical domains contain thousands of pigments however it is not clear whether and to what extent the excited singlet states can migrate in these large LHC domains during their lifetime. The size of the functional domain, i.e. the number of pigments connected via EET depends on the excited state lifetime and on the time of transfer between the pigments. The EET inside the LHCII is found to take place on the fs-ps time scale [2]. These dynamics strongly depend on the structural arrangement of the pigments which is stabilized by the protein matrix that leads to a well defined coupling of the embedded pigments. Structural arrangement and EET are strongly correlated. Even quantum entanglement might influence the ultrafast EET in LHCII [126, 127].

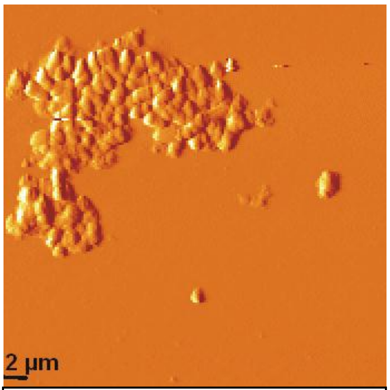

Figure 4: AFM picture of aggregated LHCII trimers prepared by detergent removal. The LHCII samples at original concentration of 10 µg Chl/ml were immobilized and dried on glass plates precoated with poly-L-lysine. The AFM images were taken in close-contact mode. For further information see ref. [45].

LHC trimers tend to aggregate strongly depending on the suspension medium and the preparation protocol. Figure 4 shows that huge LHC aggregates can be formed in diluted media. The size of the homogeneous LHCII domains in Figure 4 reaches values of up to 2 µm.

The extent of EET between photosynthetic units, termed connectivity, has been proposed to explain the sigmoidal shape of the fluorescence induction transient. Different models have been proposed, like the so called “lake model” where the reaction centres are embedded in a network of interconnected antennae [103, 132, 133, 134].

According to the concept of connected photosynthetic units the functional domain size of the LHC antenna is much larger than the number of pigments in one pigment-protein complex. Several attempts exist to estimate the domain size in thylakoids and in isolated LHCII preparations. A common approach is based on studies of excitation annihilation due to the interaction between two excited (singlet or triplet) molecules which results in the dissipation of one excitation [135] according to

$$\begin{aligned} S_1 + S_1 &\rightarrow S_n + S_0 \xrightarrow{\text{int}.conversion} S_1 + S_0 \\ S_1 + T_1 &\rightarrow T_n + S_0 \xrightarrow{\text{int}.conversion} T_1 + S_0 \end{aligned}$$

chemical equation 3

where S_i and T_i denote the i$^{\mathrm{th}}$ excited singlet and triplet state, respectively. The coexistence of two or more excited electronic states in one domain therefore leads to quenching and a reduction of the average excited-state lifetime. A theory has been developed that relates the excited-state lifetime with the domain size [136].

Kolubayev et al. [137] estimated approximate domain sizes in thylakoids and isolated LHCII of at least 200-250 Chl molecules by measuring the relative fluorescence yield as a function of excitation intensity as indicator of the singlet-triplet quenching. Gillbro et al. [138] investigated the singlet-singlet annihilation in LHCII aggregates with picosecond absorption and confirmed this minimal value of 200-250 interconnected Chl molecules for the domain size. Barzda et al. [139, 140] calculated 64 nm for the radius of excited state migration, which corresponds to a much larger number of Chl molecules. In a different approach the energetic connectivity was analyzed in aggregated and solubilised LHCII and native thylakoid membranes, employing artificial exogenous singlet quenchers, like dinitrobenzene and phenyl-*p*-benzoquinone. Different types of isolated LHCII and native thylakoid membranes were investigated with respect to the estimated functional domain size. In LHCII macroaggregates the resulting values were 15-30 LHCII trimers, corresponding to 600-1200 chlorophyll molecules. In native thylakoid membranes the domain size was equivalent to 12-24 LHCII trimers, corresponding to 500-1000 chlorophylls [45].

New investigations have shown that the different dynamics of biexcitons and higher exciton states in comparison to single excitons in coupled quantum configurations mostly contribute to the decrease of the fluorescence quantum yield of LHCII complexes at high excitation intensities [141, 142]. The main physical reason for this effect is Pauli blocking of radiative relaxation channels as described in [143], rather than singlet-singlet annihilation. Also the photon statistics of the excitation field plays an important role for the excitation dynamics if biexcitons or higher excitonic states are excited in LHCII complexes [42]. Therefore the values gathered from singlet-singlet annihilation studies might deviate systematically from the “real” domain size and the average migration radius of excitons in coupled nanostructures.

In the thesis presented here mainly single exciton dynamics in antenna complexes as it is expected for low excitation energies is investigated. Even under bright sunshine the light intensity is not high enough to excite biexcitons in plant LHCII. At high light energies efficient quenching mechanisms occur that depopulate excited states due to nonphotochemical quenching [144, 145].

Aggregates of isolated LHCII exhibit drastically shortened fluorescence lifetime [146, 147] in comparison to isolated LHC (solubilised LHC complexes). Aggregate formation has been proposed to act in the excitation quenching in vivo [148- 150]. Different views on the mechanism of quenching in aggregated LHCII were discussed [150, 151]. One possible mechanism is the formation of new quenching centres upon aggregation in most or all antenna complexes. Another concept suggests that the overall quenching results from the increased domain size, but only few or no new quenching sites are formed [152, 153].

The molecular structure of the LHCII trimer with a diameter of about 10 nm is shown in Figure 5 [154]. Each monomeric unit contains 6 Chl *b* and 8 Chl *a* molecules. In addition, four carotenoid molecules are bound per monomeric subunit, i.e. two luteins, one neoxanthin and one violaxanthin [155]. The carotenoid molecules accomplish a special regulatory function. Violaxanthin exhibits an energetically slightly higher excited state than the first excited singlet state in Chl *a* (^{1}Chl a^*), while the first excited state in zeaxanthin - which has a larger delocalised π-electron system than violaxanthin - is lower than ^{1}Chl a^*. Violaxanthin can absorb light energy and transfer it to Chl molecules via the mechanism of Dexter transfer (see chap. 3.3), whereas the energy flows from Chl to zeaxanthine. This process in the plant LHCII is regulated by the so called “Xanthophylle cycle” deepoxilating violaxanthine to zeaxanthine at high light conditions [76] by violaxanthin-deepoxidase, whereas this process is reversed by the zeaxanthine-epoxidase [156], [157].

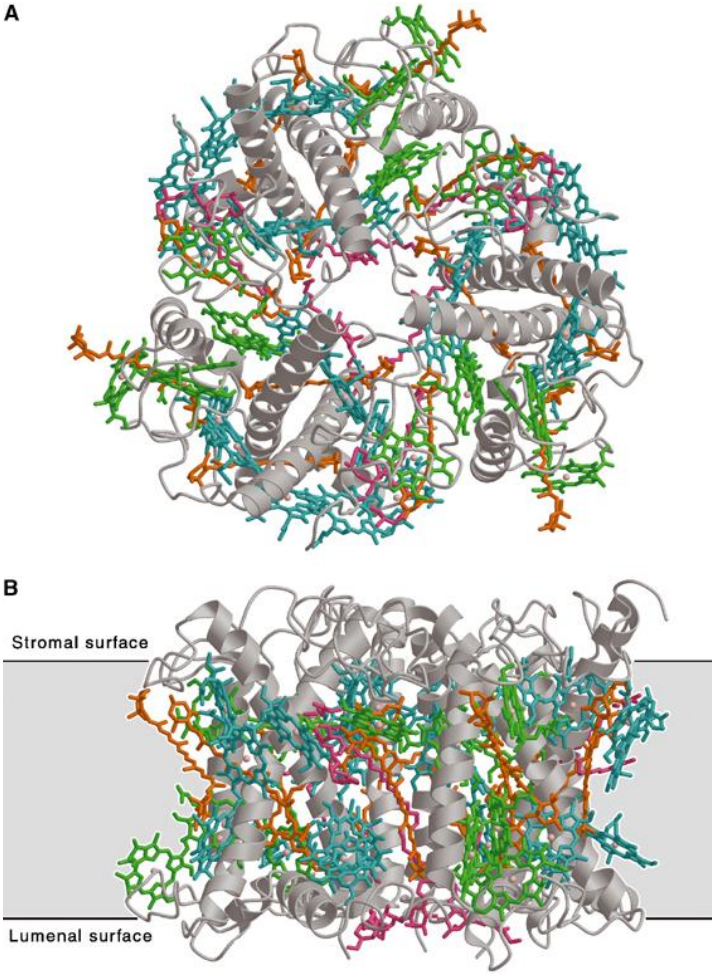

Figure 5: Molecular structure of the trimeric LHC complex according to [154]. Protein structures are shown in grey. The carotenoids are coloured in pink and orange. Chl *b* is hold in light blue and Chl *a* is pictured in green. Figure 5A shows the front view of the complex and Figure 5B presents the side view of the complex embedded in the thylakoid membrane (see also Figure 3).

Solubilised LHC trimers in buffer containing Beta-DM were measured with a commercial absorption spectrometer (lambda 19). The absorption spectrum is shown in Figure 6.

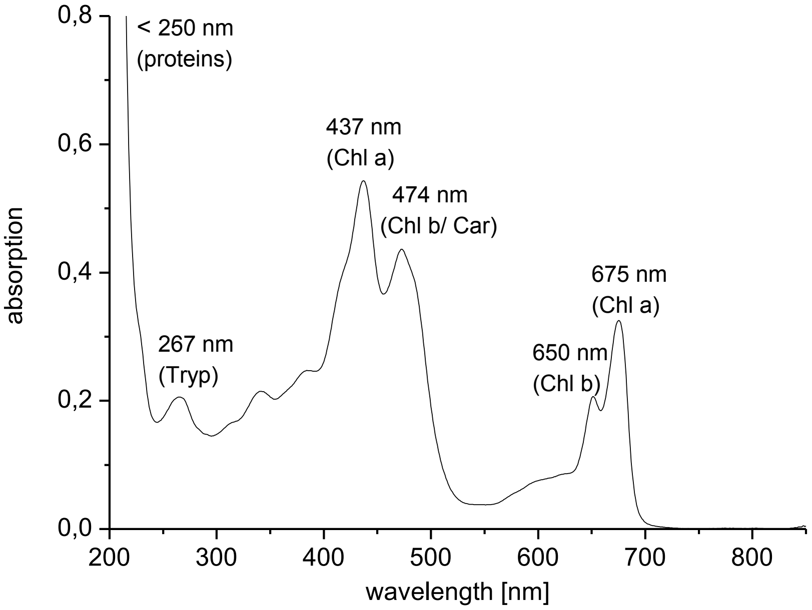

Figure 6: Absorption spectrum of LHC trimers in micelles formed in buffer with Beta-DM. The main absorption bands are directly denoted in the graph and assigned to Chl *a*, Chl *b* or carotenoids and proteins with the absorption band of tryptophan (Tryp) at 267 nm.

The absorption spectrum of solubilized LHCII (see Figure 6) exhibits bands of Chl *a* (soret band (Bx) with peak at 437 nm, Qy with peak at 675 nm) and Chl *b* (soret band (Bx) with peak at 474 nm, Qy band with peak at 650 nm) in agreement with data reported in the literature [2]. Minor absorption around 400 nm and 600 nm is assigned to the By and Qx transitions of the chlorophylls, respectively (see also Figure 10 for the absorption spectrum of Chl *d*). The strong absorption between 480 nm and 500 nm originates from carotenoids. Below 400 nm the absorption is dominated by the contribution of the proteins with the typical maximum of tryptophan with peak at 267 nm. Below 250 nm the steep increase in the absorption results from the sum of all organic molecules in the complex.

The structure of the Chl molecules is shown in Figure 7. It is characterized by the closed porphyrin ring system complexing the Mg^{2+} ion with a binding motif of 50 % covalent and 50 % coordinative binding. The phytol chain is bound to ring IV. The difference between Chl *a*, Chl *b* and Chl *d* is given by different side groups found at the binding sites of R_1 and R_2 at ring I and II, respectively (see inset in Figure 7).

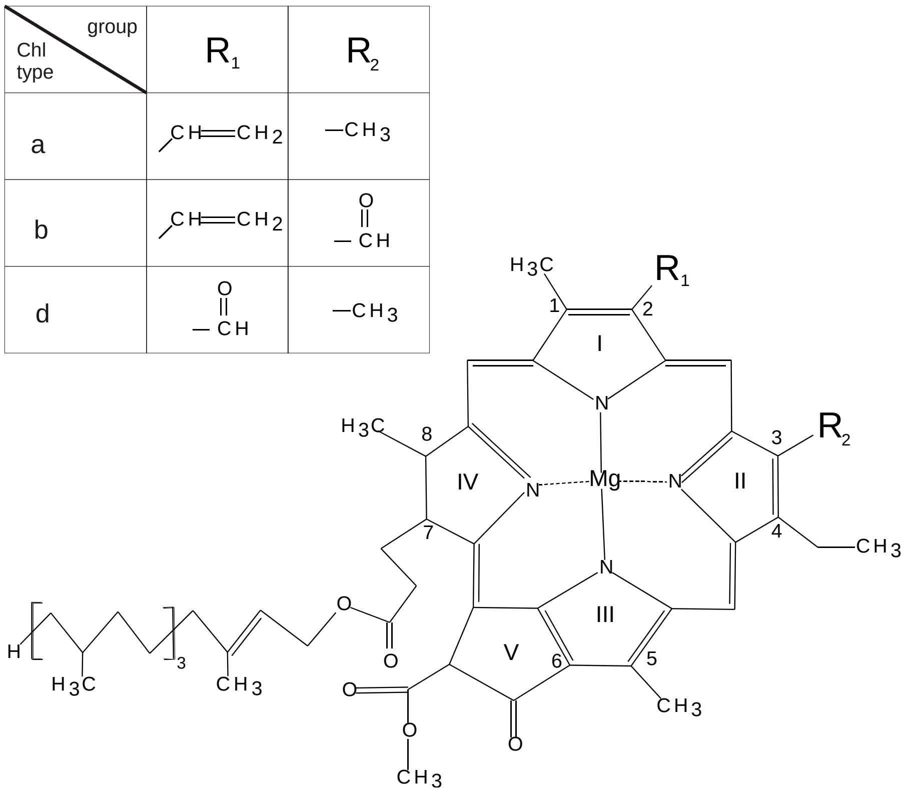

Figure 7: Molecular structure of the Chls: Chl *a*, Chl *b* and Chl *d* (see inset).

Chl *a* and Chl *b* are found in the LHCII of higher plants, while PS II complexes and PS I contain only Chl *a* molecules. The cyanobacterium *A. marina* is an exception because it contains mainly Chl *d* in the membrane intrinsic antenna and RC complexes. The Qy band of Chl *d* is red shifted to about 699 nm in ethanol solution as shown in Figure 10 compared to the absorption maximum of Chl *a* at 675 nm (see Figure 6).

The absorption maximum of the Chl *d* antenna in *A.marina* was found red shifted by another 20 nm to an absorption maximum at 719 nm for the Qy transition according to our measurements (see Figure 8), while, according to Miyashita, the Chl *d* absorption maximum appears at 714 nm in *A.marina* [160]. Former measurements showed a peak at 717 nm for the Qy band of Chl *d* in living cells of *A.marina* [161]. This red shift occurs most probable due to the influence of the surrounding protein matrix.

The spectrum shown in Figure 8, left side, is not corrected for scattered light. The whole cells with a diameter of about 1 µm exhibit strong scattering which leads to an increase of the background level at shorter wavelengths. Figure 8 also shows the absorption of the PBP antenna in *A.marina* between 610 nm and 650 nm (see chap. 1.3.5) and the Bx and By absorption bands of Chl *d* which exhibit highest absorption at 468 nm in living cells (see Figure 8 in comparison to Figure 10 for the calculated Chl *d* spectrum).

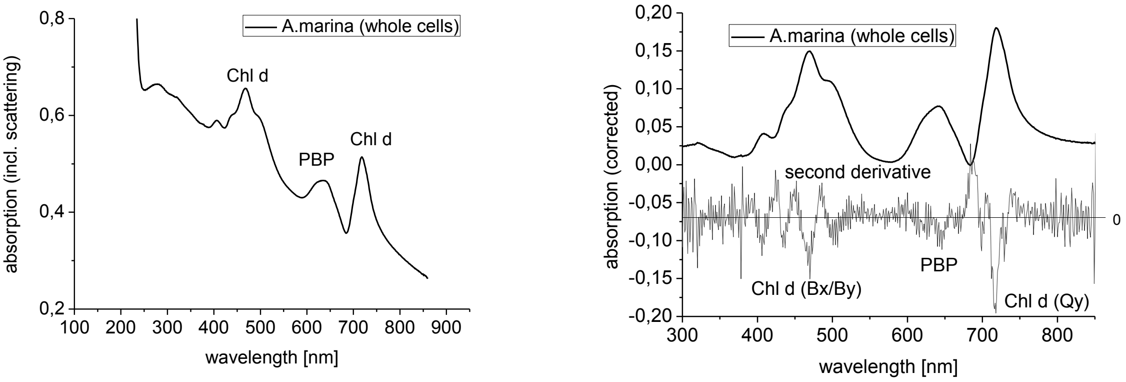

Figure 8: Absorption (without correction of scattering background) of whole cells of *A.marina*. (left side) and corrected spectrum with 2nd derivative (right side)

Figure 9 shows the energy levels and selected electronic transitions including vibrational states of Chl *d* in 40:1 methanole:acetonitrile at 170 K according to Nieuwenburg [158]. In [158] the dipole strengths and spectral linewidths of the different transitions are published as shown in Figure 9. This information was used to plot the relative contributions of these transitions to the absorption spectrum (see Figure 10). For the calculation of the spectrum the extinction coefficient for Chl *d* at 699 nm as published in [159] was used for rescaling.

The vibrational and rotational spectrum of chlorophyll is quite complex. In addition to the vibrations of the covalent bonds of the porphyrine ring system low frequency vibrations are found. They are probably related to the oscillation of the Mg^{2+}-ion. The longitudinal frequencies of the Mg^{2+} oscillation appear at 1230-1300 cm^{-1} while transversal oscillations have typical energies of 540 – 600 cm^{-1} [162]. Chl *a* and Chl *b* molecules bound to water soluble chlorophyll binding protein (WSCP) reveal vibrational side bands at 100-300 cm^{-1} [47]. These frequencies might also be explained by vibrations of the Mg^{2+} ion or by torsions of the chemical bounds inside the Chl molecules exhibiting typical frequencies of 200-350cm^{-1} [162, 163]. In addition the protein environment of the Chl molecules gives rise to a complex phonon spectrum with strong temperature dependency [47, 48, 49]. Configuration changes of the protein can explain the characteristic time delay observed between excitation of the chlorophyll and the population of states in a relaxed environment.

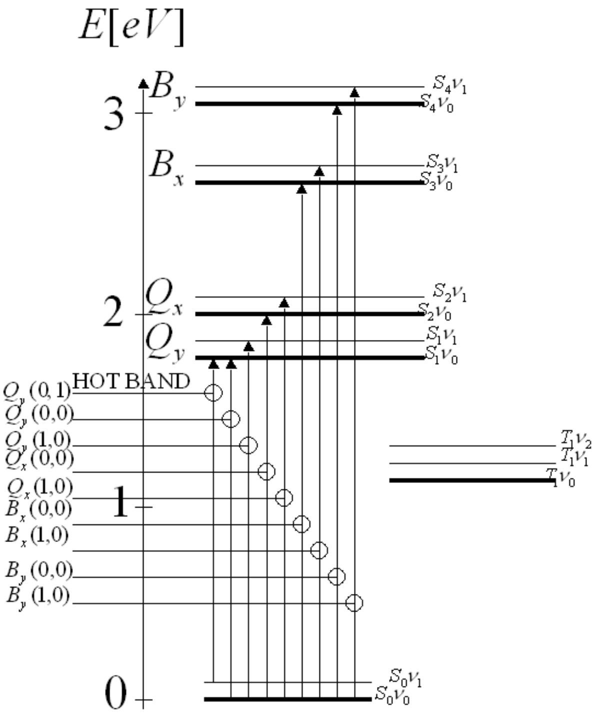

Figure 9: Energetic states and characteristic transitions of Chl *d* in 40:1 methanole: acetonitrile at 170 K according to Nieuwenburg [158]

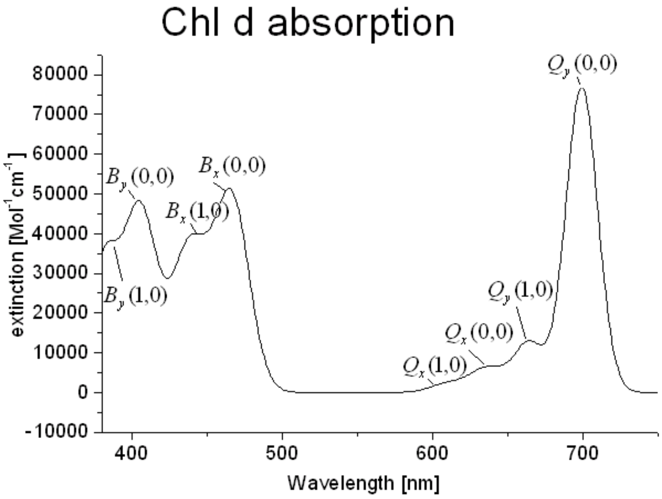

Figure 10: Calculated spectrum of Chl *d* using the transitions shown in Figure 9 and values for the dipole strengths, spectral linewidths and extinction maximum at 699 nm given in [158] and [159].

The broad absorption spectrum of pigments caused by intramolecular vibrational states is of high relevance to achieve an efficient solar energy exploitation. It fulfils the resonance condition between the fluorescence spectrum of donor pigments and the absorption of acceptor pigments due to large spectral overlap. Such overlap is necessary for an efficient energy transfer along the antenna pigments according to the mechanism of Förster Resonance Energy Transfer (FRET) (see chap. 3.3.2).

1.3.2 The LH1 and LH2 of purple bacteria

It is the intention of this short outline of the LH1 and LH2 of purple bacteria to give an impression of a typical complex where the energy pathway is mainly determined by pigment-pigment interaction, i.e. excitonic coupling and Förster Resonance Energy Transfer (FRET).

In the LH complexes of purple bacteria the excitonic coupling of the pigments results in fast equilibration of electronic excitation along ring shaped structures of the organized pigments. The absorption of these pigment-rings exhibits maxima at 800 nm and 850 nm and therefore they are denoted as B800 and B850. Figure 11 shows the pigment arrangement. For the nomenclature see also Figure 14. The bacteriochlorophyll (BChl) molecules B800 in the bigger ring structure of LH2 are less densely packed than those of the smaller structure B850. Due to the shorter distance of neighbouring dipole moments and the steric orientation of the BChl molecules the intermolecular interaction is much stronger in B850 than in B800. This leads to a stronger coupling and larger excitonic splitting in B850 in comparison to B800. The lowest excitonic state in B850 exhibits a markedly red shifted absorption maximum at 850 nm [164, 165].Therefore electronic excitation energy migrates from the outer to the inner ring according to FRET [166].

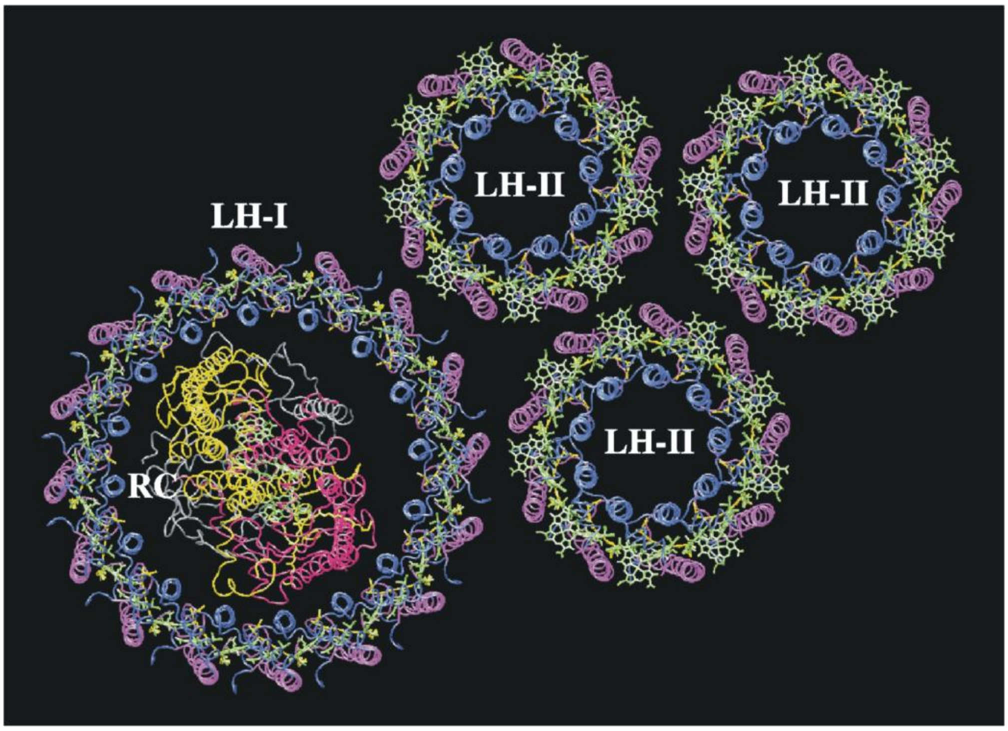

Figure 11: Ring shaped BChl arrangement of the LH complexes found in purple bacteria according to [167]. The LH2 complexes contain an inner ring structure which is slightly smaller and an outer ring structure which is slightly bigger. Similar organisation is found in the bigger LH1 structure surrounding the RC. For more details see text and Figure 12.

Figure 11 shows the BChl molecules in green and cyan. The proteins are shown in blue and purple (LH1 and LH2) and red and yellow for the L and M subunits of the the RC. The BChl organisation in the LH2 is shown in Figure 12. It is visible that the BChl molecules in the B850 are more densely packed and orientated in a tilted “sandwich configuration” while the distance of the BChls in B800 is larger and all molecules are lying in the x-y-plane. AFM pictures of the ring shaped LH2 structures of *Rubrivivax gelatinosus* are shown in Figure 13 [168]. The LH2 shows a typical 9-fold rotational symmetry.

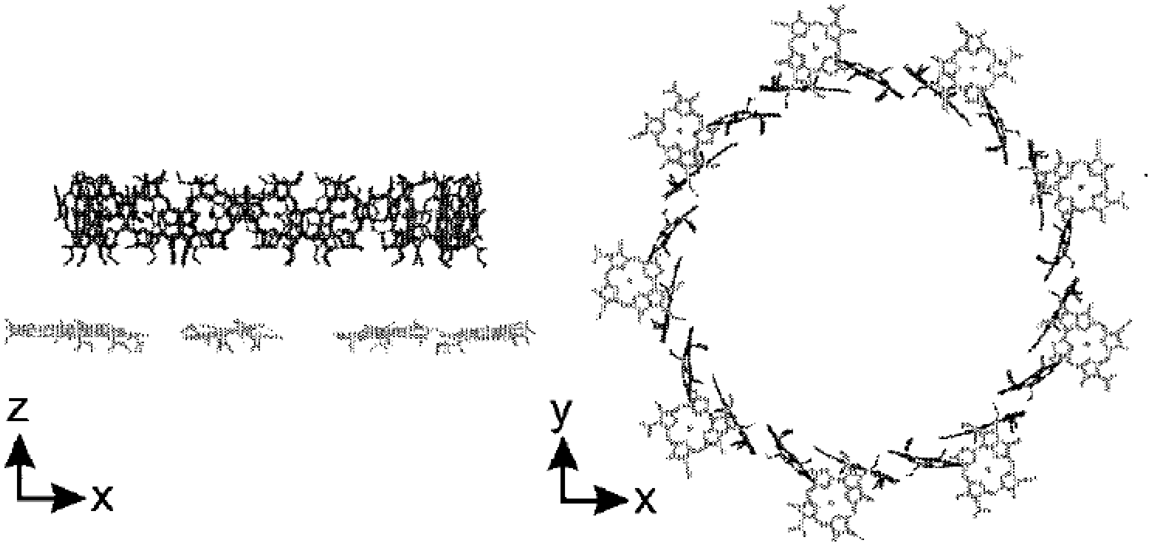

Figure 12: organisation of the 27 BChl molecules found in the LH2 antenna as published in [164]. The left side (view in x-z plane) shows the orientation of the 18 molecules of the smaller inner ring (B850) placed in z-direction above the 9 BChls of the bigger outer ring (B800) while the right side shows the view from the top (as in Figure 11) along z-direction on the x-y-plane.

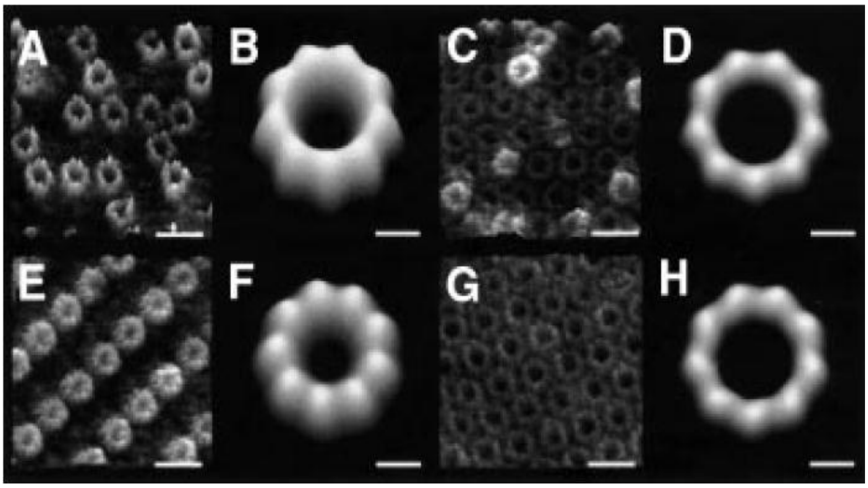

Figure 13: AFM pictures of the LH2 of *Rubrivivax gelatinosus* as published in [168] (The pictures A,C,E and G show the original AFM data while B,D,F and H represent averaged pictures of A,C,E and G, respectively). Scale bars represent 10 nm in the raw data and 2 nm in the averages.

The structural arrangement of the BChls in LH2 (see Figure 12) has strong impact on the pathway of energy transfer. Excitons formed in the B800 are efficiently transferred to the B850 due to energetic reasons. Detailed quantum chemical calculations performed by T.Renger and coworkers revealed that the excitons equilibrate with a time constant of 500 fs along the B800 BChl while the equilibration in the B850 structure occurs with a faster time constant of 100 fs [169]. The energy transfer from the B800 to B850 is nearly irreversible and takes 1.2 ps. With a time constant of 3-5 ps the excited states localise in the LH1 and after 35 ps in the RC (see Figure 14).

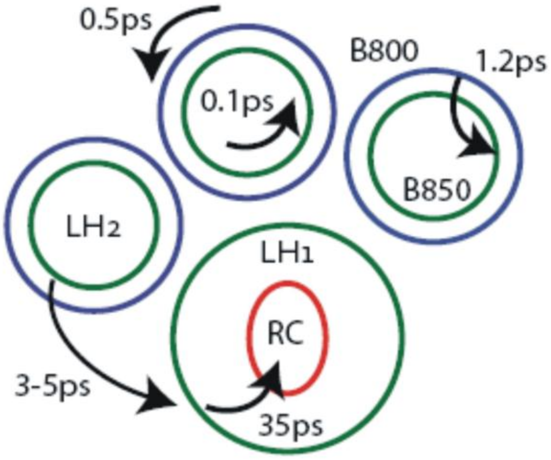

Figure 14: Time constants for the excited state transfer intra and inter the LH2 and LH1 complexes according to [169].

1.3.3 The Fenna-Matthews-Olson (FMO) complex of green sulfur bacteria

Another fascinating complex where the fine tuning of the pigments by the surrounding protein plays a more important role for the EET than in B800 and B850 is the FMO complex of green sulphur bacteria. The different site energies of the excitonically coupled BChl in the FMO leads to a defined pathway from the outer antenna complex to the RC. The FMO complex as shown in Figure 15 is described e.g. in [170, 171, 172] in more detail.

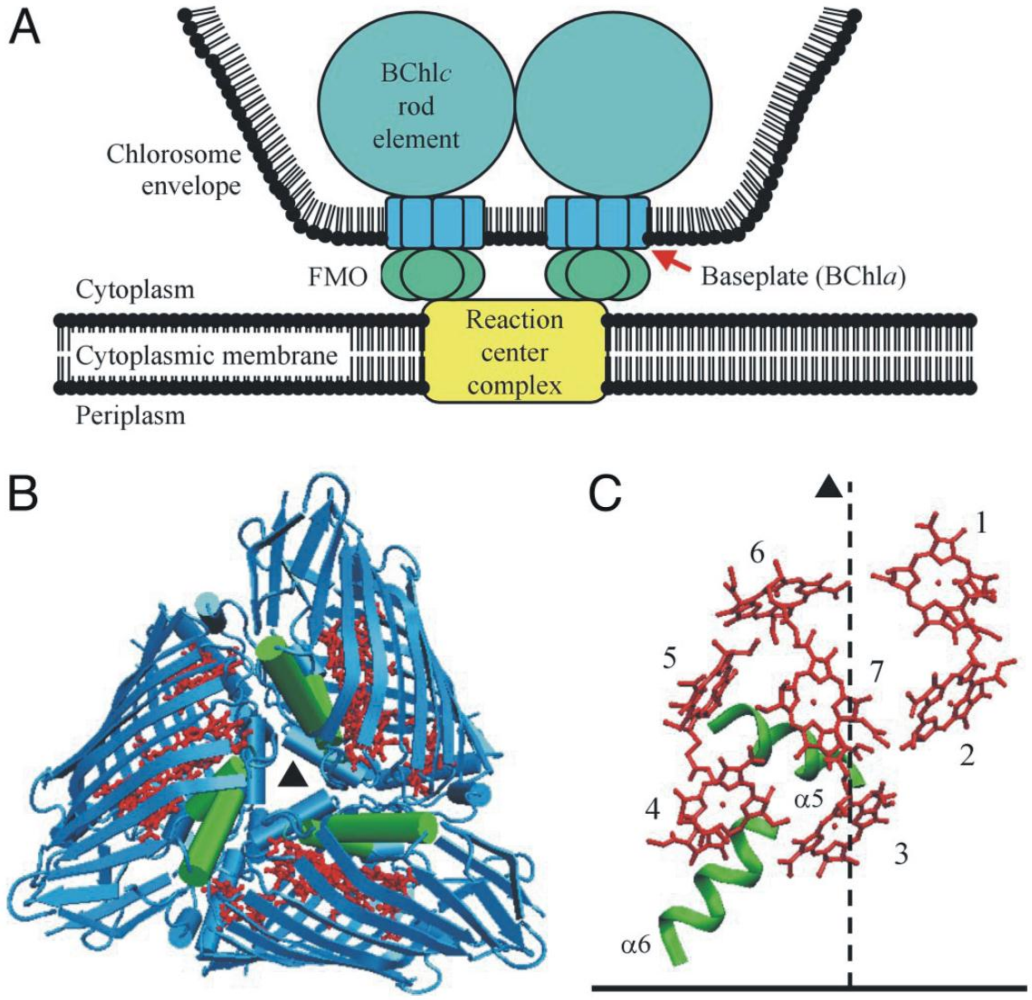

Figure 15: Schematic view of the FMO complex found in green sulfur bacteria (A). The organisation of the trimeric protein structure (green, blue) containing 8 BChl molecules (red) per subunit is shown in panel (B). In [171] it was assumed that the FMO complex contains only 7 BChl per subunit. Recent findings disclosed the existence of an eighth BChl. The detailled structural arrangement of the chlorophylls embedded in one monomer of the trimeric protein shown in panel (B) is presented in panel (C). This figure was published in [171].

The local protein surrounding of the BChl molecules in the FMO complex (see Figure 15 C)) modulates their energetic states. In Figure 15 C) only seven BChl molecules are shown while recent findings gathered from mass spectroscopic analysis unraveled the existence of an 8th BChl [172].

A fine tuning of the electronic states of the BChls leads to a localisation of the lowest energetic states near the chlorophylls number 3 and 4 which are in close contact to the RC (see Figure 15 C)). Excited electronic states populated at pigments 1 and 6 are rapidly transferred within 5 ps to the pigments number 3 and 4 [170]. The pathway of this EET is determined by pigment-protein coupling rather than pigment-pigment coupling.

The directed EET that is guided along a certain pathway is necessarily correlated with the existence of a pigment array within an asymmetric protein structure.

1.3.4 Phycobilisomes (PBS) of cyanobacteria

The antenna complexes of photosynthetic organisms enhance and regulate the effective absorption cross section by connecting a huge number of pigments to the RC as well as by regulating the connectivity and excited state lifetime. The modulation by the protein environment and the coupling of the pigments determines the probability distribution of EET pathways. Additionaly the high number of nondegenerated states of all pigments in these antenna complexes enable light absorption in a wider spectral range than by single pigment molecules.

In photosynthetic organisms different molecules are bound to peripheral antenna complexes which close the absorption gap of the chlorophyll molecules in the green spectral range and therefore rise the efficiency of the antenna. Such pigments are carotenoids in LHCII (see chap. 1.3.1) and phycobiliprotein (PBP) complexes containing phycoerythrin (PE), phycocyanin (PC) and allophycocyanin (APC) in cyanobacteria. The pigments are open porphyrin ring systems exhibiting strong absorption in the green and yellow spectral range thus being responsible for the blue color of cyanobacteria.

Figure 16, left side, shows the structure of C-PC of typical cyanobacteria like *Synechocystis* and *Synechococcus*. It is assumed that similar structures are also found in *A.marina* [43]. Each monomeric protein subunit contains three phycocyanobilin (PCB) chromophores (9 pigments in one trimer). In Figure 16, right side, the APC trimer is shown. This trimeric protein binds 6 pigments (two chromophores per monomer).

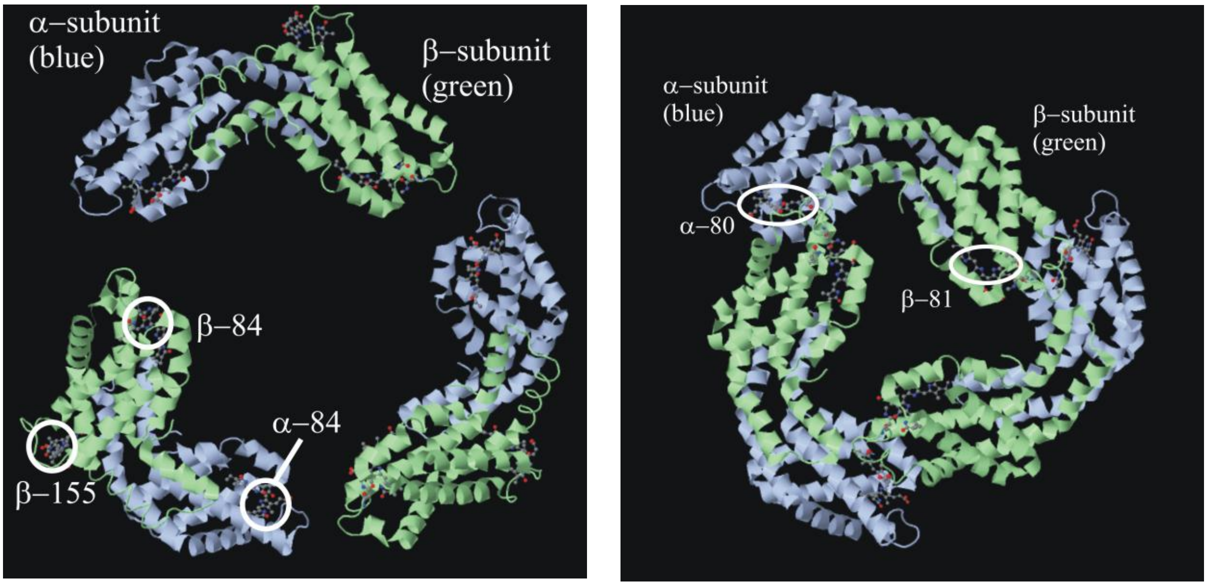

Figure 16 Three monomeric phycocyanobilin containing PCs (left side) and the tetrameric structure of APC (right side). The PC structure was generated with protein data base according to the data published in [173] and grafically enhanced with Corel Draw ®. The APC structure was generated from the data published in [174] enhanced with Corel Draw ®

The PC monomers consist of the α -subunit containing the α-84 chromophore and the β-subunit containing two chromophores, the β-84 PCB and the β -155 PCB (see Figure 16, left side). The APC monomers contain one PCB molecule in the α -subunit (α -80) and one pigment in the β -subunit (β -81) (see Figure 16, right side).

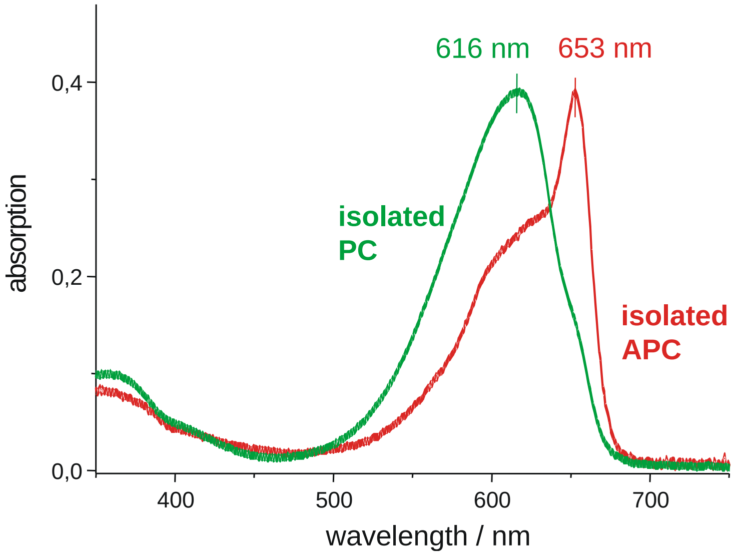

Figure 17: Absorption spectra of isolated PC trimers (green line) and isolated APC trimers (red line) in buffered aqueous solution (data redrawn from [2])

The absorption spectra of PC and APC trimers exhibit characteristic bands resulting from strong excitonic coupling of the pigments. The small shoulder in the PC absorption spectrum (green curve in Figure 17) at 650 nm most probably represents the absorption of the lowest excitonic state. This state is strongly visible in the APC spectrum shown in Figure 17 (red curve) at 653 nm. In APC trimers (see Figure 16, right side) there exists a well defined excitonically coupled dimer containing the two PCB chromophors α -80 and β-81 of different monomers. In the PC trimers all three pigments are rather weakly excitonically coupled between different monomers with the α-84 chromophore in the α–subunit of one monomer and the β-84 PC and the β -155 PC in the β-subunit of another monomer (see Figure 18, right side). Sauer and Scheer [175] calculated that the strongest coupling with a value of 56 cm^{-1} exists between α-84 and β-84 of different subunits. The exact structural constitution of the pigments in the PC and APC trimers is of high relevance for the shape of the absorption spectrum due to the formation of strongly absorbing excitonic states. Due to the coupling it is impossible to extract the optical properties of an isolated pigment from the absorption spectrum of the pigment-protein complex (e.g. a PC monomer). This was shown by Debreczeny et al. [176]. To analyse the properties of individual compounds the sample has to be decomposed into the individual constituents. This leads to a loss of information on the coupling of the pigments which is an essential physical property determining the functionality of the structure. Therefore it is not possible to analyse the function of the whole complex by studying the decomposed compartments and vice versa. The functionality is directly connected with the preservation of the whole structure. This fact is in some way related to the fact that the whole structure can not be explained by its (isolated) parts as mentioned at the beginning of the introduction [1].

The effect of excitonic coupling of PCB molecules in different protein subunits can be analysed if the absorption of PC monomers is compared with PC trimers as shown by Debreczeny et al. [177, 178]. An accurate comparison revealed that the small shoulder at 650 nm in the spectrum of isolated PC trimers (see Figure 17) is the result of the coupling between α-84 and β-84 in different monomers.
With high resolved fs-absorption spectroscopy Sharkov et al. showed that in APC trimers excitonic relaxation in the coupled α -80 / β -81 dimer between different monomers occurs with 440 fs [179-181]. Much slower excitation energy transfer processes with a time constant of 140 ps were observed between the different chromophores in one monomeric subunit.

The coupling strength of the different chromophores in PC monomers and trimers was analysed by Sauer and Scheer [175] and by Holzwarth et al. [60]. The absorption wavelengths and calculated distances of the PC molecules inside the trimeric PCB containing protein disc are shown in Figure 18.

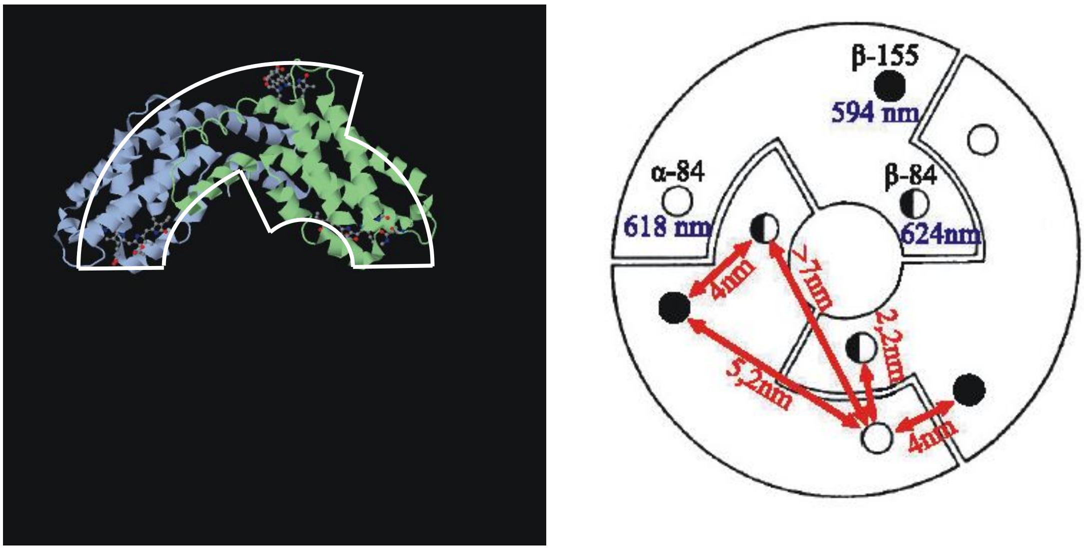

Figure 18: Structure of monomeric PC (left side) generated with protein data base according to the data published in [173] and grafically improved with Corel Draw®. The protein monomer consists of two subunits: The β-subunit shown in green binding the two chromophores β-84 and β-155 and the α-subunit (shown in blue) which binds only one chromophore, the α-84 PCB. The absorption maxima and distances between the different PCB molecules in the trimeric PC calculated by Sauer and Scheer [175] and Holzwarth et al. [60] are shown on the right side.

The strongest interaction between the pigment molecule and the protein occurs via sulfur bridge between the pyrrol ring of the PCB pigment α-84 and a cysteine group of the protein as shown in Figure 19. Hydrogen bonds help to stabilize the structure and in-plane geometry of the chromophore molecules and the protein.

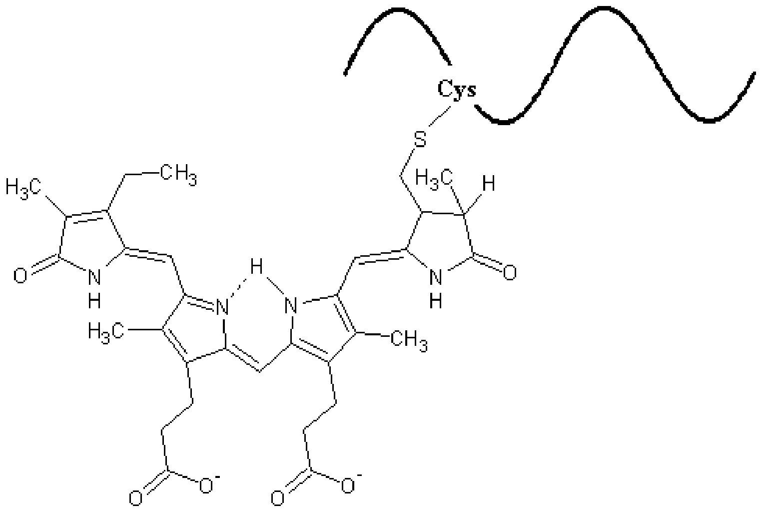

Figure 19:

PCB chromophore α-84 bound to the protein matrix via a sulfur bridge between PCB and the cysteine of the protein. Figure 19 was generated with ChemSketch V®.

In addition to the sulfur bridge shown in Figure 19 there exist several hydrophobic interactions between the pigments and the protein structure. The attractive van-der-Waals forces decay with the 6th power of distance. Therefore only the strongest interactions determine the structure.

Figure 20 shows a view on the β-84 PCB chromophore found in the monomeric PC structure that interacts with leucine along the shortest hydrophobic interaction. From this illustration one can get an idea of the flexbility of the protein matrix comparable to an ensemble of coupled springs. This spring like structural arrangement results in a broad distribution of oscillation modes that efficiently dissipates electronic excess energy in the pigments and modulates the electronic properties of the pigments bound to the protein quasistatically and dynamically. The quasistatic modulation leads to a broad Gaussian distribution of chromophore site energies while the dynamic modulation leads to a homogeneous broadening of the chromophor ensemble and is even assumed to be involved in dynamic excited state localisation effects that supports the EET.

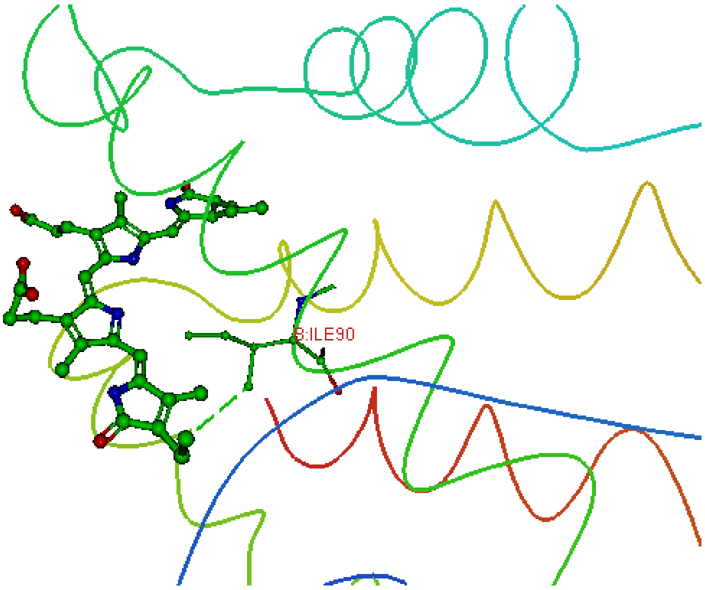

Figure 20: β–84 chromophore in PC bound to the protein β–subunit. The shortest hydrophobic interaction (3.2 °A) between the chromophore and the protein is shown as green dashed line. The figure was generated with protein data base according to the data published in [173] and grafically improved with Corel Draw ®.

The PC and APC trimers (see Figure 16) tend to aggregate further in the so called „face-to-face“ dimerisation forming hexameric structures (for further detail see e.g. [2, 60, 64]).

These hexamers undergo a further aggregation forming so called PBP antenna rods which aggregate to huge (up to 50 nm in diameter) phycobilisomes (PBS) as shown in Figure 21 and Figure 22 (left side). In Figure 22 the APC containing hexameric structures seem to be present only in form of single discs, but they also are found to form rod shaped staples of hexameric discs which are interacting with the outer thylakoid membrane.

Some cyanobacterial PBS additionaly contain phycoerithrin (PE) in addition to PC and APC hexamers in the PBS.

The properties of PBS are well understood and therefore PBS are quite a good system for reference measurements of energy transfer processes. In the study presented here measurements of PBS from the cyanobacterium *Synechocystis PCC 6803* containing PC and APC as schematically shown in Figure 22 were performed (see chap. 5.1).

It was found that energy migrates inbetween about 200 ps from PC to Chl *a* in *Synechocystis* (see chapter 5.1) which is a typical value for PBS of common cyanobacteria in agreement with Holtzwarth [60], Trissl [63] and Glazer [64].

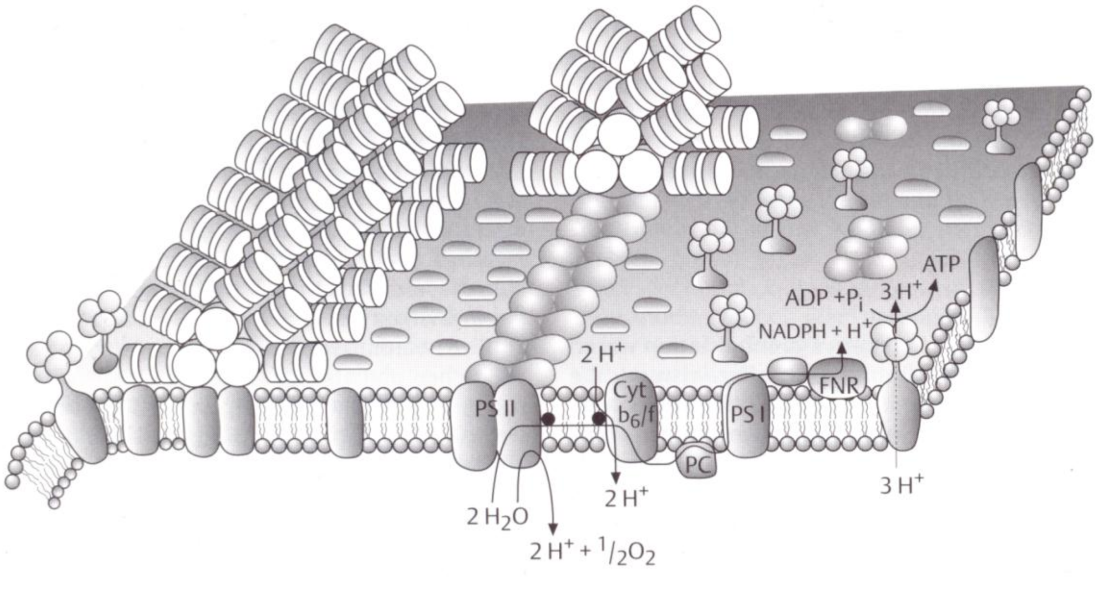

Figure 21: Schematic view of the association of PBS with the PS II inside the thylakoid membrane according to [76].

It is assumed that the PBS are mainly associated with the PS II core complex of the thylakoid membrane (see Figure 21). Most cyanobacteria contain high amounts of PBS which makes the PBS chromophores the most important light harvesting pigments found in cyanobacteria. PBS undergo state transitions from the state indicated in Figure 21 where the PBS are associated with the PS II and a state where they are associated with PS I. Other studies showed that similar behaviour is also approved for the LHCII in higher plants [182].

Figure 21 indicates the electron pathways after light absorption. Details for the electron transfer chain are found in chap. 1.1 (see Figure 2).

1.3.5 Phycobiliprotein (PBP) antenna of *A.marina*

The thylakoid membrane in *A.marina* is ring shaped [183], containing densely packed PBP antenna rods. *A. marina* has a unique composition of the light harvesting system as schematically shown in Figure 22 (right side). The PBP antenna has a simpler rod shaped structure than that of PBS in other cyanobacteria [54], [160].

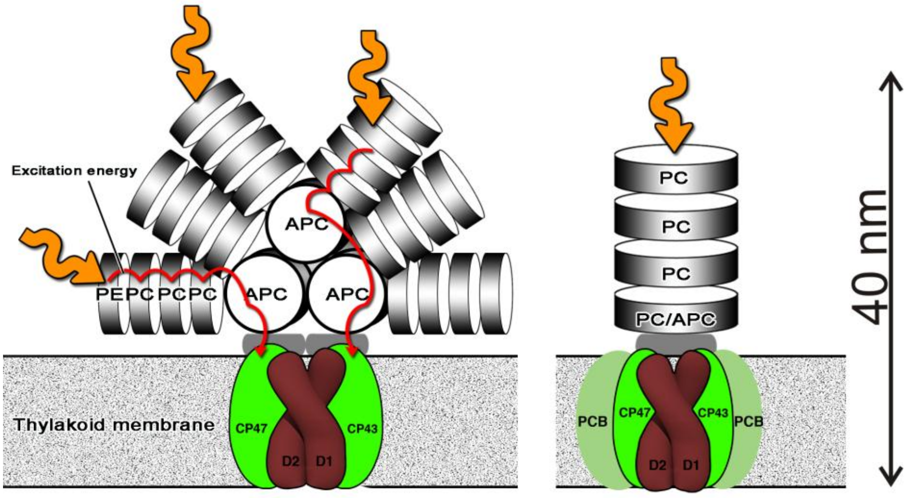

Figure 22: Overall geometry of PBS found in cyanobacteria (left side) and rod shaped PBP antenna structure of *A.marina* (right side) according to Marquardt [183], figure according to Olliges [185]. Both PBP contain PC and APC. In the PBS additionally PE is found.

In this thesis the PBP structure suggested by Marquardt et al. ([183], Figure 22) was confirmed by transmission electron microscopy of the PBP antenna complexes of *A.marina* as shown in Figure 23. In comparison to the pictures presented in [183] the PBP complexes appear slightly larger with extensions up to 40 nm in length and 20 nm in diameter. The contrast of the protein structure in the electron beam is low. Therefore a procedure of negative staining had to be performed to achieve a picture of the PBP structure.

In transmission electron microscopic studies a carbon film on a copper net as sample holder was incubated into a concentrated PBP solution in phosphate buffer for 24 h. Then the carbon film was put into a 4 % (w/w) solution of Natrium-Silicotungstate ($Na_4[W_{12}SiO_{40}]$) which contains the hevy metal tungsten (W) which has a high scattering cross section for keV electrons. The specimen is left in the $Na_4[W_{12}SiO_{40}]$ solution for about 30 min. After this negative staining procedure the sample is washed about 2 min. in destilled water and left 24 h for drying. The carbon film can be directly used in the electron microscope.

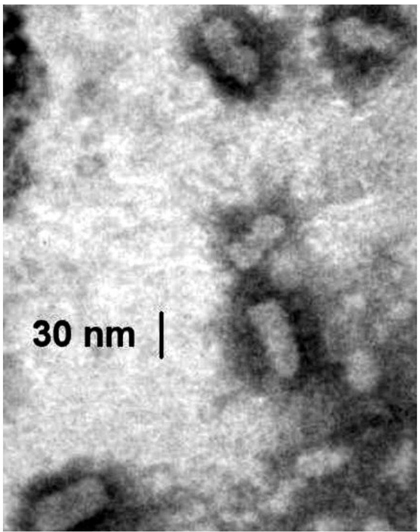

Figure 23: Electron microscopic study of PBP preparations of *A.marina* in buffer containing phosphate after negative staining with $Na_4[W_{12}SiO_{40}]$. The PBP antenna complexes appear transparent (white) due to the process of negative staining while the staining salt leads to a dark green contrast.

Due to the negative staining process the contrasting structure of $Na_4[W_{12}SiO_{40}]$ might appear slightly bigger than the PBP antennae which are embedded inside with a varying exact size dependent on the preparation protocol. Therefore it is assumed that the size determined by these electron microscopic studies as shown in Figure 23 is not necessarily significant larger than the measurement results of Marquardt [183] used to scale Figure 22.

Typical spectra of PBP antenna complexes of *A.marina* dissolved in aqueous phosphate containing buffer are shown in Figure 24 (black line). For comparison the absorption of isolated PC trimers (green curve) and isolated APC trimers (red curve) are shown (see Figure 17). The large absorption gap of Chl *d* between 500 nm and 650 nm (see Figure 10) is partially filled by the absorption of the PBP antenna as shown in Figure 24.
Interestingly the absorption spectrum of isolated PBP antenna complexes from *A.marina* (black curve in Figure 24) is less broadened than the spectrum of isolated PC trimers (green curve in Figure 24). Due to the fact that the PC trimers couple to hexamers one would expect a slight broadening of the PBP absorption compared to isolated PC trimers. In addition the PBP antenna of *A.marina* contains APC which should contribute to the red edge of the spectrum at 653 nm (see red line in Figure 24). It seems that there exists also some absorption at wavelengths > 680 nm. These long wavelength absorption states play an important role for the energy transfer between the PBP antenna and Chl *d* (see also chap. 5.1 ff.).

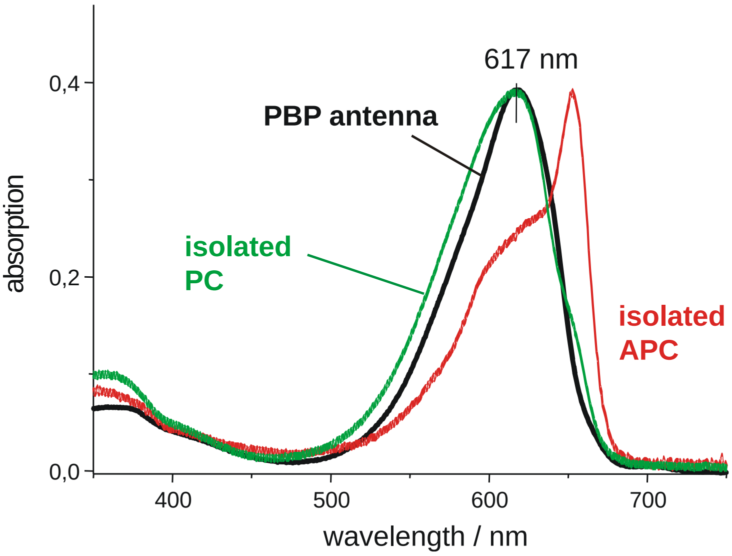

Figure 24: Absorption spectrum of PBP isolated from the cyanobacterium *A.marina* (black curve) in comparison to isolated PC trimers (green line) and isolated APC trimers (red line) as shown in Figure 17 according to Theiss [2]. The trimers were diluted in buffered aqueous solution.

The PBPs of *A. marina* have been reported to consist of four hexameric units [183, 186] (see Figure 22, right side). Each homohexamer binds 18 PCB molecules covalently as chromophores. The PC/APC heterohexamer is found to contain 9 PCB and 6 APCB chromophores (see Figure 16). Isolated PBPs from *A. marina* exhibit a fluorescence maximum at 665 nm (APC) with a shoulder at about 655 nm (PC) at room temperature [183].

In order to avoid structural changes leading to conformational changes of the pigment-protein-complex the sample has to be preserved by incubation in a buffering medium with high ionic strength. We used a phosphate containing buffering medium.

If the sample is diluted without phosphate the EET along the rod shaped antenna structure is distorted.

The absorption spectrum of PBP isolated from the cyanobacterium *A.marina* in a phosphate containing buffer medium (see Figure 25, red curve) is slightly less broadened than the absorption of PBP antenna complexes in buffer without phosphate (see Figure 25, black curve), as one would expect if the structure decomposes. In chap. 5.3 it is shown that there is no EET from PC to APC if the sample is kept in buffer without phosphate.

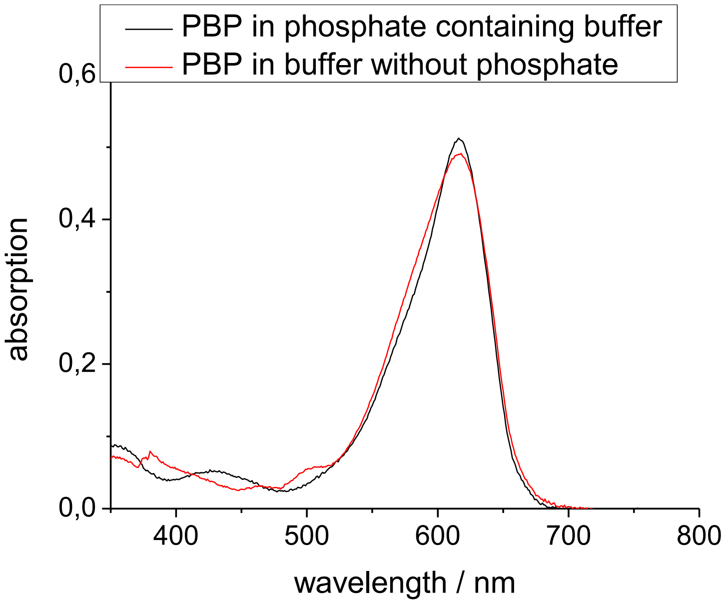

Figure 25: Absorption spectrum of PBP isolated from the cyanobacterium *A.marina* in buffer containing phosphate (black curve) in comparison to PBP in buffer without phosphate (red curve).

1.4 Core complex of PS II

The light harvesting complexes of different organisms show large variety (see sections 1.3.1 – 1.3.5). In marked contrast the core complex of PS II of all known oxygenic photsynthetic bacteria and higher plants has common architecture.

Figure 3 in chap. 1.1 and Figure 26 show that the core complex contains the D1 and D2 proteins and in addition the chlorophyll containing core antenna systems CP 43 and CP 47. D1 represents the donor side of the core complex, containing the primary donor P680 and the primary acceptor Pheo. The primary electron acceptor Q_A and the secondary plastochinone Q_B are located in D2, the acceptor side. Q_B is losely bound in its binding pocket and is continuously diffusing during the photosynthetic process.

Due to its common architecture the charge separation and stabilisation as indicated in chemical equation 2 (chap. 1.1) is similar in all oxygenic photosynthetic organisms. This is also related to the following steps of electron transfer to the PS I via Q_B and the mobile plastocyanine carrier (see Figure 3 and Figure 21). Therefore the studies of different photosynthetic organisms have a common protocol which comprises similar charge separation and electron transfer (ET) steps in the core complex but different excitation energy transfer (EET) steps in the antenna systems which are specific to every investigated species.

Details regarding the electron transfer processes that occur in the core complex are beyond the scope of this thesis. Therefore the reader is referred to the relevant literature for a detailed description [73 - 77].

The core complex of some oxygenic procaryotes like *Prochloron* and *A. marina* is assumed to be organised in form of dimers or higher oligomeric “supercomplexes” built up by two or four core complexes as described above (two structures containing D1, D2, CP43, CP47 each). Figure 26 (left side) shows the supercomplex dimer found in *Prochloron didemni* [98]. Based on transmission electron microscopic studies of negatively stained core complex preparations from *Prochloron didemni* Bibby et al. concluded that the dimer is surrounded by further distale Chl containing antenna complexes, which are called pcb antennae (see Figure 26). Additionaly other subunits are assumed to stabilize the structure (purple complexes shown in Figure 26, left side).

Contrary to all other species the core antennae CP 43 and CP 47 of *A. marina* contain mainly Chl *d* instead of the usual Chl *a*. Recent findings show that both types Chl *a* and Chl *d* are essential for the photochemistry in the core complex of *A.marina*. While the charge separation most probably starts from Chl *d* representing the accessory Chl_{D1} molecule the cation is stabilised on Chl *a* representing at least one partner of the strongly coupled P_{D1}/P_{D2} dimer [55].

Two years later (2005) Chen et al. resolved the electron microscopic picture of the tetrameric PS II core complex of *A.marina* containing four times the D1, D2, CP43 and CP47 structures surrounded by

16 pcb [99] (see Figure 26, right side. The scaling of the picture at the right side is about 50 % of Figure 26, left side).

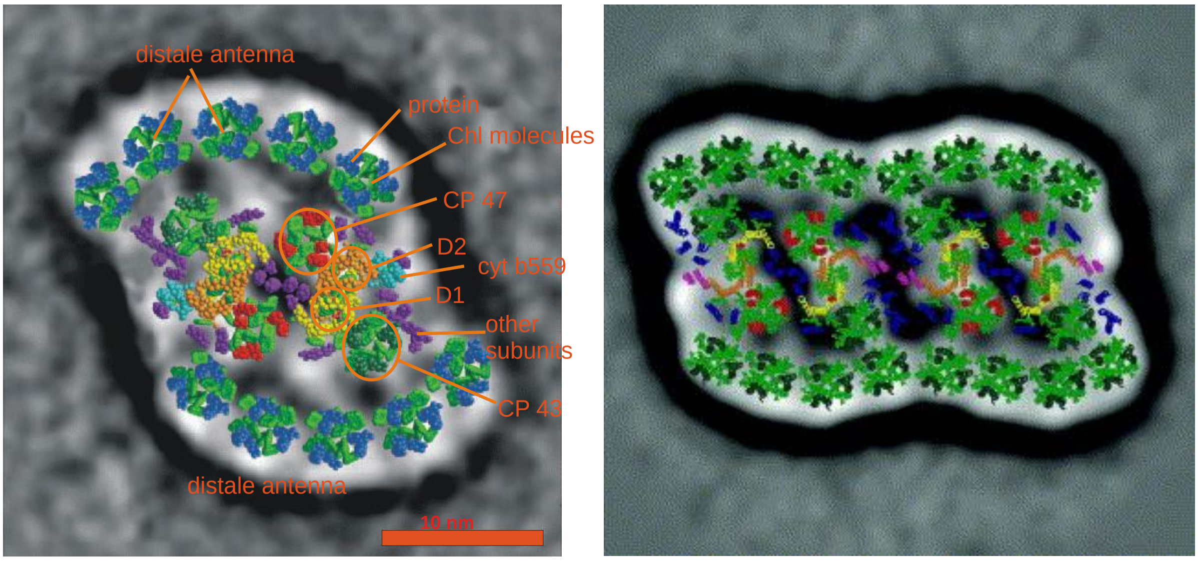

Figure 26:

Left side: Constitution of the core complex of *Prochloron didemni* according to [98]. The figure shows the assumed distribution of the photosynthetic core proteins in agreement with an electron microscopic study after negative staining. Chlorophyll molecules are shown in green while proteins are shown in blue (distale antenna proteins, pcb), red (CP47), dark green (CP43), orange (D2), yellow (D1), light blue (cyt b559) and violett (other). On the right side the tetrameric supercomplex from *A.marina* is shown as published in [99]. On the right side the cyt b559 complexes are shown in magenta. The full length of the tetramer found in *A.marina* is about 38 nm (inclusive the detergent shell)

Each dimer of the core complex of *Prochloron didemni* contains 72 Chl molecules and additional 14 Chl molecules located in each pcb (distale antenna). Interestingly, this number is the same as for Chl *a* and Chl *b* molecules in the LHCII unit of higher plants.

These numbers are even higher for the supercomplex of *A.marina*. In addition with pcb it contains 368 Chl *d* molecules corresponding with 92 Chl *d* molecules per reaction center. The Chl *a* content in *A.marina* has been reported to depend on the light intensity during the growth with Chl *d*/Chl *a* ratios of 65 at low and 29 at high light intensities [184]. The molecular weight of the tetrameric core complex is about 2300 kDa.

One PBP antenna rod (see Figure 22, right side) contains most probable 69 phycocyanobilin-chromophores associated with each reaction center (see chap 1.3.5).

In whole cells of *A. marina* the main red absorption band of the Chl *d* is observed at 714-718 nm ([161], see chap. 1.3.1). Low temperature absorption spectroscopy [187] revealed minor spectral forms of Chl *d* at 694 nm, 726 nm and 740 nm and a small Chl *a* band at 670 nm. The room temperature steady state fluorescence of *A. marina* exhibits a broad Chl *d* band at around 724 nm with minor contributions at 709 nm, 716 nm and 729 nm [188].

Chl *d* was shown to be the primary donor of the RC of PS I in *A. marina* [189]. The nature of the primary donor of PS II in *A. marina* is still a matter of debate. Mimuro et al. found a delayed fluorescence (DF) component in the 685 nm to 695 nm wavelength range with a lifetime of about 15 ns in whole cells of *A. marina* and concluded that the primary donor of PS II contains Chl *a* [184], [190]. In contrast to these results, Itoh et al. came to the conclusion that the primary donor of PS II consists of Chl *d* [191].

To address this problem experiments were performed where *A. marina* was excited at 398 nm or 440 nm exactly like in the reports of Mimuro et al. [184], [190]. Although delayed fluorescence (DF) was observed after excitation with 440 nm, no similar long lifetime of the fluorescence could be detected if *A. marina* is excited at 632 nm or 654 nm [54]. Due to the high absorption of the PBP in *A.marina* at 632 nm, the population of excited $^1Chl^*$ in the reaction center should be similar after excitation at 632 nm, 400 nm and 440 nm. So far the origin of the 14 ns-decay component observed in the 630 to 700 nm wavelength range is not clarified. But our studies show that the spectral shape of this DF is not easily reconcilable with the Chl *a* spectrum [54]. Based on these results the observed DF cannot be assigned to a delayed Chl *a*-fluorescence and therefore not used as an argument for the hypothesis that the primary donor of PS II contains Chl *a.* In a later study the flash-induced absorbance difference spectrum attributed to the formation of the secondary radical pair, $P^+Q_A^-$ in photosystem II of *A.marina* was measured in the range between 270 nm and 1000 nm at 77 K. Despite the high Chl *d* content, the flash-induced absorption difference spectrum of a 2 ms decay component fit to the spectra exhibits features which are typical of the difference spectrum seen in oxygenic photosynthetic organisms lacking Chl *d*. Therefore the data indicates that the positive charge is stabilized on a Chl *a* molecule. Next to this spectrum that is correlated with the stabilized positive charge and exhibits the signature of Chl *a* a strong electrochromic band shift, centred at 723 nm, has been observed. It is assigned to a shift of the Qy band of the neighbouring accessory Chl. From these findings it seems most likely that this accessory Chl molecule accepts excitation energy from the Chl *d* containing antenna. Based on these findings it is proposed that primary charge separation is initiated from Chl *d* which functions as the primary electron donor and in a subsequent ET step the cation is localised on a Chl *a* molecule. Therefore both chlorophylls *a* and *d* are essential for the photochemistry in photosystem II of *A.marina* [55].

For reviews on fluorescence of *A. marina* and comparison with other systems, see Mimuro [65] and Itoh [192].

1.5 Water soluble chlorophyll binding protein (WSCP)

In addition to the antennae complexes and the core complex of PS I and PS II many plants contain another type of chlorophyll-binding proteins that are characterized by different properties. First of all, these complexes are water-soluble and not integrated as pigment-protein complexes into the thylakoid membrane. Therefore, these highly hydrophilic chlorophyll proteins are denoted water-soluble chlorophyll proteins (WSCPs). Secondly, the WSCPs bind no more than one chlorophyll molecule per polypeptide subunit and none of them was found to contain carotenoids (Cars) [46, 47, 68]. The Cars play a protective role in photosynthetic pigment-protein complexes by quenching excited singlet states and Chl triplet states at high light conditions.

Despite the lack of Cars the photodegradation of Chl bound to WSCP is reduced in comparison to Chl in solution [68]. The mechanism of this photoprotective property and the functional role of WSCP is not yet clearified. One striking feature is the marked stimulation of WSCP expression upon different types of stress like drought [193], salinity [194], heat [195] or leaf detachment [196]. This finding points to a protective role against degradative processes of the photosynthetic apparatus. When taking into account the high affinity for chlorophyll binding [66, 68] it appears attractive to speculate on a regulatory role in controlling pigment synthesis or decay pathway(s), thus avoiding or diminishing deleterious photodynamic effects. There exists no evidence for the interaction of Chl bound to WSCP with other pigment protein complexes. Moreover our studies reveal that the WSCP protein is shielding the Chl molecules and diminuishes the interaction with oxygen under formation of deleterious singlet oxygen.

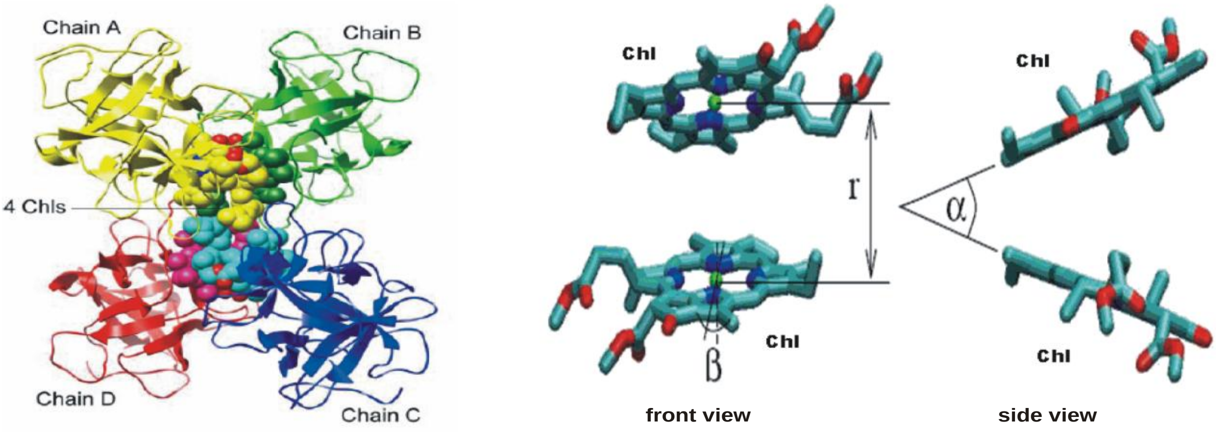

Figure 27 left side: Structure of the WSCP−Chl complex purified from leaves of *Lepidium virginicum* (class IIb WSCP) according to [70] which binds 4 Chl molecules. The four monomers are shown in yellow, green, blue and red. The principal dimers are the pairs of chains A−B and chains C−D. right side: structural arrangement in recombinant WSCP from cauliflower reconstituted with Chl *a* alone, Chl *b* alone or with mixtures of Chl *a* and Chl *b* from [38]. This class IIa WSCP binds only 2 Chl molecules instead of 4 Chl molecules like the WSCP IIb as shown on the left side.

The WSCP family can be classified into complexes that undergo conformational changes upon illumination, giving rise to a red shift of the absorption spectrum (Class I), and those remaining spectrally invariant (Class II) which were investigated in the study presented here. Class IIb WSCP was found to bind up to 4 Chl molecules as shown in Figure 27 (left side) while the class IIa WSCP, reconstituted with the recombinant protein from cauliflower, binds only 2 Chl molecules (see Figure 27, right side), (for a review, see ref [66]). After reconstitution with pigments mainly tetramers are formed [67, 68]. Detailed spectroscopic studies and theoretical analyses led to the conclusion that recombinant cauliflower WSCP reconstituted with different chlorophylls (Chl *a*, Chl *b*, Chl *d*) binds the pigments in form of an excitonically strongly coupled dimer with an “open sandwich” geometry [38, 46, 69].

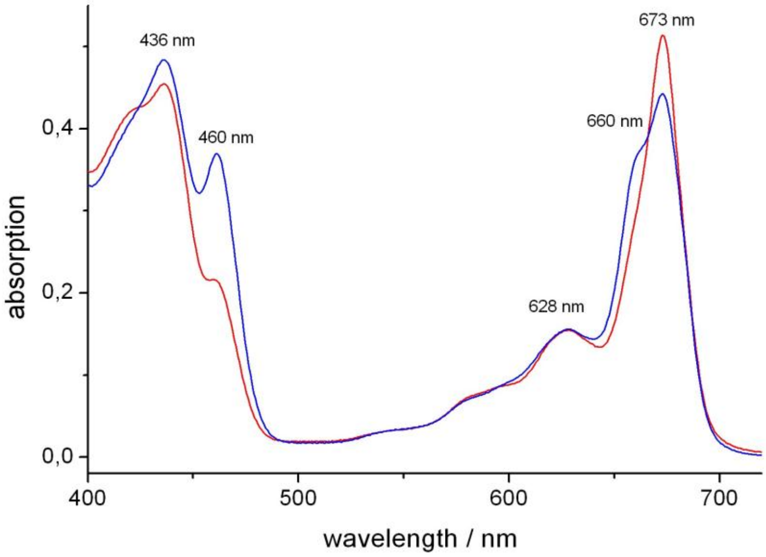

Figure 28: Ground state absorption spectra of recombinant cauliflower WSCP reconstituted with Chl *a*/Chl *b* ratios of 2.6:1 (blue lined curve) and 4.2:1 (red lined curve) measured at room temperature (Theiss et al., [46])

Figure 28 shows the ground state absorption spectra of recombinant cauliflower WSCP reconstituted with Chl *a*/Chl *b* ratios of 2.6:1 (blue lined curve) and 4.2:1 (red lined curve) measured at room temperature [46]. T. Renger et al. showed that the experimental data is well explained by the proposed “open sandwich” dimer motif for the pigment array [69] if the angle between the planes of the two Chl molecules in this configuration is about 30° [38]. This closely resembles the value of 25-27° that was obtained at virtually the same time by Horigome et al. [70] for the 2.0 A resolution X ray crystallography structure of class IIb WSCP from *Lepidum virginicum*. The structural similarity between class IIa and class IIb WSCP suggests that the pigment binding scheme is comparable in all class II WSCPs. This idea gains support by the finding that the linear absorption and CD spectra of class IIa WSCP can be simulated on the basis of the crystal structure reported by Horigome et al. [70] for class IIb WSCP [38]. This model also consistently describes the fast excited-state dynamics of Chl *a*/Chl *b* heterodimers on the fs time scale [46]. It is interesting to note that the excitonic coupling of a chlorophyll dimer in this array gives rise to an oscillator strength that is significantly higher for the upper than the lower exciton band [38, 46, 69]. This phenomenon is just the opposite of the excitonically coupled ”special pair” in bacterial RCs and similar arrays of P700 in PS I and P680 in PS II where the lower exciton band carries most of the oscillator strength. These special pairs are tailored as cofactors for the process of primary charge separation [88, 89, 90]. Strongly coupled dimers with similar structure also occur in antennae, e.g., LH1 and LH2 (see Figure 11). The higher oscillator strength of the upper excitonic band contributes to the fact that WSCP might be a perfect model system for studying pigment-pigment and pigment-protein interaction because the dimers can be selectively excited in the upper exciton band with fs light pulses and the exciton relaxation can be studied with high contrast due to suppression of the direct excitation of the lower exciton level.

The formation of a Chl dimer [197] or the interaction with the protein matrix could lead to a strong quenching of $^1\mathrm{Chl}^*$ states which would explain the photostability as the triplet state population $^3\mathrm{Chl}$ is drastically diminished. The lifetime of $^1\mathrm{Chl}\ a^*$ was found to be about 200 ps in solubilized Cyt*b*6/f, which contains a single Chl *a* molecule of unknown function [198, 199], compared to about 4.5 ns of Chl solutions and trimeric LHCII complexes in detergent micells [200]. This quenching of $^1\mathrm{Chl}^*$ in Cyt*b*6/f is ascribed to interaction of the pigment with aromatic amino acid residues [199]. The striking phenomenon of drastically shortened lifetimes of $^1\mathrm{Chl}^*$ in a natural Chl-binding protein is an attractive feature and raises questions on a possible existence of an analogous phenomenon in WSCP because structural data reveal the presence of aromatic amino acid residues close to the Chl binding sites [70]. In order to check for these possibilities, the excited-state dynamics were analyzed in WSCP.

The results obtained reveal that the spectral properties and excited singlet state dynamics can be consistently described within the framework of a model of a protein tetramer binding excitonically coupled Chl dimers that are modulated by the protein environment. The scientific results were developed in a joint work at Technical University supported by DFG (SfB 429) in Berlin. The detailed findings are presented in ref. [37, 38, 46- 48] and chap. 4 of this thesis.

A theory of light matter interaction in highly nonperiodic structures helps to predict structure related parameters up to a precision of 0.01 nm, i.e. 0.74 nm for the center-center distance of the dipole moments of the excitonically coupled Chl dimers [38]. It would be highly desireable to visualise biological complexes with highly resolved fluorescence microscopy with comparable prescision [12-15].

As a conclusion from this brief description on pigment protein complexes of the photosynthetic apparatus the question might arise how we can understand the complex hierarchic organisation of biological systems from the pure analysis of time resolved fluorescence spectra.

The physics behind a directed flow of time that is connected with irreversible processes and the determination of the dynamics of nonequlibrium systems is an actual field of research since the brilliant contributions of Prigogine [201, 202]. Schrödinger has shown that the quantization of energetic states is fundamentally necessary to understand the existence of stable complex molecules in a thermally equilibrated environment [32].

We suppose that in fact the rising complexity forming stable non-equilibrium structures surrounded by an equilibrated environment is a basic fundamental physical property of a sufficiently large non equilibrium ensemble (see also [31]).

The algorithms needed to describe such systems behaviour like e.g. described by the cellular automata of Wolfram [31] are irreducible. No algorithm exists with a calculation of the output of certain observations that is shorter than the natural time development. It might be possible that this aspect is correlated with the emergence of consciousness. At this point the reaction of the environment gives the system a feedback of the development but no algorithm exists that allows a “shortcut” in calculating the future state of the system.

2 EXPERIMENTAL SETUP AND DATA ANALYSIS

With four parameters I can fit an elephant and with five I can make him wiggle his trunk.

John von Neumann (János Neumann de Margitta), (1903 - 1957), Hungarian mathematician

2.1 Setup for time- and wavelength correlated single photon counting (TWCSPC)

For studies on light emission in the short time regime (10 ps – 100 ns) a TCSPC setup with spectral resolution was constructed as shown in Figure 29. The new system combines the advantages of the high optical throughput of a multi anode detector system with 16 output (anode) elements (PML-16 C, Becker&Hickl, Germany) allowing the registration of up to 10^6 counts/sec. with the sensitive technique of SPC and the big advantages of a mobile setup. An additional fiber connected optical system allows the targeted spectroscopy of samples in glass cuvettes, on surfaces or of whole leaves of higher plants (see Figure 31). Various pulsed lasers or LEDs can easily be connected as excitation light sources. The spectroscopy can be performed in vitro or in vivo. In addition a mobile cryostatic closed-loop helium system (see Figure 32) was built up that can be used in combination with the TWCSPC setup shown in Figure 29. Therefore the optical measuring station together with the mobile cryostatic temperature regulator can be transported to any available immobile laser excitation source within minutes allowing the utilization of all available light sources independently from their mobility.

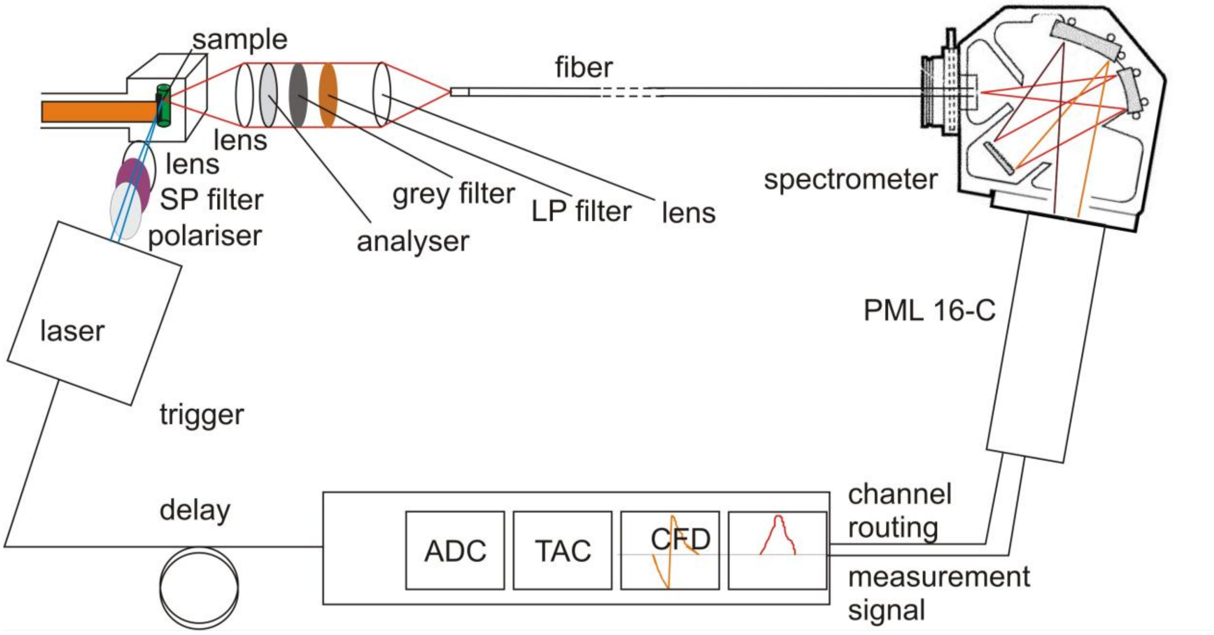

Figure 29: Measurement setup used for TWCSPC with optical path shown in blue for excitation from the laser source via optional polarizer and short pass (SP) filter. The sample temperature is variable with the cryostatic system as shown in Figure 32. The fluorescence light (red) is monitored via analyzer (optional), grey filters and long pass (LP) filter into the spectrometer system connected with the multianode photomultipliersystem PML 16-C. The PMT signal is processed via constant fraction discriminator (CFD), time to amplitude converter (TAC) and analog to digital converter (ADC).

For time resolved measurements picosecond diode laser modules were used for excitation at 632 nm (BHL-600, FWHM 60 ps, repetition frequency 20 MHz, average intensity 100 µW/10 mm², Becker & Hickl GmbH, Berlin) and 405 nm (LDH-405, FWHM 60 ps, tunable repetition frequency up to 8 MHz, Picoquant, Berlin, Germany) driven by PDL-200 or PDL-800 C (Picoquant, Berlin). Additionaly laser heads were used with wavelengths of 470 nm and 690 nm (Picoquant, Berlin, Germany) and for protein excitation a pulsed 280 nm UV light emitting diode (Picoquant, Berlin, Germany) delivering 600 ps FWHM pulses.

Excitation pulses in the spectral blue range at 430 nm and 460 nm were generated by a Ti:Sa-Oszillator (Tsunami - Spectra Physics) tunable between 720 and 980 nm followed by frequency doubling in a thin BBO crystal to obtain ultrashort excitation pulses of about 300 fs temporal bandwidth. Using a pulse picker system (Spectra Physics mod. 3980) the repetition rate of 82 MHz was reduced to 4 MHz. For details see the thesis of C. Theiss [2].

Fluorescence was detected at a right angle to the excitation beam. In order to suppress the scattered excitation light a long-pass emission filter was inserted between the cuvette and the detector (640ALP at an angle of 0° for 632 nm excitation (Omega Inc, cut-off wavelength 640 nm)).

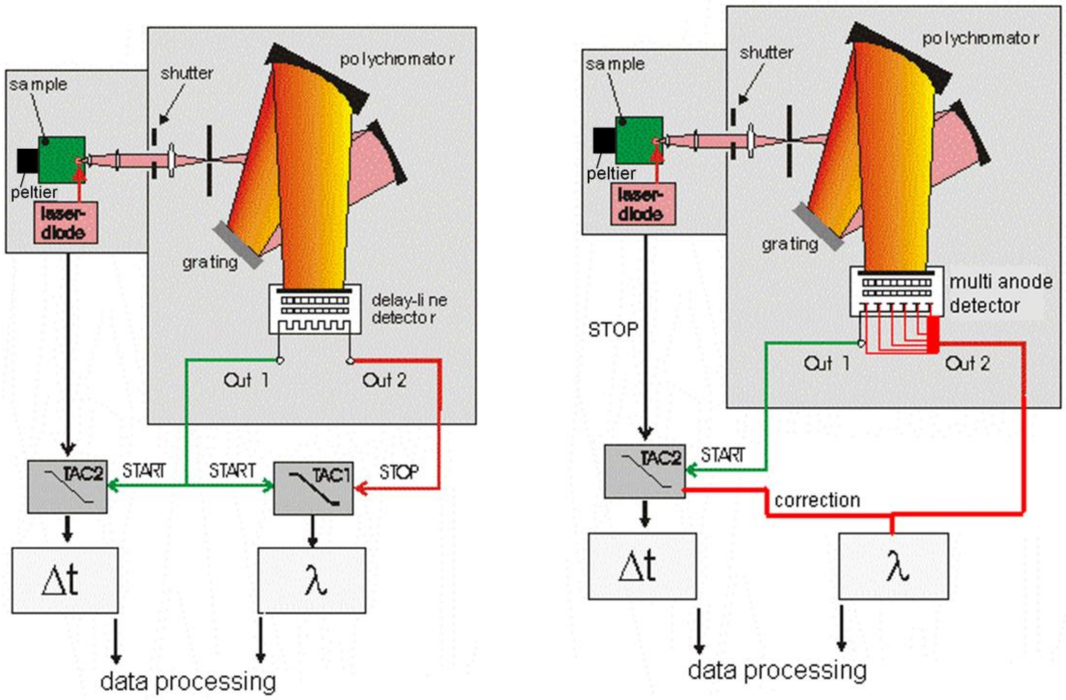

Figure 30: Different detection systems with delay line anode as described in [95] and [204] (left side) and PML-16 C (right side) as shown in Figure 29.

Figure 30 shows two different types of single photon counting systems with time- and wavelength resolution that were used during the experiments of this thesis. An additional setup is described below.

In Figure 30, left side, the system based on the technique of a delay-line detector is shown. During the measurement time- and space- correlation is used to determine simultaneously time- and wavelength information of the collected photons. Such double correlated single photon counting is achieved by using a microchannel plate photomultiplier (MCP-PMT) with delay-line anode (Europhoton GmbH, Berlin). In combination with a 120 mm crossed Czerny-Turner polychromator (MultiSpec, LOT) equipped with a 600 grooves/mm grating as a dispersive element, the space coordinate along the delay line correlates with the wavelength [95, 204]. Dependent on the wavelength the emitted photons are deflected onto the photocathode of the MCP-PMT in the focal plane of the polychromator. A photoelectron is emitted at the inner side of the cathode and amplified by two microchannel plates producing a spatially limited electron cloud, which finally hits the delay-line anode. The electric charge moves to the opposite ends of the delay-line and arrives at its both ends at different times depending on the position where the electron cloud hit the anode. The measured time difference between these two output pulses is then used to calculate the space-coordinate along the delay-line which allows the determination of the photon wavelength. The overall time-spread of a signal across the delay line is 5.7 ns [95, 204]. The two outputs of the delay-line anode are amplified by two 1GHz preamplifiers (Ortec 9306) and further processed by constant fraction discriminators (CFDs) (Tennelec TC 454). The Output of one of the CFDs provides the start signal for two time-to-amplitude converters (TACs, Ortec 457 for space domain and Tennelec TC 864 for time domain). The stop signal for the space-domain TAC is provided by the output of the second CFD.

As shown in Figure 29 and Figure 30 an electronic trigger signal provided from the laser source or laser driver is used as time trigger. Alternatively a small fraction of the excitation laser light is reflected onto a fast photodiode that provides the stop signal for the time-domain TAC.

The outputs of the two TACs shown in Figure 30, left side, are processed by a personal computer. The resulting data is stored in a two-dimensional channel matrix of size 256 x 1024, with 256 channels in the space domain corresponding to spectral resolution (wavelength coordinate) and 1024 channels in the time domain corresponding to temporal resolution (time coordinate of the fluorescence decay). The wavelength coordinate is provided directly by the output of the space-domain TAC. A correction for different photon wavelengths is applied to the output values of the time domain TAC in order to obtain the correct value of the time coordinate.

The technique of single photon counting operates with high signal to noise ratio which was $S/N \sim \sqrt{S}$ > 100 in the peak channel in all measurements performed in this study. With the setup presented in Figure 30, left side this S/N ratio can be achieved in measurement times of < 60 min. for up to 30 wavelength sections of 5-10 nm spectral widths. The instrumental response function (IRF) of this system has 150 ps full width at half maximum (FWHM), limiting the time resolution to about 15 ps.

Figure 30, right side, shows a time- and wavelength resolved setup with a multi anode detector system with 16 output (anode) elements (PML-16 C, Becker&Hickl, Germany) (see ref. [205]). Compared to the sensitive delay-line anode system the multi anode system yields a dramatically increased detection rate up to 1.000.000 counts/sec with the 20 MHz diode laser so that $S/N \sim \sqrt{S}$ > 100 is achieved within seconds in the peak channel for highly fluorescent samples. The core of the PML-16 C is a Hamamatsu R5900 16 channel multi-anode photomultiplier tube with 16 separate output (anode) elements and a common cathode and dynode system as described in [205]. The wavelength resolution of the multi anode system is limited by the number of anodes in comparison to the whole detected spectral bandwidth that is determined by the grating. Using the polychromator with a 600 grooves/mm grating the spectral bandwidth of the PML-16 C is 6.25 nm /channel.

New techniques using several photomultiplier tubes allow even higher count rates because pile up can be neglected if detector arrays containing independent detectors are used [206].

Measurements with higher time resolution performed in this thesis were achieved employing a monochromator system (McPherson Instrument) with a MCP-PM-tube (Hamamatsu). The IRF of this system was measured to be 71 ps FWHM allowing a time resolution which is shorter than 10 ps (see chap. 3, Figure 35). These measurements were done in a time window with 4096 channels and 5 ns in total. Typical calibration values were 1.22 ps per channel in the time domain.

A Peltier cooling/heating system (Peltron GmbH, Germany) allows the choice of any temperature in the range of 260 K to 330 K in every setup. The regulation of the sample temperature is necessary to avoid warming up of the sensitive cells and PPCs during the measurement. Furthermore the choice of different temperatures near the freezing point of water was necessary to investigate the influence of cold stress in photosynthetic cells (see also [43]) and decoupling effects in hybrid complexes containing semiconductor nanoparticles (CdSe/ZnS core/shell systems with dilipoic acid ligands on the surface) coupled to the PBP antenna of *A.marina* via EET (see [51, 52, 53]).

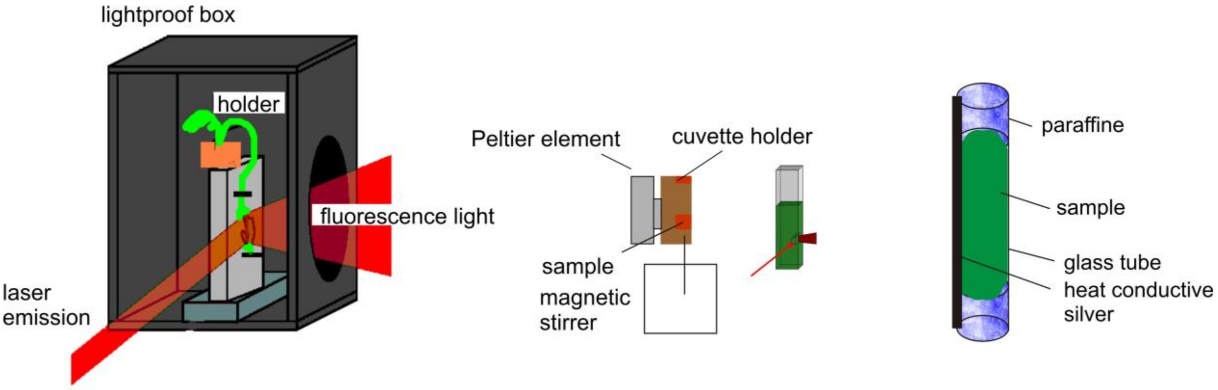

Figure 31: Leaf holder in a light proof box as constructed by M.Vitali (left side), cuvette system with copper cuvette holder coupled to a peltier heating/cooling system and optionally stirred with magnetic stirrer (middle) and glass tube cuvette thermally connected with the cold head of the crostatic system as shown in Figure 32.

For TWCSPC the most important resolution limit is the temporal time spread function of the incoming photons from the laser pulse, i.e. the elastically scattered laser light emitted from the investigated sample. This time spread function is measured as IRF (see Figure 35, chapter 3).

The total time width of the IRF is mostly broadened due to i) temporal width of the applied laser or LED pulses (from 300 fs up to 600 ps, respectively) (excitation broadening), ii) time spread of electrons inside the photomultiplier system (about 40 ps for Microchannel plate PMT and 80 ps for dynode systems) (amplifier broadening), iii) time spread during the signal processing in the measurement electronics, e.g. TCSPC card (3 ps due to Becker & Hickl), iv) time spread of the constructive interfering photons dispersed at the grating (depending on the size of the grating, about 1 cm, up to 30 ps) (spectroscopic broadening) and v) optical time spread of the collected photons at the sample focus.

The time spread of the collected photons at the sample position can be calculated assuming an impringing plane wave modulated by the diffractive strucure of the cuvette. Therefore it is principally possible to calculate the intensity distribution in the sample exactly. Also the spatial spread of the light field distribution at the sample position leads to a temporal broadening that is small in comparison to amplifier and spectroscopic broadening (60 and 30 ps, respectively).

Even if the photons are collected from a rather large volume of 1mm³ the time spread of the photons is only 3 ps. Therefore it is not so important to take care of such broading effects with TWCSPC because the orthogonal sum of the different contributions to the overall variance averages in such way that 3 ps time spread contributes < 1 ps (see eq. 1) to the overall temporal broadening.

The different broadening effects of the IRF limit the achievable time resolution of the TWCSPC setup. Strictly speaking it is the statistical dispersion associated with the broadening effects (see below) that limits the time resolution.

If we assume that the mentioned broadening effects are independent (smallest possible overall broadening), then the temporal width Δt of the overall IRF after excitation with LDH-405 (60 ps FWHM) and detection with the MCP-PMT can be roughly estimated:

1. $$\Delta t = \sqrt{\sum_i (\Delta t_i)^2} \approx \sqrt{40^2 + 60^2 + 2 \cdot 3^2 + 0.3^2}\, ps \approx \sqrt{60^2 + 40^2}\, ps \approx 72\, ps$$

This value is in well agreement with the measured $\Delta t := FWHM$ of 71 ps (see Figure 35) for the 405 nm Laser head (LDH-405, Picoquant, Berlin).

The claculated value of equation 1 does not mean that the temporal resolution of the setup is limited to about 70 ps. If the IRF is sufficiently stable one can measure the broadened curve and deconvolute the IRF signal from the measurement data. The deconvolution process is exact if the measurement data do not contain any noise. Therefore long measurement times are necessary for the detection of very small deviations between IRF and the measurement results and therefore representing a tool that enables the resolution of very short decay times. In principle, an idealistic setup should allow an infinite time resolution if the measuring time is extended to infinity. This is not realistic in practice, but very accurate measurements of the IRF with specially (e.g. thermally) stabilised setups achieve a much better principal resolution than the FWHM of the IRF [19, 27, 30]. Nevertheless it is not possible to stabilise the setup in an ideal way because there are always long term drift effects that reduce the best resolution typically to about 10 % of the FWHM of the IRF. Therefore it is also necessary to reduce the FWHM of the IRF to the smallest possible value.

Other techniques used to obtain fluorescence signals of high quality with short IRF and/or small spatial extention of the fluorescent area are i) use of optimized optical elements with highest numerical aperture, ii) black cuvettes (absorbing inner surface) with very small opening apertures, iii) pinholes and apertures (see examples for time integrated fluorescence in [141, 142]).

The thermal connection shown in Figure 29 can be coupled with a peltier element as shown in Figure 30. Measurements with widely varying temperature in the range between 10 K and 350 K were performed with a self-built variable-temperature cryostat (10-300K, CTI-Cryogenics 8001/8300) as mobile cryostatic system. It allows mobility between different measurement setups. A schematic representation of this cryostatic system is shown in Figure 32.

Instead of the automatic heating control that works with a PID feedback system to control the temperature in the cryostate a simple copper wire was used that is connected to a power supply and encircled around the cold head that is connected to a thermocouple. Due to the relation between temperature and resistance of the copper material the heating power of this setup automatically equilibrates at a temperature level that only depends on the quality of the vacuum and the voltage. Therefore the setup was calibrated to figure out the dependency of the temperature on the voltage set at the power supply (see Figure 32). The thermocouple can be used for an additional temperature control.

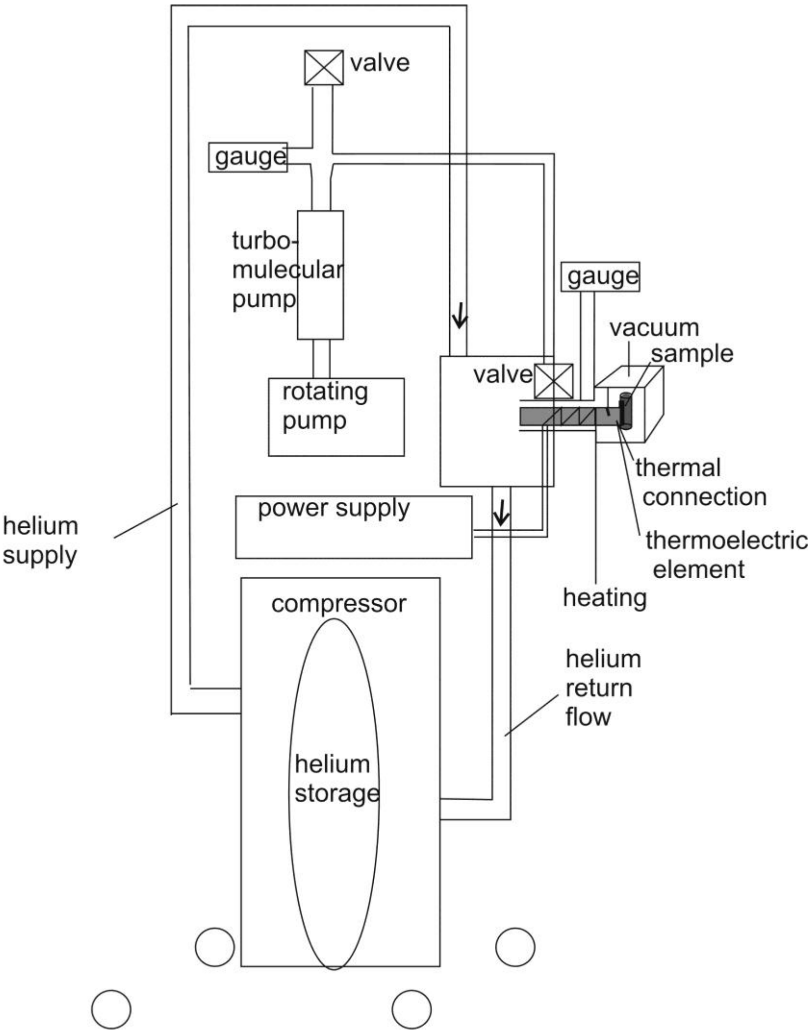

Figure 32: Mobile cryostatic system (10-300K, CTI-Cryogenics 8001/8300) with compressor, helium cartridge and expander. The vacuum is generated with rotating and turbomolecular pump. Temperature regulation is performed with an additional electric heating that consists of a copper wire connected with a power supply. The pressure is measured with two gauges inside the vacuum chamber and near the turbomolecular pump. The temperature is controlled via a thermoelectric element connected with the cold head.

2.2 Data analysis

Recent progress in computational physics lead to very different approaches for analysing spectral data. The fit of the decay curves in the time domain is only one approach. Inverse Laplace transformations of time and wavelength resolved decay curves or principal component analysis are techniques for a fully unbiased study of the measurement data. In this work mainly the multiexponential fit of decay curves in the time domain was applied because it allows a straightforward check of a proposed model for EET and ET reactions.

2.2.1 Data acquisition and fit routine

Figure 33 a), published in [56], shows typical fluorescence decay curves of whole cells of *A.marina* collected after excitation with 632 nm at room temperature performed with the delay-line setup shown in Figure 30, left side under continuous stirring in the cuvette shown in Figure 31, middle panel. The number of the registered photons at each wavelength and each time channel was stored in a 2-dim. 256 x 1024 data matrix as described in chap. 2.1. In Figure 33 a), this data matrix is shown as a color intensity plot (CIP). A CIP is a plot of the fluorescence intensity (pictured by the color) as a function of wavelength (y-axis) and time (x-axis). Therefore the CIP contains the time- and wavelength-resolved fluorescence emission data and provides information on the steady state fluorescence spectra and the lifetimes and dynamics of different emitter states. A vertical plot at a constant time t_0 results in the time-resolved emission spectrum $F(t_0, \lambda)$ (Figure 33 c)) while a horizontal intersection delivers the fluorescence decay at a constant emission wavelength λ_0 (Figure 33 b)). Time resolved spectra provide information on the fluorescence of certain fluorophores at distinct times, when the fluorescence emission of other pigments or scattered light already decayed or after energy transfer when the main emission shifted in time from the donor pigment to the acceptor pigment.

The spectral resolution of this spectrometer system is limited to about 2 nm (spectrometer entrance slit < 0,5 mm) due to the distance of the delay-line meanders and electrical crosstalk between the meander lines [95, 204].

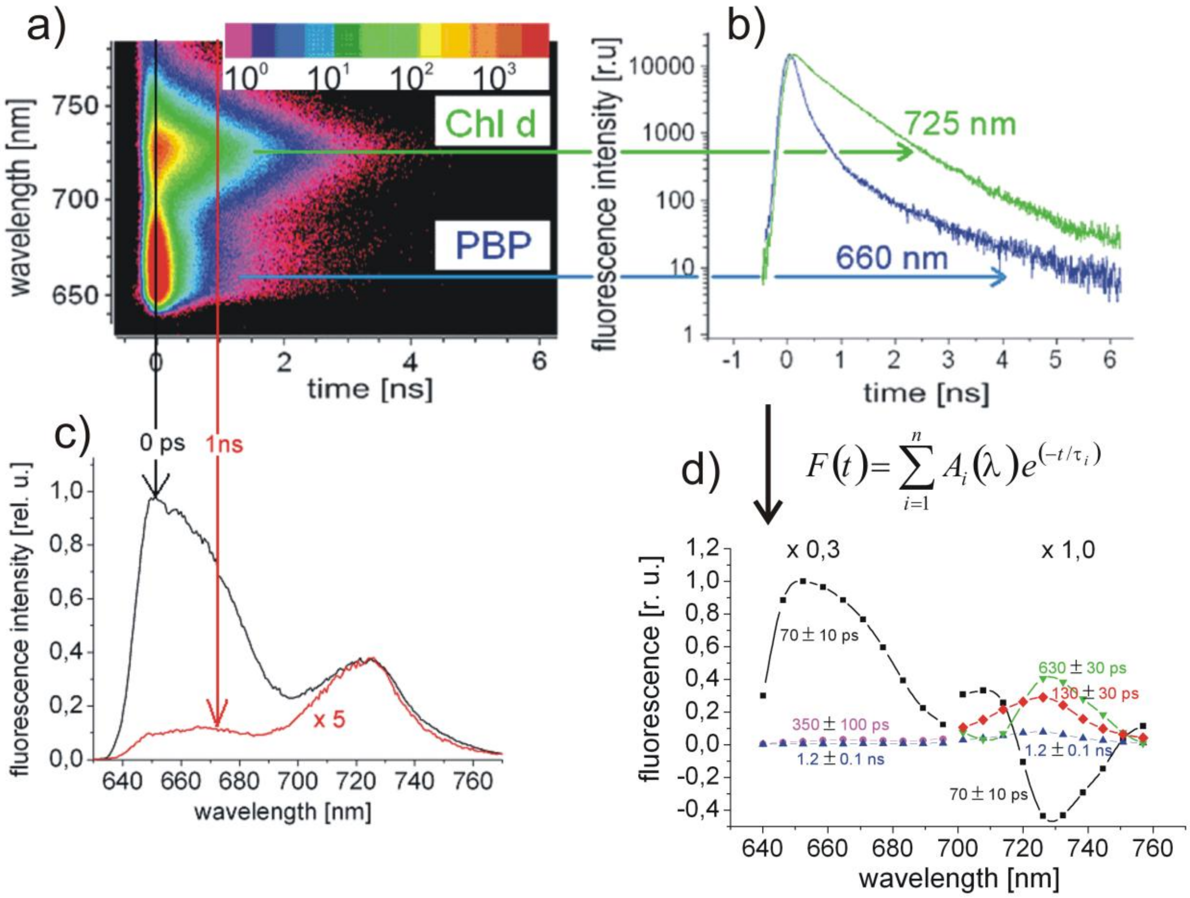

Figure 33: a) Color Intensity Plot (CIP) of a measurement on *A.marina* after excitation at 632 nm at 298 K. b) Fluorescence decay curves at 660 nm and 725 nm. c) Time resolved Fluorescence spectra at 0 ps and 1 ns (at 1ns multiplied with a factor 5). d) Decay associated spectra (DAS) of a global fit in the range 640 nm – 690 nm (multiplied with a factor 0.3) and a global fit in the range 700 nm – 760 nm (see text). The figure is published in [56].

Figure 33b) shows the decay curves of *A.marina* at 660 nm and 725 nm. It is seen that the fluorescence at 660 nm decays much faster than the emission at 725 nm. A closer look at the emission maximum on top of Figure 33 b) reveals a very small temporal shift between the 660 nm and the 725 nm decay curves. The 725 nm decay is slightly shifted to later times in comparison to the 660 nm decay. A data fit shows that the small temporal shift in the following called “fluorescence rise kinetics” has a similar time constant as the fluorescence decay at 660 nm. Both curves are convoluted with the instrumental response function (IRF) which leads to the small visible difference.

In Figure 33 c) the main emission is observed at 645 – 660 nm (PBP emission) immediately after excitation (0 ps) while after one nanosecond (1 ns) the strongest fluorescence band occurs at 725 nm (Chl *d* emission). For better illustration the spectrum after 1 ns is multiplied by a factor of 5. At longer times the Chl *d* emission exceeds the PBP emission.

Detailed analyses of the fluorescence decay curves were performed by iterative reconvolution of a polyexponential decay model with the IRF using a global lifetime analysis minimizing the quadratic error sum χ^2 employing a Levenberg-Marquardt algorithm (for details see [56, 47]). The IRF was measured using destilled water as scattering medium. The multiexponential fits of all decay curves measured in one time- and wavelength resolved fluorescence spectrum were performed as global fits with common values of lifetimes τ_j (linked parameters) for all decay curves and wavelength-dependent pre-exponential factors $A_j(\lambda)$ (non-linked parameters, see Figure 33 d)). The result of such a fit analysis is usually plotted as a graph of $A_j(\lambda)$ for all wavelength independent lifetimes τ_j . This plot represents the so called "decay associated spectra" (DAS) thus revealing the energetic position of individual decay components (for details see [47]).

The PBP emission (640 – 690 nm) (see Figure 33 d) is strongly dominated by a 70 ps decay component. Additionally, the DAS of the 70 ps-fluorescence contains a band with negative amplitude at 725 nm i.e. a rise kinetics of the Chl *d*-fluorescence. This fluorescence rise term is even better resolved at cryogenic temperatures (data not shown, see [54]). Therefore we ascribe the 70 ps component to an excitation energy transfer from the PBP antenna to the Chl *d* containing membrane integral antenna complex of *A.marina* [54]. The small slower decay component of τ = 350 ps in the 640 – 690 nm range result from PBP antenna complexes that are not coupled to the Chl *d* antenna and from conformationally distorted PBP antenna complexes (see also [43]).

A sufficient fit of the fluorescence kinetics in the Chl *d* range (700 – 760 nm) requires four decay components. The rise kinetics representing the population of Chl *d* via energy transfer from the PBP complexes exhibits a time constant of 70 ps (see Figure 33 d). Additionally there exist two dominating decay components with 130 ps and 630 ps with nearly equal amplitudes as shown in Figure 33 d). According to our previous findings the 630 ps-component is ascribed to PS II with open reaction centers. The slow decay component with a lifetime of 1.2 ns has only very small amplitude. It originates from a small fraction of PS II with closed reaction centers as shown by the increase of its initial amplitude upon closure of the RC of PS II (data not shown, for details see [54]). The fast 130 ps-decay of the 725 nm fluorescence component is only slightly affected by closure of the PS II RCs and therefore assigned mainly to PS I according as published in [54].

During iterative reconvolution of the IRF the reduced local χ_{lr}^2 is minimized. χ_{lr}^2 depends on a parameter set $(p_1,....,p_n)$ of the chosen fit function $FIT(t_\nu,\lambda_\rho,p_1,...,p_n)$ for the temporally discrete fluorescence points $F(t_\nu,\lambda_\rho)$. The function χ_{lr}^2 is evaluated at each time channel t_ν and averaged over all time channels:

2. $$\chi^2(p_1,\ldots.,p_n)=\frac{1}{L}\sum_{\rho=1}^{L}\underbrace{\frac{1}{K-(n-1)}\left(\underbrace{\sum_{\nu=1}^{K}\left(\frac{F(t_\nu,\lambda_\rho)-FIT(t_\nu,\lambda_\rho,p_1,\ldots,p_n)}{\sqrt{F(t_\nu,\lambda_\rho)}}\right)^2}_{\chi_l^{\,2}}\right)}_{\chi_{l,r}^{\,2}}$$

At first the weighted and local $\chi_l^{\,2}$ are evaluated for each wavelength section. Therefore the difference of $F(t_\nu,\lambda_\rho)=F_{\nu\rho}$ (time channel ν and wavelength section ρ) and the value of the fit function $FIT(t_\nu,\lambda_\rho,p_1,\ldots,p_n)$ depending on *n* free parameters is calculated. This difference is weighted in relation to the expected standard deviation in the fluorescence matrix $F_{\nu\rho}$: $\sigma_{\nu,\rho}=\sqrt{F(t_\nu,\lambda_\rho)}$ and summed quadratically along all time channels *K*. The standard deviation is the average deviation of the measured data points. Therefore the whole sum over *K* delivers $\chi_l^{\,2}\approx K$ if all deviations are of statistical nature.

To obtain an error function that is virtually independent of K the reduced local chi-square $\chi_{lr}^{\,2}$ is introduced with $\lim\limits_{K\to\infty}(\chi_{lr}^{\,2})=1$ if the number of parameters *n* is limited and only statistical deviations contribute to the deviation of the best fit. The global χ^2 is found by averaging all local error functions of the L wavelength sections. $\chi^2(p_1,\ldots.,p_n)$ is a general valuable tool to judge the quality of a curve matching.

The Levenberg-Marquardt algorithm generally uses the method of gradient-search to minimize $\chi^2(p_1,\ldots.,p_n)$. If n free parameters are given $\chi^2(p_1,\ldots.,p_n)$ is embedded into a n-dimensional hyper surface. In this case the gradient search might converge in a local minimum of $\chi^2(p_1,\ldots.,p_n)$. To avoid this effect the fit should start with a low number of parameters and their number should be increased during the fit (see also [95, 207]).

The best method is an investigation of the solution´s stability and a statistical interpretation of the results.

The idealized fluorescence decay $F(t,\lambda_i)$ of an ensemble of coupled states that are connected via EET rate constants is described by a multiexponential decay at a certain wavelength λ_i (see chapter 3.2.4):

3. $$F(t,\lambda_i)=\sum_{j=1}^{n}A_j(\lambda_i)\,e^{-t/\tau_j}$$

The parameters $A_j(\lambda_i)$ denote the amplitude and τ_j the time constant of the contribution of the j$^{\text{th}}$ exponential decay component at a certain wavelength position λ_i.

The ideal fluorescence decay $F(t,\lambda_i)$ is convoluted with the IRF of the experimental setup. Additionally a background noise exists because during the measurement always uncorrelated stray light and dark noise of the setup is collected that is taken into account by $F_0(\lambda_i)$. With a continuous time axis *t* the exact fit function $FIT(t,\lambda_\rho, p_1,..., p_n)$ used in the fitting routine performed in each wavelength channel λ_i denotes to

$$\textbf{4.} \quad FIT(t,\lambda_i, p_1,..., p_n) = F_0(\lambda_i) + \int_0^\infty \left(IRF(\lambda_i, t') \cdot \sum_{j=1}^{n} A_j(\lambda_i)\ e^{-(t-t')/\tau_j} \right) dt'$$

The final fit function as given by eq. 4 is the ideal fluorescence decay as given by eq. 3 iteratively convoluted with the measured $IRF(\lambda_i, t')$ and compared with the measurement data. At each wavelength position λ_i the FIT function of eq. 4 principally contains the free fit parameter set $(p_1,..., p_n) = A_j(\lambda_i)$, $F_0(\lambda_i)$ and τ_j. Generally only one set of τ_j values was chosen for all wavelength sections λ_i (i= 1…m) reducing the number of free parameters (global fit).

If the fit is performed with four exponential functions (*j*=1..4) for 16 wavelength sections (*i*=1..16) measured with the setup shown in Figure 30, right side, then we have 48 free parameters for $A_j(\lambda_i)$, 16 free parameters for $F_0(\lambda_i)$ and 4 free parameters for τ_j. These are *n*=68 parameters to simultaneously fit 16 fluorescence decay curves.

At first glance the fit problem seems to be overparameterized. Therefore the fit results were analysed for stability of the gathered fit results and the variance of single parameters was investigated. The most important fit result are the four free time contants τ_j. In general a fit with the equation 4 often shows strong variance in the amplitude distribution for $A_j(\lambda_i)$. The variance of the time constants τ_j was found to be much smaller.

The number of free parameters found in $A_j(\lambda_i)$ can be strongly reduced by assuming (e.g. Gaussian) lineshape functions for the emission of different fluorophores. If a system with two coupled 2-level systems coupled via EET is fit with known emission wavelengths for both 2-level systems only the amplitudes in two wavelength positions for each of the four components (6 free parameters) and in addition the spectral width of the two Gaussian emission spectra for each component (8 free parameters) are free parameters reducing the number of fit parameters found in the amplitude values $A_j(\lambda_i)$ from 48 to 14.

The parameter denoting the background noise can also be controlled by an accurate measurement of the noise accumulation in each channel during the measuring time.

The accumulated noise during a fixed time of the measurement in darkness delivers the possibility to determine the expected lower bound on the dark noise per channel with high accuracy. This reduces the number of 16 free parameters of $F_0(\lambda_i)$ for *i*=1..16 to zero. We assume two coupled emission states with known wavelength maximum that are fit with 4 global time constants and two Gaussian emission lineshape functions. Performing the steps of parameter reduction accurately reduces the number of free parameters used to fit the decay curves to 14 $A_j(\lambda_i)$ and four τ_j. That means there are 18 free parameters only to fit simultaneously 16 decay curves with four different exponential decay components. This procedure was not performed in that detail for all measurements but shows that the number of free parameters can be controlled also in complex systems.

In eq. 3 and 4 the time coordinate is treated as continuum but the evaluation of the fit curve given in eq. 4 has always to be pointwise (see eq. 2).

The time resolution is limited by the temporal width of the IRF and its stability during the whole measuring time which both represents a bottleneck for temporal resolution. The detailed discussion of the measured IRF for the setup used in the work presented here is outlined in the following chapter 3.1. The fitting routine was performed with the software of Globals Unlimited (University of Illinois, Urbana, USA) and a self written Matlab® routine was used, for further details see also ref. [16].

The multiexponential decay dynamics as given by eq. 3 can be derived from a system of linear differential equations of first order as suggested for the description of the coupled system of emitter states (see chap. 3.2). The multiexponential fit is satisfying for most systems with up to four decay components and agrees well with the experimental data.

The time constants τ_j given in eq.3 are the negative inverse eigenvalues of the so called “transfer matrix” which is the coefficient matrix of a linear differential equation system. The entries of the transfer matrix have the physical meaning of decay rates (see chap. 3.2.4 and ref. [95]). The spectral distribution of these decay rates is given by the j^th^ eigenvector U_j of the transfer matrix which has to satisfy the boundary conditions, i.e. the initial population densities at time t = 0 when the system is excited.

Chap. 3.2.4 describes in full detail that the total time and wavelength dependent excited state population of a certain fluorescence emitter $N_i(t)$ is multiexponential and therefore proportional to eq. 3 for each component at a certain wavelength position (see ref. [204] and [95]) :

5. $$N_i(t) = \sum_{j=1}^{n} U_{ij}\, e^{-t/\tau_j}$$

Each fluorescence emitter $N_i(t)$ contributes with a characteristic line shape function $s_i(\lambda)$

6. $$F(t,\lambda)=\sum_{i=1}^{n} s_i(\lambda)k_{F,i}N_i(t)$$

That has to be weighted with the intrinsic radiative emission rate constant (the inverse natural excited state lifetime) $k_{F,i}$.

The spectral line shape function $s_i(\lambda)$ denotes the probability that a single photon emitted by the emitter *i* is observed at the wavelength λ.

In photosynthetic pigment-protein complexes inhomogeneous broadening is dominating the line shape function due to the individual environment of each chromophore in the antenna complexes [204]. The protein environment is able to modulate the energetic states of the involved molecules (see chap. 1.3.3) and can form an energetic cone for energy funneling to the reaction center. The modulation by the protein can shift the energetic position of individual chromophores up to some nm (see chap. 4). This inhomogeneous broadening leads to a Gaussian lineshape of the applied $s_i(\lambda)$. In fact the lineshape of $s_i(\lambda)$ would be gaussian in the frequency domain assuming inhomogeneous broadening. This leads to a Gaussian $s_i(\lambda)$ in the wavelength domain for the 1st order Taylor approximation of the lineshape function. A refined theory however led to the conculsion that the lineshape is not perfect a Gaussian in the frequency domain (for a calculation for WSCP see e.g. ref. [38]). The determination of the exact lineshape function is beyond the scope of this work and therefore Gaussian lineshape functions at deep temperatures and Lorentzian lineshape functions at room temperature were used to fit the fluorescence emission spectra in the frequency domain. It was found that these lineshape functions led to satisfying fit results. The results were then transformed back to the wavelength domain and displayed in wavelength dependent graphs.

Homogeneous broadening like the lifetime broadening is about $\Delta\lambda \approx \frac{\lambda^2}{2\pi c\cdot\Delta t}$ (for a derivation of this relation see eq. 23 in chap. 3) which is in the order of $\Delta\lambda \approx \frac{\left(680\cdot 10^{-9}\right)}{2\pi\cdot 3\cdot 10^{8}\cdot 10ps} \approx$ 0.25 nm for an excited state lifetime of 1 ps e.g. due to excitonic relaxation or fast energy transfer processes. Therefore only if the lifetime becomes smaller than 1 ps the lifetime broadening should be taken into account and a Voigt or Lorentz-profile has to be used as lineshape function $s_i(\lambda)$. However a Lorentzian lineshape was found at room temperature.

As suggested by [204] employing the normalized Gaussian line shape function

7. $$s_i(\lambda)=\frac{1}{\sqrt{\pi}\delta_i}\exp\left(-(\lambda-\lambda_i)^2/\delta_i^{\,2}\right)$$

described by the center emission wavelength of the ith chromophore λ_i and the spectral linewidth δ_i the expression for the common formula of the wavelength dependent fluorescence emission denotes to

8. $F(t,\lambda) = \sum_{j=1}^{n} A_j(\lambda)\ e^{-t/\tau_j}$ according to eq. 3 to 6 with

9. $A_j(\lambda) = \sum_i \frac{k_{F,i}}{\sqrt{\pi}\delta_i} U_{ij} \exp\left(-(\lambda-\lambda_i)^2 / \delta_i^{\,2}\right)$

If the different emitter states are spectrally overlapping, the parameters $A_j(\lambda)$ are linear combinations of the spectral shapes $s_i(\lambda)$ of the different contributing emitters as given by eq. 9.

The plot of the parameters $A_j(\lambda)$ as a fit result of the TWCSPC spectra in form of DAS (see Figure 33) is generally used for data analysis of the emitter states and their temporal dynamics by comparison with simulated DAS according to a suggested coupling scheme (see chap. 3).

Employing the formalism given by eq. 8 and 9 one can simulate the expected DAS and compare them with the fit results (see chap. 3.2.5 for the theory of the simulations and chap. 4 and 5 for examples that were carried out according to the described procedure).

2.2.2 Optimal χ^2 and size of the parameter space

The multiparameter fitting procedure of complex decay schemes delivers results with high variance and is prone to problems of overparametrisation.

In general there are mainly two basic statistical problems that cause variance of the gathered results. At first the number of parameters used for the fit according to eq. 4 is not specified in detail.

If the system is not known and the expected fluorescence decay can not be predicted the choice of the number of exponential functions used for the fit is not determined. An overparametrisation delivers results as a statistical linear combination of basis functions (i.e. exponential functions) found in the space of all possible solutions.

But even if the number of exponential functions is determined and therefore the size of the parameter space is known the results gathered by evaluating the function $\chi^2(p_1,....,p_n)$ according to eq. 2 are not unambiguous (for a detailed discussion of $\chi^2(p_1,....,p_n)$ see [208]).

The main reason for this behavior is the fact that the signal of TWCSPC is always noisy, i.e. there is always a Poissonian distribution of count noise found in each channel. Therefore there exists a certain variance of the fitting scheme which can not be specified in full detail with the given experimental signal (for an example of this problem see [209]).

According to eq. 2 the reduced local $\chi_{l,r}^{2}$ of a fit of a single wavelength curve with four decay components which have free time constants and amplitudes as well as one free parameter for the background noise, calculates to $\chi_{l,r}^{2}(opt.)=1.002$ determining $\chi_{l,r}^{2}$ over 4096 time channels. That means the expected value of χ^{2} is exactly χ^{2}=1.002 in the ideal case of a “perfect” fit, i.e. the fit function matches the measurement data in a perfect way and the remaining residua between the measurement data and the fit are of pure statistical nature. We denote this best expected $\chi_{l,r}^{2}(opt.)=1.002$ as „optimal“ χ_{lr}^{2}.

In dependency on the size of the free parameter set $(p_1,...,p_n)$ and the number of data points the value of $\chi_{l,r}^{2}(opt.)$ varies strongly, but is always $\chi_{l,r}^{2}(opt.)>1.000$. Due to the stochastic nature of the measurement noise the value of $\chi_{l,r}^{2}(opt.)$ itself exhibits a standard deviation for an individual experiment $\Delta\chi_{l,r}^{2}(opt.)$ that can be calculated by the division of the actual local contribution $\left(\frac{F(t_\nu,\lambda_\rho)-FIT(t_\nu,\lambda_\rho,p_1,...,p_n)}{\sqrt{F(t_\nu,\lambda_\rho)}}\right)^{2}$ to the overall value of $\chi_{l,r}^{2}(opt.)$ and the square root of the actual measurement signal in the corresponding time channel $\sqrt{F(t_\nu,\lambda_\rho)}$ (see [207]):

10. $$\Delta\chi_{l,r}^{2}(p_1,....,p_n)=\frac{1}{K-(n-1)}\sum_{\nu=1}^{K}\frac{1}{\sqrt{F(t_\nu,\lambda_\rho)}}\left(\frac{F(t_\nu,\lambda_\rho)-FIT(t_\nu,\lambda_\rho,p_1,...,p_n)}{\sqrt{F(t_\nu,\lambda_\rho)}}\right)^{2}$$

When a fit procedure is performed and it turns out that $\chi_{l,r}^{2}<\chi_{l,r}^{2}(opt.)-\Delta\chi_{l,r}^{2}$ then the resulting value of $\chi_{l,r}^{2}(opt.)$ is “too good”. That means that the analysis of the experimental data is most probably overparametrisized. This could be a hint for the maximum paremeter space size to match $\chi_{l,r}^{2}=\chi_{l,r}^{2}(opt.)$ but not to be “better”, i.e. $\chi_{l,r}^{2}<\chi_{l,r}^{2}(opt.)$. $\chi_{l,r}^{2}=\chi_{l,r}^{2}(opt.)$ can only be achieved if the measurement is completely free of systematic deviations.

If we assume the hypothetical situation that $F(\lambda_\rho)\approx 10000$ for all time channels then $\Delta\chi_{l,r}^{2}(p_1,....,p_n)\approx 0.01$.

To estimate the appropriate size of the parameter space, one can use the so called F-statistics as published by Lakowicz [208].

The F-statistics gives an estimation suitable to judge the eligibility to use a further decay component in eq. 4 for the data fit, or, more general, to judge the necessity to introduce an additional parameter to the given parameter space.

In detail the F-statistics suggests that a better fit has at least a certain minimal value to be improved if an additional component is added to the fit function and the F-statistics can be used to calculate the confidence intervals $\Delta\chi_{l,r}{}^2$ of $\chi_{l,r}{}^2$ comparable to eq. 10. Only if $\chi_{l,r}{}^2(p_1,...,p_{n+1}) - \chi_{l,r}{}^2(p_1,...,p_n) > \Delta\chi_{l,r}{}^2$ the introduction of parameter p_{n+1} is justified. If $\chi_{l,r}{}^2(p_1,...,p_{n+1}) - \chi_{l,r}{}^2(p_1,...,p_n) = \Delta\chi_{l,r}{}^2$ then the experimenter has a probability of 68 % that the data really contains an additional parameter needed to find the accurate fit of the data but still a probability of 32 % that the improvement of the fit has just statistical reasons.

Therefore the highest number of allowed parameters (n+1) was chosen as a number that still leads to an improvement $\chi_{l,r}{}^2(p_1,...,p_{n+1}) - \chi_{l,r}{}^2(p_1,...,p_n) > \Delta\chi_{l,r}{}^2$.

At this point the scientist has to keep in mind the maximum information content that can be gathered from an experiment. The photonic fluxes contain a certain amount of information that is estimated to be around 50 bit / photon [71]. This information is composite of several parameters: the time of the photon arrival, the wavelength of the photons, the polarization of the photons etc. In fact we can reduce this problem to the information that is hidden in the structure of the correlation functions found in all parameters that describe the photon ensemble. If the flux is totally uncorrelated in all parameters then the information content found in the flux is maximal and vice versa.

Molecular diffusion or generally large diffusive reaction processes can lead to total loss of information of single time constants inside an ensemble of partners connected via FRET (for an elaborated work on such FRET experiments see Lakowicz [208]).

The distribution of different similar pigments inside the protein matrix can lead to stretched exponential functions, e.g. of the form $F(t,\lambda) = \sum_{j=1}^{n} A_j(\lambda)\, e^{-t/\tau_0 - \sqrt{t/\tau_j}}$ with strong variations of the dynamics if further restrictions like one- or two dimensional transfer occur (see [208] and references therein). Molecular dynamics, mesomeric transitions, protein oscillations influence the functional behavior of the excited state dynamics.

For many biological investigations it turned out that a kind of intuitive experience plays a role for the interpretation of the results, even if it might dispute the reductionists.

3. THEORY, FORMALISM AND RELATED EXPERIMENTS

In this chapter a short overview is given on selected theoretical concepts used to describe light and the interaction between light and matter. The general concept of rate equations used for the description of the most experimental results (chap. 3.2) is presented. In addition it is shown how the interaction of light and matter is described in classical electrodynamics (chap. 3.1) and quantum theory (chap. 3.3 and chap. 3.4). The theory of EET processes in the framework of Förster Resonance Energy Transfer (FRET) is introduced and discussed in chap. 3.3. Finally we close the theoretical investigations with a short outlook onto thermodynamic aspects and their relation to rate equations (chap. 3.5).

3.1 Light and matter

Fünfzig Jahre angestrengten Nachdenkens haben mich der Antwort auf die Frage »Was sind Lichtquanten?« nicht näher gebracht. Heute bilden sich Hinz und Kunz ein, es zu wissen. Aber da täuschen sie sich.

Albert Einstein (1879 - 1955), in a letter to M. Besso, 1951

3.1.1 Description of short laser pulses

From the time dependent Maxwell equations in vacuum

11. $\nabla \cdot \overline{E} = 0$

12. $\nabla \times \overline{E} + \dot{\overline{B}} = 0$

13. $\nabla \cdot \overline{B} = 0$

14. $\nabla \times \overline{B} = \frac{1}{c^2} \dot{\overline{E}}$

for the dynamics of electric fields $\overline{E}(\overline{r}, t)$and magnetic fields $\overline{B}(\overline{r}, t)$, one can derive a wave equation for the electric field with help of equations 11, 12 and 14:

$$\nabla \times \overline{B} = \frac{1}{c^2} \dot{\overline{E}} \xrightarrow{\partial_t} \nabla \times \dot{\overline{B}} = \frac{1}{c^2} \ddot{\overline{E}} \xrightarrow{eq.12}$$

$$-\nabla \times \left(\nabla \times \overline{E}\right) = \frac{1}{c^2} \ddot{\overline{E}} \rightarrow -\nabla\left(\nabla \cdot \overline{E}\right) + \Delta \overline{E} = \frac{1}{c^2} \ddot{\overline{E}} \xrightarrow{eq.11.}$$

15. $\Delta \overline{E} - \frac{1}{c^2} \ddot{\overline{E}} = 0$

The general solution of eq. 15 is an arbitrary linear combination of plane waves which depends on space coordinate $\overline{r}$ and time *t*:

16. $\overline{E}(\overline{r},t)=\int \tilde{E}(\omega)e^{i(\overline{k}(\omega)\overline{r}-\omega t)}d\omega$

where $\overline{k}(\omega)$ denotes the wave vector which depends on the frequency ω and $\tilde{E}(\omega)$ is the frequency dependent electric field amplitude.

Equation 16 solves 15 with the dispersion relation of the vacuum

17. $c^2 = \frac{\omega^2}{k^2}$

The coordinate system can be shifted arbitrarily and the observation can be fixed to one spatial point. If the point $x = y = z = 0$ is chosen then solution 16 simplifies to

18. $\overline{E}(t)=\int \tilde{E}(\omega)e^{i\omega t}d\omega$

which is the Fourier transformed of $\tilde{E}(\omega)$. Due to the Fourier Theorem equation 18 and therefore especially 16 represents any desired solution for the electric field $\overline{E}(t)$ denoted in equation 18, if it is periodic in time or vanishes in infinite time. If $\tilde{E}(\omega)=\overline{E}_0\delta(\omega-\omega_0)$ then $\overline{E}(t)=\overline{E}_0e^{i\omega_0 t}$ becomes an infinitely oscillating function and vice versa.

A pure delta-distribution in the frequency domain does not exist physically.

Especially in molecular physics functions $\tilde{E}(\omega)$ that interact with matter are often spectrally broad functions. In addition to the homogeneous lifetime-broadening there are several inhomogeneous broadening effects like the specific environment of different pigments [95].

The emission lines of laser materials are also often not Lorentz shaped as expected by homogeneous lifetime broadening but several additional inhomogeneous effects are relevant. For example Doppler broadening is highly relevant in gas lasers. The band structure determines the wavelength distribution of diode lasers. For a monography about lasers and laser pulses see [210].

For simplicity we assume that the probability distribution for frequency shifts in between inhomogeneous broadened laser lines is a gaussian distribution that is determined by the the center frequency ω_0 and the spectral bandwidth γ:

19. $\tilde{E}(\omega)=\overline{A}e^{-\frac{(\omega-\omega_0)^2}{\gamma^2}}$

The function denoting the time dependency of the electric field is the Fourier transformed of equation 19:

$$\bar{E}(t)=\int \bar{A}e^{-\frac{(\omega-\omega_0)^2}{\gamma^2}} e^{i\omega t}d\omega = \int \bar{A}e^{-\frac{(\omega-\omega_0)^2}{\gamma^2}} e^{i(\omega-\omega_0)t}e^{i\omega_0 t}d\omega =$$

$$\int \bar{A}e^{-\frac{(\omega-\omega_0)^2 - i\gamma^2(\omega-\omega_0)t - \frac{\gamma^4}{4}t^2 + \frac{\gamma^4}{4}t^2}{\gamma^2}} e^{i\omega_0 t}d\omega =$$

$$\int \bar{A}e^{-\frac{\left(\omega-\omega_0-\frac{i\gamma^2}{2}t\right)^2}{\gamma^2}} e^{-\frac{\gamma^2}{4}t^2} e^{i\omega_0 t}d\omega = \bar{A}\gamma\sqrt{\pi}e^{-\frac{\gamma^2}{4}t^2}e^{i\omega_0 t}$$

with the field amplitude $\bar{A}\gamma\sqrt{\pi} := \bar{E}_0$ as normalization factor. With the renotation $\frac{2}{\gamma} := \sigma$ we get:

20. $\bar{E}(t) = \bar{E}_0 e^{-\frac{t^2}{\sigma^2}} e^{i\omega_0 t}$

In this simplified picture the electric field in the time domain is (according to the simplifications done) time dependently oscillating with the frequency ω_0 and modulated by a gaussian intensity function $E_0 e^{-\frac{t^2}{\sigma^2}}$. An example how the interference of certain longitudinal modes inside a laser resonator forms a Gaussian shaped temporal intensity distribution (for example in case of mode locking) is plotted in Figure 34:

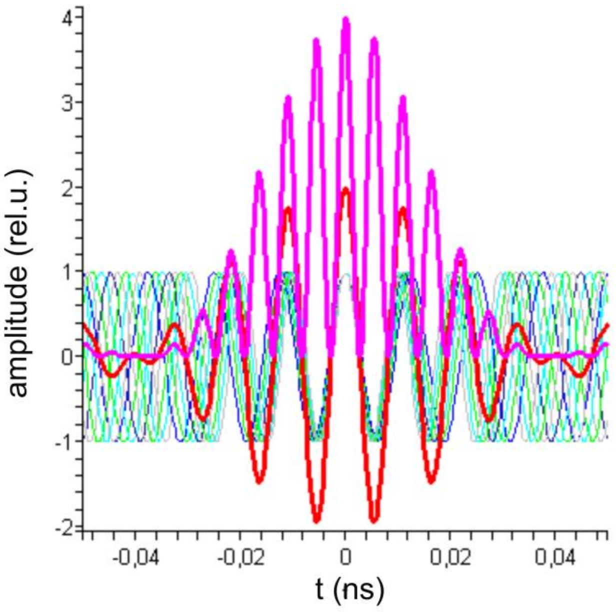

Figure 34: Exemplary plot of the temporal intereference pattern (red, multiplied with 0.25) of 8 longitudinal laser modes (blue, green, light green, navy, grey, some colors are used twice) which are iteratively shifted by the frequency shift $\Delta\omega/\omega = 0.04$. The red curve denotes the resulting electric field that oscillates with the center frequency ω_0. The red curve is multiplied with 0.25 for better visibility of the basic laser modes. The magenta curve shows the square of the electric field (red) as the resulting intensity function.

Figure 34 shows the resulting electric field according to eq. 20 if one summarizes 8 longitudinal modes instead of the continuous wave package as given in eq. 18 and 19 (red curve, scaled with a factor of 0.25) . The resulting intensity function oscillating with the frequency of $2\omega_0$ is shown in magenta.

In fact ultrashort laser pulses like fs Ti:Sa pulses are not oscillating with a temporally independent frequency but characterised e.g. by chirp [2, 210, 211, 212].

σ denotes the Gaussian linewidth in the time domain and γ the Gaussian linewidth in the frequency domain: $\frac{2}{\gamma} = \sigma$. This represents the low limit of the relation of uncertainty of time and energy due to Heisenberg:

21. $\Delta\omega\Delta t \geq 1$

The energy of the radiation field is quantisized in form of photons according to M. Planck [213]:

22. $E = \hbar\omega = h\nu$

for the energy of one photon E which is related to the frequency of the photon by the Planck constant *h*.

The theory for photon propagation is a statistic theory in full quantum mechanical sense. In the Fock space the number of photons is an observable and therefore the treatment of the radiation field as a quantisized field is understood as the “invention” of quantum mechanics. If it is mentioned for an example that 0.01 photons are detected per excitation cycle this is supposed as the detection of an average number of one photon per 100 excitation pulses while in average 99 times of 100 no photon is detected.

The laser pulse is formed by an ensemble of photons. Most measurements were performed with ps-laser diodes emitting at 632 nm (BHL-600, Becker&Hickl, Germany) with 70 ps FWHM at a repetition rate of 20 MHz and 405 nm (LDH-405, Picoquant, Berlin, Germany) delivering 60 ps FWHM pulses, driven at a repetition rate of 8 MHz. According to B&H and Picoquant both systems emit typically Gaussian laser pulses in the time domain with small afterpulses of < 1 % amplitude. The spectral bandwith was measured to be about 3 nm. According to the Fourier-limitation as denoted in the relation 21 the minimal spectral bandwidth can be calculated for 60 ps laser pulses at a wavelength of 405 nm to:

23.
$$\begin{aligned} &\Delta\omega\Delta t \geq 1 \Rightarrow \Delta\omega = 2\pi c\left(\frac{1}{\lambda_1} - \frac{1}{\lambda_2}\right) \approx 2\pi c\frac{\Delta\lambda}{\lambda^2} \approx \frac{1}{\Delta t} \\ &\Rightarrow \Delta\lambda \approx \frac{\lambda^2}{2\pi c\Delta t} = \frac{\left(405\cdot10^{-9}\right)^2}{2\pi\cdot3\cdot10^8\cdot60\cdot10^{-12}}m \approx 0.0015\,nm \end{aligned}$$

The most narrow possible line of a 60 ps laser pulse with 405 nm emission wavelength is about 2.7 GHz or 0.0015 nm. Therefore our laser pulses are not spectrally bandwidth limited. It is known for semiconductor lasers used in the study presented here that the band structure of the material is the limiting factor for the emitted laser radiation [210]. It was observed that the spectral bandwidth of the laser pulses varies strongly with the current used to pump the semiconductor material.

For time resolved measurements of pigment protein complexes exhibiting phonon broadened absorption- and emission lines with 10 nm FWHM or more, the spectral distribution of the laser line is well approximated by a delta-distribution in the frequency domain. In fact, no significant differences between excitation with fs laser pulses of 8 nm spectral bandwidth and ps diode laser pulses of 2 nm spectral bandwidth of the excitation source were observed for time resolved measurements of the fluorescence emission of photosynthetic pigment-protein complexes (see e.g. [47]).

For the evaluation of the data in the time domain the temporal shape of the laser flash is measured as instrumental response function (IRF) (see chap. 2). The IRF of the LDH-405 is shown in Figure 35 and Figure 36 in linear scale and logarithmic scale, respectively. The temporal bandwidth of the laser pulses of 60 ps corresponds to a length of the pulse trace of 1.8 cm in air. The IRF shown in Figure 35 and Figure 36 was measured with a monochromator system (McPherson Intrument) equipped with a MCP-PM-tube (Hamamatsu) as detector as described in chapter 2.

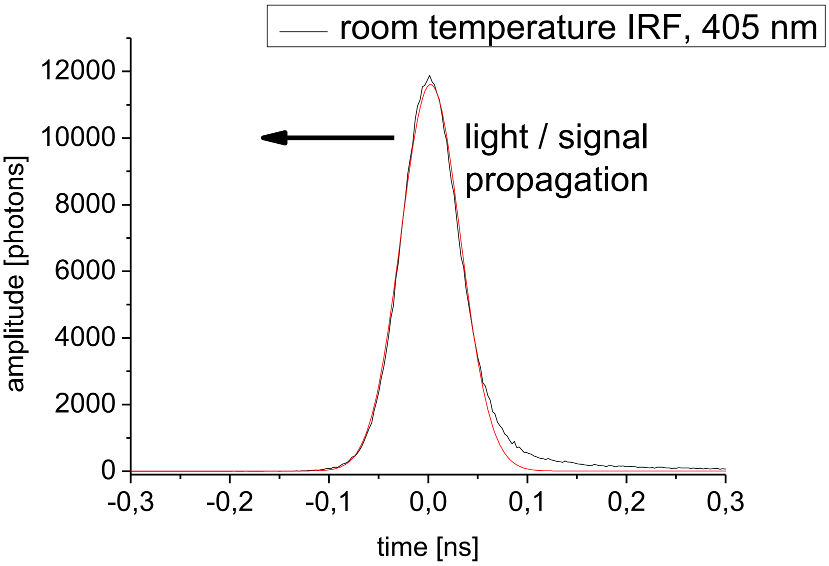

Figure 35: IRF of the LDH-405 at room temperature (black curve) measured with the McPherson monochromator and MCP-PM-tube from Hamamatsu as mentioned in chapter 2.1. The best Gaussian fit of the IRF with 71 ps FWHM is shown in red. The rising slope of the signal is found at the left side while the falling slope on the right side contains a small shoulder which is deviating from the Gaussian fit.

Figure 35 shows the IRF of the blue 405 nm excitation laser diode (LDH-405) at room temperature (black curve) and a Gaussian fit of the IRF signal. The best fit as presented in Figure 35 and Figure 36 exhibits 71 ps FWHM. While the deviation of the IRF from the Gaussian fit is only small in the rising slope of the signal there exists a remarked shoulder about 200 ps after the pulse maximum which is better visible in the logarithmic plot shown in Figure 36.

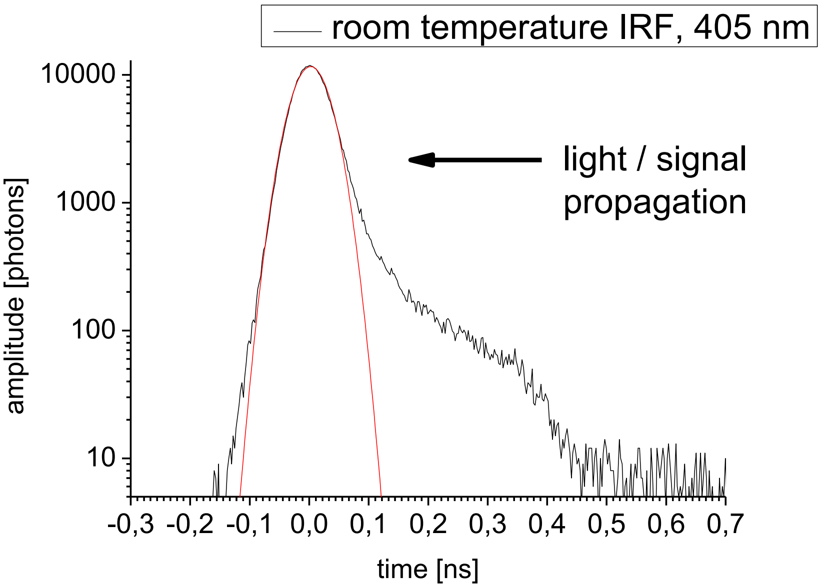

Figure 36: Logarithmic plot of the IRF (black curve) and the Gaussian fit (red curve) shown in Figure 35

The integral of the gaussian fit contains 94.2 % of all photons measured in the time window shown in Figure 36.

Due to this experimental result we assume the IRF to be well described by a temporal Gaussian distribution but we should keep in mind that the shoulder 200 ps after the pulse is a significant deviation. Therefore all fit procedures done in this work were performed with the IRF directly measured on the same sample. For further details regarding data analysis and deconvolution see [43, 47, 51-54] and chapter 2.2.

As mentioned above the laser pulse is accurately described by a temporal Gaussian and a spectral delta-function. This is considered by the formula given in eq. 20: the electric field of all photons should follow the pulse function $\overline{E}(t)=\overline{E}_0 e^{-\frac{t^2}{\sigma^2}} e^{i\omega_0 t}$. Equation 20 describes the temporal evolution of the electric field vector at a fixed point in space.

In the most simple picture of density dependent absorption and emission processes we will focus on the intensity of the laser pulse:

The time dependent energy density *u*(t) (i.e. the energy per space unit) in the electric field denotes to:

24. $$u=\frac{1}{2}\varepsilon_0\left|\overline{E}(t)\right|^2=\frac{1}{2}\varepsilon_0\overline{E}_0{}^2 e^{-\frac{2t^2}{\sigma^2}}$$

Introducing the spatial photon density *n*(t) of the photons in the pulse with the expected frequency ω_0 equation 24 must be equal to

$$\textbf{25.}\ u = n(t)\cdot\hbar\cdot\omega_0 = \frac{1}{2}\varepsilon_0\left|\overline{E}(t)\right|^2 = \frac{1}{2}\varepsilon_0\overline{E}_0{}^2 e^{-\frac{2t^2}{\sigma^2}}$$

We find that the photon density *n*(t) for the incoming photons in time is proportional to the square of the electric field as calculated from the Maxwell equations 11-14:

$$\textbf{26.}\ n(t) = \frac{\varepsilon_0\overline{E}_0{}^2}{2\hbar\cdot\omega_0}e^{-\frac{2t^2}{\sigma^2}}$$

From equation 25 we can easily calculate the time dependent intensity distribution of the laser pulse employing the continuity equation:

$$\textbf{27.}\ I = c\cdot u(t) = \frac{1}{2}c\varepsilon_0\overline{E}_0{}^2 e^{-\frac{2t^2}{\sigma^2}}$$

and with help of 26 we find the photon current (photons per area and time) in analogy to equation 27

$$\textbf{28.}\ j_{phot} = c\cdot n(t) = \frac{c\varepsilon_0\overline{E}_0{}^2}{2\hbar\omega_0}e^{-\frac{2t^2}{\sigma^2}}$$

which fullfills the relation $I = j_{phot}\cdot\hbar\omega_0$

Our description focuses on the time dependent evolution of an average electric field, intensity and photon density propagating with the laser pulse.

3.1.2 Interaction between light and matter

In classical electrodynamics the interaction of light described as an electric field or electromagnetic field with a certain material is given by Maxwell´s equations in matter:

$$\textbf{29.}\ \nabla\times\overline{E} + \dot{\overline{B}} = 0$$

$$\textbf{30.}\ \nabla\cdot\overline{B} = 0$$

$$\textbf{31.}\ \nabla\cdot\overline{D} = \rho$$

$$\textbf{32.}\ \nabla\times H - \dot{\overline{D}} = \bar{j}$$

The material parameters are found in the displacement field

$$\textbf{33.}\ \overline{D}(\bar{r},t) = \varepsilon_0\overline{E}(\bar{r},t) + \overline{P}(\bar{r},t) = \varepsilon_0\overline{E}(\bar{r},t) + \varepsilon_0\chi_e\overline{E}(\bar{r},t) = \varepsilon_0\varepsilon_r\overline{E}(\bar{r},t)$$

which is formed by the time and space dependent electric field $\overline{E}(\bar{r},t)$ and the polarisation $\overline{P}(\bar{r},t)$. The polarisation depends on the electric susceptibility χ_e which determines the relative dielectric constant $\varepsilon_r = (\chi_e + 1)$.

In general the electric field $\overline{E}(\bar{r},t)$ is not necessarily parallel to the polarization $\overline{P}(\bar{r},t)$ as given by eq. 33 but there might be an anisotropy of the polarisation leading to an angle between $\overline{E}(\bar{r},t)$ and $\overline{P}(\bar{r},t)$. In that case the susceptibility has to be a mathematical entity which can turn the electric field vector, i.e. $\overline{\overline{\chi}}_e$ is a tensor and not a scalar. In that general case the polarisation calculates to

$$\textbf{34.}\ \overline{P}(\bar{r},t) = \varepsilon_0 \overline{\overline{\chi}}_e \overline{E}\ .$$

For strong electric fields the polarization $\overline{P}(\bar{r},t)$ as given by eq. 33 is not necessarily proportional to the electric field $\overline{E}(\bar{r},t)$. The expansion as a Taylor series generally denotes to

$$\textbf{35.}\ \overline{P}(\bar{r},t) = \varepsilon_0 \left(\overline{\overline{\chi}}_e^{(1)} \overline{E} + \overline{\overline{\chi}}_e^{(2)} \overline{E}^2 + \overline{\overline{\chi}}_e^{(3)} \overline{E}^3 + \ldots \right).$$

Eq. 35 contains anistropy effects due to the tensor character of $\overline{\overline{\chi}}_e$ but also the nonlinear relation between $\overline{E}(\bar{r},t)$ and $\overline{P}(\bar{r},t)$. According to eq. 35 the polarisation is treated to depend linearily on the electric field as 1st order approximation $\overline{P}(\bar{r},t) \approx \varepsilon_0 \overline{\overline{\chi}}_e^{(1)} \overline{E}$ with corrections of 2nd order $\overline{\overline{\chi}}_e^{(2)} \overline{E}^2$ and higher orders.

In full analogy to eq. 33 the magnetic response of the material denotes to $\overline{B}(\bar{r},t) = \mu_0 \left(\overline{H}(\bar{r},t) + \overline{M}(\bar{r},t) \right) = \mu_0 \left(\overline{H}(\bar{r},t) + \chi \overline{H}(\bar{r},t) \right) = \mu_0 \mu_r \overline{H}(\bar{r},t)$ with the magnetic field $\overline{B}(\bar{r},t)$, the magnetizing field $\overline{H}(\bar{r},t)$, and the magnetization $\overline{M}(\bar{r},t)$ which is determined by the relative magnetic permeability $\mu_r = (1 + \chi_M)$ or magnetic susceptibility χ_M. For non ferromagnetic materials which are only slightly diamagnetic or paramagnetic $\mu_r \approx 1$, i.e. the magnetic suceptibility vanishes and the material is transparent for magnetic fields. This is the case for all pigment-protein complexes studied in this thesis. Therefore we neglect the magnetic properties of our materials and focus on the electric properties only. In the following $\mu_r \approx 1$ is assumed.

The relative dielectric constant ε_r contains effects of absorption and refraction . Therefore ε_r must be a complex tensor. For the simple case of isotropic media and linear response ε_r is a complex number $\tilde{\varepsilon}_r = \varepsilon_1 + i\varepsilon_2$ with the real part ε_1 of the electric field denoting the refraction and reflection of the electric field amplitude and the imaginary part ε_2 which denotes the damping of the electric field amplitude.

The dielectric constant is the square of the complex refraction index $\tilde{n}$: $\tilde{\varepsilon}_r = \tilde{n}^2 = (n + i\kappa)^2$ with the real part *n* and the imaginary part κ. From that one can derive $\varepsilon_1 = n^2 - \kappa^2$ and $\varepsilon_2 = 2n\kappa$

3.1.3 The plasmon resonance of gold nanoparticles

It is the aim of this short chapter to give an example how the classical theory of Maxwell (chap. 3.1.1 and 3.1.2) is used to calculate the absorption spectrum of a certain dielectric or metallic structure, how it is possible to explain and predict optical spectra and how one can use this information for applications.

If the polarisation shown in eq. 33 is driven by the electric field like a Lorentz oscillator (Drude-Lorentz-model) then the wavelength dependent resonance of the polarisation can be calculated by solving an oscillator equation as described in [212]. This calculation is performed for nanoparticles in dependency of the particle size in [212]. An example of the optical response for metallic Au-nanoparticles is presented in the following (see also [25] for the discussion of the optical properties of Au-nanoparticles).

The size-dependent plasmonic resonance of Au nanoparticles determines a characteristic absorption spectrum. Especially the diffuse stray light of thin layers of gold nanoparticles shows remarkable absorption due to the plasmon resonance and therefore exhibits a characteristic spectrum. This can be used to visualize gold nanoparticles in the dark field microscope and identify them by their characteristic spectrum. The microscopic picture (Figure 38) presented in the following shows how it is possible to identify and localize these nanoparticles even in strongly inhomogeneous media (living cells).

According to the Drude-Lorentz model one can start to arrange the oscillator equation for a damped negatively charged particle (charge *e*) of the mass *m* that moves along y-direction due to the driving external field $\overline{E}(t)$:

$$\textbf{36.}\quad m\ddot{\bar{y}}(t) + m\Gamma\dot{\bar{y}}(t) + m\omega_0{}^2\bar{y}(t) + e\overline{E}(t) = 0$$

Γ denotes the damping constant due to scattering processes at the metallic band structure and ω_0 denotes the eigenfrequency of the undamped free oscillator.

Inside a metallic sphere the oscillating electrons bound to the positive charge of the radius (*R*)-dependent number of positively charged holes *N*(*R*) are confined to the sphere.

The force driving back the electrons can be approximated by solving the electric field inside a homogeneously charged sphere (radius *R*) carrying the overall charge *N*(*R*)*e*. The strength of the electrical field inside a homogeneously charged sphere is linear in the distance to the center of the sphere (i.e. *y*(*t*)) and calculates to $\frac{N(R)e}{4\pi\varepsilon_0 R^3}\bar{y}(t)$ (for details regarding the calculation see e.g. [214]).

The polarization of the sphere $\bar{P}(t) = e\bar{y}(t)$ is introduced and eq. 36 multiplied with an elementary charge *e* :

$$\textbf{37.}\ \ m\ddot{\bar{P}}(t) + m\Gamma\dot{\bar{P}}(t) + \frac{N(R)e^2}{4\pi\varepsilon_0 R^3}\bar{P}(t) + e^2\bar{E}(t) = 0$$

Comparing eq. 37 with eq. 36 one finds the eigenfrequency of the undamped oscillator: $\omega_0 = \sqrt{\frac{N(R)e^2}{m4\pi\varepsilon_0 R^3}}$.

Eq. 37 can be solved with eq. 34 and the ansatz $\bar{E}(t) = \bar{E}_0 e^{i\omega t}$ for the electric field:

$$\textbf{38.}\ \ -m\varepsilon_0\chi_e\omega^2 + im\Gamma\varepsilon_0\chi_e\omega + \frac{N(R)e^2\chi_e}{4\pi R^3} + e^2 = 0$$

The relation between polarisation and the electric field considers the material parameters in this theory. From this formalism it is possible to approximate the optical properties of the metallic sphere.

To find the absorption spectrum one has to solve eq. 38 for the electric susceptibility χ_e which is a function depending on the light frequency ω. The final absorption is the imaginary part of the complex refraction index $\tilde{n} = \sqrt{\tilde{\varepsilon}_r} = \sqrt{1+\chi_e}$ (see [24] and [25] for further details).

We will not go into deeper details of this evaluation of the Maxwell´s equations shown in eq. 29-32. At this point it is our aim to show how theory and experiment are strongly connected if one wants to investigate for example gold nanoparticles as described by the Drude-Lorentz model (eq. 37).

For the experimental purpose we visualized the gold nanoparticles at first employing scanning electron microscopy (contrast of electron transmission and energy dispersive spectra) and atomic force microscopy to determine the structure and composition of the Au nanoparticles with about 40 nm in diameter. The atomic force microscope was equipped with a light microscope to find and measure the same structures on the sample that had been investigated with the scanning electron microscope before (see Figure 37), [24].

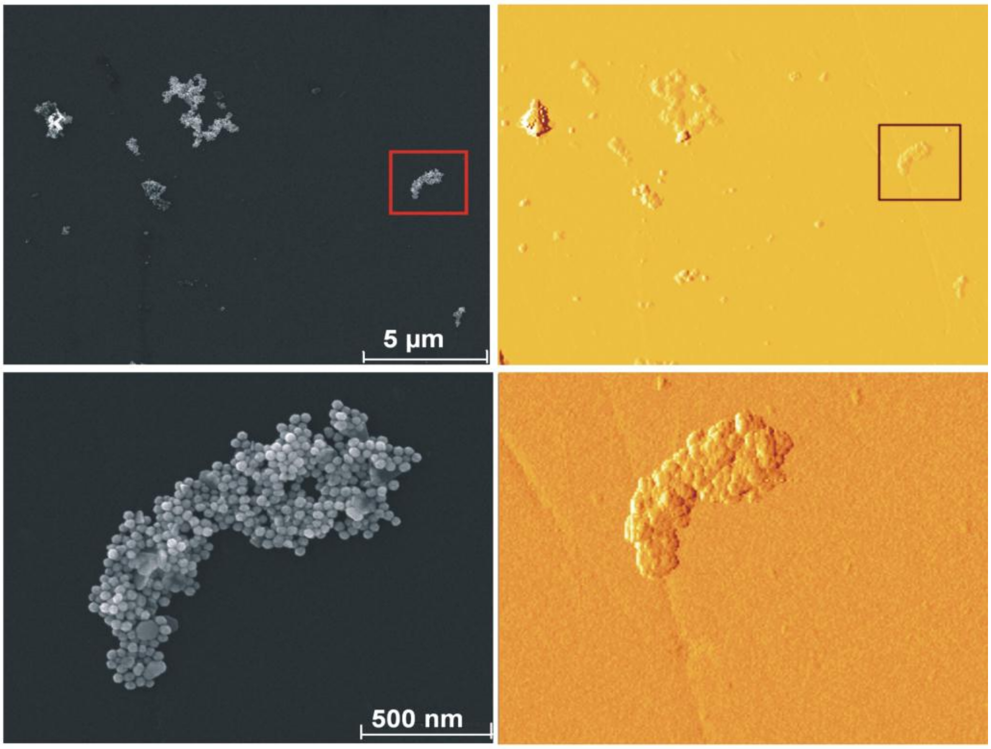

Figure 37: Gold nanocrystals with about 40 nm diameter in the scanning electron micropscope (left side) and atomic force microscope (right side). The electron microscopic study was supported by Zelmi of TU Berlin [24].

As shown in Figure 38 the nanoparticles exhibit a typical red color due to the plasmon resonance and scattering effects in the short wavelength regime (see Figure 39).

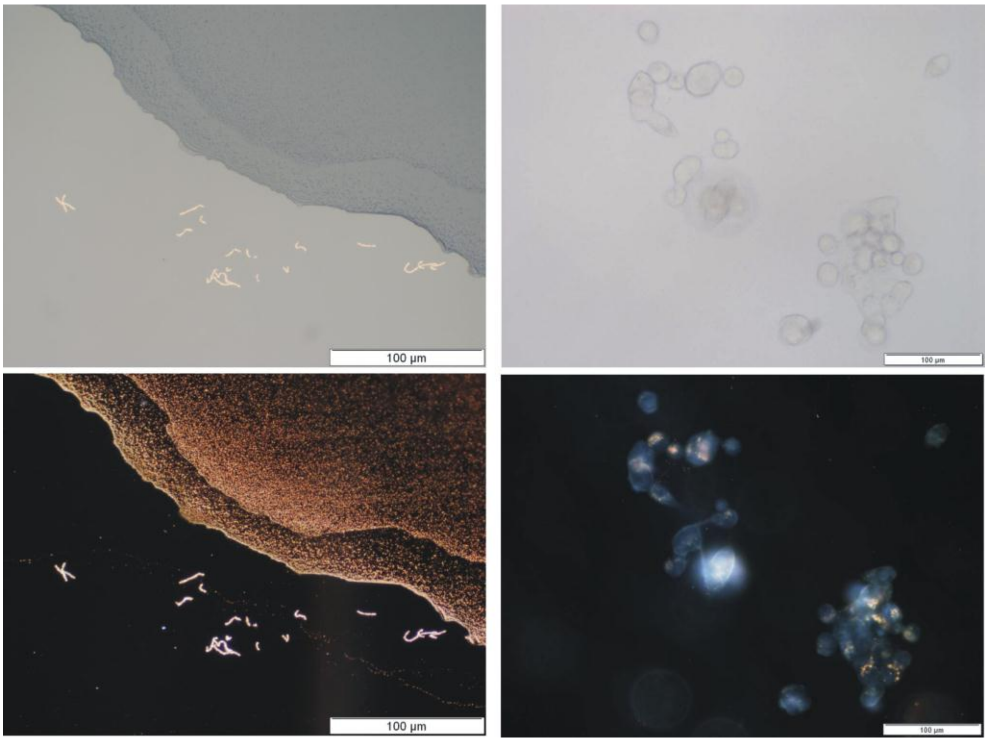

Figure 38: The plasmonic resonance results in good contrast of the nanoparticles in the dark field microscope. Pure nanoparticles appear red (left panel) in the dark field microscope (upper left panel: bright field microscopy, lower left panel: dark field microscopy). Inside HCT-cells (right panel) the nanoparticles tend to aggregate similar to the dry aggregates out of the wavefront shown in the left panel. The aggregates appear gold (upper right panel bright field, lower right panel dark field). The pictures are supported by Zelmi of TU Berlin.

The dark field technique (Figure 38, lower panels) delivers a tool for the study of nanostructures in strongly inhomogeneous media if the spectral contrast of the distribution of the scattered photons is high enough between the medium and the nanostructures. In the bright field microscope the integration of more photons including the ones which did not interact with the sample, leads to a much lower contrast (Figure 38 upper panel).

The graphs in Figure 39 show the imaginary part of the complex refractive index calculated from the Drude-Lorentz model as presented in eq. 37 with an additional ω^4 dependent and an additional constant scattering background.

The calculated curves (Figure 39, left side) qualitatively fit the experimental results (Figure 39, right side). Deviations between theory and experiment appear due to the approximations made and due to the formation of nanoparticle aggregates. The latter effect was investigated measuring the absorption spectra of aggregated nanoparticles (data not shown). The radius dependent values $N(R)$ and the damping constant Γ were used as fit parameters for the theoretical curves shown in Figure 39. For further details of the calculation see [25].

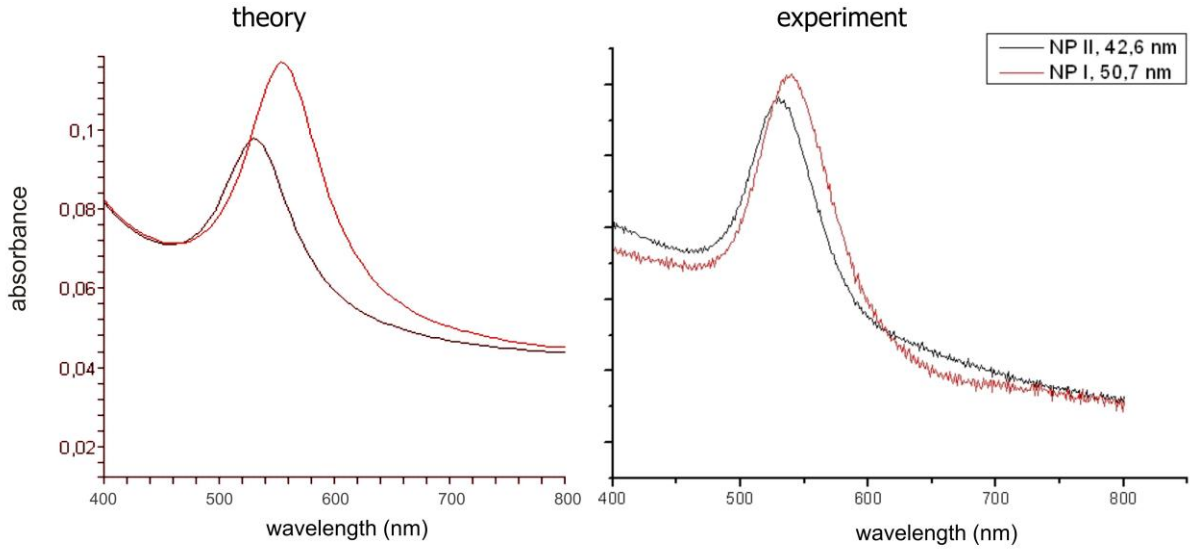

Figure 39: Theoretically fit and experimental absorption spectra of gold nanoparticles with 42.6 nm in diameter (black curve) and 50.7 nm in diameter (red curve)

As mentioned above the intention of this short excursion to microscopic pictures and spectra of gold nanoparticles shall demonstrate the power of the synergetic interplay of theory and experiment.

The theory makes the experimental results understandable (Figure 39) and it suggests further experiments or applications and forecasts the results (i.e. the possible identification of metallic nanoparticles sized far below the resolution limit of optical microscopes with a dark-field microscope, Figure 38). The experiment on the other hand tests the theory and selects the approaches that are able to describe reality from failing concepts.

3.1.4 Quantum mechanical description of molecule complexes

Generally the Maxwell´s equations in materia as presented in chap. 3.1.1 - 3.1.3 are macroscopic equations, i.e. the material parameters are assumed to be macroscopic parameters which are common mathematical entities for the whole solid state (see eq. 34). This is suitable to explain qualitatively the spectra of gold spheres containing several million gold atoms (Figure 39), but this theory will fail explaining the behaviour of single molecules bound to protein structures which can absorb energy and transfer the energy via electromagnetic coupling to neighbouring molecules (see chap. 1.3). In the following the quantum mechanics of the solid state is shortly introduced and it is shown how Bloch waves are suitable solutions for the eigenfunctions describing these systems assuming periodic potentials and the Born Oppenheimer approximation.

Due to the fact that the potential of Pigment-Protein complexes is nonperiodic it is not possible to use Bloch waves to describe pigment-protein-complexes. The theory has to be improved and was widely improved for the description of organic supermolecules like photosynthetic pigment-protein conplexes.Today a good agrement between the calculated and measured time dependent spectra of coupled biological pigment-protein complexes is achieved with new theoretical approaches [37-41]. The quantum formalism presented in this chapter is beyond the scope of this thesis. Our calculations of optical spectra are performed with the formalism of rate equations as shown in the following chap. 3.2.

The possible energy values measurable on a quantum system characterized by a Hamiltonian $\hat{H}$ are described by the time independent Schrödinger equation:

39. $\hat{H}\left|\Psi\right\rangle = E\left|\Psi\right\rangle$

The quantum dynamics of states, e.g. time dependent polarisation and population follows the time dependent Schrödinger equation:

40. $i\hbar\left|\dot{\Psi}\right\rangle = \hat{H}\left|\Psi\right\rangle$

In general we will focus on the temporal dynamics of the population of excited states. The most simple form of the Hamiltonian of a single electron bound to a potential $V(\bar{r})$ denotes to

41. $\hat{H} = \frac{\hat{p}_{el}^{\ 2}}{2m} + V(\bar{r})$

The potential $V(\bar{r})$ has to contain all electromagnetic contributions that influence the electron.

determining the quantum dynamics of the electronic state $\left|\Psi\right\rangle$.

The Hamiltonian denoted in eq. 41 contains all energetic contributions in form of operators that contribute to the total energy of the electronic ground or excited state ${}^{0}S$ or ${}^{1}S$, respectively. These are the energies of the free electron $\frac{\hat{p}_{el}^{\,2}}{2m}$ and all terms of the potential $V(\bar{r})$ contributing to the energy. Generally the potential $V(\bar{r})$ is composed by the Coulomb-potentials of the nuclei $\hat{H}_C$, the electronic repulsion of other electrons $\hat{H}_{el-el}$, the interaction with vibrations $\hat{H}_{el-phon}$ or any other interaction $\hat{H}_{WW}$:

42. $$\hat{H} = \hat{H}_0 + \hat{H}_C + \hat{H}_{el-el} + \hat{H}_{el-phon} + \hat{H}_{WW} \cdots$$

From the stationary Schrödinger equation (eq. 39) one can achieve an estimation for the absorption spectrum of a molecule.

If the potential of a single molecule is modeled e.g. with a rectangular quantum well one finds that the difference between ground and first excited state shrinks with the size of the quantum well.

In fact the bigger the delocalized Pi-electron system of a molecule is, the lower the energy difference of the transition ${}^0S \rightarrow {}^1S$.

As mentioned $\hat{H}$ is not a simple function for the coupled pigments in a protein environment.

The Hamiltonian generally looks like [215]:

43. $$\begin{aligned}
\hat{H} &= \sum_i \frac{\hat{p}_i^{\,2}}{2m_e} + \sum_j \frac{\hat{P}_j^{\,2}}{2M_j} \\
&+ \frac{1}{4\pi\varepsilon_0}\left(\sum_{j>j'} \frac{e^2 Z_j Z_{j'}}{|\bar{R}_j - \bar{R}_{j'}|} - \sum_{i,j} \frac{e^2 Z_j}{|\bar{r}_i - \bar{R}_j|} + \sum_{i>i'} \frac{e^2}{|\bar{r}_i - \bar{r}_{i'}|} \right) \\
&= \frac{-\hbar^2}{2m_e} \sum_i \Delta_{r_i} + \frac{-\hbar^2}{2} \sum_j \frac{\Delta_{R_j}}{M_j} \\
&+ \frac{1}{4\pi\varepsilon_0}\left(\sum_{j>j'} \frac{e^2 Z_j Z_{j'}}{|\bar{R}_j - \bar{R}_{j'}|} - \sum_{i,j} \frac{e^2 Z_j}{|\bar{r}_i - \bar{R}_j|} + \sum_{i>i'} \frac{e^2}{|\bar{r}_i - \bar{r}_{i'}|} \right)
\end{aligned}$$

where the kinetic terms of electrons with mass m_e and the kinetic terms of nuclei with variable mass M_j for the nucleus j with charge eZ_j are described as well as the coulombic interaction of the nuclei, between the electrons and the nuclei and between the electrons themselves. Principally all neighbouring charges have to be summarized. Simplifications can be done by assuming only the next neighbouriong charges in the lattice.

In eq. 43 those couplings between the spin momentum of the electrons and cores are neglected which either have to be included into the Schroedinger equation separately or which are calculated from relativistic formulations of the electron dynamics. As rate equations are used for the description of optical spectra in this thesis these aspects are not elaborated here. For an elaborated discussion of the quantum mechanical description of electrons see [216-221], for large molecules see [222].

According to the Born-Oppenheimer approximation the wave function $\left|\Psi_k\left(r_i, R_j\right)\right\rangle$ solving the Hamiltonian of eq. 43 factorises into the wave function of the electrons and the nuclei:

44. $\left|\Psi_k\left(r_i, R_j\right)\right\rangle = \left|\Psi_k\left(r_i\right)\right\rangle\left|\Psi_k\left(R_j\right)\right\rangle .$

The wave functions solving 43 could be found employing the concept of Bloch waves if the potential given in the Hamiltonian is periodic. These Bloch waves comprise a term expressing the structural lattice, multiplied with a plane wave part.

45. $\left|\Psi_k\left(r, R_j\right)\right\rangle = e^{ikr}\phi_k\left(R_j\right)$

According to eq. 16 every solution for a given time point can be expressed by a superposition of spatial Bloch waves forming a wave packet

46. $\left|\Psi_{k0}\left(r_i, R_j\right)\right\rangle = \int a(k) e^{i\bar{k}\bar{r}} dk$

The electromagnetic interactions between the electrons is different for electrons in the ground state or in the excited state (see Figure 40). In addition we have modulations of the ground and excited states due to the coupling of the electrons and the phonons in the system.

The spectrum of possible interactions of electrons in a crystal lattice or protein environment covers electron-electron interaction (see Figure 40, 1st row), electron-phonon interaction (see Figure 40, 2nd row), light coupling and other couplings (see Figure 40, 3rd row). For simplicity the electronic states are often treated as two-level system.

Coupled two-level states can undergo several transitions, e.g. by spontaneous emission of light or phonons or by inter system crossing (ISC). These transitions are discussed later and evaluated at the experimental data. Schematic illustrations of excitation energy transfer transitions also including electron delocalisation and electron transfer are shown in Figure 40, 4th row.

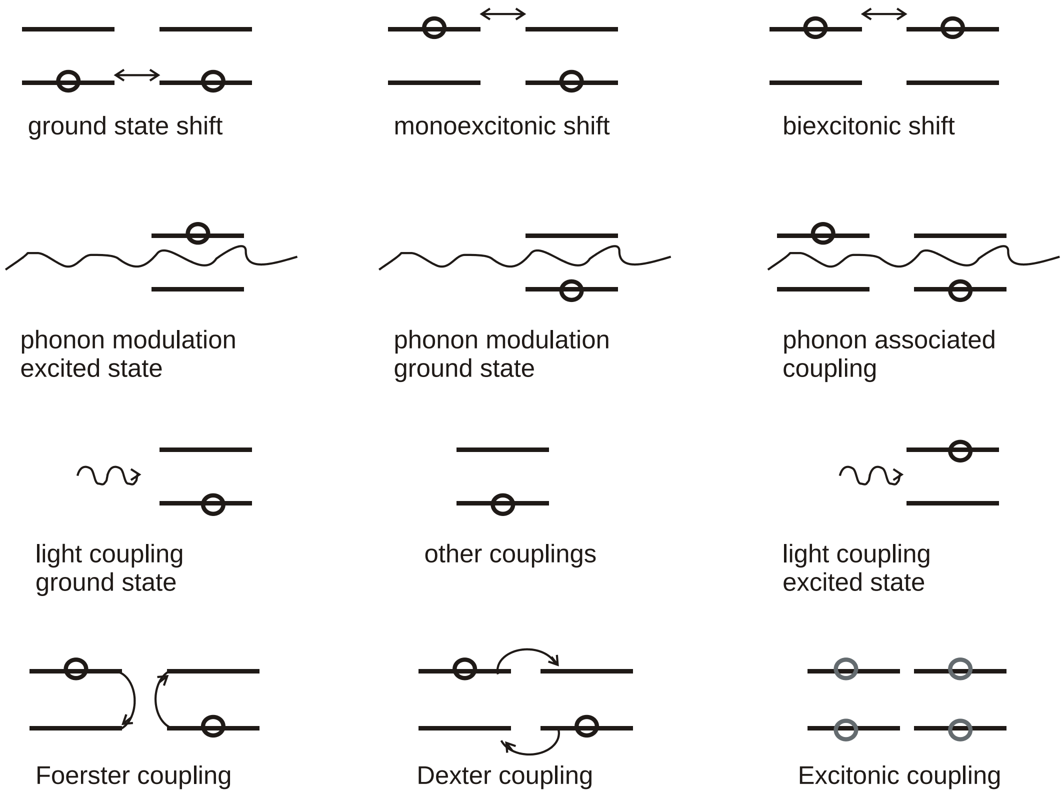

Figure 40: Interactions and EET/ET processes of coupled 2-level systems bound to a protein matrix.

The electron-phonon interaction as pointed out in Figure 40 shifts lifetimes (i.e. the transition probabilities) and the energy of the states.

In this case the Born-Oppenheimer approximation is not longer valid and the electronic wave function does not factorise into electronic and vibrational part (of the core lattice) as shown in eq. 44 [222].

If the electron is assumed to move in a periodic potential one finds a description of the electron where it is treated perturbatively like a free particle with an effective mass describing the inertia of the electronic mass:

47. $$\frac{1}{m_{eff.}} = \frac{1}{\hbar^2} \frac{\partial^2 E}{\partial k_i \partial k_j}$$

In the case of pigment-protein complexes the lattice is not periodic. Therefore the Born-Oppenheimer approximation and eq. 44-47 are not valid. Especially $\left|\Psi_k\left(r, R_j\right)\right\rangle = e^{ikr}\phi_k\left(R_j\right)$ in eq. 45 can not be expressed as a periodic wave function. Therefore the electron can not be treated like a free particle with an effective mass as given in eq. 47.

The harmonic oscillator can be described by the creation and annihilation operators. It had been shown that this formalism is suitable for the description of pigment-protein complexes [39]. For a complete elaboration of this formalism see [217].

The Hamiltonian of the 1-dim harmonic oscillator denotes to

48. $\hat{H} = \hbar\omega(a^{+}a + \frac{1}{2})$

where a^{+} denotes the creation operator and a the annihilation operator which are defined according to

49.
$$a^{+} = \frac{1}{\sqrt{2}}\left(-\frac{d}{dq} + q\right)$$
$$a = \frac{1}{\sqrt{2}}\left(\frac{d}{dq} + q\right)$$

with $q = \sqrt{\frac{m\omega}{\hbar}}x$.

With eq. 49 the Schroedinger equation 48 reads as

50. $\hat{H} = \frac{\hbar\omega}{2}(-\frac{d^2}{dq^2} + q^2) = -\frac{\hbar^2\Delta_x}{2m} + \frac{1}{2}m\omega^2x^2 = \frac{\hat{p}_{el}{}^2}{2m} + V(\bar{r})$

which is the well known form of a free electron in the harmonic potential $V(\bar{r}) = \frac{1}{2}m\omega^2x^2$ according to eq. 41. In that notation one can write the uncoupled part of the electron and phonon Hamiltonian of a big pigment-protein complex containing N chlorophyll molecules as

51. $\hat{H}_0 = \hat{H}_{0,el.} + \hat{H}_{0,phon} = \sum_{i=1}^{N}\left(\varepsilon_{gi}a_{gi}{}^{+}a_{gi} + \varepsilon_{ei}a_{ei}{}^{+}a_{ei}\right) + \sum_{j=1}^{M}\hbar\omega_j b_j{}^{+}b_j$

where the energies ε_{gi} of the ground state of pigment number *i* with the corresponding operators $a_{gi}{}^{+}$ and a_{gi} and the energies of the excited states ε_{ei} with the corresponding operators $a_{ei}{}^{+}$ and a_{ei} are summarized for the electrons. The Chlorophyll molecules are treated as 2-level systems of single electrons which can exist in the ground state or excited states and the term $\hat{H}_{0,phon} = \sum_{i=1}^{M}\hbar\omega_j b_j{}^{+}b_j$ is the operator for the phonon energy $\hbar\omega_j$ of the jth phonon mode in the system. $b_j{}^{+}$ and b_j describe the creation and the annihilation operator, respectively, for phonons in the jth eigenmode.

The eigenvalue of $\sum_{i=1}^{N}\left(a_{gi}{}^{+}a_{gi} + a_{ei}{}^{+}a_{ei}\right)$ is $N = N_g + N_e$ denotes the numbers N_g and N_e of Chl molecules in the ground state and excited state, respectively. The eigenvalue of $b_j{}^{+}b_j$ is the number of phonons in the jth eigenmode. Therefore the eigenvalue of eq. 51 is the overall energy in the uncoupled system summarizing all energies of ground state electrons, excited state electrons and phonons.

Many couplings between electrons and between electrons and phonons in the pigment-protein-complex exist that have to be incorporated in the Hamiltonian of eq. 51 (see Figure 40).

With electric dipole approximation the light coupling of the ground state electrons is described as

$\hat{H}_{el-h\nu} = \sum_{i=1}^{N} \overline{E}(t) \cdot \hat{\overline{d}}_i a_{ei}{}^{+} a_{gi} + h.c.$, denoting the fact that the incoming electric light field $\overline{E}(t)$ (see eq. 20) couples to the electric dipole operator of the ith Chl molecule $\hat{\overline{d}}_i$ and leads to an annihilation of a ground state while an excited state is created. The hermitian conjugated expression (h.c.) describes the induced emission annihilating an excited state while the ground state is populated.

According to Richter et al. [39] all the couplings shown in Figure 40 are incorporated into the coulomb interaction-Hamiltonian. The coulomb coupling is containing all relevant electronic interactions of electrons bound to ground or excited states:

$$\hat{H}_C = \sum_{i>j} V_{ij}{}^{gg} a_{gi}{}^{+} a_{gj}{}^{+} a_{gj} a_{gi} + \sum_{i \neq j} V_{ij}{}^{eg} a_{ei}{}^{+} a_{gj}{}^{+} a_{gj} a_{ei} + \sum_{i>j} V_{ij}{}^{ee} a_{ei}{}^{+} a_{ej}{}^{+} a_{ej} a_{ei} + \sum_{i \neq j} V_{ij}{}^{F} a_{ei}{}^{+} a_{gj}{}^{+} a_{ej} a_{gi}$$

$\hat{H}_C$ contains all terms for ground state shift due to the potential $V_{ij}{}^{gg}$ of the neighbouring electrons in ground states, monoexcitonic shifts due to the potential $V_{ij}{}^{eg}$ and biexcitonic shift due to $V_{ij}{}^{ee}$ (see Figure 40).

The term $V_{ij}{}^{F}$ denotes the dipole coupling between neighbouring Chl molecules, i.e. the Förster coupling. If Förster coupling occurs between the ith pigment in the ground state and the jth pigment in the excited state, then the Förster Resonance Energy Transfer leads to an annihilation of the ground state of pigment i and the excited state of pigment j while a ground state of pigment j and an excited state of pigment i is created.

The electron–phonon coupling for the electrons in the excited state can be formulated as following:

$$\hat{H}_{el-phon} = \sum_i \sum_j \left(g_{ij}{}^{(c)} b_j + g_{ij}{}^{(c)^*} b_j{}^{+} \right) a_{ei}{}^{+} a_{ei}$$

where the electron-phonon coupling is described by the matrix elements $g_{ij}{}^{(c)}$ expressing the probability for phonon absorption or phonon emission. $g_{ij}{}^{(c)}$ is given by the spectral density function which can be determined by experiments or molecular mechanic calculations [39].

The problem is rather complex. Therefore we will later show a simplified time independent Hamiltonian containing the Coulomb coupling terms only to estimate the excitonic splitting in the optical spectra of phycocyanin in comparison to pure phycobilin molecules in vacuum (see chap 3.5). The full analysis according to the quantum mechanical formalism presented here was done by our cooperation partners [37, 38, 39].

3.2 Rate equation formalism

Most calculations presented in this thesis were done with rate equations. The concept of rate equations is assumed to be a general and basic theory that is suitable to predict the dynamics of any system that can be described by a mathematical expression denoting its “state” if the transition probabilities between the states are known. In fact rate equations are not only used to describe EET and ET processes but many systems as optical transitions, particle reactions, complex chemical reactions and more general information processing in complex networks. Rate equations can be used to describe complex systems like e.g. sociological networks [223].

3.2.1 Axiomatic motivation

To motivate the rate equation formalism we start from two very basic axioms:

1) The system is described by a "state", which is everything that one can possibly know about a system in order to predict probabilities of future measurement outcomes.
2) The state changes over time. More specific, its time evolution can be described by some differential equation.

From 1) we conclude that it is helpful to introduce a sign denoting the “state”. For this sign we use N_i with i = 1...N forming a tupel of numbers that characterizes the state. To avoid misleading interpretations in comparison to the literature on photosynthesis we denote each component N_i of the overall system as own ith state of the system in the following.

From 2) we conclude that $\frac{dN_i}{dt}$ exists and $\frac{dN_i}{dt} \neq 0$.

Due to $\frac{dN_i}{dt} \neq 0$ there must exist a function *f* with $\frac{dN_i}{dt} = f_i\left(x_j, N_k, t\right)$. The temporal evolution of the states has to depend on a function *f* which in the most general case could depend on time t, the states N_k themselves and other variables we denote as x_j. The function *f* can be expressed in the form

$$\textbf{52.}\quad f_i\left(x_j, N_k, t\right) = \sum_k T_{ik}\left(x_j, N_j, t\right) N_k(t).$$

Principally $f_i\left(x_j, N_k, t\right)$ could be a nonlinear function in the states. We assume that the states N_i themselves can be parametrized in a way that they depend linearily on the measurement probability. That means that the states N_k are proportional to the probability to find the system in the state N_k after a measurement. Further we investigate the most simple case that $f_i\left(x_j, N_k, t\right)$ is linear in the states and does not depend on any additional x_j (all x_j should be contained in the states which exhibit all information that is experimentally accessible):

53. $f_i(N_k, t) = \sum_k T_{ik}(t) N_k(t).$

If the system of states is closed (i.e. conservative) then there is no temporal change of the dynamical behaviour (in analogon to time independent Hamiltonians). In that case the proportionality factors $T_{ik}(t)$ do not depend on the time and we get

54. $f_i(N_k, t) = \sum_k T_{ik} N_k(t).$

As we will see in chap. 4 (excited state dynamics in water soluble chlorophyll binding protein) the protein environment of a molecule can be assumed to introduce additional states (e.g. “relaxed” or “unrelaxed” states of the system) and therefore the treatment of a closed system is in principal suitable to analyse even open systems if the states of the environment are known and incoroporated into the theory.

Therefore from our simple axioms that there exist states and dynamics a kind of classical master equation formalism follows.

Equation 54 can be derived from the axiomatic postulation that any ensemble can be described by states and dynamical change leading to transitions between the states. The number of transitions that are released from one state is proportional to the population of this state

These axioms deliver a dynamical formulation of the temporal change of our states:

55. $\frac{dN_i}{dt} = \sum_k T_{ik} N_k(t)$

with the transfer matrix $T_{ik} = \overline{\overline{T}}$. If we separate the supplying processes and the emptying processes (i.e. we separate the sum avoiding summation over k=i) we get:

56. $\dot{N}_i = \sum_{k \neq i} T_{ik} N_k(t) - \sum_{k \neq i} T_{ki} N_i(t)$

For an excellent depiction of rate equations, the master equation and their applications see ref. [223].

Eq. 56 is a master equation of a probability evolution of population probabilities. The probability to find a certain state populated denotes to

57. $P_i = \frac{N_i}{\sum_j N_j(t)}$

If the set is complete, i.e. $\frac{d}{dt}\sum_j N_j(t) = 0$ then this formulation delivers the general master equation:

58. $\dot{P}_i = \frac{\dot{N}_i}{\sum_j N_j(t)} = \sum_{k \neq i} T_{ik} \frac{N_k(t)}{\sum_j N_j(t)} - \sum_{k \neq i} T_{ki} \frac{N_i(t)}{\sum_j N_j(t)} = \sum_{k \neq i} \left(T_{ik} P_k(t) - T_{ki} P_i(t) \right)$

It has to be pointed out that eq. 56 is a simplified and linearised form of rate equations. The full general form is found in eq. 52. For example eq. 56 does not describe bimolecular processes or processes that amplify or inhibit themselves (e.g. a cell devision process or an allosteric protein regulation). But from eq. 52 a description for any process that is thinkable in the context of states and their change can be found. Eq. 52 can be solved numerically for all cases. We will later suggest an algorithm how eq. 52 can be solved numerically with arbitrary constraints on the transition matrix T_{ik} (see chap. 3.2.4).

The time reversible/ equilibrium case is equivalent to the existence of equilibrium probabilities P_k and P_i in such a manner that each term on the right side of eq. 58 vanishes separately, i.e. $T_{ik}P_k = T_{ki}P_i$. The master equation (58) is then called to be at detailed balance. From eq. 58 we can see that due to this detailed balance condition the population probabilities are reciproke to the transition matrix´ elements for all times: $\frac{N_k}{N_i} = \frac{T_{ki}}{T_{ik}}$. That means the equilibrium is reached if there is no time dependency of the population densities (i.e. the population densities do not change in time).

The relation of transition probabilities for forward and backward reaction are proportional to the relation of the populated states, i.e. forward and backward transfer of two coupled states are found to satisfy the Boltzmann relation

59. $$\frac{T_{ki}}{T_{ik}} = e^{\frac{(E_i - E_k)}{k_B T}}$$

where E_i denotes the energy of the state *i* and $k_B T$ the thermal energy at temperature *T*. As we would expect from a single electron spreading along empty states the overall equilibrium population denotes to (see [223]):

60. $$\frac{N_k}{N_i} = e^{\frac{(E_i - E_k)}{k_B T}}$$

For degenerated states eq. 60 has to be extended to (see [223])

61. $$\frac{N_k}{N_i} = \frac{g_k}{g_i} e^{\frac{(E_i - E_k)}{k_B T}}$$

if N_k is g_k-fold degenerated and N_i is g_i-fold degenereted.

The formalism of rate equations as presented here has several advantages:

1) The theory contains all information about the population of the states in the system.
2) Only two basic axioms and the linearity condition are sufficient to motivate the basic theory.
3) The equations are rather simple (DGL 1st order).
4) The theory allows to incorporate further aspects by extending the space of states.
5) There exist algorithms for solving and fitting the rate equations under any constraints (see chap. 3.2.4).

3.2.2 Absorption and emission of light

The classical description of the interaction of light and matter with the Maxwell equations is presented in chap. 3.1.1-3.1.3 while the quantum mechanical approach is presented in chap. 3.1.4.

The spectra for light absorption and light emission can be qualitatively understood by a full quantum mechanical picture assuming rate constants for the absorption and emission of light quanta. The absorption of photons leads to a transfer of the system from the electronic ground state N_0 to an electronically excited state N_1 as shown in Figure 41:

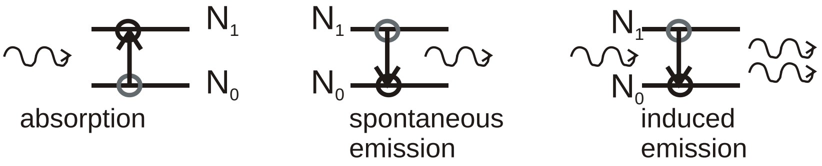

Figure 41 absorption (left panel) spontaneous emission (middle panel) and induced emission (right panel) of light due to electronic transitions between the electronic ground state N_0 and the excited state N_1

In full accordance to chap. 3.2.1 such systems are described by linear differential equations containing the ground state N_0, the excited state N_1, probability coefficients which are called the "Einstein coefficients" and the frequency dependent energy density $u(\omega) = n(\omega) \cdot \hbar \cdot \omega$ where $n(\omega)$ describes the frequency dependent photon density according to eq. 25 for the monochromatic beam.

If the laser exclusively excites the first excited state (N_1) then the change of the ground state population denotes to:

62. $\dot{N}_0 = T_{01}N_1(t) - T_{10}N_0 = (B_{01}(\omega) \cdot u(\omega) + A_{01}) \cdot N_1(t) - B_{10}(\omega) \cdot u(\omega) \cdot N_0(t)$ in full accordance to the general master equation formulation presented in eq. 55.

In eq. 62 the transfer matrix elements are $T_{10} = B_{10}(\omega) \cdot u(\omega)$ for the absorption process and $T_{01} = A_{01} + B_{01}(\omega) \cdot u(\omega)$ for the spontaneous emission (A_{01}) and the induced emission $(B_{01}(\omega) \cdot n(\omega))$.

The probability for absorption and induced emission is strongly dependent on the wavelength distribution of the photon flux with the maximum probability for $\omega = \omega_0 = \frac{E_1(N_1) - E_0(N_0)}{\hbar} := \frac{E_1}{\hbar}$ $(E_0(N_0) := 0)$.

To analyse the relation between the Einstein coefficients and the population densities a general system of the two states N_i and N_k is investigated in the equilibrium, i.e. $\dot{N}_i = \dot{N}_k = 0$. Then eq. 62 claims (here the indices i and k stand exemplarily for the two states N_i and N_k) :

63. $B_{ik}(\omega) \cdot u(\omega) \cdot N_k(t) + A_{ik} \cdot N_k(t) = B_{ki}(\omega) \cdot u(\omega) \cdot N_i(t)$

We can look at eq. 63 for the special case of a system of quantisized energy levels coupled to a thermal radiation field (i.e. the absorption, the emission and the induced emission is just due to the thermal radiation that couples to the system).

In that case we can express the equilibrium population of N_k / N_i according to eq. 61: $\frac{N_k}{N_i} = \frac{g_k}{g_i} e^{\frac{(E_i - E_k)}{k_B T}}$ and eq. 63 writes as:

$$\textbf{64.}\quad B_{ik}(\omega) \cdot u(\omega) \cdot \frac{g_k}{g_i} e^{\frac{(E_i - E_k)}{k_B T}} + A_{ik} \cdot \frac{g_k}{g_i} e^{\frac{(E_i - E_k)}{k_B T}} = B_{ki}(\omega) \cdot u(\omega)$$

Eq. 64 can be solved for the energy density of the black body radiation field $u(\omega)$ to

$$\textbf{65.}\quad u(\omega) = \frac{A_{ik} \cdot \frac{g_k}{g_i} e^{\frac{(E_i - E_k)}{k_B T}}}{B_{ki}(\omega) - B_{ik}(\omega) \cdot \frac{g_k}{g_i} e^{\frac{(E_i - E_k)}{k_B T}}} = \frac{\frac{A_{ik}}{B_{ik}(\omega)}}{\frac{B_{ki}(\omega)}{B_{ik}(\omega)} \frac{g_i}{g_k} e^{\frac{(E_k - E_i)}{k_B T}} - 1} = \frac{\frac{A_{ik}}{B_{ik}}}{\frac{B_{ki}}{B_{ik}} \frac{g_i}{g_k} e^{\frac{\hbar\omega}{k_B T}} - 1},$$

where the fact that the energy of the radiation $\hbar\omega$ must be equal to the energetic difference $\hbar\omega = E_k - E_i$ is used. A more accurate derivation would use the spectral line shape functions for $B_{ik}(\omega)$ and $B_{ki}(\omega)$ in eq. 65.

Now the Einstein coefficients in eq. 65 can be identified. In the thermal radiation field one expects that the energy density distribution is given as Max Planck´s derivation of the black body radiation field:

$$\textbf{66.}\quad u(\omega) = \frac{2\hbar\omega^3}{\pi^2 c^3} \frac{1}{e^{\frac{\hbar\omega}{k_B T}} - 1}$$

If eq. 66 is compared with eq. 65 it is found:

$B_{ki} g_i = B_{ik} g_k$, i.e. the probability per time unit for the absorption equals the induced emission with respect to the degeneration of the states and

$\frac{A_{ik}}{B_{ik}} = \frac{2\hbar\omega^3}{\pi^2 c^3}$ regarding the relation between spontaneous emission A_{ik} and induced emission B_{ik}, i.e. the induced emission becomes more probable for longer wavelengths with the third power of the photon wavelength.

The most experiments presented in this study were performed with very low radiation intensities and therefore the induced emission is not relevant and all calculations were evaluated taking into account only the absorption and the spontaneous emission.

Induced emission is the dominant process for all laser effects. For a monograph regarding lasers see [210].

In first order perturbation theory the probabilty for the transition from a state i to a state j is proportional to the square of the matrix element V_{ji} which is known as Fermi´s Golden rule. This approximation calculates the Einstein coefficient for the spontaneous emission to $A_{01} = \left| \left\langle \Psi_0 \left| \hat{p} \right| \Psi_1 \right\rangle \right|^2$, where $\left| \Psi_1 \right\rangle$ and $\left| \Psi_0 \right\rangle$ denote the excited and the ground state, respectively.

3.2.3 Relaxation processes and fluorescence dynamics

Excited states can relax along different channels (see Figure 42). These relaxation channels are often visualized by a so called “Jablonski diagram” which contains the energetic scheme of states of the relevant molecule.

The absorption process occurs instantaneously, i.e. it is faster than the resolution limit of the picosecond fluorescence setup (10 ps). In literature there is still a discussion about the duration of an absorption process ranging from the assumption that absorption takes the time light needs to cross a molecule (i.e. about 10^{-17}s = 0.01 fs) up to the time the electron needs to cross the molecule (i.e. about 10^{-14} s = 10 fs). The (one electron) excited states of molecules typically exhibit spin multiplicity 1 (singlet states) or 3 (triplet states). We distinguish this by the notation S_i for the ith excited singlet state and T_i for the ith excited triplet state.

According to the Franck Condon principle the absorption process does not excite the vibronic ground state of an electronically excited singlet state $S_i \nu_0$, but a higher vibronic level $S_i \nu_j$. Due to the shift of the energy parabola between ground and exited state along the reaction coordinate, the overlap between the wave functions of the vibronic ground states (j=0) of the electronic ground and 1st excited state ($S_0 \nu_0$ and $S_1 \nu_0$, respectively) is smaller than the overlap between $S_0 \nu_0$ and $S_1 \nu_k$ (k>0) (see inset of Figure 42).

This energetic picture can be understood from the fact that the molecular configuration of the nuclei is different between the electron in the ground state and first excited state. Therefore the nuclei start to move if one electron is excited and the lattice takes up a phonon.

The relaxation by light emission (luminescence) can not emit the same amount of energy absorbed before. Therefore the fluorescence must be red shifted with respect to the absorption. This red shift of the fluorescence light is called “Stokes shift”.

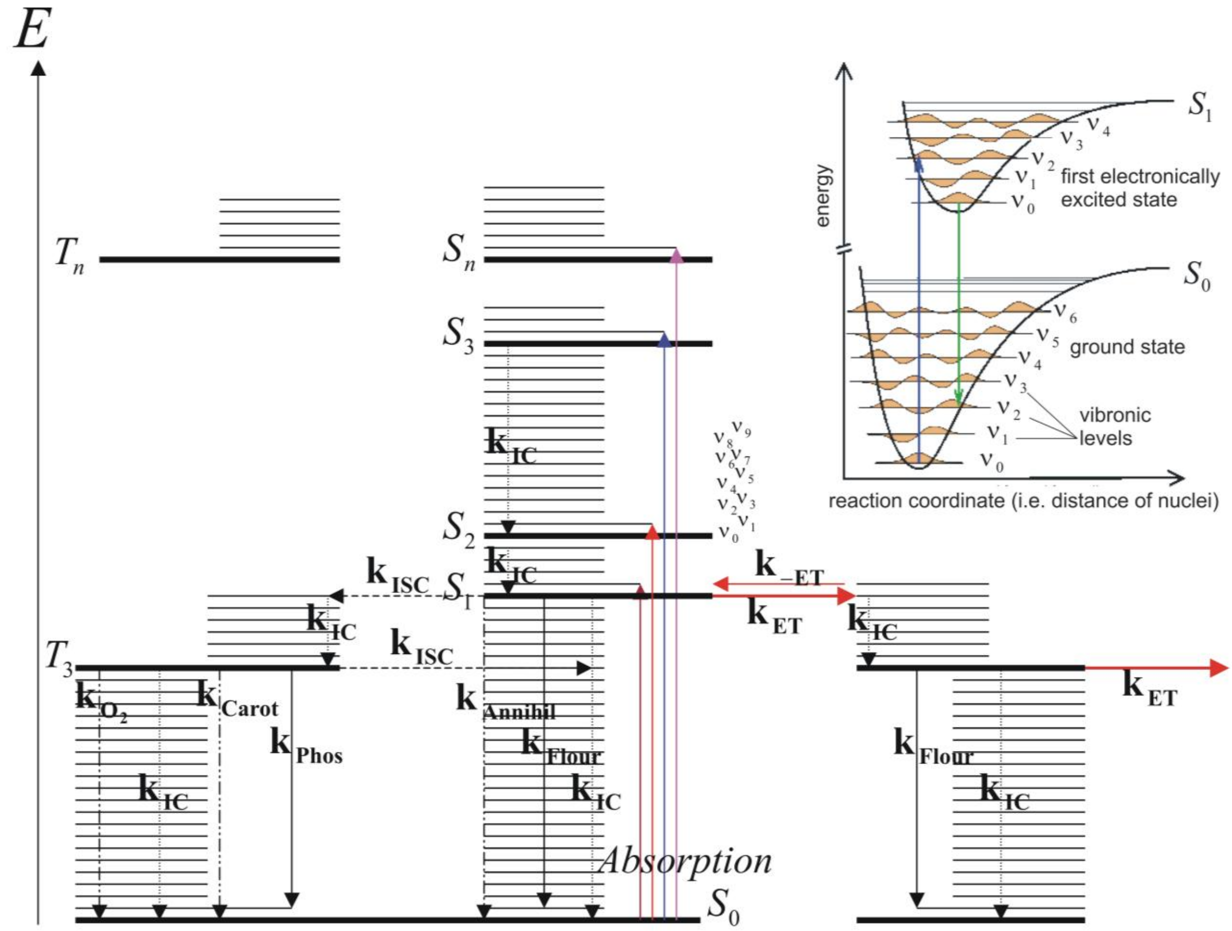

Figure 42: Jabloski diagram for chlorophyll coupled to a neighbouring molecule. The shown energetic states of chlorophyll are the singlet states S_0, S_1, S_2, S_3 and S_n and exemplarely the triplet states T_3 and T_n with vibronic levels that are denoted as ν_j. The indicated transitions are explained in the text. The inset is showing the parabola for the ground state and the first excited state with the most probable transitions for absorption and fluorescence according to the Franck-Condon principle.

With rate constants $k_{IC} \sim \frac{1}{\tau_{IC}} \sim 10^{12} s^{-1}$ the electrons relax from $S_1\nu_j$ into the state $S_1\nu_0$ due to internal conversion (phonon emission). Due to the Franck-Condon principle the subsequent radiative relaxation into the electronic ground state terminates again in a higher vibronic level $S_0\nu_k$.

The electronic relaxation from $S_i > S_1$ into S_1 occurs with $k_{IC} > 10^{11} s^{-1}$ and therefore much faster than the intrinsic fluorescence decay which is about $k_F \approx 6.7 \cdot 10^7 s^{-1}$. From S_1 to S_0 the vibrational relaxation k_{IC} is improbable for Chlorophyll and therefore fluorescence can be observed especially from S_1 with wavelengths $\lambda > 680$ nm for Chl *a*. The improbable k_{IC} from S_1 to S_0 is caused by the rigid structure of the prophyrine ring system. Therefore the vibrational modes are energetically separated and the wave functions overlap only slightly.

The highest occupied molecule orbital of the ground state of chlorophyll contains two electrons. Due to the internal spin-orbit (LS)-coupling it should be improbable that a spin flip occurs during the transition from S_0 to S_1 when the chlorophyll molecule is excited. But there exist intramolecular aberrations of the potential leading to high probabilities for the spin flip which is called „Inter System Crossing (ISC)“. It has a probability of $k_{ISC} \approx 1{,}5 \cdot 10^8$ in chlorophyll. The spin flip results in an electronically excited triplet state, which is most probable T_3 or T_4 [37].

The rate constants for k_F, k_{IC} and k_{ISC} were in detail investigated for Chl *a* and Chl *b* homodimers bound to the water soluble chlorphyll binding protein. It was found that k_{ISC} seems to be strongly temperature dependent for Chl *b* homodimers in WSCP which can be explained by a thermally activated transition to a higher triplet state T_4. A detailed descritpion of this phenomenon is found in [37] and shortly summarized in chap. 4. In Chl *a* homodimers the rate constant k_{ISC} is less dependent on temperature.

Due to the Pauli principle spontaneous emission from the triplet states to the singlet ground state can occur only after a further spin flip. Therefore at least the lowest triplet state T_1 is long lived with typical decay rates of $k_{Ph} \approx 10$.

While the fast relaxation from excited singlet states is called “fluorescence” this long lived emission from the triplet states is called “phosphorescence”.

For photosynthetic organisms the existence of long lived triplet states formed from excited Chl singlet states ${}^1Chl*$ is a disadvantage because Chl triplet states ${}^3Chl*$ tend to interact with environmental oxygen which is found in the triplet ground state ${}^3O_2$ forming highly reactive singlet oxygen ${}^1O_2*$:

$$\begin{aligned} &{}^1Chl* \xrightarrow{ISC} {}^3Chl* \\ &{}^3Chl* + {}^3O_2 \rightarrow {}^1Chl + {}^1O_2* \end{aligned}$$

chemical equation 4

The singlet oxygen oxidizes neighbouring molecules and cell structures. The rate constant for the formation of singlet oxygen via triplet-triplet interaction is denoted with k_{O_2} in Figure 42.

There exist several other relaxation channels for excited singlet states. The S_1 can e.g. interact with other singlet states of coupled pigments and lead to a strong fluorescence quenching via singlet-singlet annihilation ($k_{Annihil}$). This process is a nonlinear relaxation that depends quadratically on the concentration of excited singlet states $\langle S_1 \rangle$ in the sample.

Efficient photosynthesis occurs via the excitation energy transfer (EET) from the antenna pigments to the photochemically active reaction center (see Figure 3). To achieve quantum efficiencies for charge separation in the RC after light absorption up to 99 % EET rate constants in the order of

$k_{ET} \approx 10^{10}$ are necessary. This process of EET and the subsequent electron transfer (ET) determines the dynamics of the excited states and therefore the fluorescence dynamics.

In spite of the concurrence of the efficient EET the photosynthetic active organisms exhibit a small amount of fluorescence of about 1 % of the absorbed light energy. Triplet states of the Chl molecules are efficiently quenched by the reaction with Carotenoid triplets (k_{Carot} in Figure 42). Carotenoids are very flexible molecules that dissipate their excitation energy fast via internal conversion. It is well known that Carotenoids also act as quenchers for excited Chl singlet states (see [57] and references therein).

The relaxation of an excited singlet state population probability $\langle S_1 \rangle$ occurs with the sum of all decay rates according to the general formulation of eq. 56 (see Figure 42):

67. $$\frac{d\langle S_1 \rangle}{dt} = -\left(k_{Fluor} + k_{Annihil} + k_{ET} + k_{IC} + k_{ISC}\right)\langle S_1 \rangle$$

Eq. 67 can be integrated and the solution (i.e. the excited state dynamics) is an exponential decay:

68. $$\langle S_1 \rangle(t) = \langle S_1 \rangle(0)\, e^{-(k_{Fluor}+k_{Annihil}+k_{ET}+k_{IC}+k_{ISC})t} := \langle S_1 \rangle(0)\, e^{-\frac{t}{\bar{\tau}}}$$

with the average apparent fluorescence lifetime

69. $$\bar{\tau} = \frac{1}{k_{Flour} + k_{Annihil} + k_{ET} + k_{IC} + k_{ISC}}.$$

The fluorescence dynamics depends on all possible relaxation channels. The observable fluorescence $F(t)$ is proportional to the actual population probability of the excited state $\langle S_1 \rangle$:

70. $$F(t) = k_{Flour}\langle S_1 \rangle(t) = k_{Flour}\langle S_1 \rangle(0)\, e^{-\frac{t}{\bar{\tau}}} := F(0)\, e^{-\frac{t}{\bar{\tau}}}$$

The quantum efficiency of the fluorescence Φ_F is defined as the relation between the emitted fluorescence photons per time unit and the overall number of relaxing excited states in the same time interval:

71. $$\Phi_F := \frac{k_{Flour}}{k_{Flour} + k_{Annihil} + k_{ET} + k_{IC} + k_{ISC}} = \frac{\bar{\tau}}{\tau_0}$$

with the intrinsic fluorescence lifetime $\tau_0 = \frac{1}{k_{Flour}} \approx 15ns$ for chlorophyll.

As mentioned above the radiative relaxation of excited Chl molecules $^1Chl^* := \langle S_1 \rangle$ happens with $k_{Flour} = (15ns)^{-1} = 6.7 \cdot 10^7 s^{-1}$ for Chl *a* and somewhat slower fluorescence relaxation $k_{Flour} = (23ns)^{-1} = 4.3 \cdot 10^7 s^{-1}$ for Chl *b* (see [37]) and $k_{ISC} = (6.7ns)^{-1} = 1.5 \cdot 10^8 s^{-1}$ for both species at room temperature. In Chl *b* an additional thermally activated ISC channel might exist that enhances k_{ISC} at higher temperatures [37]. Therefore the apparent fluorescence lifetime of Chl *a* calculates to $(k_{Flour} + k_{ISC})^{-1} = 4.6ns$ while a slightly faster relaxation is expected for Chl *b* at room temperature but a slightly slowlier relaxation in comparison to Chl *a* at 10 K (see chap. 4). In WSCP the 1st electronically excited states splits into two excitonic levels with smaller oscillator strength of the lower excitonic state. We measured a typical Chl *a* excited state lifetime of $(k_{Flour} + k_{ISC})^{-1} = 5.2\,ns$ in WSCP while Chl *b* relaxes slightly faster with $(k_{Flour} + k_{ISC})^{-1} = 4.8\,ns$ in WSCP at room temperature (see [47] and chap. 4).

The resulting fluorescence quantum yield calculates to $\Phi_F^{ChlaWSCP} = \frac{\bar{\tau}}{\tau_0} \approx \frac{k_{Flour}}{k_{Flour} + k_{ISC}} = \frac{5.2}{15} \approx 35\%$ for WSCP containing Chl *a* and $\Phi_F^{ChlbWSCP} = \frac{4.8}{23} \approx 21\%$ for Chl *b*. The temperature dependency of the lifetime of the 1st excited singlet state is discussed in detail in chap. 4.

3.2.4 Rate equations in photosynthesis and an efficient algorithm for the solution

In photosynthetic systems the formalism of rate equations can be incorporated treating different molecules as localised states. Generally this will lead to rather complex equation systems of up to a thousand coupled differential equations. A simplified model respects the given resolution of the measurement setup employing the concept of “compartments” as suggested e.g. by Häder [76].

According to this compartmentation model a rather complex system can be treated in form of “compartments” if the energetic equilibration between the coupled molecules which are treated as a compartment is fast in comparison to the achievable resolution of the measurement setup.

The advantage of the compartmentation model is a reduction of the number of states. For example one can treat the LHC, the core antenna complexes and the reaction center (see Figure 3) as compartments of thylakoid membrane fragments and therefore as single states instead of a treatment of each single molecule. The whole light harvesting complex including the core antenna and the Chl molecules in the reaction center might even be treated as one single compartment.

The states and their couplings are visualized in the scheme as shown in Figure 43. Here five arbitrary states are coupled via EET exhibiting one and the same rate constant *k* for all transitions to neighbouring states. In addition there exists the relaxation to the ground state which which occurs with the rate ($k_Q + k_F$) when the excitation energy interacts with a quenched state as shown in Figure 43. The probability for relaxation to the ground state from all states without quencher is k_F.

In the scheme shown in Figure 43 the state N_4 is bound to a quencher (e.g. a reaction center) and therefore exhibits reduced lifetime. The asterix (*) indicates that intitally (time t = 0) the state N_1 is excited while all other molecules are found in the ground state.

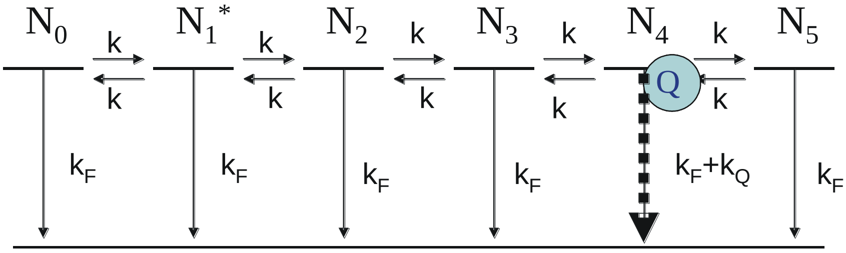

Figure 43 Scheme of 5 coupled states that can transfer energy to neighbouring molecules. States 1,2,3 and 5 have equal relaxation probabilities from the excited to the ground state (rate constant k_F) while state 4 is connected with a quencher and therefore exhibits a higher relaxation probability $k_F + k_Q$.

From the schematic model as presented in Figure 43 one can formulate the rate equations for the time derivative of each state. For molecule N_2 this equation exemplarily denotes to

$$\frac{dN_2}{dt} = -2kN_2 - k_F N_2 + kN_3 + kN_1$$

The final set of five coupled linear differential equations of 1st order can be solved to obtain the excited state dynamics of all five molecules/states.

The fluorescence intensity is proportional to the time dependent population density of the fluorescing states that is calculated from the solution of such a set of coupled linear differential equations 1st order. (see [95] for mathematical details).

This set of equations is solved by a sum of exponential functions with different time constants. In a non-degenerated set with n pair wise different eigenvalues of the transfer (coefficient) matrix $\overline{\overline{T}}$ describing the change $\dot{\overline{N}}$ of all *n* state population densities, the set of differential equations can be written according to eq. 55 (for details of the following computation see also ref. [43]):

72. $\dot{\overline{N}} = \overline{\overline{T}}\,\overline{N}$

If the entries of $\overline{\overline{T}}$ are not known yet, we still have at least some information about the symmetry of $\overline{\overline{T}}$ e.g. according to eq. 59. It is a necessary condition for the equilibrium case that $\frac{T_{ki}}{T_{ik}} = e^{\frac{(E_i - E_k)}{k_B T}}$ according to eq. 60. The derivation of eq. 60 is shown in chap. 3.5.

As a simplifiction the relaxing system might be treated as locally equilibrated.

In that case eq. 59 helps us to reduce the nondiagonal elements of $\overline{\overline{T}}$ to ½ of their quantity.

The solution for the i th state population density is given by

73. $$N_i(t) = \sum_{j=1}^{n} U_{ij} e^{\gamma_j t}$$

where γ_j is denoting the j$^{\text{th}}$ eigenvalue and U_{ij} the i$^{\text{th}}$ component of the j$^{\text{th}}$ eigenvector of $\overline{\overline{T}}$. For a nondegenerated system equation 73 is proportional to the assumed fluorescence decay:

74. $$F(t,\lambda) = \sum_{i=1}^{n} A_i(\lambda) e^{(-t/\tau_i)}$$

with $\gamma_j = -(\tau_j)^{-1}$ according to the proportionality between fluorescence intensity and excited state population density. If one ore more $\gamma_j = 0$, one can reduce the dimensionality of $\overline{\overline{T}}$ to a smaller size with all eigenvalues being nonzero and nondegenerated. In such case eq. 74 is suitable to calculate the expected fluorescence emission in the time domain from the transfer matrix $\overline{\overline{T}}$. Vice versa $\overline{\overline{T}}$ can be reconstructed if the fluorescence kinetics of all molecules is measured.

For that purpose the eigenvector matrix $\overline{\overline{U}}$ and the eigenvalues in the diagonal matrix $\overline{\overline{\Gamma}}$ have to be used to calculate the transfer matrix $\overline{\overline{T}}$:

75. $$\overline{\overline{T}} = \overline{\overline{U}}\,\overline{\overline{\Gamma}}\,\overline{\overline{U}}^{-1}$$

Eq. 75 is unique if one knows the amplitudes and time constants of all exponential decay components for each compartment in the sample.

The time dependent fluorescence of emitters described by a coupled system of differential equations as given by eq. 74 occurs multiexponentially with up to *n* decay components (i.e. exponential decay time constants) for *n* coupled subsystems (i.e. *n* coupled excited states with respect to eq. 72).

Therefore the average decay time as shown in eq. 69 can not be used. In the case of coupled states the average decay time can be defined as a time constant proportional to the overall fluorescence intensity (see [208] for further details):

76. $$\bar{\tau} = \frac{\int_0^{\infty} F(t)dt}{F(0)} = \frac{\int_0^{\infty} \langle S_1 \rangle (t) dt}{\langle S_1 \rangle (0)}$$

If one evaluates eq. 76 with the multiexponential decay curves as given by 74 it follows that

77. $$\bar{\tau}(\lambda) = \frac{\int_0^{\infty} F(t)dt}{F(0)} = \frac{\left[\sum_{i=1}^{n} \tau_i A_i(\lambda) e^{(-t/\tau_i)} \right]_0^{\infty}}{\sum_{i=1}^{n} A_i(\lambda)} = \frac{\sum_{i=1}^{n} A_i(\lambda) \tau_i}{\sum_{i=1}^{n} A_i(\lambda)}$$

at a certain wavelength position.

Usually one does not find all eigenvector components (i.e. when some state populations do not show fluorescence or when not all fluorescence decay components can be resolved). In that case equation 75 can not be used to find a unique transfer matrix $\overline{\overline{T}}$. But a reasonable assumption of $\overline{\overline{T}}$ with iterative comparison of the eigensystem ($\overline{\overline{U}}$,$\overline{\overline{T}}$) with the fluorescence decay helps to find a solution for $\overline{\overline{T}}$ which is consistent with the globally observed fluorescence dynamics in all wavelength sections according to equation 74. Such an iterative comparison of the measurement data (eigenvectors and eigenvalues) and a reasonable transfer matrix $\overline{\overline{T}}$ can be used to calculate a suggestion for the transfer rates of a system of arbitrary complexity which leads to the observable fluorescence decay.

Our computation was highly efficient employing an algorithm that starts with an arbitrary reasonable transfer matrix $\overline{\overline{T}}_{\text{Start}}$. At first the eigenvectors and eigenvalues of $\overline{\overline{T}}_{\text{Start}}$ are calculated. In the next step one will use the observed decay times for all eigenvalues $\gamma_j = -(\tau_j)^{-1}$ instead oft he eigenvalues of $\overline{\overline{T}}_{\text{Start}}$. Therefore the eigenvalues are changed but the eigenvectors are not. Doing the transformation according to eq. 75 with the changed (experimentally observed) eigenvalues one will find an improved suggestion $\overline{\overline{T}}$ for the transfermatrix $\overline{\overline{T}}_{\text{Start}}$.

There exist some symmetry constraints for the transfer matrix $\overline{\overline{T}}$. For example the rate constant for the energy transfer from the pigment one to the pigment two has to be the same as the energy reception at pigment two according to this energy transfer. Additionally we mentioned already the Boltzmann equilibrium which gives rise to eq. 59 as symmetry argument for the transposed entries and therefore this symmetry condition might also be used as constraint.

According to the suggested algorithm all violated constraints are corrected in the transfer matrix $\overline{\overline{T}}$. After that one can again calculate the eigenvectors and eigenvalues of $\overline{\overline{T}}$. The observed decay times for all eigenvalues are again set to $\gamma_j = -(\tau_j)^{-1}$. Then the algorithm starts from the beginning and, doing the transformation according to eq. 75 with the changed (experimentally observed) eigenvalues, leads to a further improvement of $\overline{\overline{T}}$.

The described algorithm converged for calculating the transfer rates in *A.marina* in five iterations only and therefore was faster than other algorithms found in literature. There exist several other correlations between experiment and calculation which could be implemented into the algorithm. For example one could also use the observed amplitudes of the different fluorescence components to correct the eigenvectors of $\overline{\overline{T}}_{\text{Start}}$ instead of the eigenvalues.

3.2.5 Simulated decay associated spectra

According to the formalism presented in chap. 3.2.4 the decay associated spectra can be simulated for each pigment or compartment in a coupled system. At first we start with a simulation of the DAS of the coupled chain shown in Figure 43 but without the quencher molecule bound to the state N_4.

The DAS of the individual pigments exhibit multiphasic relaxation dynamics at each molecule of the coupled chain:

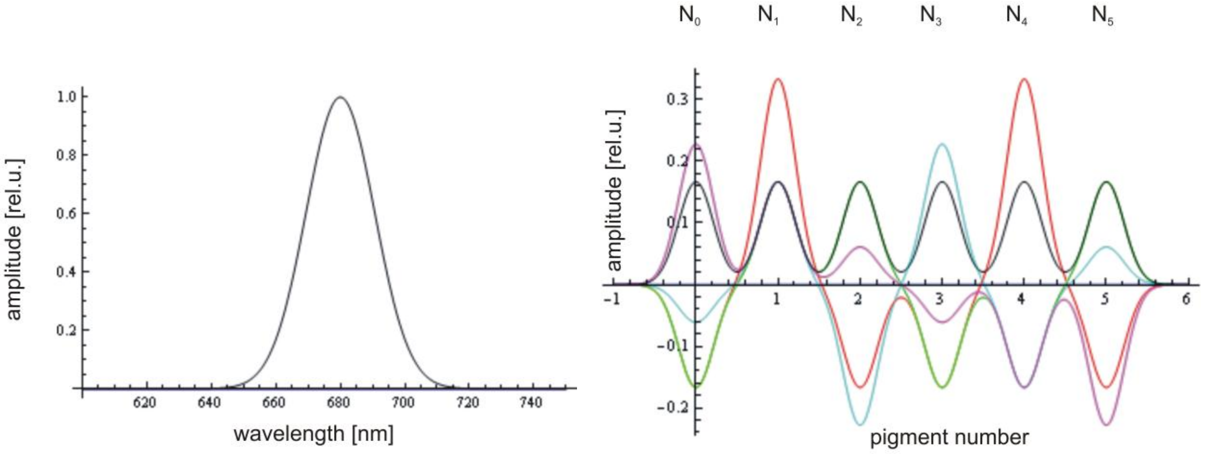

Figure 44: Simulated decay associated spectra for the system shown in Figure 43 (without the quencher at N_4) with a Gaussian lineshape function in the wavelength domain (left side) and in the “pigment” domain (right side). The black curve on the left side denotes a single exponential decay component with a time constant of 4 ns. At the right side we see a complex DAS pattern distributed along all coupled states. The time constants are 2.7 ps (cyan), 3.3 ps (red), 5 ps (green), 37 ps (magenta) and 4 ns (black).

In the simulation shown in Figure 44 it is assumed that k_F= 4ns and k = 10 ps. The simulation is performed without the quencher located at the molecule N_4. The initial excitation is set to pigment N_1 as indicated in Figure 43. In the spectral domain there occurs only one monoexponential decay with a typical 4 ns decay time because all molecules are isoenergetic (Figure 44, left side). In the spatial domain the DAS is rather complex and each pigment exhibits an individual time dependent population and therefore fluorescence emission.

The structure of the spatially resolved DAS pattern, especially the symmetry of the DAS shown in Figure 44, right side, is shortly discussed in the following.

The interpretation of the DAS, Figure 44 is in full accordance with the finding that the dominant decay of each pigment exhibits a time constant of 4 ns (decay) and all other time constants describe the EET inside the coupled structure. The excited pigment N_1 transfers the excitation energy fast to the neighbouring pigments N_0 and N_2 (red curve, 3.3 ps). These exhibit the characteristic rise kinetics with 3.3 ps time constant (red curve). The red curve shows a mirror symmetry along the axis between N_2 and N_3. Therefore the rise kinetics (negative amplitude) is also found at N_3 and N_5 whereas

N_4 contains a high amplitude of the 3.3 ps decay kinetics (positive amplitude) similar to the initially excited pigment N_1.

From the DAS shown at the right side of Figure 44 it can be seen that the DAS components with time constants of 4 ns (black) and 3.3 ps (red) appear mirror symmetric to the center of the chain while the time constants with values of 2.7 ps (cyan), 5 ps (green) and 37 ps (magenta) are anti-symmetric according to the mirror plane between N_2 and N_3. In addition the evaluation delivers a 10 ps component which has amplitude zero in the whole range of states and therefore is not visible in the fluorescence.

It has to be pointed out strictly that the complexity that is found in the DAS of Figure 44 can not yet be resolved experimentally. Even if it would be possible to resolve single molecules in the spatial domain (e.g. the states denoted as N_i in Figure 43 which might be possible with time resolved STED microscopy or with tip enhanced single molecule fluorescence spectroscopy) one can not expect to find a DAS as depicted in Figure 44, right side, because the time constants of 2.7 ps, 3.3 ps and 5 ps are hardly distinguishable with the technique of TSCSPC employing a laser system with 70 ps FWHM of the IRF. Here fluorescence up conversion would be a technique that delivers the time resolution but applied high resolution techniques like STED or tip enhanced AFM would influence the excited state lifetime of the single molecules and therefore also do not represent the natural state of the system.

Most probably the experimenter will find a clearly resolved 4 ns decay kinetic (black curve) and the pronounced 37 ps component (magneta curve) with high positive amplitude at the states N_0 and N_1 and negative amplitude at states N_4 and N_5. All other (fast) rise and decay components will appear as one additional very fast component. The amplitude of this fast component is comparable to the sum of the amplitudes of all fast components (2.7 ps (cyan), 3.3 ps (red) and 5 ps (green)) shown in Figure 44, right side.

This situation of a DAS that could be resolved experimentally (still assuming single molecule resolution in the spatial domain) is presented in Figure 45.

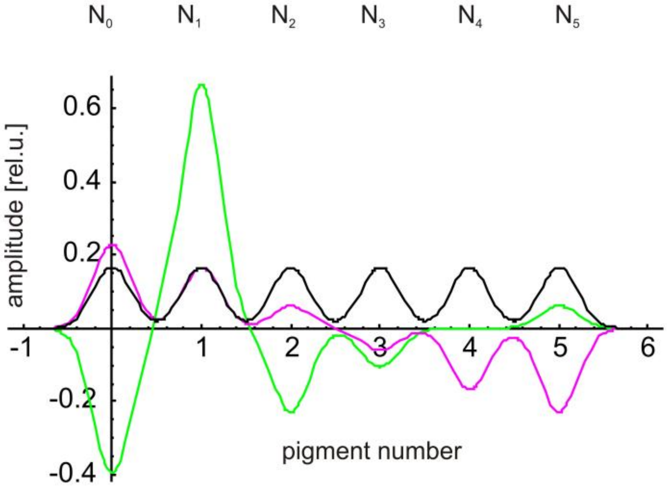

Figure 45: DAS for the system shown in Figure 43 (without the quencher position at N_4) with a Gaussian lineshape function in the “pigment” domain. The fast components shown in Figure 44 (cyan, red, green curve) are summed to one component here (shown in green). In addition the 37 ps (magenta) and 4 ns (black) component are shown.

One expects that the positive decay kinetics of all pigments that are not directly excited is mainly dominated by the 4 ns fluorescence decay (black curve in Figure 45).

The initially excited pigment N_1 decays with very fast (3-5 ps, green curve) decay kinetics which appears as fluorescence rise at the neighbouring molecules (negative amplitude).

The 37 ps component represents the overall energy transfer along the coupled chain of molecules with positive amplitude at pigment N_0 and N_1 which exhibit mainly donor character and negative amplitude at pigment N_4 and N_5 which exhibit an acceptor character for the overall energy equilibration process.

This overall time spread in the ensemble measurement is restricted by the geometry and symmetry of the pigment chain as shown in Figure 43 rather than by certain transfer "steps" inside the system.

The interaction time between the single subunits is much faster than this averaged overall energy transfer (magneta curve) and the amplitude distribution reflects the average pathway of the energy caused by the geometrical constitution of the sample.

It is interesting how the distribution of positive and negative amplitudes of the corresponding fluorescence components are distributed along the pigment chain if the initial excitation changes. One might investigate a situation where N_1 and N_4 are initially excited instead of only N_1 as presented in Figure 46, left side.

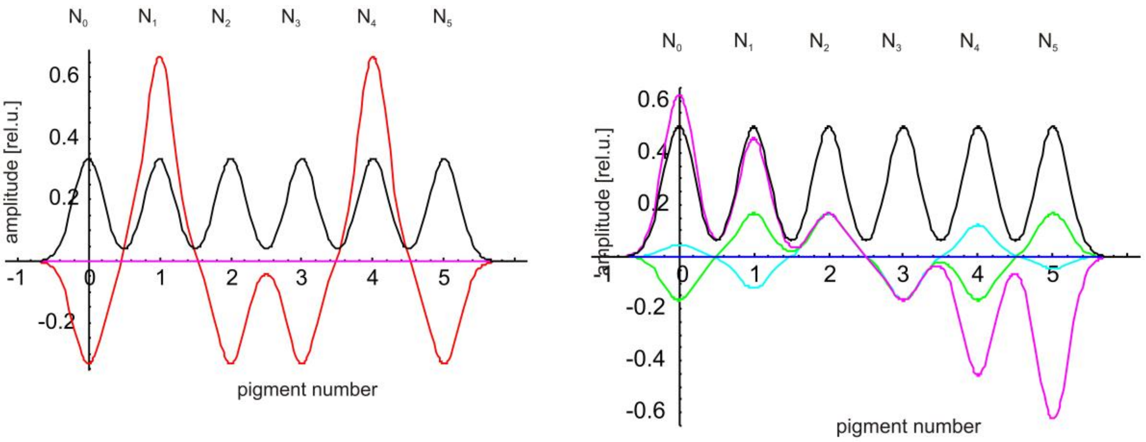

Figure 46: Simulated decay associated spectra for the system shown in Figure 43 (without the quencher position at N_4) with a Gaussian lineshape function according to Figure 44 but with initial population $N_0(t=0)=N_2(0)=N_3(0)=N_5(0)=N_6(0)=0$, $N_1(0)=1$, $N_4(0)=1$ (left side, full symmetric case) and $N_0(t=0)=N_1(0)=N_2(0)=1$, $N_3(0)=N_4(0)=N_5(0)=0$ (right side, full antisymmetric case)

In Figure 46, left side, the DAS pattern of a full mirror symmetric initial condition is simulated with $N_0(t=0)=N_2(0)=N_3(0)=N_5(0)=N_6(0)=0$, $N_1(0)=1$, $N_4(0)=1$. On the right side the situation of a primary excitation of N_0, N_1 and N_2 is shown, i.e. a fully antisymmetric condition $N_0(t=0)=N_1(0)=N_2(0)=1$, $N_3(0)=N_4(0)=N_5(0)=0$ at the right side.

All fast decay components except the dissipative decay component for the relaxing system after equilibration (which is independent from the initial condition, 4 ns component, black curve) represent the symmetry of the initial condition according to a suggested mirror plane in the middle of the structure.

Functional PS II preparations exhibit a markedly reduced excited state lifetime due to the presence of photochemical quenchers, i.e. the reaction center of PS II where charge separation occurs.

This situation is simulated in Figure 47 for the coupled pigment chain shown in Figure 43 assuming the initial excitation of pigment N_1 and the quencher located at pigment N_4.

The simulation was performed with the rate constants $k_F= (4ns)^{-1}$, $k_Q= (2\ ps)^{-1}$ and $k = (10\ ps)^{-1}$.

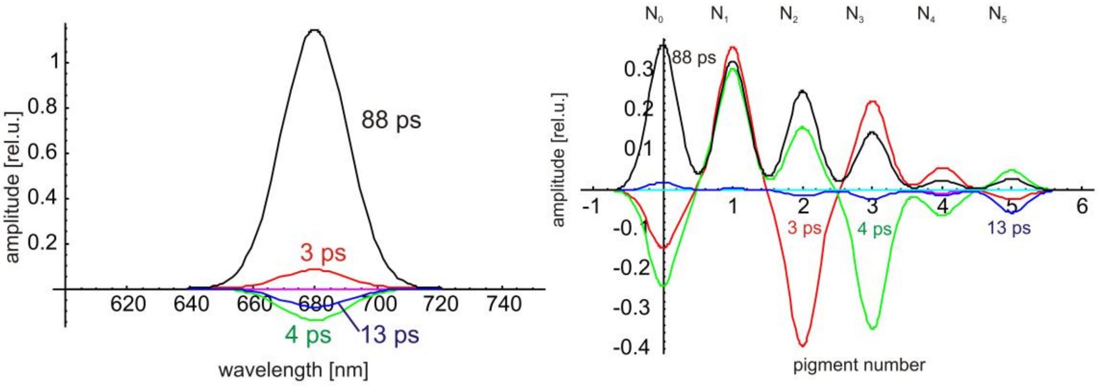

Figure 47: Simulated decay associated spectra for the system shown in Figure 43 (including the quencher position at N_4) with a Gaussian lineshape function in the wavelength domain (left side) and in the “pigment” domain (right side). The black curve denotes the main relaxation of the coupled system occurring as strictly positive decay component with a time constant of 88 ps. In addition we find fast time constants with 3 ps (red), 4 ps (green) and 13 ps (blue).

As visible in Figure 47 the decay is not longer monoexponential in the wavelength domain (left side of Figure 47) after introduction of the quencher. The main decay component exhibits a lifetime of 88 ps which is composed by the quencher efficiency k_Q, the EET rate constant k and the distance between the initially excited state and the quencher.

The model simulates a “random walk” of the initially excited electron until it is quenched to the ground state (for a description of such random walk models in photosynthesis research see [95]).

The EET and the apparent domain size, i.e. the spatial regime that exhibits a sufficient high excitation probability due to exciton diffusion, was in detail investigated for isolated and solubilized LHC trimers and aggregates of LHC trimers [45].

Due to the coupling of several pigments the amplitude distribution of the decay components that are found in the fluorescence kinetics can be rather complex.

Generally fast decay components that are related to the direct EET to the neighbouring pigments exhibit positive amplitude at the initially excited compartment, but negative amplitudes at the neighbouring ones. As it can be seen in Figure 47 this is the case for the fastest component with 3 ps decay time (red curve) that exhibits a positive amplitude at pigment N_1 but negative amplitude at the neighbouring pigments N_0 and N_2. This component is positive at pigment N_3 again. The same situation is found for the fastest 2.7 ps component of the system without quencher (cyan curve in Figure 44).

As described the solution of the rate equation systems delivers the time resolved fluorescence spectra and DAS. Therefore one can determine k_{FRET} from the experimental data. In the following chapter 3.3 we will see how the Förster Energy Transfer rate constant can be calculated independently from time integrated fluorescence spectra (equation 90 with help of the the rate equations 72 and the reverse transformation 74). Therefore the Förster Resonance Energy Transfer can be evaluated independently using the time integrated spectra of the donor and the acceptor but it also can be fitted to the time resolved spectra comparing the solution of the rate equations with the measurement results.

Sometimes k_{FRET} calculated from the time integrated spectra deviates strongly from k_{FRET} calculated from the time dependency of the fluorescence (e.g. due to absorption changes of the coupled systems, bleached donor or acceptor pigments etc…). An accurate analysis should deliver unambiguous results where the analysis of the time integrated fluorescence and the time resolved results are in good agreement. An example of such a study for complexes of CdSe/ZnS nanocrystals coupled to the PBP antenna of *A.marina* is presented in ref. [51].

In many cases there is a lack of information for the direct calculation of the distance (R_{12}) dependent rate constant $k_{FRET}\left(R_{12}\right)$ due to the fact that there are missing parameters like the pigment dipole orientation factor κ (see next chap. 3.3).

For a full understanding of the advantages of the Förster Resonance Energy Transfer and its limitations we will shortly outline the basic concept of FRET (see fig. 3.3.2).

3.3 Transition probabilities in coupled pigments

In the last chapters we mentioned the mechanism of Förster Resonance Energy Transfer (FRET) as an approximation to estimate the transition rate constant between sufficiently weakly coupled pigments. The mathematical concept of rate equations is suitable to analyse the synergetic behaviour of a complex coupled network if the coupling strength and the transition probabilities between single states are known or if measurement results for the fluorescence dynamics exists. We will now have a look at the underlaying concept of the theory of coupled pigments and the derivation of the rate constants for EET and ET processes.

3.3.1 Excited states in coupled pigments

If two pigments are coupled via an excitation energy or electron transfer the rate constant k_{ET} can be approximated according to Fermi´s Golden rule [76, 217, 219, 221] in first order perturbation theory:

78. $$k_{ET} = \frac{2\pi}{\hbar}\left|V_{12}\right|^2 \rho_{eff}(E)$$

The rate constant k_{ET} which is a probability per time unit (for a transition) can be calculated as the product of the square of the absolute value of the transition matrix element $\left|V_{12}\right|^2$ and the effective density of states $\rho_{eff}(E)$ of the initial and final states. In photosynthetic complexes the density of states is determined by the vibrational spectrum of the interacting species and the states of their microenvironment [224]. The transition matrix element $V_{12} = \left\langle \Psi_2 \left| H_{WW} \right| \Psi_1 \right\rangle$ ist the scalar product of the initial state $\left| \Psi_1 \right\rangle$ and the final state $\left| \Psi_2 \right\rangle$ under the influence of the interacting potential, which is represented by the interaction operator H_{WW}, e.g. a Coulomb potential $H_{WW} = V_{Coulomb}$, as denoted in eq. 43. If we investigate the situation where the excited state of one pigment in a coupled dimer is transferred to the coupling partner one can formulate the product states

79. $$\left| \Psi_1 \right\rangle = \frac{1}{\sqrt{2}} \left| \Phi_1(1)^e \Phi_2(2)^g - \Phi_1(2)^e \Phi_2(1)^g \right\rangle, \quad \left| \Psi_2 \right\rangle = \frac{1}{\sqrt{2}} \left| \Phi_1(1)^g \Phi_2(2)^e - \Phi_1(2)^g \Phi_2(1)^e \right\rangle$$

where $\left| \Phi_i(j)^{e,g} \right\rangle$ denotes the electronic wave function of the j^th^ electron in the excited (e) or ground state (g) located at the i^th^ pigment.

The quantum mechanical derivation of the transition probabilities for the states described in eq. 79 assumed as two level systems at different coupling strengths can be found e.g. in [96] whereas the treatment of the band structure (instead of two-level systems) is discussed e.g. in [225].

Evaluating Fermi´s Golden Rule (eq. 78) with the product states as denoted in eq. 79 delivers matrix elements of the form

80. $\left\langle \Phi_2(2)^e \Phi_1(1)^g \middle| \Phi_1(1)^e \Phi_2(2)^g \right\rangle$, $\left\langle \Phi_2(1)^e \Phi_1(2)^g \middle| \Phi_1(2)^e \Phi_2(1)^g \right\rangle$ denoted Coulomb terms

and

81. $\left\langle \Phi_2(1)^e \Phi_1(2)^g \middle| \Phi_1(1)^e \Phi_2(2)^g \right\rangle$, $\left\langle \Phi_2(2)^e \Phi_1(1)^g \middle| \Phi_1(2)^e \Phi_2(1)^g \right\rangle$ denoted exchange terms.

While the Coulomb terms also deliver significant contributions in the weak coupling regime the exchange terms require a direct overlap of the electronic wavefunctions between the ground state wave functions and the excited state wave functions of both pigments (for details see [96]).

This direct overlap is only significant if the distance of the interacting fluoropheres is very low. In this case the electronic wave function is no longer localised at one pigment only but is delocalised among all coupled pigments.

The dominating mechanism for the EET is called "Dexter transfer", denoting a direct electron exchange due to the delocalisation of the electronic probability of presence. For the Dexter transfer the selection rules are different from selection rules of weakly coupled pigments including triplet-triplet transfer as proposed for strongly coupled Chl and carotenoid molecules.

In agreement with the exponential decay of the electronic wave functions Dexter transfer occurs at very small distances typically near to the Van- der Waals- distance in the order of 0.1 - 1 nm [76]. Concomitantly with the amplitudes of the electronical wave functions the transfer rate constant decreases exponentially with the distance r of the coupled pigments:

82. $k_{ET} \sim e^{-\alpha r}$

where α denotes the so called "Dexter coefficient".

Due to the short distance of the pigments the excitonic coupling leads to a significant shift of the energetic levels and therefore to a change of the optical spectra. The excitonic coupling leads to excitonic splitting (see chap. 3.4). For excitonically coupled states the relaxation from the higher excitonic level to the lower excitonic level are typically very fast (< 10 ps) and can not be resolved with time- and wavelength correlated single photon counting.

In many strong coupled photosynthetic pigments the Dexter transfer is the dominating EET mechanism, i.e. between Chlorophyll molecules in the LHC and in PBS of cyanbacteria and probably also in the PBP antenna of *A.marina* [226, 227].

The two Chl molecules bound to WSCP are strongly coupled with a distance < 1 nm (see chap. 4). It was found that the time resolved fluorescence spectra of WSCP can be described by an excitonically coupled Chl dimer that is modulated by the protein environment [47].

Sometimes it is not fully clear if the suitable approximation for the dominating EET mechanism is Dexter or Förster. For example in the PBP antenna the transport between different trimers has to bridge distances of about 2 nm which is inbetween both validity areas [227].

At distances above 2 nm the electromagnetic potential of the involved chromophores can be estimated with the model of point-dipole approximation [224]. In this case a significant probability for energy transfer can be observed up to a distance of 10 nm [208]. The mechanism of EET using the point-dipole approximation for V_{12} in eq. 78 is called “Förster Resonance Energy Transfer” (FRET).

3.3.2 Förster Resonance Energy Transfer (FRET)

The formulation of the point dipole approximation for the resulting energy transfer rate constant was done by T. Förster in 1948 [228]. The distance regime of the coupled molecules where this approximation holds (1-10 nm) needs to allow the approximation of the dipole of one pigment seen from the other pigment approximatly as point source (i.e. the distance has to be clearly bigger than the dipole length). Förster already suggested that the FRET mechanism could be the dominating proess for energy transfer inbetween coupled molecules in photosynthetic organisms. For Chl *a* he calculated the distance R_0 (Förster Radius) to be 8 nm, when the probability for the energy transfer is the same like the sum of all other relaxation processes [228]:

$$\textbf{83.}\quad k_{ET}\left(R_0\right)=k_{FRET}\left(R_0\right)=\frac{1}{\bar{\tau}_D}$$

At the distance R_0 50 % of the donor pigment´s energy is transferred to the acceptor pigment (i.e. the probability of the transfer is 50 %). In eq. 83 $\bar{\tau}_D$ denotes the apparent average fluorescence lifetime of the excited donor state in absence of the acceptor (i.e. the average excited state lifetime denoted as $\bar{\tau}$ in eq. 69, but without the energy transfer rate constant k_{ET} (absence of the acceptor)). If the fluorescence decay does not occur monoexponentially, eq. 83 has to be treated carefully and $\bar{\tau}_D$ should be calculated from the experimental data according to eq. 77 only after a multiexponential fit of the donor system´s fluorescence decay (without the acceptor, see ref. [208]). For further fluorescence spectroscopic findings of Förster see [229].

Measurements of the depolarisation of fluorescence light in dependency of the fluorophore concentration were done mainly by two groups in 1924, Gaviola and Pringsheim and Weigert and Käppler. From these measurements J. Perrin deduced in 1925 that a direct electromagnetic coupling between the dye molecules must occur and the transfer of energy between the pigments is not only a pure emission and reabsorption effect of real photons that leads to an energy transfer of excited states. Förster himself denoted in [228] in his own words that this energy transfer mechanism „[...] prinzipiell verschieden [ist] von einem solchen, der den Energieübergang durch den trivialen Mechanismus der Reabsorption der Fluoreszenz darstellen würde, da in diesem Ausstrahlung und Übergang nicht nebeneinander, sondern hintereinander ablaufende Prozesse wären.“

Förster used Fermi´s golden rule as given by eq. 78 to calculate $k_{ET}=k_{FRET}$. He assumed the dipole interaction as V_{12}. As given by eq. 79 the wave functions of the two pigments can be expressed as a product state of the wave function of pigment one $\left|\Phi_1^{e,g}\right\rangle$ and pigment two $\left|\Phi_2^{e,g}\right\rangle$ in excited (e) or ground (g) state [224]:

$$\textbf{84.}\quad V_{12} = \left\langle \Phi_1^{\,g}\Phi_2^{\,e}\left| V_{Coulomb} \right| \Phi_1^{\,e}\Phi_2^{\,g} \right\rangle$$

For a distance typically $R_{12} > 2$ nm between the center points of the coupled transition dipole moments of the two coupled pigments the dipole potential is well described by the point-dipole approximation (see Figure 48):

$$\textbf{85.}\quad V_{12} = \frac{1}{4\pi\varepsilon_0\varepsilon_r}\left(\frac{\bar{\mu}_1\bar{\mu}_2}{(R_{12})^3} - 3\frac{(\bar{\mu}_1\bar{R}_{12})(\bar{\mu}_2\bar{R}_{12})}{(R_{12})^5}\right)$$

In eq. 85 $\bar{\mu}_i$ denotes the dipole moment of the i. pigment and $\bar{R}_{12}$ denotes the vector that points from the center of $\bar{\mu}_1$ to the center of $\bar{\mu}_2$ (see Figure 48). The dipole strength which is proportional to $|\bar{\mu}|^2$ can be calculated from the absorption spectrum of the acceptor pigment and from the time resolved emission of the donor pigment. Due to the vector products in eq. 85 the coupling strength V_{12} strongly depends on the orientation of the interacting dipoles (for the nomenclature see Figure 48):

$$\textbf{86.}\quad V_{12} = \frac{|\mu_1||\mu_2|}{4\pi\varepsilon_0\varepsilon_r(R_{12})^3}\left(\cos\Theta_{12} - 3\cos\Theta_1\cos\Theta_2\right)$$

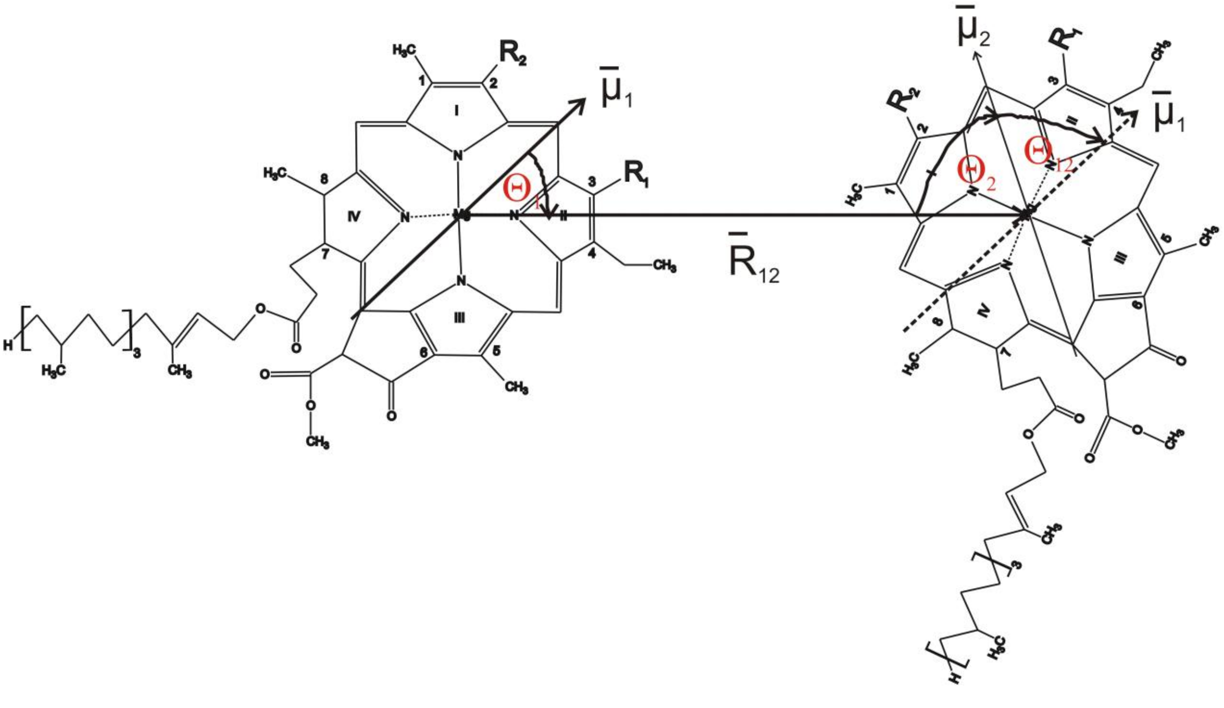

Figure 48: Scheme of the angels Θ_1 between $\bar{\mu}_1$ and the center-center vector $\bar{R}_{12}$, Θ_2 between $\bar{\mu}_2$ and $\bar{R}_{12}$, Θ_{12} between $\bar{\mu}_1$ and $\bar{\mu}_2$. $\bar{\mu}_1$ and $\bar{\mu}_2$ are the two Q_y dipole moments of two coupled chlorophyll molecules.

With help of the real part *n* of the complex refraction index of the medium between both molecules (surrounding medium) (see chap. 3.1.2) and the dipole orientation factor $\kappa := \left(\cos\Theta_{12} - 3\cos\Theta_1 \cos\Theta_2\right)$ the energy transfer rate for Förster transfer $k_{ET} = k_{FRET}$ as given in eq. 78 using the potential in eq. 86 can be written as

87. $$k_{FRET}\left(R_{12}\right) = \frac{2\pi}{\hbar} \frac{\left|\mu_1\right|^2 \left|\mu_2\right|^2 \kappa^2}{\left(4\pi\varepsilon_0\right)^2 n^4 \left(R_{12}\right)^6} \rho_{eff}\left(E\right)$$

Eq. 78, i.e. Fermi´s Golden Rule, is a formula to analyse the transition probability of any coupled quantum states if the coupling is weak enough. Eq. 87 is a formula to calculate the probability for energy transfer according to the assumption of a point-dipole-approximation of these states (Förster coupling).

The point dipole approximation is good if the distance of the molecules is much bigger than the extension of the dipole moments (~ 1 nm). Typical distances of coupled pigments in photosynthetic pigment protein complexes are of the order of some nm. Better approximations take into account higher orders of the multipole extension of the Coulomb potential or describe the dipole extension in form of the so called “extended dipole” approximation which assumes monopole moments from partial charges found along the dipole extension in the molecule [224]. When we discuss such approximation we additionally should keep in mind that already Fermi´s Golden Rule as given by eq. 78 is an approximation as first order perturbation theory for weak couplings.

Additionally there are further approximations used in the Förster formula. One prominent simplification is the assumption of a dipole embedded in a homogeneous and isotropic refractive medium which can be described by a simple number of the dielectricity. If we look at the two chlorophyll molecules exemplarily shown in Figure 48 and a typical protein environment of the chromophores as it is for example shown for the chlorophylls in the LHC in Figure 5 and for phycocyanin bound to PBS structures in the Figure 16, Figure 18 and Figure 20 it becomes clear that there is not an homogeneous and isotropic medium surrounding the chromophores. A better theory therefore should not only take into account the refractive index of the surrounding medium but should also take care about the spatial variations of the electric susceptibility $\overline{\overline{\chi}}_e$. Therefore one would not only need a tensorial expression of $\overline{\overline{\chi}}_e$ as given by eq. 35 but a spatial resolution of this tensor $\overline{\overline{\chi}}_e\left(\bar{r}\right)$ at each point of the pigment-protein structure.

The partially classical description of the Förster transfer rate (eq. 87) deviates strongly when the wave functions of the electrons located in in the excited states of the pigments one and two start to overlap directly as mentioned above (i.e. in these short distances the full quantum mechanical Dexter transfer has to be evaluated). This also becomes clear from the quantum mechanical point of view where the definition of several clearly defined distances and angels as necessary for the formulation of eq. 87 fails.

As mentioned above the dipole strength of $\overline{\mu}_1$ and $\overline{\mu}_2$ can be derived from the optical spectra. Förster showed that the term $|\mu_1|^2 |\mu_2|^2 \rho_{eff}(E)$ is proportional to the expression $\dfrac{\int_0^\infty F_D(\lambda)\varepsilon(\lambda)\lambda^4 d\lambda}{\overline{\tau}_D \cdot \int_0^\infty F_D(\lambda) d\lambda}$, i.e. the energetic resonance between the fluorescence spectrum $F_D(\lambda)$ of the donor pigment and the spectral extinction $\varepsilon(\lambda)$ of the acceptor divided by the (average) lifetime of the donor pigment in absence of the acceptor $\overline{\tau}_D$ (see [208], [228] and [229]). The dipole strength of the acceptor pigment $|\overline{\mu}_2|^2$ corresponds to the molar extinction coefficient $\varepsilon(\lambda)$ while the dipole strength of the donor $|\overline{\mu}_1|^2$ is expressed by the isolated donor piments´ average excited state lifetime $\overline{\tau}_D$.

The transition probability per time unit k_{FRET} as it was derived by Förster himself [230] finally denotes to

88. $$k_{FRET}(r) = A \frac{\kappa^2}{(R_{12})^6 \tau_0 n^4} \frac{\int_0^\infty F_D(\lambda)\varepsilon(\lambda)\lambda^4 d\lambda}{\int_0^\infty F_D(\lambda) d\lambda}$$

with the normalised overlap integral between the fluorescence of the donor and the extinction of the acceptor $\dfrac{\int_0^\infty F_D(\lambda)\varepsilon(\lambda)\lambda^4 d\lambda}{\int_0^\infty F_D(\lambda) d\lambda} := J(\lambda)$, the constant $A = \dfrac{9000(\ln 10)}{128\pi^5 N_A} cm^3 = 8{,}8 \cdot 10^{-25} cm^3 mol$ (dimension of the wavelength $[\lambda] = cm$) and the extinction coefficient $[\varepsilon(\lambda)] = (M \cdot cm)^{-1}$. Then the overlap integral has the dimension $[J(\lambda)] = \dfrac{cm^3}{M}$. A clear description how to evaluate the Förster Formula as given by eq. 88 numerically is found in ref. [208]. Combining the formulas 83 and 88 one can rewrite the Förster radius to

89. $R_0 = \left(A\Phi_F \dfrac{\kappa^2}{n^4} J(\lambda) \right)^{\frac{1}{6}}$ (measured in cm) with $\Phi_F = \dfrac{\overline{\tau}_D}{\tau_0}$ as found in eq. 71 for the donor molecule. The rate constant for the Förster transfer can be expressed as

90. $$k_{FRET}(R_{12}) = \frac{1}{\overline{\tau}_D} \left(\frac{R_0}{R_{12}} \right)^6$$

In many cases there is a lack of information for the direct calculation of the distance (R_{12}) dependent rate constant $k_{FRET}\left(R_{12}\right)$ from eq. 90. For example the value of the orientation factor κ^2 is not known for many pigment-protein complexes. For molecules in solution $\kappa^2 = \frac{2}{3}$ but in photosynthetic complexes κ^2 can be of much higher values. Certain pathways along the PBP antenna are strongly surpressed due to very small values of κ^2 near to zero leading to selected pathways of the EET along the PBS strcutures of cyanobacteria [226, 227]. It is found that there exist pairwise coupled pigments with $\kappa^2 \approx 1$ in all photosynthetic complexes and therefore FRET helps to figure out the structural organisation of pigment-protein complexes as we presented in study [52].

In the expressions of the Förster formulas given (eq. 88 to eq. 90) there might occur definition problems if the fluorescence decay is multiphasic. For coupled systems of different states of equal or comparable energy (isoenergetic states) the eq. 69 to 71 gathered from integration of the uncoupled system are not valid and the quantum yield for the fluorescence decay can not be simply calculated by $\Phi_F := \frac{k_{Flour}}{k_{Flour} + k_{Annihil} + k_{ET} + k_{IC} + k_{ISC}} = \frac{\bar{\tau}}{\tau_0}$ as proposed by eq. 71 because $k_{Flour} + k_{Annihil} + k_{ET} + k_{IC} + k_{ISC} \neq \frac{1}{\bar{\tau}}$. Eq. 69 is strictly valid for a monoexponential decay only, i.e. if there is not a backwards transfer k_{-ET} in the coupled system (see Figure 42). That means that the inverse average lifetime of a fluorophore is not well described by the sum of all rate constants (see also Figure 42) as there is a high probability for a backward transfer from the acceptor molecule to the donor if the donor and the acceptor pigment are isoenergetic or of comparable energy.

If we look at Figure 42 the primary quantum yield for energy transfer from an excited state $\Phi_{ET}\left(R_{12}\right) = \Phi_{FRET}\left(R_{12}\right)$ can be defined according to

$$\textbf{91.}\quad \Phi_{FRET}\left(R_{12}\right) := \frac{k_{ET}\left(R_{12}\right)}{\sum_i k_i} = \frac{k_{FRET}\left(R_{12}\right)}{\left(\bar{\tau}_D\right)^{-1} + k_{FRET}\left(R_{12}\right)}$$

focussing on Förster Resonance Energy Transfer $k_{ET} = k_{FRET}$ as dominating EET mechanism (see eq. 83). It is assumed that all other rate constants appearing in the time development of the excited state are concurring mechanisms to the EET via FRET. This is not the case if rate constants exist which populate the state (instead of depleting it, i.e. if the energy is transferred from the acceptor to the donor pigment).

In that case eq. 91 does not describe the final EET from the donor pigment to the acceptor pigment (i.e. the average amount of energy transferred after equilibration of the system) but it only describes the relative probability that the excitation energy is transferred to the neighbouring molecule directly after excitation. Eq. 91 therefore does not describe the final efficiency of Förster Resonance Energy

Transfer from the donor to the acceptor after the full equilibration of the excited state but the initial probability for EET.

This difference is of high importance for the understanding of the difference of average times of energy transfer in comparison to rate constants of the energy transfer. Looking at a typical photosynthetic system as shown in Figure 43 (imagine this figure without the quencher positioned at state N_4) we find that if the energy is located at pigment N_0 at zero time and if $k_{FRET}\left(R_{12}\right) >> \left(\bar{\tau}_D\right)^{-1}$ then $\Phi_{FRET}\left(R_{12}\right) \approx 1$. But due to the strong coupling of all 6 states shown in Figure 43, 1/6 (16,7 %) of the excitation energy will still relax from state N_0 after equilibration and therefore this amount is not transferred effectively from N_0 to other pigments of the chain shown in Figure 43 if no quencher exists.

In the following it is pointed out that the effective energy transfer (the amount of energy that is really transported to the acceptor after equilibration of the system) can not be calculated by eq. 91 which is denoting the probability for a single transfer step only and we suggest an alternative calculation.

$k_{FRET}\left(R_{12}\right)$ as generally defined is a rate constant describing the faith of a single exciton. We want to derive the typical formulas for the quantum yield $\Phi_{ET}\left(R_{12}\right) = \Phi_{FRET}\left(R_{12}\right)$ as they are found in literature sometimes after derivation from eq. 91 (see [208]), which is not correct. Due to the mentioned aspect we will not call $\Phi_{FRET}\left(R_{12}\right)$ as denoted by eq. 91 the „efficiency“ of FRET (which would be an expression regarding the equilibrated system) but we will call it the “quantum yield” of FRET (which is an expresssion valid for a nonequilibrium situation).

Combining eq. 90 and eq. 91 delivers

$$\textbf{92.}\quad \Phi_{FRET}\left(R_{12}\right) = \frac{k_{FRET}\left(R_{12}\right)}{\left(\bar{\tau}_D\right)^{-1} + k_{FRET}\left(R_{12}\right)} = \frac{\frac{1}{\bar{\tau}_D}\left(\frac{R_0}{R_{12}}\right)^6}{\frac{1}{\bar{\tau}_D} + \frac{1}{\bar{\tau}_D}\left(\frac{R_0}{R_{12}}\right)^6} = \frac{R_0{}^6}{R_{12}{}^6 + R_0{}^6}.$$

For the simplified monoexponential chromophores with $\left(\bar{\tau}_D\right)^{-1} = \sum_i k_i - k_{FRET}\left(R_{12}\right)$ and $\left(\bar{\tau}_{DA}\right)^{-1} = \left(\bar{\tau}_D\right)^{-1} + k_{FRET}\left(R_{12}\right) = \sum_i k_i$ one obtains

$$\textbf{93.}\quad \Phi_{FRET}\left(R_{12}\right) = \frac{k_{FRET}\left(R_{12}\right)}{\left(\bar{\tau}_D\right)^{-1} + k_{FRET}\left(R_{12}\right)} = \frac{\sum_i k_i - \left(\sum_i k_i - k_{FRET}\left(R_{12}\right)\right)}{\sum_i k_i} = 1 - \frac{\bar{\tau}_{DA}}{\bar{\tau}_D}$$

Looking at the formulas 92 and 93 as they are found in literature (see e.g. [208]) one can immeditaley see the contradiction by interpretation of a system as shown in Figure 43 without the quencher positioned at the state N_4 if the energies of the electronic states of all coupled pigments are equal and the distance between the coupled pigments $R_{12} = 0$. In that case the fluorescence decay lifetime of the coupled ensemble does not change if no additional dissipative channels are occurring (see the simulation of the DAS of the described system in Figure 44, left side). One would get $\Phi_{FRET}\left(R_{12}\right)=1-\frac{\bar{\tau}_{DA}}{\bar{\tau}_{D}}=0$ from equation 93 but $\Phi_{FRET}\left(R_{12}=0\right)=\frac{R_{0}{}^{6}}{R_{12}{}^{6}+R_{0}{}^{6}}=1$ from eq. 92. In summary the Förster formulas given in the equations 92 and 93 are only valid if the donor pigment and the acceptor pigment are spectrally clearly separated and there is no back transfer from the acceptor to the donor, i.e. if $\frac{hc}{\lambda_{\max}{}^{D}}-\frac{hc}{\lambda_{\max}{}^{A}}>>k_{B}T$ with $\lambda_{\max}{}^{D}$ as the maximum emission wavelength of the donor state and $\lambda_{\max}{}^{A}$ being the maximum emission wavelength of the acceptor state. In that case the transfer is in an "equilibrated" state from the point of view of the donor pigment after the transfer to the acceptor and we get $k_{Flour}+k_{Annihil}+k_{ET}+k_{IC}+k_{ISC}=\frac{1}{\bar{\tau}}$ as the necessary assumption underlaying all the derivations given here.

Both formulas, eq. 92 and eq. 93 are found in the famous ref. [208]. Eq. 93 can be understood as a FRET efficiency even if the donor and acceptor pigment do not decay monoexponentially if $\bar{\tau}_{DA}$ and $\bar{\tau}_{D}$ are calculated according to formula 77 as an appropriate calculation of the average decay times for multiexponentially decaying systems (see [208]). But as pointed out in chap. 3.2.5 these lifetimes $\bar{\tau}_{D}$ and $\bar{\tau}_{DA}$ can not simply be gathered from the DAS (see Figure 44, left side), but one would need molecular resolution to analyse the excited state lifetime of the donor pigment in presence of the acceptor $\bar{\tau}_{DA}$ as given in Figure 44, right side.
The eq. 92 denotes the quantum yield for an initial FRET process but not an overall efficiency.

Independently from the coupling strength an isoenergetic ensemble of pigments is not necessarily quenched (situation without the quencher at position N_4 in Figure 43) but all pigments exhibit the same apparent fluorescence decay time $\bar{\tau}_{D}$. This case is found for example for the strongly coupled Chlorophyll complex of the solubilised LHCII trimer. In LHCII $\bar{\tau}_{D}=\bar{\tau}_{DA}$ if we compare $\bar{\tau}_{D}$ of the monomeric LHC structure or even of single chlorophyll molecules with $\bar{\tau}_{DA}$ of the solubilized LHC trimers (see [45] and references therein).

Eq. 93 becomes valid if the average lifetimes of the donor and the acceptor are not measured from the ensemble but with single molecule resolution. At the moment this is not possible in the experiment for structures as shown in Figure 43 because one would need an optical resolution in the order of 1 nm (less than the distance of 2 pigments). As shown in Figure 44, left side, the DAS in the wavelength domain of a structure as shown in Figure 43 (without the quencher located at state N_4) exhibits a single decay constant for the whole spectral range as shown in Figure 44 (left side).

If one could perform a superresolution experiment delivering the possibility to get individual decay curves for the chromophores in the coupled structure shown in Figure 43, then it would be possible to construct spatial DAS indicating the amplitude spread of individual decay components along the space coordinate instead of the wavelength coordinate (se Figure 44, right side). In such a case a correct calculation of the average fluorescence lifetimes of the donor in absence or presence of the acceptor $\bar{\tau}_D$ and $\bar{\tau}_{DA}$, respectively as given by eq. 77 would enable the principal possibility to correct formula 93 so that it is also valid for single isoenergetic molecules in a coupled chain as shown in Figure 43.

Eq. 93 combined with eq. 77 directly delivers the well known intensity- formulation for $\bar{\tau}_{DA} \neq \bar{\tau}_D$:

$$\textbf{94.}\quad \Phi_{FRET}(R_{12}) = 1 - \frac{\bar{\tau}_{DA}}{\bar{\tau}_D} = 1 - \frac{\left[\sum_{i=1}^{n} A_i(\lambda)\tau_i\right]_{DA}}{\left[\sum_{i=1}^{n} A_i(\lambda)\tau_i\right]_{D}} = 1 - \frac{\left[\int_0^\infty F(t)dt\right]_{DA}}{\left[\int_0^\infty F(t)dt\right]_{D}} = 1 - \frac{I_{DA}}{I_D}$$

Calculating the spatially resolved DAS as shown in Figure 44, right side, the formula 94 is independent from the restrictions mentioned above if the spectra are normalised, i.e. $\left[\sum_{i=1}^{n} A_i(\lambda)\right]_D = \left[\sum_{i=1}^{n} A_i(\lambda)\right]_{DA}$. This is fullfilled if the absorption of the donor and acceptor in the donor-acceptor pair is the same as the absorption of the isolated donor only.

Evaluating $\frac{\bar{\tau}_{DA}}{\bar{\tau}_D}$ in the spatial „pigment domain“ for the single chromophores (Figure 44, right side with help of eq. 77) one obtains a value of about $\frac{\bar{\tau}_{DA}}{\bar{\tau}_D} \approx 0.16$ for the initially excited donor pigment N_1 in the exemplarily shown molecule chain of Figure 43 if we neglect the contributions $\left[\sum_{i \neq 4ns} A_i(\lambda)\tau_i\right]_{DA} << \left[A_i(\lambda)4ns\right]_{DA}$. In fact $\frac{\bar{\tau}_{DA}}{\bar{\tau}_D}$ becomes exactly 0.16 for $k \to \infty$ (see Figure 43) as is expected from theory. This value of 0.16 is also expected for the relation $\frac{I_{DA}}{I_D}$ if one evaluates the intensity of the donor pigment N_1 in comparison to the fluorescence of all five acceptor pigments N_0 and N_2 to N_5. Therefore the real FRET efficiency after equilibration calculates to 84 % as it is expected from the structure of the system employing eq. 94.

With the use of eq. 77 the eq. 93 (right side) and therefore also eq. 94 are correct for the FRET efficiency after equilibration of the system. In such case the efficiency should be denoted with $\eta_{FRET}(R_{12})$. Eq. 92 describes the quantum efficieny $\Phi_{FRET}(R_{12})$ of a single excited state to undergo a single FRET transition.

The final formula is therefore suggested to denote to

95. $\eta_{FRET}\left(R_{12}\right)=1-\frac{\bar{\tau}_{DA}}{\bar{\tau}_{D}}=1-\frac{I_{DA}}{I_{D}}$, where it would be necessary to achieve a signal with superresolution from a single molecule which acts as donor in a strongly coupled chain and calculate the $\bar{\tau}_D$ and $\bar{\tau}_{DA}$, respectively, as given by eq. 77, and

96. $\Phi_{FRET}\left(R_{12}\right)=\frac{k_{FRET}\left(R_{12}\right)}{\left(\bar{\tau}_{D}\right)^{-1}+k_{FRET}\left(R_{12}\right)}=\frac{R_{0}^{6}}{R_{12}^{6}+R_{0}^{6}}$ for the real „quantum efficiency“ describing the transfer probability of a single quantum state.

In fact, the mentioned problems are not complete. Eq. 95 contains additional problems. For example, the fluorescence intensity and average lifetime of the donor pigment in presence of the acceptor, I_{DA} and $\bar{\tau}_{DA}$, respectively, might change due to quenching effects without an energy transfer from the donor to the acceptor pigment. In such cases one might get a kind of “donor depletion efficiency” instead of EET efficiency employing eq. 95.

To avoid these problems that especially affect the evaluation of the donor fluorescence we focused on the fluorescence rise kinetics observed at the acceptor pigment (see chap. 3.2.5), comparing the fluorescence dynamics of the acceptor in absence of the donor with the fluorescence dynamics in presence of the donor pigment. It was found that this method is most stable against uncertainties. Unfortunately the rise kinetics at the acceptor pigment is hard to resolve.

One additional approximation found in eq. 88 is the fact that the calculation of $k_{FRET}\left(R_{12}\right)$ is usually performed using the fluorescence and absorption spectra of the isolated pigments. But the optical properties of donor and acceptor states might slightly change due to the coupling as we showed e.g. in ref. [53]. Therefore it is always necessary to analyse the stability of the obtained solutions for FRET efficiencies against variations of the parameters used for the calculation and compare the experimental results with complementary methods.

3.4 The optical spectra of coupled pigments in pigment-protein complexes

The optical line shape functions used for the fit of the fluorescence spectra are chosen as Lorentzian lines for room temperature spectra and Gaussian lines for deep temperature emission as mentioned in chap. 2.2. To achieve a full understanding of coupled systems it is especially necessary to look at the influence of pigment-pigment and pigment-protein coupling onto the energetic states.

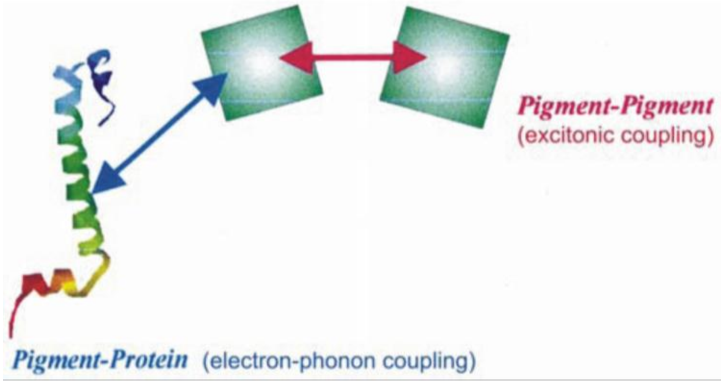

Figure 49: Schematic view of the pigment-pigment and pigment-protein coupling, figure taken from ref. [48].

The energetic states are changing due to pigment-pigment coupling and pigment-protein coupling as schematically shown in Figure 49. In case of FRET this effect is rather low because the coupling is sufficiently weak. But as stronger coupling occurs remarkable shifts are observed. As shown below (see Figure 51) the excitonic coupling of energetic states results in new excitonic states that are spectrally separated even if the coupled pigments were degenerated in energy. The pigment-pigment coupling can be calculated with the Hamiltonian given in eq. 43. The energy transfer processes for strongly coupled pigments are understood as relaxation of the excited electron in the excitonically splitted states while the long range Förster coupling is described as a dipole coupling of distinguishable (localized) states.

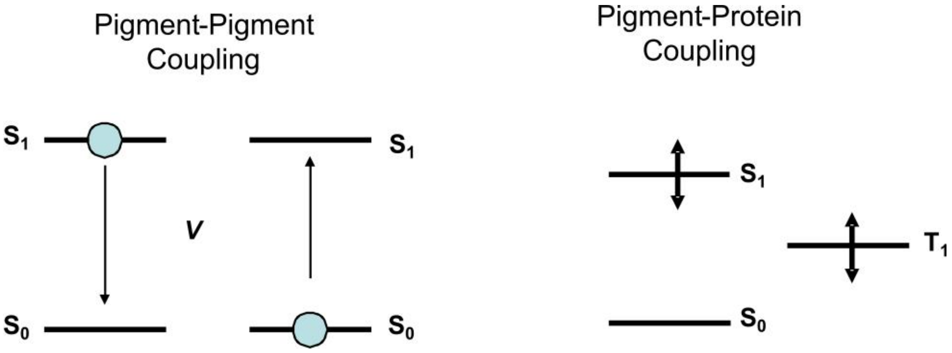

Figure 50: Scheme for the pigment-pigment coupling and the pigment-protein coupling occuring in pigment-protein complexes, graphics kindly provided by T. Renger [231].

As shown in Figure 50 next to pigment-pigment coupling also the pigment-protein coupling leads to a modulation of the energetic states of the coupled pigments. The protein represents the environment of the excited structure. It leads to a broad spectrum of electron-phonon coupling (see Figure 40) next to the vibrational spectrum of the pigments itself.

In contrast to simple situations of pigment-pigment coupling the pigment-protein coupling can not be calculated analytically strightforward. The rather complex protein structure and the corresponding eigenmodes of phononic spectra can be modeled as a stochastic influence of the protein onto the energetic states of the pigments (see ref. [224]). In dependency of the time scale of the involved protein vibrations these shifts are separated either into quasistatic modulations that result in a distribution of energetic states inside an ensemble of pigments or as dynamic modulations that occur as active modulation of the excited states due to the fast fluctuating protein matrix. Quasistatic shifts are induced by conformational distributions of the proteins appearing quasi statically in comparison to the lifetime of an electronic excitation. The quasistatic shifts lead to inhomogeneous and therefore Gaussian broadening of the spectra.

The dynamic modulations of the energetic states lead to homogeneous spectral broadening (i.e. Lorentzian line shapes). The dynamic modulations are correlated with protein vibrations that are much faster than the excited states´ lifetime. It is an interesting task to analyse the influence of the dynamics of the surrounding medium that appears on a comparable time scale to the excited state lifetime. These vibrations are neither quasi static nor dynamic and might appear as a single relaxation of the environment during the excited state lifetime.

Dynamic modulations that occur in coherence with the electronic relaxation of the excited states are assumed to lead to dynamical localization effects of excited states in pigment-protein complexes that could have a physiological relevance in photosynthetic energy transfer processes [126, 127, 231].

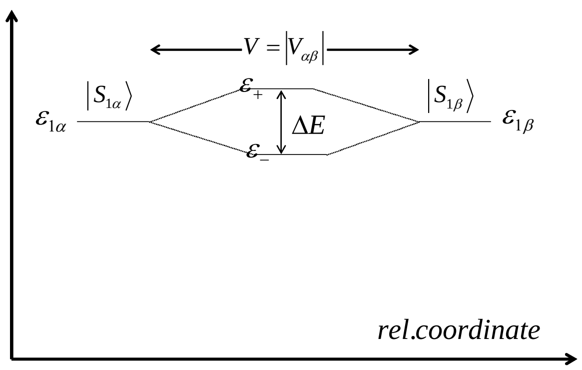

Figure 51: Energetic scheme of two uncoupled states $|S_{1\alpha}\rangle$ and $|S_{1\beta}\rangle$ approaching each other. The x-axis should be understood as a nonlinear “spatial” coordinate. When the states approach each other a shift of each

state occurs due to the energetic potential of the other state. Isoenergetic (degenerated) states start to split forming energetically shifted states separated by the value ΔE.

From the stationary Schroedinger equation (eq. 39) one could calculate the energetic states of any complex coupling scheme by diagonalisation of the Hamiltonian. To analyse the problem shown in Figure 51 qualitatively one can look at the problem in the basis of the uncoupled states denoted as $\left|S_{1\alpha}\right\rangle = \begin{pmatrix} 1 \\ 0 \end{pmatrix}$ and $\left|S_{1\beta}\right\rangle = \begin{pmatrix} 0 \\ 1 \end{pmatrix}$. If the molecules are well seperated from each other the corresponding Hamiltonian denotes to

97. $$\hat{H} = \begin{pmatrix} \varepsilon_{1\alpha} & 0 \\ 0 & \varepsilon_{1\beta} \end{pmatrix}$$

with the coupling potential V=0. In the case that these molecules approach each other this coupling potential no longer vanishes and we have to treat it as off-diagonal elements $V = \left|V_{\alpha\beta}\right| = \left|V_{\beta\alpha}\right|$.

The Hamiltonian gets the form

98. $$\hat{H} = \begin{pmatrix} \varepsilon_{1\alpha} & V_{\alpha\beta} \\ V_{\beta\alpha} & \varepsilon_{1\beta} \end{pmatrix}$$

The Hamiltonian shown in eq. 98 can be understood as the formulation of the coupled problem in the basis of the uncoupled states.

To solve this problem one has to solve the eigensystem of the Hamiltonian shown in 98. In a simple system where the wave functions of the ground and excited state are not treated explicitely and the difference in the Van-der-Waals energy of ground state and excited state pigments is not taken into account the eigenvalues calculate to:

99. $$\varepsilon_{\pm} = \frac{\varepsilon_{1\alpha} + \varepsilon_{2\alpha} \pm \sqrt{(\varepsilon_{1\alpha} - \varepsilon_{2\alpha})^2 + 4V^2}}{2}$$

These are two new energetic states which are different from each other in energy even if the former states $\left|S_{1\alpha}\right\rangle$ and $\left|S_{1\beta}\right\rangle$ were energetically degenerated. ε_{+} and ε_{-} are separated by

100. $$\Delta E = \sqrt{(\varepsilon_{1\alpha} - \varepsilon_{2\beta})^2 + 4V^2}$$

In complex pigment-protein systems several (N) pigments are coupled. In that case one has to extend the two dimensional Hilbert space to a dimension that equals the number of coupled states:

101. $$\hat{H} = \begin{pmatrix} \varepsilon_1 & & & & \\ & \varepsilon_2 & V_{mn} & & \\ & & \ldots & & \\ & V_{mn} & & \ldots & \\ & & & & \varepsilon_N \end{pmatrix}$$

If the Hamitlonian shown in 101 is e.g. evaluated with the coupling scheme for 9 PC chromophores inside a trimeric C-PC –protein disc as a PBP antenna compartment as shown in Figure 18, right side, then an excitonic splitting occurs as qualitatively shown in Figure 52. For the calculation result shown in Figure 52 the electronic coupling of the excited states was assumed to follow a distance dependency $V_{12} \sim \frac{1}{(R_{12})^3}$ with a normalisation to $V_{\alpha 84-\beta 84} = 56cm^{-1}$ as strongest coupling between the α_{84} and β_{84} chromophore and the distance $R_{\alpha 84-\beta 84} = 2.2nm$ according to [175]. Therefore for all other pigments The coupling of all other pigments is estimated as $V_{ij} \sim 56cm^{-1} \frac{(2.2nm)^{-3}}{(R_{ij})^3}$. These values differ slightly from the values for the C-PC trimer found in literature [60, 175] because the different orientations of the dipole moments are not taken into account. The aim of this example is just to give an impression how excitonic coupling leads to a split of the energetic states in coupled nanostructures as shown in Figure 52. As pointed out the exact calculation of the optical spectra of complex coupled systems is beyond the scope of this work. An elaborated calculation of the optical spectra of the strongly coupled Chl molecules in WSCP is found e.g. in [37] and [38].

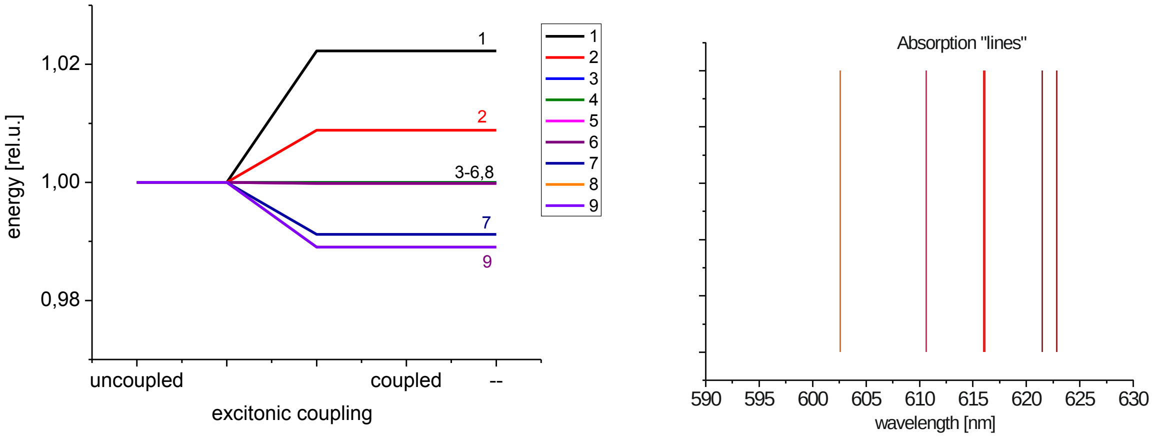

Figure 52: Eigenvalues of the Hamiltonian shown in eq. 101 for 9 coupled pigments that resemble a trimeric PC containing disc of the cyanobacterial PBP antenna as shown in Figure 18. The coupling strength is roughly estimated to $V_{ij} \sim 56cm^{-1} \frac{(2.2nm)^{-3}}{(R_{ij})^3}$ (see Figure 18).

3.5 Thermodynamic aspects of photosynthesis

“The fundamentals of thermodynamics are based on a symmetry law and an asymmetry law in time. The first law of thermodynamics is a law of preservation based on the symmetry of time. The second law of thermodynamics is a law of time asymmetry which describes the direction of the processes”
Rudolf Julius Emanuel Clausius, (1822 - 1888), German physicist

“Contrary to the generally accepted view, primary photochemistry in plants can, in principle, proceed with negative entropy formation”
Robert C. Jennings, Italian biologist, 2007 published in [234]

The statements of Jennings as published in [232- 234] denote that the 2nd law of thermodynamics might stand in contradiction to the primary photochemistry in plants. This gives rise to the necessity to discuss the basic underlaying thermodynamic concepts and their relation to photosynthesis. In fact it is hard to proof that photosynthesis does not proceed with negative entropy formation. As for all thermodynamic processes that might violate the 2nd law of thermodynamics no plants are observable that grow with an universe overall negative entropy formation. It turns out that plants grow in local nonequilibrium situations in the stationary overall equilibrium of the energy flux from the sun that interacts with the earth and leads to a high entropy production on the earth surface. We strongly believe and make suggestions for a proof that no process violates the 2nd law of thermodynamics because this law mainly reveals that unlikely conditions relax to the most probable distribution if no work is applied. That statement seems to be intuitively correct. This aspect of physics and living matter is shortly treated in the following chapters.

3.5.1 Gibbs free energy and entropy

The photosynthetic reaction denoted in chemical equation 1 is endergonic if the absorbed photons are neglected. The reaction is taking up heat and is simultaneously reducing the entropy of the product in comparison to the educt compounds. The endothermic character is shown by the difference of the enthalpy (H) which is $\Delta H = + 2808$ kJ/mol. The reduction of entropy (S) can be calculated to $\Delta S = -259.1$ J/(mol*K) (see [235]). Therefore at room temperature (T) (295 K) one gets $T\Delta S = -76.4$ kJ/mol.

Generally a process occurs spontaneously if the change of Gibbs free energy (G) is negative (i.e. if the Gibbs free energy of the product compounds is smaller than the Gibbs free energy of the educt compounds, $\Delta G<0$):

102. $$\Delta G = \Delta H - T\Delta S$$

Without the photon contribution the resulting Gibbs free energy of the photosynthetic reaction described in chemical equation 1 calculates to $\Delta G = + 2884.4$ kJ/mol according to equation 102 indicating the endergonic character of the reaction. The equilibrium of the chemical equation 1 is far at the left side of the reaction, i.e. at the side of the chemical educts.

The analysis of the photosynthetic processes leading to the production of one mol glucose shows that at least 60 photons are absorbed per single molecule glucose that is generated [76, 236].
The absolute minimal value for the energy uptake should at least correspond to the absorption of 4 photons for the oxidation of one water molecule (two turnover cycles of PS I and PS II, each) and therefore to 48 photons per mol glucose. The splitting of 2 H_2O to 4 H^+ and O_2 is releasing 4 electrons in the photosystem II (PS II) only. These electrons have to be pumped from the PS II via PS I to the place where NAD+ is reduced (see Figure 2 and [84, 90-92]). PS I and PS II are working hand in hand which doubles the absorbed number of photon quanta per mol glucose. In fact, 8 photons are absorbed to split 2 water molecules, i.e. 48 photons are absorbed per mol glucose (see chemical equation 1).
This leads to a photonic contribution of at least $\Delta H^{phot} = 48 \cdot N_A h\nu$ per mol that is delivered by the photon energy [232]. The longest absorbed wavelength in the PS I is about 700 nm and therefore an additional $\Delta H^{phot} = 48 \cdot N_A h\nu \approx 8200$ kJ/mol is involved into chemical equation 1.
For detailed thermodynamic considerations the eq. 102 has to be evaluated for each single chemical step inside a plant. Such accurate thermodynamic analysis of photosynthesis is a very complicated task. It might be the reason for the recent discussions whether or not photosynthesis might violate the 2nd law of thermodynamics [232-234, 237].
One mol of absorbed red photons with 700 nm wavelength contains an energy of 171 kJ. It is not fully consistently answered in the literature how much entropy a single photon contains or even if it is possible to define the entropy of a single photon. The entropy of the photon ensemble can be described by the entropy of the Planck spectrum and therefore thermal single photons exhibit a probability distribution that carries the corresponding amount of entropy.

The absorbed light energy of 8200 kJ/(mol glucose) seems to carry a huge amount of “excess” energy in comparison to the energy consumption $\Delta G = + 2884,4$ kJ/mol in chemical equation 1.
Sometimes it is found in literature that this “excess energy” shows that photosynthesis could be much more efficient. We believe that this point of view is too simple because it is of an important question how the directed transfer of photon energy to the chemical Gibbs free energy of glucose is possible. During the reaction sequence highly energetic compounds are formed as ATP which is urgently necessary to drive the functional work of the cell. It is not possible to drive the photosynthetic processes without energy dissipation.

The transformation of solar radiation to free energy is possible due to the low entropy per enthalpy (H) ratio S/H of the sunlight. If the volume and pressure do not change during a thermodynamic process, as we assume for the absorption of a photon, then dH = dU and 1/T = S/H.

The inverse temperature of the solar radiation and therefore $(S/H)^{solar}$ is much lower than the $(S/H)^{earth}$ ratio of thermal photons that are released after absorption on the earth surface. The wavelength maximum (λ_{max}) of the emitted black body radiation determines the so called colour temperature (T_C) of radiation which is associated with the S/H ratio according to Wien´s law:

103. $$\frac{S}{H} = \frac{1}{T_C} = \frac{\lambda_{\max.}}{2897{,}8\mu mK}$$

Equation 103 shows, that the wavelength maximum (λ_{max}) of electromagnetic radiation is proportional to the entropy per enthalpy ratio. Therefore S/H is much lower for solar light than for thermal radiation of a 280 K black body.

In that sense the plant uses a pool of “negative entropy” from sunlight. There exist different estimations of the effective colour temperature T_C determined by the light spectrum that is available for photosynthetic organisms taking into account scattered light or light absorbed by the earth atmosphere [235], but for all estimations the available light spectrum corresponds to $T_C > 1000$ K in marked contrast to the typical entropy content of thermal baths in the sea or the earth atmosphere at T = 280 K. The formation of highly organised structures is a dissipative process in accordance to the 2nd law of thermodynamics because the process occurs during the equilibration of sun radiation and earth temperature. The plants grow driven by a fractally local nonequilibrium.

As we have seen the photosynthesis is a quantum process which is driven by absorption of single photons. Entropy is a statistical quantity which is not well defined for single particles.

Generally the equation

104. $$\frac{\Delta S}{\Delta Q} \geq \frac{1}{T}$$

holds where the equality denotes reversible processes when the uptake of heat goes along an isothermal path while the inequality is characteristic for irreversible processes, i.e. when the system is dissipative and the dynamics is not restricted to a thermodynamic path.

At this point it has to be clearly stated that the photosynthetic process does not occur in the equilibrium. The equations of thermodynamics are only valid assuming local equilibrium conditions. This might not be possible for light absorption and the interaction of excited states with the surrounding environment. The reader should therefore keep in mind that our considerations suggest extentions of formulas that are valid in equilibria conditions in spite of strong nonequilibrium conditions.

Evaluating equation 103 we can make a rough suggestion for the average entropy of a single photon by identifying it´s energy with enthalpy and heat: $Q = H = h\nu$.

The equality of heat and enthalpy is fulfilled for an isobar thermodynamic process if the pressure remains constant which can be assumed to be valid for reactions of the photon gas.
From that simple consideration we would suggest

105. $S_{phot} \approx \dfrac{hc}{2.8978 \cdot 10^{-3} mK} = 6.9 \cdot 10^{-23} J/K$

as contribution of the probability distribution of the single photon to the entropy. Interestingly S_{phot} as given by eq. 105 is a fixed value idependent from the photon wavelength and qualitatively comparable to the value $S_{phot} \approx k_B = 1.38 \cdot 10^{-23} J/K$ as presented in [238].

Kirwan Jr. [238] suggests a comparable value for the photon entropy as shown here, while Gudkov [239] takes the viewpoint that “light is a form of high grade energy which carries no thermodynamic entropy”. Already Planck calculated the black body radiation spectrum considering the thermodynamic entropy of the radiation field. The thermal black body radiation which is in thermal equilibrium with the environment carries no Gibbs free energy: $\Delta G = 0$ which corresponds to $\Delta H = \Delta Q = T\Delta S$ according to eq. 102.

The necessary rise of the overall entropy when a plant works in the nonequilibrium (e.g. relaxing after light absorption) must be correlated with dissipation of energy into the environment. If a system absorbs photons and is then relaxing to a final state emitting more photons than previously absorbed (it is shown that in particular the production of phonons or any bosons fullfills the necessary increase of entropy) then the final state can be of lower entropy than the initial state in full accordance to the 2nd law of thermodynamics because the environment takes up entropy. On the other hand a single quantum process might violate the 2nd law of thermodynamics but it becomes arbitrary improbable that this happens for huge complex systems.
At the moment there is no reason to assume that photosynthesis violates the 2nd law of thermodynamics as done by Jennings et al. [232] and answered by detailed description of the processes which are in line with the 2nd law of thermodynamics by Lavergne [236] which let to further comments of Jennings ([233], [234]).

Generally entropy is a quantity of an ensemble describing the probability of an ensemble´s state. The most general formulation of this property is given by the Shannon entropy

106. $S = -k_B \sum_i p_i \ln p_i$

calculating the entropy from the single probabilities p_i of each state i that occurs in the thermodynamic equilibrium (k_B is the Boltzmann constant). A more general formulation where $p_i(t)$ is time dependent and the system is not necessarily in an equilibrium is suggested by Haken [223].

107. $S = -k_B \sum_i p_i(t) \ln p_i(t)$

In eq. 107 $p_i(t)$ might be calculated from rate equations. We will use equation 106 and equation 107 to estimate the probability of a forward in comparison to backward steps in the rate equations as given by eq. 59 (see chap. 3.2.1). Equation 107 is a generalisation of the problem of calculating entropy in the nonequilibrium case which helps us to understand the correlation of dynamics of probabilities and entropy when a photosynthetic complex relaxes after light absorption.

In the thermodynamic equilibrium equation 106 and equation 103 connect the macroscopic observables of thermodynamics (here: temperature T as given in eq. 103) with the microscopic probabilities of certain distributions of space and momentum in an ensemble of states (equation 106). Therefore the combination of equation 106 and 103 is the most important step for a statistical motivation of thermodynamics.

Eq. 59 and 60 ((see chap. 3.2.1) can be derived from eq. 106 if we use the 2nd law of thermodynamics which postulates that the Shannon entropy function of eq. 106 is at maximum in the equilibrium case of a closed system.

Then $\delta S = 0 = \delta\left(\sum_i p_i \ln p_i\right) = \delta\left(\sum_i p_i \ln p_i - \lambda\left(\sum_i p_i - 1\right) - \beta\left(< E > - \sum_i p_i E_i\right)\right)$

where λ is an arbitrary Lagrange parameter with $\delta\lambda = 0$ that can be added because $\sum_i p_i = 1$ and β is an Lagrange Parameter that can be added because $< E >= \sum_i p_i E_i$

Accomplishing the variation one gets:

$$e^{(\lambda-1)} = \frac{1}{\sum_i e^{-\beta E_i}} \Rightarrow p_i = \frac{e^{-\beta E_i}}{\sum_i e^{-\beta E_i}}$$

Taking eq. 104 (the equality for the reversible processes) and eq. 106 one gets:

$$S = -k_B\left(\sum_i p_i \ln p_i\right) = \frac{Q}{T}$$

$$\Rightarrow -k_B\left(\frac{\sum_i e^{-\beta E_i}\left(-\beta E_i\right)}{\sum_j e^{-\beta E_j}}\right) = \frac{Q}{T} \Rightarrow k_B \beta \langle E \rangle = \frac{Q}{T}$$

For the thermally equilibrated system without work $\langle E \rangle = Q$ one finds: $\beta = \frac{1}{k_B T}$

And therefore

108. $$p_i = \frac{e^{-\frac{E_i}{k_B T}}}{\sum_i e^{-\frac{E_i}{k_B T}}} := \frac{e^{-\frac{E_i}{k_B T}}}{Z}$$

where Z denotes the standard canonical partition function.
From eq. 108 the proposed Boltzmann distribution for state populations according to eq. 60 and for rate constants according to eq. 59 follow directly.

3.5.2 The entropy in the ensemble of coupled pigments

As mentioned shortly in the last chapter 3.5.1 the rate equation formalism as e.g. given by eq. 55 and 72 delivers a thermodynamic approach to excited states that migrate in systems of coupled pigments. In the equilibrated case the probabilities of excited state populations follow the Boltzmann distribution:

109. $$\begin{aligned} S &= -k_B \sum_i p_i \ln p_i = -k_B \sum_i \left(\frac{e^{-\frac{E_i}{k_B T}}}{\sum_j e^{-\frac{E_j}{k_B T}}} \ln \frac{e^{-\frac{E_i}{k_B T}}}{\sum_j e^{-\frac{E_j}{k_B T}}} \right) = -k_B \sum_i \left(\frac{e^{-\frac{E_i}{k_B T}}}{\sum_j e^{-\frac{E_i}{k_B T}}} \left(\frac{-E_i}{k_B T} - \ln \sum_j e^{-\frac{E_j}{k_B T}} \right) \right) \\ &= k_B \ln Z + k_B \sum_i p_i \frac{E_i}{k_B T} = k_B \ln Z + \frac{\langle E \rangle}{T} \end{aligned}$$

In the dissipative (nonequilibrium) situation the solution of eq. 72 for the time dependent excited state population can be used to estimate the entropy dynamics:

110. $$\begin{aligned} S(t) &= -k_B \sum_i p_i(t) \ln p_i(t) \\ &= -k_B \sum_i \left(\frac{N_i(t)}{\sum_j N_j(t)} \ln \frac{N_i(t)}{\sum_j N_j(t)} \right) = -k_B \sum_i \left(\frac{\sum_j A_{ij} e^{-k_j t}}{\sum_k \sum_j A_{kj} e^{-k_j t}} \ln \frac{\sum_j A_{ij} e^{-k_j t}}{\sum_k \sum_j A_{kj} e^{-k_j t}} \right) \end{aligned}$$

In the following eq. 110 will be shortly evaluated. For that purpose we choose the most simple system in this context, i.e. two coupled states as shown in Figure 53. In the initial moment only the energetically higher state is excited and after excitation the system relaxes. For the sake of simplicity we assume that the excited states can not decay into the ground state. This is a good approximation for strongly coupled systems where the energy transfer processes and the thermal equilibration occur much faster than the excited state relaxation.

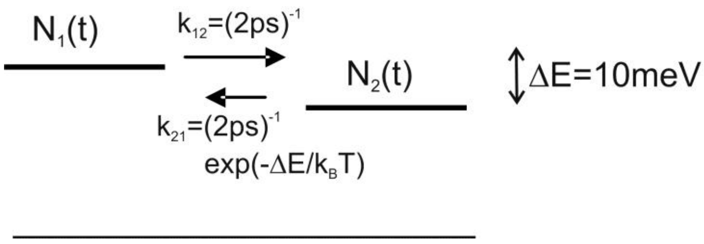

Figure 53: Two coupled excited states which are separated by ΔE=10 meV. The energy transfer from state one to state two has a probability of (2 ps)$^{-1}$. The back transfer propbability follows the Boltzmann distribution.

With the formalism described in eq. 73 in chap. 3.2.4 one can easily calculate the excited state population of the system shown in Figure 53. Then eq. 110 can be used to calculate the time dependent entropy of the system shown in Figure 53. While a numerical solution of the problem is possible independently from the complexity of the coupled system the problem given in Figure 53 can be solved analytically and the result denotes to:

$$N_1(t) = \left(1/\left(1+\exp\left(-\Delta E/k_B T\right)\right)\right)e^{-k_{12}\left(1+\exp\left(-\Delta E/k_B T\right)\right)t} + \exp\left(-\Delta E/k_B T\right)/\left(1+\exp\left(-\Delta E/k_B T\right)\right)$$
$$N_2(t) = -\left(1/\left(1+\exp\left(-\Delta E/k_B T\right)\right)\right)e^{-k_{12}\left(1+\exp\left(-\Delta E/k_B T\right)\right)t} + 1/\left(1+\exp\left(-\Delta E/k_B T\right)\right)$$

For that system the entropy according to eq. 110 takes the form

$$S(t) = -k_B\left(N_1(t)\ln\left(N_1(t)\right) + N_2(t)\ln\left(N_2(t)\right)\right) := -k_B\left(p(t)\ln\left(p(t)\right) + \left(1-p(t)\right)\ln\left(1-p(t)\right)\right)$$

This entropy function has a maximum of $S^{\max} = k_B \ln 2$ for the equal population probability of $N_1(t) = N_2(t)$:

$$\frac{\partial S(t)}{\partial p(t)} = 1 + \ln\left(p(t)\right) - 1 - \ln\left(1-p(t)\right) \overset{!}{=} 0 \Rightarrow p(t) = N_1(t) = \frac{1}{2} = N_2(t)$$

The time $t^{\max}$, when this maximum is reached denotes to:

$$t^{\max} = \frac{1}{k_{12}} \frac{-\ln\left(1/2 - 1/2 \cdot \exp\left(-\Delta E/k_B T\right)\right)}{1+\exp\left(-\Delta E/k_B T\right)}$$

For $\Delta E \to \infty$ or $T = 0$ we get

$$t^{\max} = \ln 2/k_{12}$$

While for $\Delta E = 0$ or $T \to \infty$ the entropy maximum is coincident with the equilibrium $N_1(t) = N_2(t)$ for $t^{\max} \to \infty$

That means that $S(t)$ exhibits a local maximum for all cases where $\Delta E > 0 \wedge T < \infty$ which is the case for all relaxations that correspond to time directed (dissipative) processes.

The time dependent excited state population for $N_1(t)$ and $N_2(t)$ calculated according to eq. 73 for 300 K and the entropy curves $S(t)$ at different temperatures are shown in Figure 54:

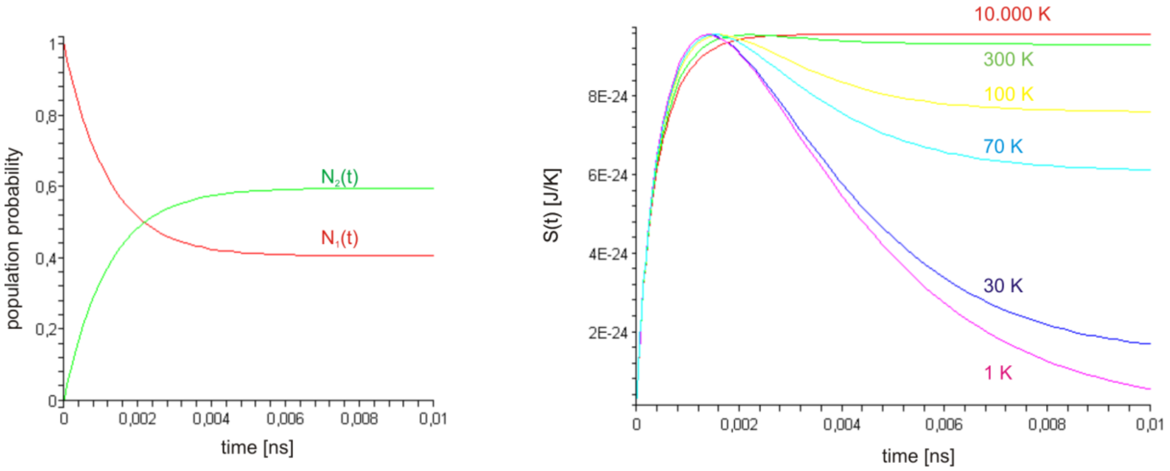

Figure 54: Time dependent population at 300 K of N$_1$(t) (red curve, left side) and N$_2$(t) (green curve, left side) for the system shown in Figure 53 and calculation of the entropy of the system shown in Figure 53 according to eq. 110 at 10.000 K (red curve, right side), 300 K (green curve, right side), 100 K (yellow curve, right side), 70 K (light blue curve, right side), 30 K (dark blue curve, right side) and 1 K (magenta curve, right side)

As expected for the high temperature limit the entropy rises monotonously to the maximum that is reached with the equilibrium of the system (Figure 54, right side, red curve for 10.000 K).

The situation is different at lower temperatures. At room temperature (Figure 54, right side, green curve for 300 K) the system entropy reaches the maximum in the time scale near to the inverse transition probability (about 2 ps) fast but decays afterwards to a somewhat lower level.

For very low temperatures the entropy calculates to $\lim_{T \to 0} S(t \to \infty) \to 0$. The difference of the maximal entropy $S^{\max}$ and the entropy $S(t \to \infty) := S^{\inf}$ in dependency on the temperature is shown in Figure 55, left side. While this difference is rather low at physiological temperatures the relaxation to the thermal equilibrium leads to a strong reduction of the system entropy in comparison to $S^{\max}$ at lower temperatures. The system generally goes through an entropy maximum and afterwards the entropy decays significantly to $S^{\inf} < S^{\max}$ if $k_B T < \Delta E$. Therefore a local entropy maximum is observed if $\Delta E > k_B T$.

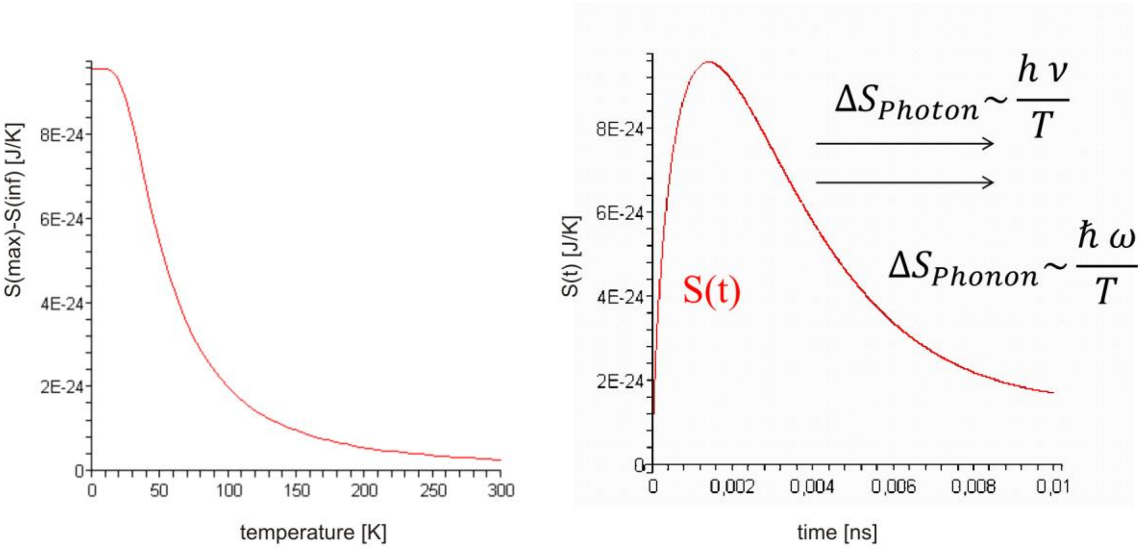

Figure 55 left side: Temperature dependent difference of the maximal entropy $S^{max} = k_B \ln 2$ and the entropy after full relaxation S^{inf} calculated for the system shown in Figure 53; right side: schematic cartoon how photons and phonons transfer entropy to the local environment during relaxation of the system shown in Figure 53.

At first glance the local maximum of the entropy function at temperatures $\Delta E > k_B T$ might look as if the system given in Figure 53 could violate the 2nd law of thermodynamics. But such a violation is surely not the case. In fact it should be kept in mind that a relaxation of the pure isolated system as given in Figure 53 could not occur if there would not exist surrounding states that are able to dissipate ΔE.

The environment effectively takes up the value $\frac{1}{1+e^{-\frac{\Delta E}{k_B T}}}\Delta E$ during the dissipation process which leads to a rise of the environmental entropy that is bigger than the reduction of the isolated system´s entropy during the transition $S^{max} \rightarrow S^{inf}$. This preserves the 2nd law of thermodynamics and it becomes clear that the system complexity could never rise if a system would not be able to interact with its environment.

There is no violation of the laws of thermodynamics. Jennings mentioned that if we analyse a photosynthetic system from the lowest energy limit, we could observe a violation of the 2nd law of thermodynamics [232, 233, 234].

This might be true for a single photon of 680 nm wavelength that is absorbed by a plant and drives a single quantum process in the photosynthetic nanomachine.

But this is neither the continuos reality of a growing plant nor is it a process that is forbidden due to the thermodynamic laws as long as it counts for a single absorbed photon only which can violate the 2nd law of thermodynamics according to the Jarzynski equality which denotes the probability for a trajectory violating the 2nd law of thermodynamics similar to eq. 59 (see e.g. ref. [240] and references therein for details). The 2nd law of thermodynamics is a pure statistic interpretation of ensembles. It is not a law that can be applied to a single quantum process. As denoted by the Jarzynski equality a single molecular process is allowed to violate the 2nd law of thermodynamics in a transient way. In the time- or the ensemble average the laws of thermodynamics hold.

The calculation of the entropy as given in eq. 110 for the nonequilibrium ensemble enables a suggestion of a nonequilibrium partition function that would enable the calculation of all thermodynamic variables for a full nonequilibrium situation in systems that can be generally described by excited state probabilities. With eq. 111 all the nonequlibrium obersvables of the ensemble like the time dependent temperature T(t), the time dependent Gibbs energy G(t) etc… can be calculated. However, we used the denotation of the entropy as given in the eq. 109 that is only valid for the equilibrium. To achieve an nonequilibrium situation the expectation value $\langle E\rangle(t)$ of the energy and the "momentary" temperature T(t) would have to be treated time dependently:

111.

$$
\begin{aligned}
S(t) &= -k_B \sum_i p_i(t)\ln p_i(t) = k_B \ln Z(t) + \frac{\langle E\rangle(t)}{T(t)} \\
Z(t) &= \exp\left(-\sum_i p_i(t)\ln p_i(t) - \frac{\langle E\rangle(t)}{k_B T(t)}\right) = \exp\left(-\frac{\langle E\rangle(t)}{k_B T(t)}\right)\prod_i \exp\left(-p_i(t)\ln p_i(t)\right) \\
Z(t) &= \exp\left(-\frac{\langle E\rangle(t)}{k_B T(t)}\right)\prod_i \exp\left(\ln\left(p_i(t)^{-p_i(t)}\right)\right) \\
Z(t) &= \exp\left(-\frac{\langle E\rangle(t)}{k_B T(t)}\right)\prod_i \frac{1}{p_i(t)^{p_i(t)}}
\end{aligned}
$$

4 EXCITED STATE DYNAMICS IN WSCP

Water soluble chlorophyll binding proteins (WSCP) are special pigment-protein complexes (for a review article see [48]). Compared to all antenna complexes and RCs the WSCPs are characterized by unique properties:

i) each polypeptide subunit binds no more than one chlorophyll molecule,

ii) the size of each WSCP subunit of about 20 kDa [196] is comparable with the size of LHCII and related members of the LHC family of antenna complexes of plants which bind several pigments per subunit (for reviews see [73], [78]) and

iii) two chlorophylls in the tetramer are excitonically coupled. Therefore WSCP is a most suitable model system for detailed studies on pigment-pigment and pigment-protein interactions in chlorophyll containing proteins (see chap. 1.5.).

WSCPs are the only Chl binding proteins known so far that do not contain carotenoids (Cars) [68]. Despite the lack of carotenoids (Cars) the photodegradation of Chl bound to WSCP is highly reduced in comparison to Chl in solution. This property is of high interest for the construction of switch-able photosensitizers if it is possible to destabilize the protein structure by an external stimulus (e.g. light). In this case the light induced generation of reactive oxygen species (ROS) might be switch-able, i.e. activatable, by switching off the protein barrier that prevents the Chl triplets from interaction with ground state triplet oxygen. The scientific results that led to the conclusion of the existence of such a protein barrier are shortly outlined in the following (for detailed description of the conclusions drawn from TWCSPC studies see [47] and [48]). The impact of these findings might help to construct a switch-able protein as an advanced drug delivery vehicle e.g. in applying WSCP in the photodynamic therapy (PDT). One main aim of the spectroscopic studies on WSCP was to clarify the mechanisms of the suppressed reaction of Chl bound to WSCP with the surrounding environment.

4.1 The electronic structure of Chl dimers bound to class IIa WSCP

Spectroscopic studies were performed to investigate pigment-pigment and pigment-protein interactions of Chl *a* and Chl *b* bound to the recombinant protein of class II WSCP from cauliflower. In this complex two Chls form a strongly excitonically coupled open sandwich dimer within the tetrameric protein matrix (see chap 1.5, Figure 27 and Figure 56). In marked contrast to the mode of excitonic coupling of Chl and BChl molecules in light harvesting complexes and reaction centers of all photosynthetic organisms, the unique structural pigment array in the Chl dimer of WSCP gives rise to an upper excitonic state with a large oscillator strength of the transition dipole moment (see Figure 56).

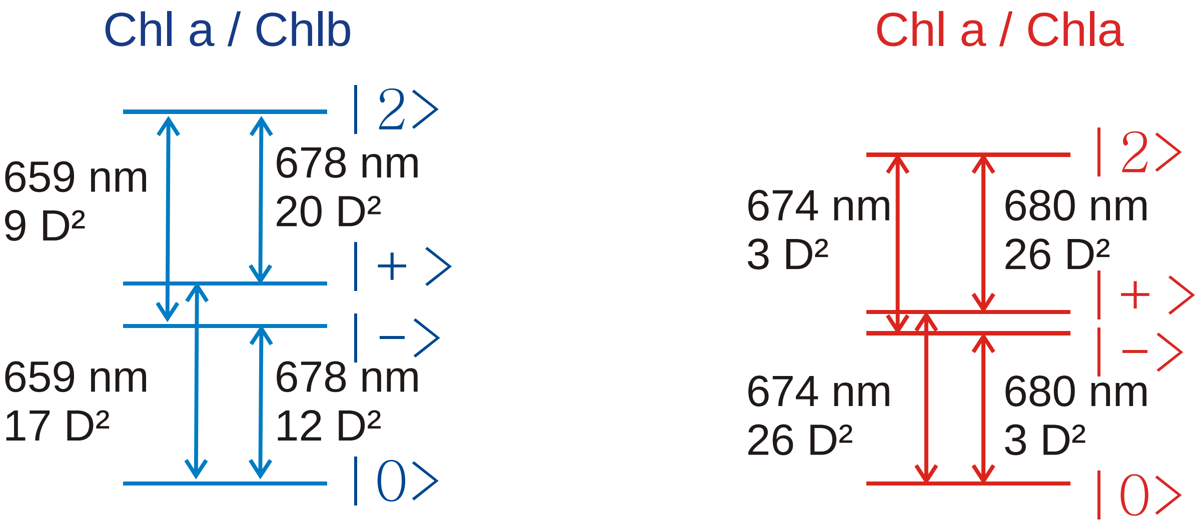

Figure 56: Excitonic splitting in Chl*a*/Chl*b* heterodimers (left side, blue) and Chl*a*/Chl*a* homodimers (right side, red) bound to WSCP as published in ref. [46]. The excitonic splitting is calculated for the monexcitonic states $\left|+\right\rangle$ and $\left|-\right\rangle$ of the upper and the lower excitonic level, respectively.

Figure 56 shows the ground state $\left|0\right\rangle$ and the biexcitonic state $\left|2\right\rangle$ and in addition the excitonically splitted monoexcitonic states $\left|+\right\rangle$ (upper excitonic level) and $\left|-\right\rangle$ (lower excitonic level) of WSCP containing a Chl*a*/Chl*b* heterodimer (Figure 56, left side) and a Chl*a*/Chl*a* homodimer (Chl *a* only WSCP) (Figure 56, right side). The arrows indicate the electronic transitions which are characterised by the strength of the transition dipole moments (in D^2) and the corresponding wavelengths. As pointed out in [46] the excitonic splitting of the single excitonic state in the Chl dimer can be analysed with ground state absorption and circular dicroism spectra. Additionally hole burning spectroscopic studies revealed the excitonic splitting [48, 49]. Elaborated theoretical analysis of the problem lead to a well agreement between the experimental data (see [46, 69]) and the calculated structure (see [38]) which closely resembles the structureal scheme of the Chl molecules obtained at virtually the same time by Horigome et al [70] for the 2.0 A resolution X ray crystallography structure of class IIb WSCP of *Lepidum virginicum* Chls (as mentioned in chap. 1.5).

Theoretical calculations predicted the time of exciton relaxation from the upper $\left|+\right\rangle$ to the lower $\left|-\right\rangle$ level to be about 80 fs in homo-dimers and 450 fs in hetero-dimers, when using a modified Redfield theory that takes into account strong exciton-phonon coupling, respectively [38]. An elaborated review of different calculations of the exciton relaxation and the fs absorption spectroscopic results together with proposed models for strongy and weakly coupled Chl dimers in WSCP [46] is found in ref. [48].

Laser flash induced transient absorption changes measured by C. Theiss [46] were monitored with a time resolution of 200 fs. Therefore the predicted exciton relaxation kinetics in Chl *a*/Chl *b* heterodimers are expected to be resolved. On the other hand, the expected corresponding kinetics in homo-dimers cannot be quantitatively resolved at a time limitation of 200 fs. But there exist qualitative hints for the expected behaviour (see [46]).

The transient difference absorption spectra at different delay times t_d between the pump pulse (460 nm, in the Soret band of Chl *b*) and the probe pulse that were monitored in WSCP with a stoichiometric Chl *a*:Chl *b* ratio of 2.6:1 exhibit a pronounced band with a peak at around 660 nm in the Chl *b* spectral region. This band is assigned to the population of the upper excitonic level $\left|+\right\rangle$ of strongly coupled heterodimers (see Figure 56). At longer delay times the extent of bleaching of this state decreases concomitantly with a progressing increase of the bleaching around 680 nm which is assigned to the lower excitonic level $\left|-\right\rangle$ in agreement with Figure 56. This band bleaching approaches a maximum value at $t_d = 0.9$ ps and a peak maximum at 679 nm. In the time domain of $t_d > 1$ ps the absorption maximum shifts back to shorter wavelengths and a virtually constant peak position at 675 nm is reached after a delay time of about 10 ps concomitant with shoulders of the bleaching at around 660 nm and 680 nm.

In agreement with the shift of the bleaching maximum the recovery of the bleaching at 660 nm band ($\left|+\right\rangle$) can be satisfactorily described by a biphasic kinetics with time constants of 400 fs and 7-8 ps after temporal deconvolution of the data [46]. The 400 fs kinetics are in close agreement with the time constant of 450 fs calculated for the relaxation from the upper to the lower exciton state in a strongly coupled Chl *a*/Chl *b* hetero-dimer when using the modified Redfield theory [38].

The 400 fs kinetics is therefore ascribed to exciton relaxation of strongly coupled Chl *a*/Chl *b* hetero-dimers. This finding is an illustrative example of the potential of class IIa WSCP as a model system for detailed theoretical studies on pigment-pigment interactions in Chl binding proteins that can be clearly ascribed to experimental data gathered from this system.

Questions arise on the origin of the 7-8 ps kinetics. Among possible interpretations (see [48]) the most convincing explanation for the 7-8 ps kinetics implies the existence of Chl *a*/Chl *b* dimers that are weakly coupled due to a larger separation of the Chl moieties. This idea comprises a putative sample heterogeneity within an ensemble of reconstituted recombinant tetrameric class IIa WSCP complexes containing Chl *a*/Chl *b* dimers with a different pigment array as is shown in [46] and [48]. Another possibility for the apparent 7-8 ps time constant could be a characteristic conformational change of the protein that occurs with such 7-8 ps time constant at room temperature (see below).

4.2 Fluorescence spectroscopic studies on WSCP

The data of transient absorption spectroscopy do not allow an analyse of the fate of the excited electron after equilibration among the excitonic states, i.e. the lifetime of excited states on the ns time scale as it is necessary to understand the possible mechanism that prevents the interaction between Chl and environmental oxygen. Therefore detailed time integrated and time resolved fluorescence spectroscopic studies were performed with the experimental setup described in chap. 2.

4.2.1 Time integrated fluorescence spectra at room temperature

Figure 57 shows the published [47] normalized fluorescence spectra of Chl *a* only WSCP (top panel) and Chl *b* only WSCP (bottom panel), respectively, measured at room temperature under excitation with 632 nm pulses in samples containing 50 % glycerol.

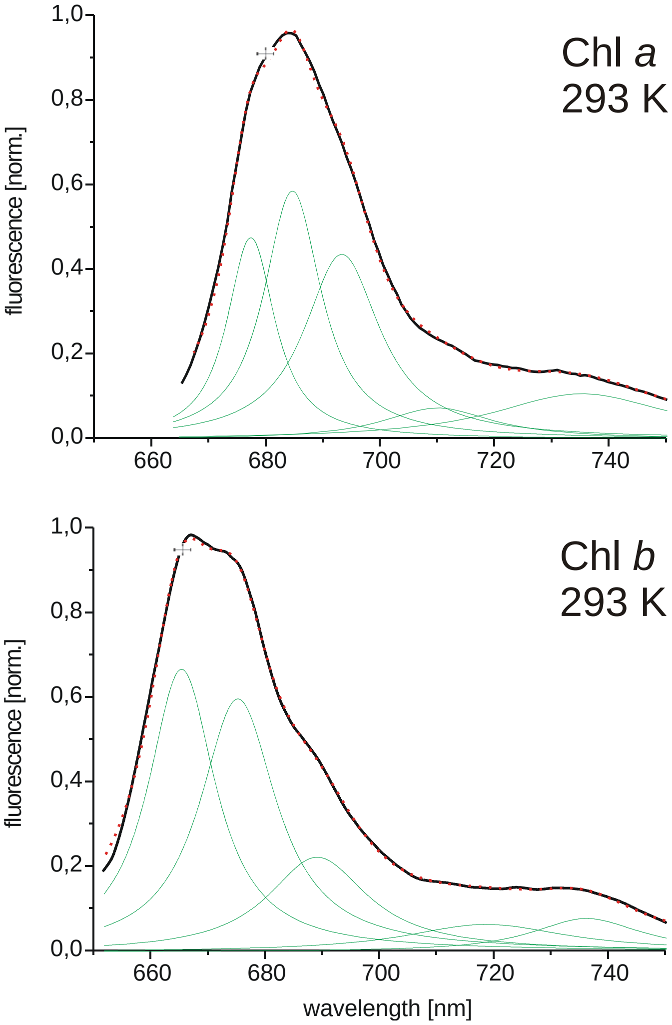

Figure 57: Normalized fluorescence spectra of WSCP containing Chl *a* only (top panel) or Chl *b* only (bottom panel) at room temperature. Deconvolution into Lorentzians (green curves) was performed in frequency domain and the curves were rescaled to the wavelength region (the sum of all subbands is represented by the red dotted curve). The crosses positioned near the emission maxima indicate the standard deviation of the wavelength positions of the integrated fluorescence spectrum. (Figure taken from ref [47]).

In both cases (Chl *a* only and Chl *b* only) broad spectra are obtained that can be deconvoluted into three main bands of Lorentzian shape with maxima at 677 nm, 684 nm and 693 nm (+/- 2 nm) in the case of Chl *a* only WSCP, and at 665 nm, 675 nm and 689 nm (+/- 2 nm) for Chl *b* only WSCP. In addition, minor bands are obtained in the long wavelength region that probably originate from vibrational transitions in the Qy emission spectrum. The use of Lorentzian lineshapes appears to be justified by the fact that electron-phonon coupling leads to a symmetric, non-Gaussian tailing of the absorption and corresponding fluorescence bands of pigments embedded into amorphous protein matrices with thermal occupation of vibrational energy levels at elevated temperatures, as shown previously for the antenna complex LHCII [241], [242]. Furthermore, a theoretical analysis revealed that at room temperature lifetime broadening of the optical bands becomes important [38].

In agreement with the energetic levels of the excitonically splitted first excited state $\left|+\right\rangle$ (674 nm in absorption) and $\left|-\right\rangle$ (680 nm in absorption) (see Figure 56) the two Lorentzian emission bands at 677 nm and 684 nm of Chl *a* only WSCP are ascribed to the emission from the upper ($\left|+\right\rangle$) and lower ($\left|-\right\rangle$) excitonic level, respectively. The emission band at 693 nm seems to be related with a phonon transition in the surrounding protein structure (see below, cryostatic measurements).

The fluorescence emission bands at 665 nm and 675 nm in Chl *b* only WSCP are accordingly ascribed to $\left|+\right\rangle$ and $\left|-\right\rangle$, respectively, in the Chl *b* homodimer, while the 689 nm band is ascribed to a phonon sideband in Chl *b* only WSCP.

The normalized time-integrated emission spectra of Chl *a* only and Chl *b* only WSCP presented in Figure 57 were obtained under excitation with 632 nm pulses. The shape should be independent of the excitation wavelength, since the equilibration of excited state populations is much faster than the decay due to intersystem crossing, internal conversion and fluorescence.

However, an analogous feature is not necessarily expected for WSCP samples that are reconstituted with mixtures of Chl *a* and Chl *b* because in that case the sample ensemble contains different populations of Chl *a* and Chl *b* homodimers and Chl *a*/Chl *b* heterodimers. The calculations presented in ref. 46 for Chl *a*/ Chl *b* heterodimers (see Figure 56, left side) can not be investigated experimentally in a straightforward manner because a WSCP sample containing only Chl *a*/ Chl *b* heterodimers is not available. Only samples containing both Chl *a*/ Chl *b* heterodimers and homodimers, that should be formed statistically during the reconstitution process, were available. It would, of course, be very interesting to perform time resolved single complex spectroscopy.

For measurements on the ensemble different excitation wavelengths were used to excite preferentially Chl *a* or Chl *b*. Measurements were performed on WSCP containing Chl *a*:Chl *b* at a ratio of 4.2:1 where the sample is preferentially excited in the Soret band of either Chl *a* with 430 nm wavelength or Chl *b* with 460 nm wavelength. The absorption spectra of WSCP containing different amounts of Chl *a*/ Chl *b* heterodimers are shown in Figure 28 (see chap. 1.5). Comparing the spectra of WSCP containing Chl *a*:Chl *b* at a ratio of 4.2:1 with WSCP containing Chl *a*:Chl *b* at a ratio of 2.6:1 it becomes clear that the 460 nm absorption peak is related to the absorption of Chl *a*/ Chl *b* heterodimers.

The results obtained are shown in Figure 58 and compared with the spectra taken from Figure 57 for Chl *a* only (dashed curve) or Chl *b* only (dot dashed curve) WSCP.

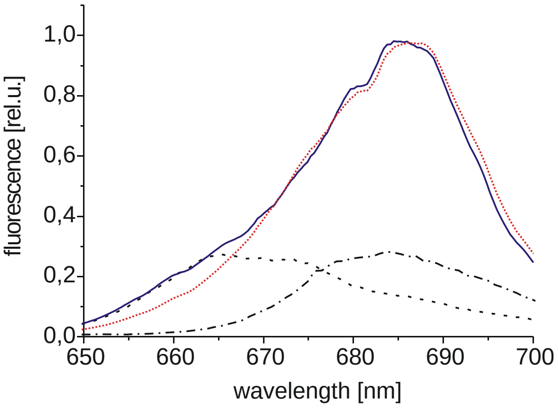

Figure 58: Normalized spectra of the integrated fluorescence F(λ) at room temperature of WSCP containing Chl *a* and Chl *b* at a ratio of 4.2:1; excitation wavelength: 430 nm (red, dotted curve) and 460 nm (blue, full-lined curve). The experimental spectra of Chl *a* only (dot dashed curve) or Chl *b* only (dashed curve) of Figure 57 are depicted for comparison. The figure was published in ref. [47].

Inspection of this data reveals that the emission in the region of Chl *b* (650 - 670 nm) is more pronounced under 460 nm illumination (blue full-lined curve) while less fluorescence is emitted at 650 – 670 nm when the samples are excited at 430 nm (red dotted curve). After excitation with 460 nm laser wavelength additional fluorescence occurs at 660 nm in well agreement with the energy of the upper excitonic level $|+\rangle$ in heterodimers (see Figure 56).

These features qualitatively reflect the existence of both Chl *a*/Chl *a* homo- and Chl *a*/Chl *b* heterodimers together with minor fractions of Chl *b*/Chl *b* homodimers within the overall assembly of WSCP complexes and the results of this two-color experiments show that in the ensemble the Chl *a*/Chl *b* heterodimers are characterized by an additional emission state at about 660 nm.

As the thermal equilibration between the two exciton states is faster than 1 ps in the strongly coupled and still faster than 8 ps in potentially weakly coupled heterodimers (see below and Ref. [46]), the spectral shape of the heterodimer emission is expected to depend only slightly on the excitation wavelength. On the contrary, at 430 nm the Chl *a*/Chl *a* homodimers and Chl *a*/Chl *b* heterodimers are preferentially excited while at 460 nm excitation the Chl *a*/Chl *a* homodimers are less preferentially excited.

Therefore after excitation with 460 nm the contribution of Chl *a*/Chl *b* heterodimers (and additionally possible small amounts of Chl *b*/Chl *b* homodimers) to the overall emission is relatively larger than after excitation with 430 nm because in the latter case preferentially the fraction of Chl *a*/Chl *a* homodimers is excited.

From the pure statistical point of view we expect that in the sample containing Chl *a*:Chl *b* at a ratio of 4.2:1 about 65 % of all complexes should contain Chl *a* homodimers, 31 % should contain Chl *a*/Chl *b* heterodimers and 4 % Chl *b*/Chl *b* homodimers. The strong increase of the emission at 660 nm after excitation with 460 nm in comparison to 430 nm can not be explained by the contribution of Chl *b*/Chl *b* homodimers only (see also cryostatic measurements below). With 460 nm excitation wavelength the properties of the Chl *a*/Chl *b* heterodimers become more clearly visible and this is mainly the observation of emission found at 660 nm ascribed to the upper excitonic level $\left|+\right\rangle$ in heterodimers which is not found in Chl *a*/Chl *a* homodimers.

4.2.2 Time integrated fluorescence spectra at cryostatic temperatures

The distribution of the excitation energy between the excitonic states is expected to occur according to the Boltzmann statistics and therefore the fluorescence spectrum to be strongly temperature dependent. To check for this effect the fluorescence spectra of WSCP were measured in the wide range between room temperature and 10 Kelvin.

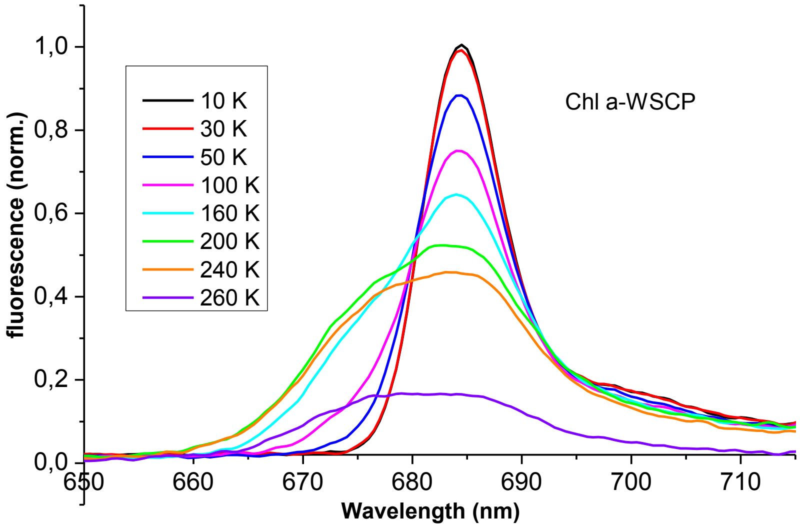

Figure 59: Temperature dependent fluorescence spectra of WSCP containing Chl *a* only homodimers in the temperature range between 10 K (black curve) and 260 K (violet curve) after excitation with 632 nm laser wavelength. The spectra are not normalized.

Figure 59 shows the temperature dependent fluorescence spectra of Chl *a* homodimers bound to WSCP after excitation with 632 nm. The fluorescence measurements were performed in the mode of reflection spectroscopy. Therefore the signal quality is strongly enhanced after freezing of the sample in phosphate containing buffer (< 260 K) while the spectra at 260 K and higher temperatures (data not shown) exhibit strongly reduced amplitudes due to lower reflectivity of the sample.

A comparison of the data of the temperature dependent fluorescence spectra at 240 K (orange curve in Figure 59) and 10 K (black curve in Figure 59) reveals that the emission band which was fit to 677 nm (see Figure 57) decreases with lower temperatures until it completely vanishes at temperature < 50 K as it would be expected from the Boltzmann statistics for the population of the upper excitonic level ($\left|+\right\rangle$). Concomitantly the amplitude of the 684 nm emission band increases in amplitude at lower temperatures. The overall emission is only slightly changing with temperature (evaluation of data not shown). This is an additional strong indicative that the 677 nm emission band of Chl *a*/ Chl *a* homodimers is related to the absorption maximum of the $\left|+\right\rangle$ excitonic level with an absorption maximum at 674 nm (see Figure 56) and the population of this emission band completely vanishes at low temperatures so that only the fluorescence at 684 nm from the $\left|-\right\rangle$ level is observed (680 nm in absorption, see Figure 56).

In addition to the emission from the states $\left|+\right\rangle$ and $\left|-\right\rangle$ a series of long wavelength bands exists that are clearly seen in the 10 K emission spectra shown in Figure 60. Some of these transitions are known to be characteristical vibrationally coupled transitions found in pure chlorophyll molecules. But in WSCP the structure of these sidebands is more complex.

The 10 K fluorescence spectra of all available WSCP samples are shown in Figure 60 in the whole spectral range. As expected, the shape of the bands is significantly sharpened in comparison to the room temperature spectra shown in Figure 57 especially because there is no more emission from the higher excitonic level $\left|+\right\rangle$. Especially the spectra of WSCP containing Chl *a* / Chl *b* heterodimers (Figure 60, panel C and panel D) do not exhibit significant fluorescence at 665 - 670 nm. Only in the sample with a Chl *a*:Chl *b* ratio of 2.6:1 there is a rather weak fluorescence visible at 670 (+/- 3) nm (Figure 60, panel D). The main emission is located at 685 nm.

Based on these findings a significant amount of uncoupled Chl *b* or Chl *b* homodimers with fluorescence peaking at 668 nm (see Figure 60, panel B) can be ruled out in WSCP containing Chl *a*:Chl *b* at a ratio of 2.6. For WSCP containing Chl *a*: Chl *b* with a ratio of 4.2 the emission spectra show that the contribution of uncoupled Chl *b* or Chl *b* homodimers is < 1%.

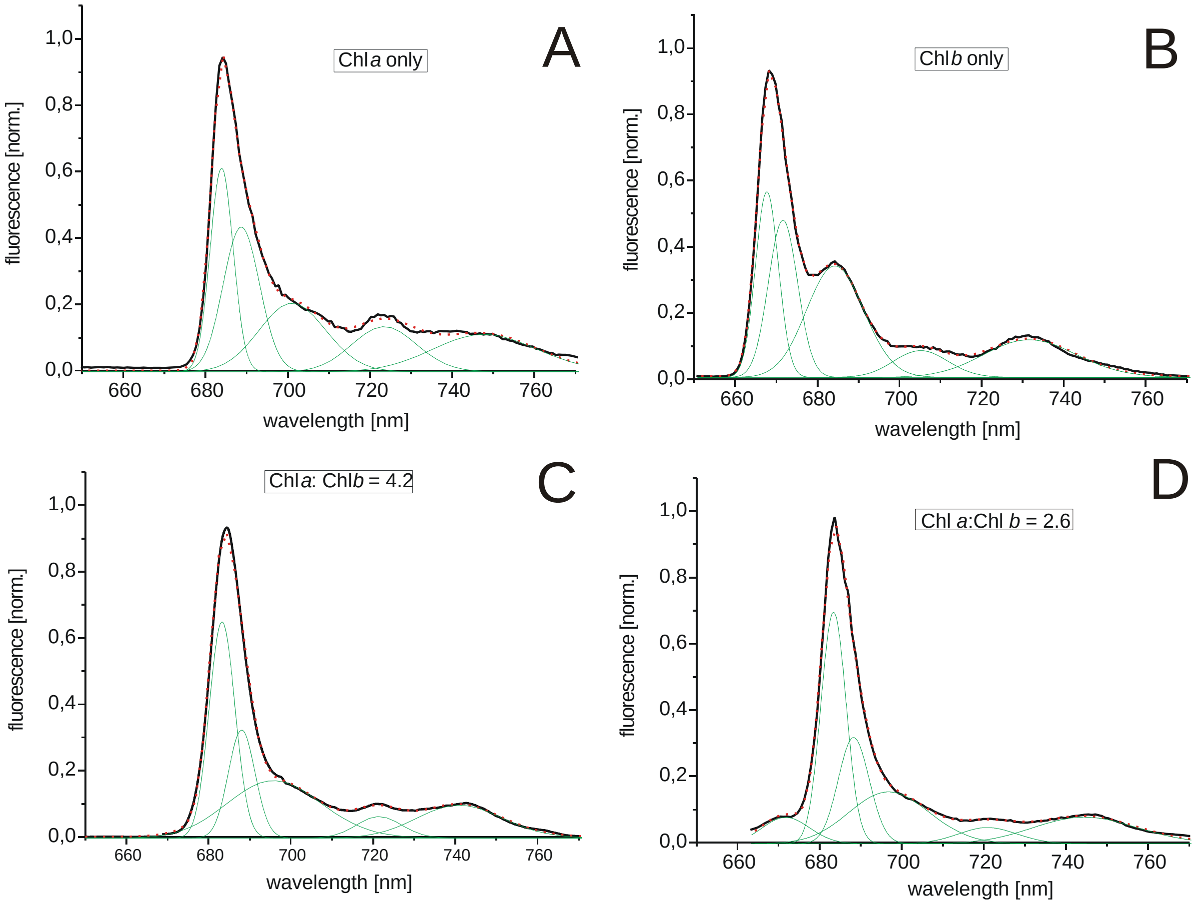

Figure 60: Gaussian fits of the normalized emission spectra of WSCP samples containing Chl *a* only (A), Chl *b* only (B) and Chl *a*:Chl *b* at ratios of 4.2:1 (C) and 2.6:1 (D) at 10 Kelvin. The dotted curves show the sum of all Gaussian bands in comparison to the measured fluorescence (full-line curves). Fits were performed in the frequency domain and the data rescaled to the wavelength domain.

A value of < 1 % Chl *b*/ Chl *b* homodimers in WSCP containing Chl *a*:Chl *b* at a ratio of 4.2:1 is clearly smaller than it is expected from simple statistical considerations that result in 3.7 % Chl *b*/ Chl *b* homodimers. For WSCP containing Chl *a*:Chl *b* at a ratio of 2.6:1 this value should be about 8 %. Therefore the low temperature measurements show that there is a reduced probability for the formation of Chl *b*/ Chl *b* homodimers in WSCP. The reason for this pheonomenon could be a reduced affinity of the protein to Chl *b* in comparison to Chl *a* as it was found by Satoh et al. for certain forms of WSCP [67] or mentioned by Theiss et al. [46].

The emission bands at 10 K presented in Figure 60 are well fit by a sum of Gaussians. The use of Gaussian functions in the fit of low temperature spectra in contrast to that of Lorentzian functions at room temperature takes into account that at low temperatures the spectra are more likely dominated by inhomogeneous broadening. In the wavelength region < 700 nm the main emission bands at 668 nm of WSCP containing Chl *b* only (Figure 60 B) and at 685 nm of WSCP containing Chl *a* only (Figure 60 A) or Chl *a* and Chl *b* at ratios of 4.2:1 (Figure 60 C) and 2.6:1 (Figure 60 D)) are shown to be the composite of two sharp Gaussians.

It is somewhat unexpected that the main emission band is composed by two emission bands at 10 K. According to the Boltzmann equilibrium the population probability of the higher exciton state at 10 K is < 10^{-5} (the difference between the upper and lower exciton states is of the order of 150 cm^{-1} in homodimers and 400 cm^{-1} in heterodimers (see Figure 56 and refs. [37, 38, 46]). Therefore, at 10 K the detected emission should originate exclusively from the lowest exciton state in all WSCP samples.

As mentioned above there might exist possible subpopulations of strongly and weakly coupled dimers in WSCP [46] which could explain the existence of several subbands. Since the spectral absorption properties of our WSCP samples were found to be dominated by the strongly coupled dimers [46] it appears most reasonable to assign the major band in the deconvoluted 10 K emission spectra to the lower excitonic state of this pigment array.

The slightly red-shifted Gaussian could indicate heterogeneity (e.g. due to two types of Chl dimers in WSCP, strongly and weakly coupled ones as suggested according to the results of absorption spectroscopy in ref. [46]). Possibly this band can be explained by a heterogeneity in the protein conformation or a conformational transition of the protein. This assumption is supported by the time resolved analysis of the WSCP fluorescence dynamics (see below).

Questions also arise as to the origin of the minor bands observed at 685 nm for Chl *b* homodimers and at around 692 – 702 nm for the other complexes. These bands with markedly larger FWHM values can most probably be assigned to vibrational bands.

The situation is even more complex for WSCP containing Chl *a* and Chl *b* because in this case the ensembles contain complexes with homo- and heterodimers with very similar bands in the Chl *a* region. We therefore refrain from any speculative discussion on possible band assignment of hetrodimers.

A closer inspection of the vibronic side bands of Chl *a*/ Chl *a* homodimers bound to WSCP (see Figure 61) shows that next to the 700 nm sideband there exist minor contributions at 720 nm, 745 nm and a band at 760 nm that was not resolved in the room temperature spectrum shown in Figure 57 and the 10 K spectrum shown in Figure 60. The spectra shown in Figure 61 were monitored by using the USB fluorometer system of StellarNet (EPP2000) which has high sensitivity also in the NIR region up to 860 nm.

This was not the case for measurements depicted in Figure 60 where the spectra were taken with the time resolved Delay line measurement setup (as described in chap. 2) and subsequently integrated along the time axis. The Delay Line exhibits a lower sensitivity at 760 nm than at 680 nm and therefore the spectral correction which was done with a thermal reference spectrum of a filament lamp leads to a loss of spectral resolution in the NIR. This problem does not exist when using the USB spectrometer setup (3 nm spectral resolution) used for the results shown in Figure 61 and Figure 62.

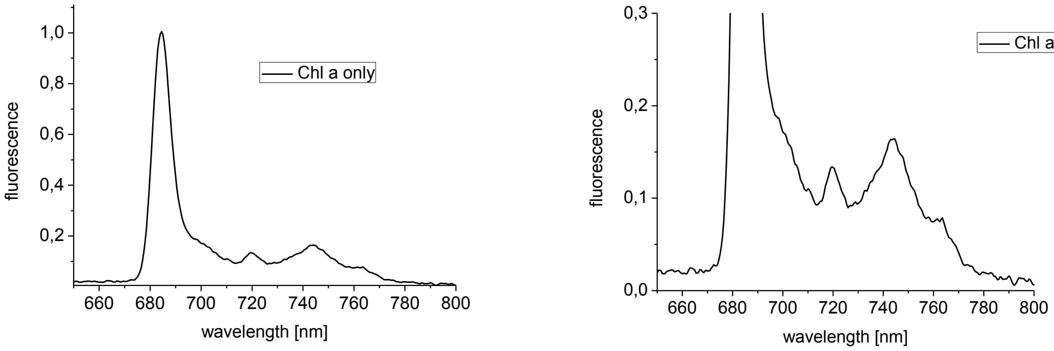

Figure 61: Normalized spectra of integrated fluorescence emission at 10 K of Chl *a* only WSCP in buffer containing 50 % glycerol. The phonon sidebands are shown in magnification on the right side.

The spectra of Chl *b* containing homodimers (Figure 62) exhibit similar vibronic sidebands as Chl *a* homodimers (Figure 61) at 684 nm, 704 nm and 730 nm in agreement with the measurements shown in Figure 60 and the additional red shifted band at 740 nm that was not resolved in Figure 60.

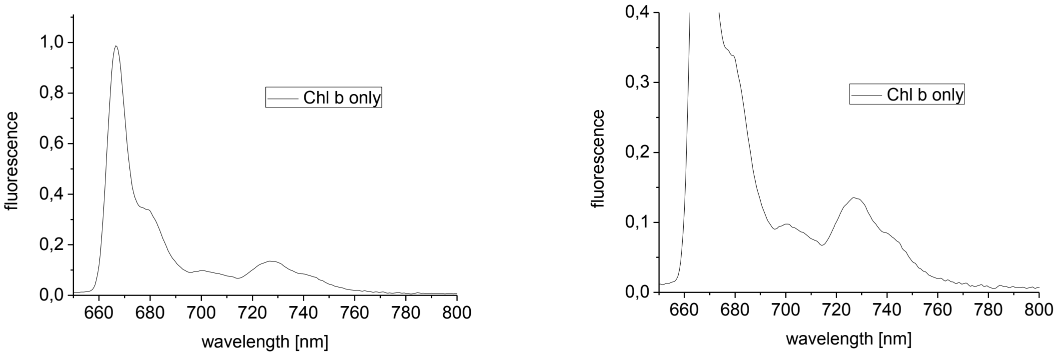

Figure 62: Normalized spectra of integrated fluorescence emission at 10 K of Chl *b* only WSCP in buffer containing 50 % glycerol. The vibronic sidebands are shown in magnification on the right side.

A comparison of the spectra of the vibronic sidebands of Chl *a* homodimers and Chl *b* homodimers reveals that the energetic position of the phonon associated transitions relatively to the zero phonon line are comparable in Chl *a* and Chl *b* but they differ strongly in amplitude (see Figure 63).

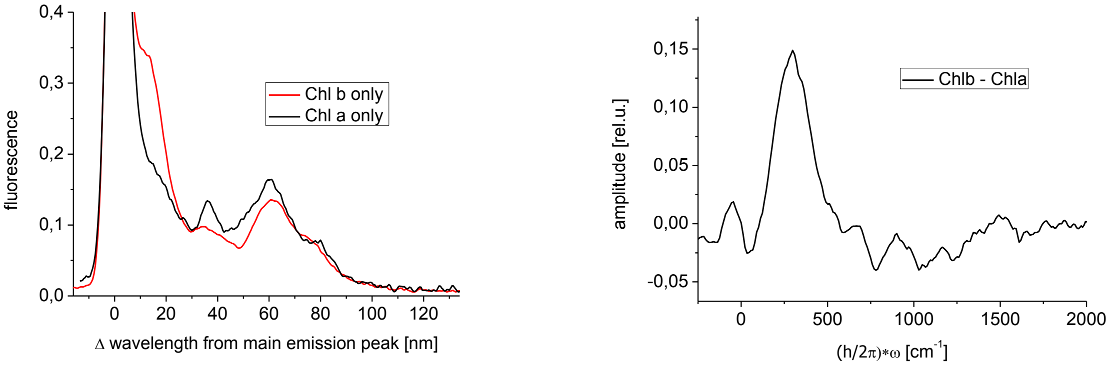

Figure 63 Left side: Vibronic sidebands of the fluorescence of Chl *b* only WSCP (red curve) and Chl *a* only WSCP (black curve) in direct comparison. The main emission (Qy-transition) of Chl *a* only WSCP and Chl *b* only WSCP are located at the same position. At the right side the difference spectrum of Chl *b* homodimers (red curve) and Chl *a* homodimers (black curve from left side) is shown in the frequency domain.

In Figure 63 a direct comparison of the spectrum of Chl *a* only WSCP and Chl *b* only WSCP is shown. At the right side Figure 63 displays the difference between the spectra of Chl *b* only WSCP and Chl *a* only WSCP after positioning to the same emission maximum (of the Qy-transition).

At 10 K the Qy transition emitting from the lower excitonic state $\left|-\right\rangle$ is found at 684.5 nm for Chl *a* homodimers and at 666.5 nm for Chl *b* containing WSCP (see Figure 61 and Figure 62). The sideband occurring at 684 nm in Chl *b* only WSCP and about 703 nm in Chl *a* only WSCP ($\Delta\lambda$ =18 nm) therefore corresponds to a vibration with an energy of 350 – 400 cm^{-1}. In Figure 63, right side, the strong difference of the amplitude of this transition in Chl *b* only WSCP in comparison to Chl *a* only WSCP is clearly visible. The additional phonon sidebands with peak at about 700-750 cm^{-1} and 1200-1250 cm^{-1} corresponding to the sidebands at 701 nm ($\Delta\lambda$=35 nm) and 726 nm ($\Delta\lambda$=60) in Chl *b* WSCP and 720 nm ($\Delta\lambda$=35 nm) and 745 nm ($\Delta\lambda$=60) in Chl *a* WSCP are slightly stronger in Chl *a* WSCP than in Chl *b* WSCP. A sideband of equal strength is found at 741 nm ($\Delta\lambda$=75 nm) in Chl *b* WSCP and 760 nm ($\Delta\lambda$=75 nm) in Chl *a* WSCP

4.2.3 Lifetimes of excited singlet states in homo- and hetero-dimers of class IIa WSCP

As mentioned above WSCPs are lacking carotenoids (Cars) which are essential constituents of all antenna complexes and reaction centers protecting Chls in pigment-protein complexes from degradative attack by reactive singlet oxygen formed via a reaction which is sensitized by Chl triplets (for reviews, see [73, 78], see also ref. [76]).

In spite of lacking Cars the binding of Chl to WSCPs gives rise to a surprisingly high stability compared to that of Chl in solution [68]. Basically three different underlying mechanisms could be responsible for this striking phenomenon: a) efficient kinetic competition with intersystem crossing (ISC) by drastic shortening of the lifetime of the lowest excited singlet state, thereby diminishing the probability of triplet state (^{3}Chl) population and subsequent sensitized formation of singlet oxygen which is responsible for destructive reactions, b) suppression of the sensitized reaction by strong acceleration of the ^{3}Chl decay, or c) shielding of the bound Chls from interaction with ground state triplet oxygen by an efficient diffusion barrier built by the protein matrix.

In order to clarify this point, detailed studies were performed on the lifetime of excited singlet states of Chl bound to WSCP.

Experiments were performed in the wide range of temperatures from 10 K to 295 K. Samples suspended in buffer solutions containing 50 % glycerol or either sucrose or imidazole exhibit virtually monoexponential decay kinetics at room temperature with time constants of 5.2 ns for samples containing Chl *a* only or Chl *a*:Chl *b* mixtures and of 4.8 ns for Chl *b* only WSCP (data not shown, for details see [47]). Additionally there might exist fast relaxation kinetics with time constants of 20 ps for Chl *a* containing WSCP (see Figure 65) and up to 35 ps for Chl *b* containing WSCP (data not shown) which are hard to resolve. At room temperature the main fluorescence decay is dominated by a relaxation kinetics with a time constant of about 5 ns.

This finding readily shows that compared to Chl in solution or detergent micelles [147] the lifetime of the lowest excited singlet state is not changed by the pigment binding to WSCP. At room temperature both excitonic states of the lowest excited singlet state are populated. The relaxation between different excitonic levels which occurs with a time constant of 8 ps or less can not be resolved. It might be responsible for additional fast components found in the spectra. A pure monoexponential kinetics with contribution of very fast components as measured for this system fulfils the expectation.

The lifetime measurements on WSCP unambiguously show that mechanism a) can be definitely ruled out as to be responsible for the significantly enhanced stability of Chl bound to WSCP. The alternative possibility b) of a significant lifetime shortening of ^{3}Chl cannot be entirely excluded. However, this mechanism appears to be highly unlikely because at present no reasonable mechanism is known for this type of ^{3}Chl quenching by Chl-Chl or Chl-protein interactions. Therefore, based on our results and considerations, only one possibility remains to be considered as a reasonable mechanistic explanation for the high stability of Chl bound to the WSCP: The protein matrix establishes a high diffusion barrier to O_2 transport thereby drastically reducing the interaction between Chl and O_2 as suggested by Horigome et al. [70] for class IIb WSCP containing four Chl molecules.

The upper panel (panel a and panel b) of Figure 64 shows typical traces of fluorescence decay curves monitored at 10 K as published in [47]. A semilogarithmic data plot (panel a) reveals that the fluorescence decay kinetics at 10 K are wavelength dependent and not strictly monoexponential for WSCP containing either Chl *b* homo-dimers or samples reconstituted with Chl *a*:Chl *b* mixtures. Furthermore, the Chl *b* only WSCP exhibits discernible rise kinetics (see panel b) with a time constant of 80-120 ps at 10 K. These characteristic kinetics, which are either rising or decaying, dependent on wavelength, are designated as “rise term” in the following description. It was found that at least 3 decay components are required for accurate fits of the decay curves [47].

In order to obtain more detailed information the data were analyzed by deconvolution into decay associated spectra (DAS) as described in chap. 2.2. The panels c) and d) of Figure 64 show the results of global fits of experimental data on WSCP containing either Chl *a*:Chl *b* at a ratio of 2.6:1 (panel c) or Chl *b* only (panel d). The traces were fitted with three time constants: of 6.0 (+/- 0.3) ns, 2.5 (+/- 0.4) ns and 120 (+/- 20) ps (panel c) and 7.0 (+/- 0.3) ns, 3.6 (+/- 0.4) ns and 80 (+/- 20) ps (panel d, for details, see [47]. Inspection of the DAS reveals that the 2-4 ns component exhibits a very small amplitude and a blue shift compared to the main emission. It seems possible that this component is caused by sample heterogeneity but alternative explanations like a very slow conformational change of the protein environment with a time constant of 2-4 ns cannot be fully ruled out even though it seems highly unlikely. The performed simulations support the idea of a sample heterogeneity because the strongly excitonically coupled Chl dimer which is modulated by the protein matrix reveals (see below) only fluorescence components with time constants much faster than 2-4 ns in addition to the main relaxation kinetics.

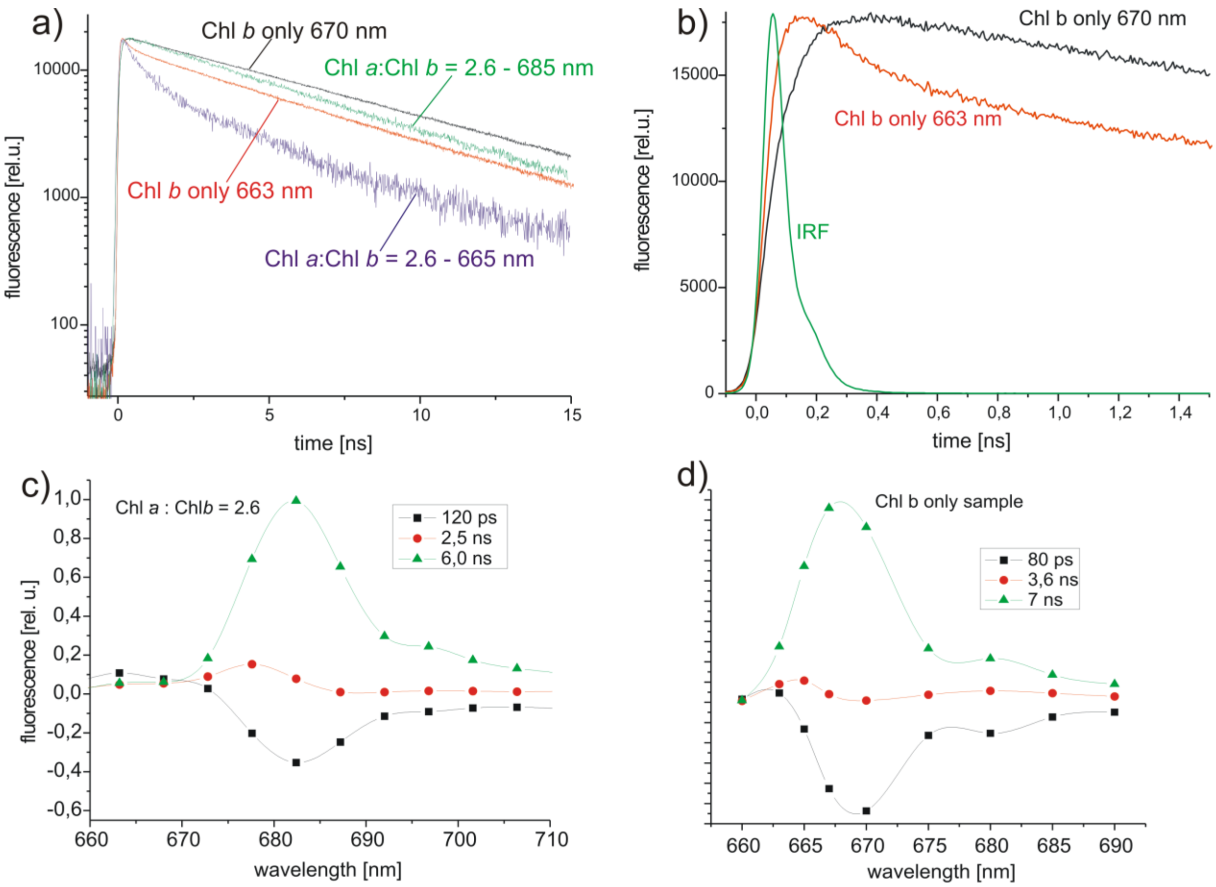

Figure 64 Top: Semilogarithmic plot (panel a) of the fluorescence decay measured at 10 K on WSCP samples containing Chl *b* only (monitored at 663 nm and 668 nm) and WSCP containing Chl *a* and Chl *b* at a ratio of 2.6:1 (monitored at 665 nm and 685 nm); excitation wavelength: 632 nm (the curves are normalized and therefore the S/N ratio is different) and linear plot (panel b) of the fluorescence transients at 663 nm and 668 nm of Chl *b* only WSCP and the instrument response function (IRF).
Bottom: Decay associated spectra (DAS) at 10 K of WSCP samples containing either Chl *a*:Chl *b* at a ratio of 2.6:1 (panel a) or Chl *b* only (panel b) in frozen buffer solution containing 50 % glycerol.
For experimental details, see ref. [47].

The rise term is an unexpected and interesting feature which is observed in all samples analyzed so far and characterized by a temperature dependent amplitude and time constant. In Chl *b*/Chl *b* homodimers the time constant varies from 80 ps at 10 K to 35 ps at room temperature and concomitantly the amplitude decreases at higher temperatures (see ref. [47]). The negative sign indicates that this component reflects a rising transient population of the low energy emitter state(s). However, the time constants are too large to be assignable to intra-dimer exciton relaxation from the upper to the lower exciton state in strongly coupled dimers or Förster type EET between weakly coupled pigments. On the other hand, these kinetics compare favourably to the effective dephasing times determined for the terminal (fluorescing) electronic states of trimeric LHCII [242], [243] and CP29 [10]. Therefore we assigned the “rise term” to a protein relaxation process in the excited electronic state [47]. This idea also explains the pronounced temperature dependence of the rise term (see below).

Unfortunately it turns out that the exact value of the time constant of the rise kinetics is highly variable and exhibits quite large variance (see for this problem also [208]).

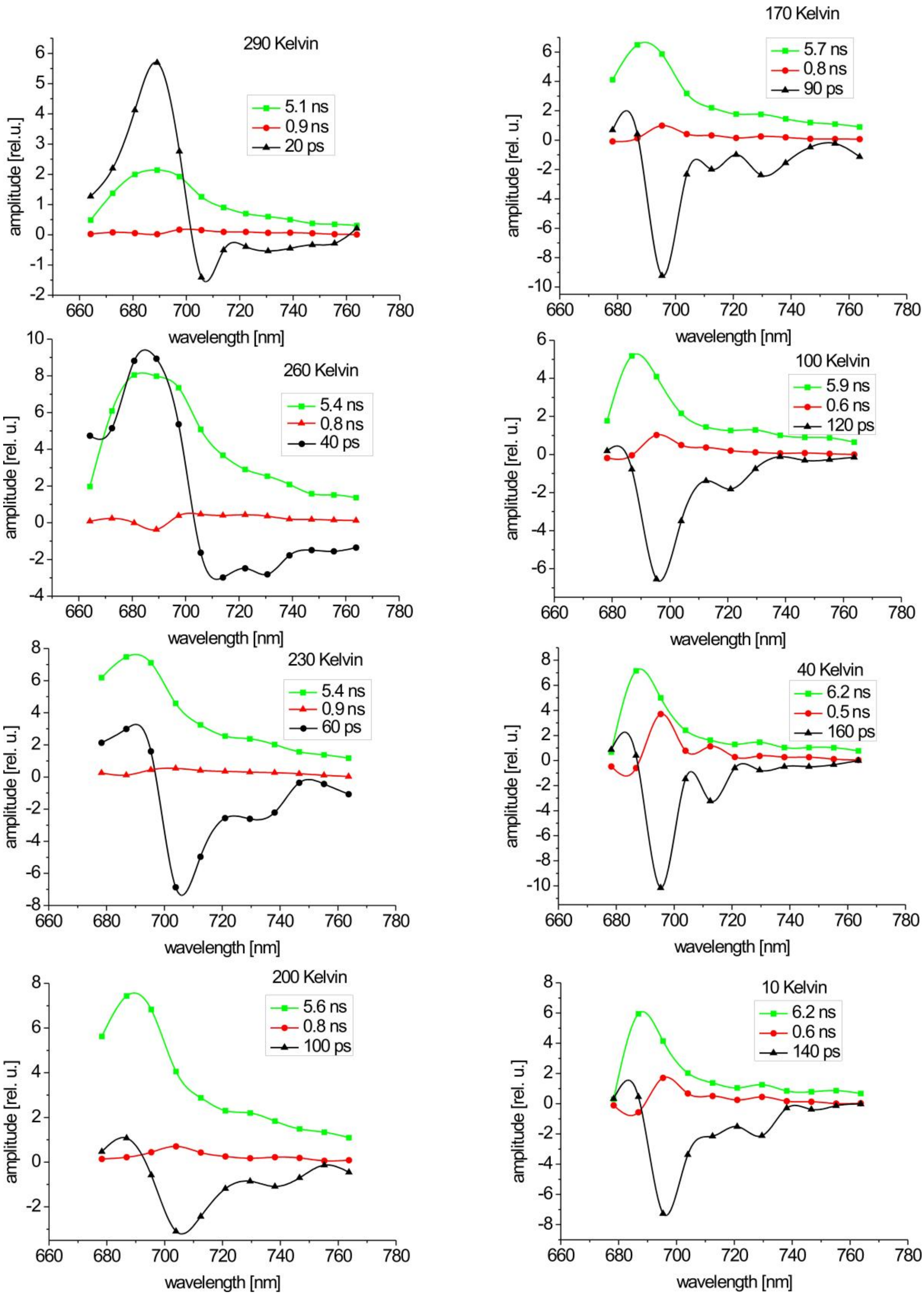

Figure 65: DAS of Chl *a* / Chl *a* homodimers bound to WSCP. All DAS wer fitted with 3 decay components of the fluorescence emission after excitation with 632 nm laser wavelength. The temperature was varied between Room temperature (290 K, upper left panel) via 260, 230, 200 K (left column) and via 170, 100 and 40 K (right column) down to 10 K (lower right panel).

Figure 65 shows a series of DAS of Chl *a* / Chl *a* homodimers bound to WSCP at different temperatures between 10 and 290 K. In spite of the strong variance of the exact time constants this series of DAS can be considered as a “typical” temperature dependency of the DAS of Chl *a* only WSCP. All DAS were fitted with 3 decay components of the fluorescence emission after excitation with 632 nm laser wavelength to enable a straightforward comparison of the results gathered at different temperatures. The graphs are not normalized and the absolute amplitude of the graphs is shown in arbitrary units. Only the relative distribution of the different curves in the DAS are comparable.

Clear trends can be seen by closer data inspection (Figure 65):

i) The dominating fluorescence decay component of the samples containing Chl *a* only rises from 5.1 ns at 300 K to 6.2 ns at low temperature (green curves).

ii) The time constant of the rise term increases from 20 ps at room temperatures to up to 160 ps at cryostatic temperatures. (black curves in Figure 65, see also Figure 66, left side)

iii) At temperatures above 230 K the rise term exhibits only a small negative amplitude at longer wavelengths (red shifted) while the positive contribution around 680 nm is much more pronounced at these higher temperatures. At temperatures < 230 K the rise term exhibits a clear negative amplitude and the minimum shifts to the blue with lower temperatures (black curves in Figure 65, see also Figure 66, right side).

iv) The decay component with a time constant varying between 500 ps and 1 ns (red curves) has very low amplitudes at temperatures above 160 K. At low temperatures this time constant exhibits a partial mirror symmetry to the amplitude of the rise term (compare red curves and black curves).

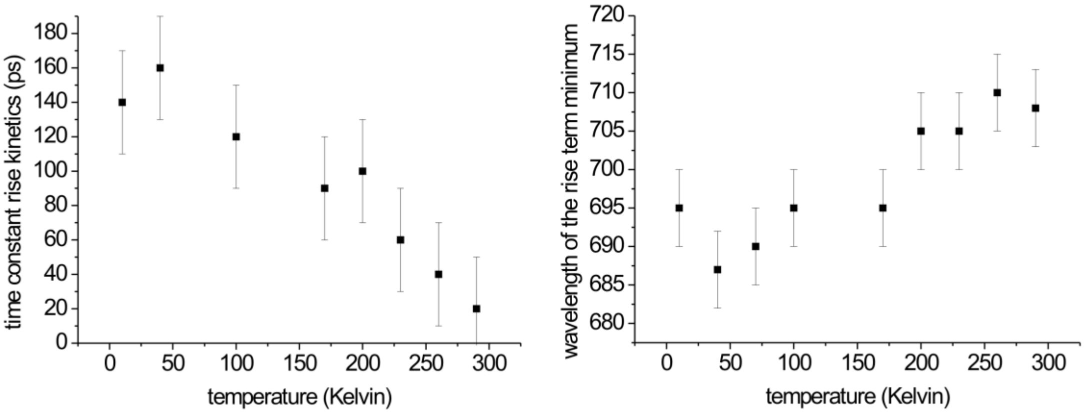

Figure 66: Time constant of the rise term (left side) and peak position of the negative DAS band (see black curves in Figure 65) as a function of temperature.

4.3 Simulation of the temperature dependent DAS of Chl dimers bound to WSCP

The temperature dependency of the fluorescence kinetics is simulated with the formalism of rate equations as presented in chapter 3.2 assuming equilibrium distributions that are described by Boltzmann statistics.

It turns out that the excited state dynamics can be explained assuming different states resulting from pigment-pigment and pigment-protein coupling. Especially the rise term observed in the fluorescence dynamics of Chl *a* containing WSCP seems to be the result of pigment-protein coupling. The rise term shows a change in the dynamics of the time constant and peak wavelength in the regimes of 150 K – 200 K (see Figure 66)

4.3.1 Double well potential for different configuration states of the protein

A change of dynamics and spectral shift of the DAS measured on WSCP possibly introduced by the environment at temperatures below 150 K compared to temperatures above 200 K correlates with the glass transition, i.e. the onset of thermally activated conformational flexibility as recently shown for PS II membrane fragments [244]. Based on these observations it seems reasonable to identify the rise term as a protein relaxation process that can be described by a transition within a double well potential curve as schematically shown in the top panel of Figure 67. The DAS at 10 K reveal that the rise term exhibits a rather small positive amplitude in the range of 660–665 nm and a pronounced negative amplitude with a peak near 668 nm in Chl *b* only WSCP (Figure 64 d) and at about 685 nm in samples containing Chl *a*:Chl *b* at a ratio of 2.6:1 (Figure 64 c). WSCP comtaining Chl *a* only exhibits a positive amplitude at 685 nm and a pronounced negative amplitude at 695 nm at deep temperatures (see Figure 65). At higher temperatures above 230 K the negative values of the rise term diminishes while fast decay kinetics appear with higher amplitude. This is shown for Chl *a* containing WSCP in Figure 65, left column. Similar effects were found in Chl *b* homodimers and Chl *a* and Chl *b* containing heterodimers (data not shown).

The observed feature for Chl *b* only WSCP was simulated using a model with a double well potential for the excited state (see top panel of Figure 67) and a relaxation kinetics of the protein environment of 100 ps at 10 K as it is illustrated by the calculated DAS on the bottom panel of Figure 67. The structure of the ground state potential does not affect the simulation.

The double well structure of the excited state is assumed to be the composite of two excited state parabolas located at slightly different coordinates of the protein nuclei.

The DAS curves are simulated with this double well structure of the excited state and the result obtained (Figure 67, bottom panel) fits the experimental data of Figure 64 d (for details, see [47]). The calculation is based on the assumption that the transition probability from the 663 nm state to the ground state is lower than that from the 668 nm state by a factor of 6. This factor is an additional parameter in the simulation scheme that can be used to vary the amplitude of positive fast fluorescence decay at 663 nm. Until now it is not clarified why the transition dipole moment should be lower in a different protein environment and lead to more intense fluorescence in the relaxed protein conformation.

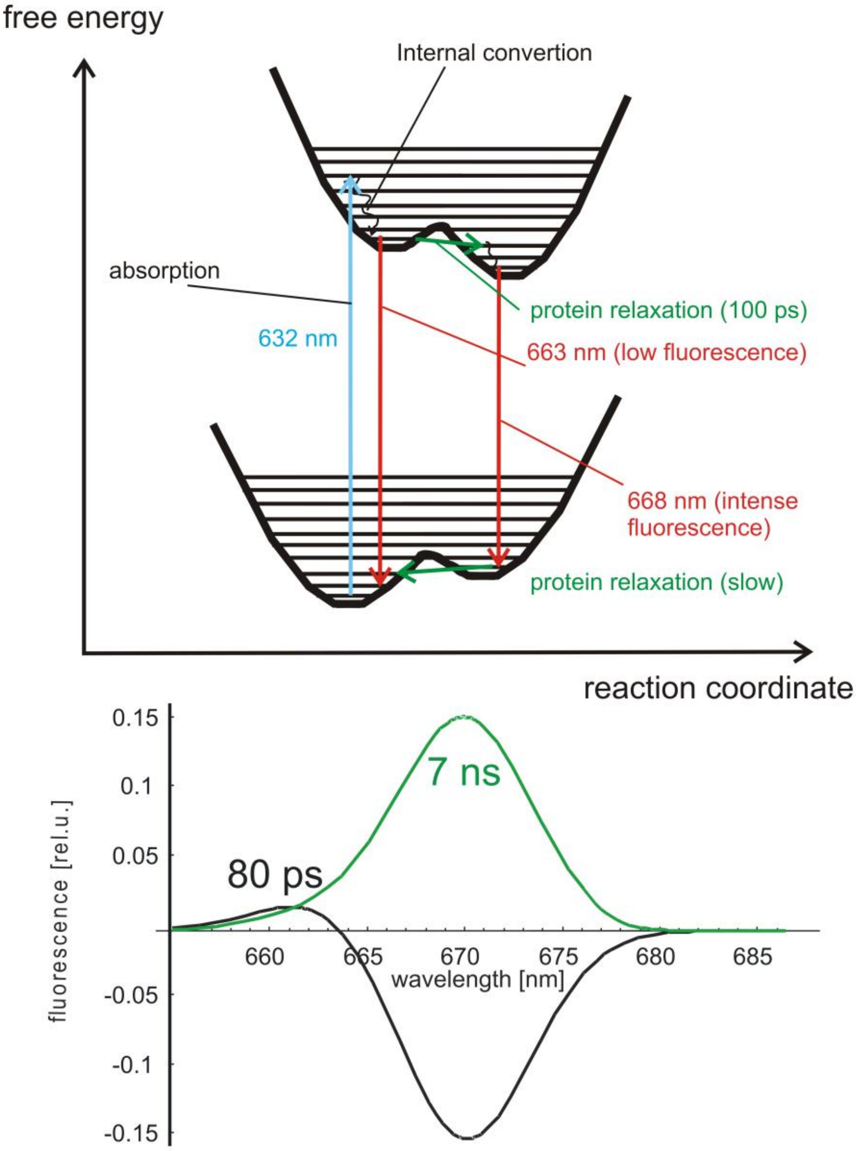

Figure 67: Simplified 1-dimensional scheme of the free energy surfaces of a two-level system for the ground and excited state of WSCP containing Chl *b* only (top panel) and simulated DAS of such a system consisting of two states with emissions at 663 nm and 668 nm connected via a conformational transition of the excited state with a rate constant of (100 ps)$^{-1}$ and no conformational relaxation of the ground state during the lifetime of the excited singlet state. The probability of fluorescence emission is assumed to be smaller for the 663 nm state in comparison to the 668 nm state (bottom panel)

4.3.2 Pigment-protein coupling in WSCP

The fluorescence rise term which is observed in all samples (see Figure 64, panel c) and d) and Figure 65) exhibits a characteristic temperature dependency of the apparent time constant (see Figure 66, left side) and peak wavelength (see Figure 66, right side). Unfortunately the determination of the exact time constant of the fluorescence rise kinetics turns out to be difficult due to significant variations between different measurements (see error bars in Figure 66). The rise kinetics is too slow to be explained by the excitonic relaxation from the upper excitonic state $\left|+\right\rangle$ to the lower excitonic state $\left|-\right\rangle$. In order to account for this fact a double well potential is proposed similar to Figure 67 with a parabolic double well structure for both, the upper $\left|+\right\rangle$ and lower $\left|-\right\rangle$ esxcitonic state. Both protein configurations are separated by an energy barrier Δε. The double well is a simplified model for a possible multi-well configuration of the protein matrix. A model including the two excitonic states of the Chl dimer in each potential well is shown in Figure 68.

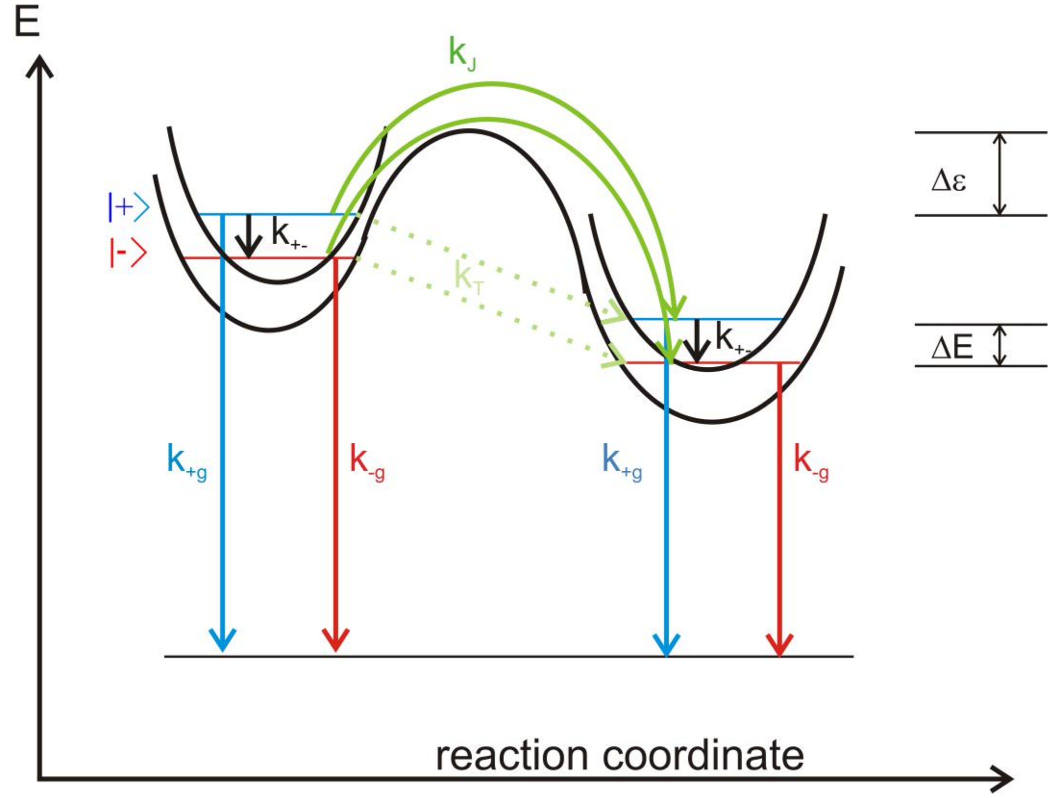

Figure 68: Extended model of the double well potential shown in Figure 67. The two excitonically splitted states $\left|-\right\rangle$ (red) and $\left|+\right\rangle$ (blue) are localized in form of parabolic potentials in each protein configuration. The excitonic relaxation from $\left|+\right\rangle$ to $\left|-\right\rangle$ occurs with the rate constant k_{+-} (black arrows) while the electronic relaxation to the ground state occurs with the time constant k_{+g} from the upper excitonic level $\left|+\right\rangle$ (blue arrows) and with the rate constant k_{-g} from the lower excitonic level $\left|-\right\rangle$ (red arrows). The relaxation from one parabola to the other is assumed to occur via a tunneling process k_T (light green) or via the thermally activated channel k_J (dark green).

The relaxation of the exciton inside such a double well potential as shown in Figure 68 from the energetically higher to the energetically lower parabola has to overcome an energy barrier $\Delta\varepsilon$. This conformational change can occur thermally activated for $\Delta\varepsilon < kT$. In that case one would find a strongly temperature dependent rate constant k_J. On the other hand there should exist a temperature independent tunnelling process with rate k_T that leads to a configurational change of the protein even at very low temperatures.

At first one can study the population of the low energy protein configuration (parabola at the right side in Figure 68) and analyse qualitatively the temperature dependency of the fluorescence rise term as shown in Figure 66 left side. Due to the fact that the exciton relaxation occurs much faster (< 100 fs, see [38]) than the rise term (20 ps – 150 ps) one can neglect the excitonic relaxation for a rough qualitative estimation of the rise term. The fluorescence decay time (5.2 – 6.2 ns) on the other hand is much slower than the fluorescence rise term and therefore also has minor influence on the time constant of the rise term. Such simplified model used to fit the time constant of the fluorescence rise term is presented in the following (see eq. 112 and Figure 69). The more elaborated simulation of the DAS employing the whole model as presented in Figure 68 including the excitonic relaxation and the fluorescence lifetime is shown in Figure 70.

An estimation of the the overall protein relaxation kinetics $(\tau_R)^{-1} = k_R$ from the higher to the lower configurational state can be described in a simplified manner by the probability weighted sum of the thermally activated configuration change and the tunnelling probability which leads to an equilibration of the protein configurations until electronic relaxation because $(\tau_R)^{-1} = k_R > k_T, k_J > k_{+g}, k_{-g}$:

112. $$(\tau_R)^{-1} = k_R = \frac{k_T + k_J \exp\left(-\Delta\varepsilon / k_B T\right)}{1 + \exp\left(-\Delta\varepsilon / k_B T\right)} \qquad \text{(see Figure 68)}$$

Equation 112 can be used to fit the observed temperature dependency of the fluorescence rise kinetics in WSCP containing Chl *a* only as shown in Figure 69:

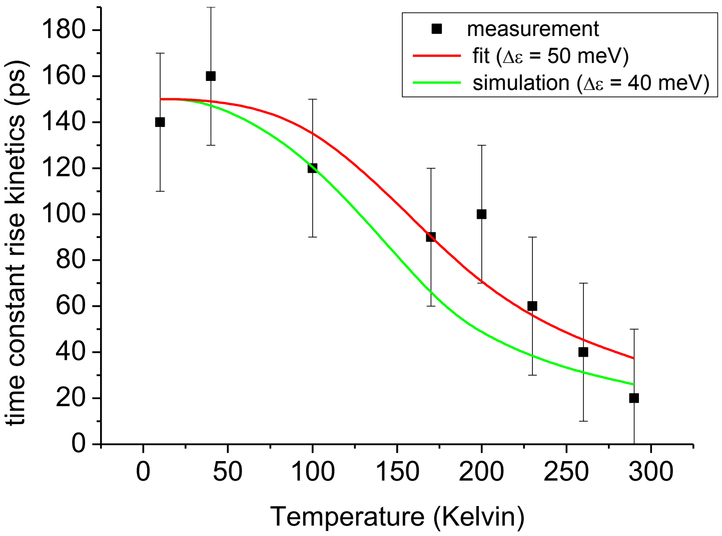

Figure 69: Fit (red curve) of the temperature dependency of the fluorescence rise kinetics observed in WSCP containing Chl *a* only as shown in Figure 66 (black squares) according to the equation 112. The best fit was obtained with $\Delta\varepsilon = 50\ meV$. The green curve exhibits the theoretically expected temperature dependency with $\Delta\varepsilon = 40\ meV$.

The fit presented in Figure 69 was done with free parameters for $\Delta\varepsilon$ and k_J. The value k_T must be set to values around $(150\,ps)^{-1}$ as the interpolation of the measurement data to 0 K does not allow strong deviation from this value. If one evaluates eq. 112 it is found that the best fit is achieved with $k_J = 8\,ps$ and $\Delta\varepsilon = 50\ meV$. The measurement data does not allow strong variations from these values. While k_J determines the the resulting rate constant $(\tau_R)^{-1} = k_R$ at room temperature (see red curve in Figure 69), the position of the inflexion point of the slope is mainly determined by $\Delta\varepsilon$. This value shifts from about 170 K for $\Delta\varepsilon = 50\ meV$ (see red curve in Figure 69) to about 150 K for $\Delta\varepsilon = 40\ meV$ (see green curve in Figure 69) .These results predict an energy barrier of about $\Delta\varepsilon = 50\ meV$ that separates the two protein conformations.

While the simplified model of eq. 112 is suitable to simulate the observed fluorescence rise kinetics, we will now focus on the full simulation of the model shown in Figure 68.

The exact dynamics of the model presented in Figure 68 can be calculated with a system of linear differential equations with the rate equation formalism as described in chap. 3.2. One would expect that the observed fluorescence dynamics exhibit 4 exponential terms as four states are involved into the transitions depicted in Figure 68.

But due to the very fast excitonic relaxation kinetics from $\left|+\right\rangle$ to the lower excitonic state $\left|-\right\rangle$ in the order of 100 fs the overall fluorescence dynamics is described by two very fast components related to the excitonic relaxation (data not shown) in the two protein configuration states. Such two fast components exhibit time constants in the order < 100 fs and can not be resolved separately. Therefore the two amplitudes of the two very fast fluorescence components (time constant faster than 100 fs) were summed in the simulated DAS presented in Figure 70. These DAS were obtained with the parameter values

$k_{+-} = 10^{13} s^{-1} = (100\,fs)^{-1}$

$k_{+g} = 2.6 \cdot 10^{8} s^{-1}$

$k_{-g} = 1.6 \cdot 10^{8} s^{-1}$

$\Delta E = 16 meV$

$\Delta\varepsilon = 50 meV$

In addition the spectral width of the observed emission lines from the different states were varied between 10 nm at 10 K and 25 nm at 290 K to match qualitatively the spectral distribution of the DAS components.

The resulting „protein relaxation“ is calculated according to eq. 112. The fluorescence lifetime in the higher protein configurational state calculates to

113. $$k_F{}^{+} := \frac{k_{-g} + k_{+g} \exp\left(-\Delta E / k_B T\right)}{1 + \exp\left(-\Delta E / k_B T\right)}$$

where k_{+g} and k_{-g} comprise radiative and non-radiative decay from each excitonic level. The corresponding energy gap $\Delta \mathrm{E}$ between both states is given by the energy gap between the upper and the lower exciton states $|+\rangle$ and $|-\rangle$ of the dimer, respectively, T denotes the absolute temperature and $\mathrm{k_B}$ the Boltzmann constant. The Boltzmann factor $\exp\left(-\Delta \mathrm{E} / \mathrm{k_B T}\right)$ takes into account a fast equilibration of excitons between the upper and lower level prior to radiative or non-radiative decay.

While k_{+g} and k_{-g} are assumed to be temperature independent for Chl *a* WSCP the non-radiative ISC is assumed to be temperature dependent in Chl *b* containing WSCP. For details regarding these calculations see ref. [37]. For the sake of simplicity the calculations presented here do not comprise effects of static disorder as taken into account in ref. [37].

All rate constants k_i are assumed to be partially reversible according to the thermal activation of back reactions k_{-i} with $k_{-i} = k_i \exp\left(-(hc)(1/\lambda_D - 1/\lambda_A)/k_B T\right)$ where λ_D denotes the maximum emission wavelength oft he donor state and λ_A the maximum emission wavelength of the acceptor state. In agreement with recent results obtained on WSCP containing Chl *a* only [49] the wavelengths of emitting states used for the simulation shown in Figure 70 were set to

$\lambda_{left\ parabola}^{+} = 670 nm$, $\lambda_{left\ parabola}^{-} = 679 nm$, $\lambda_{right parabola}^{+} = 674 nm$, $\lambda_{right parabola}^{-} = 683 nm$

where the states in the higher (left parabola) and lower (right parabola) configurational state are denoted and the higher/ lower excitonic level are marked with +/ - , respectively. As initial condition it was assumed that the state $\lambda_{left\ parabola}^{+} = 670\,nm$ is populated with probability one while all other states are empty.

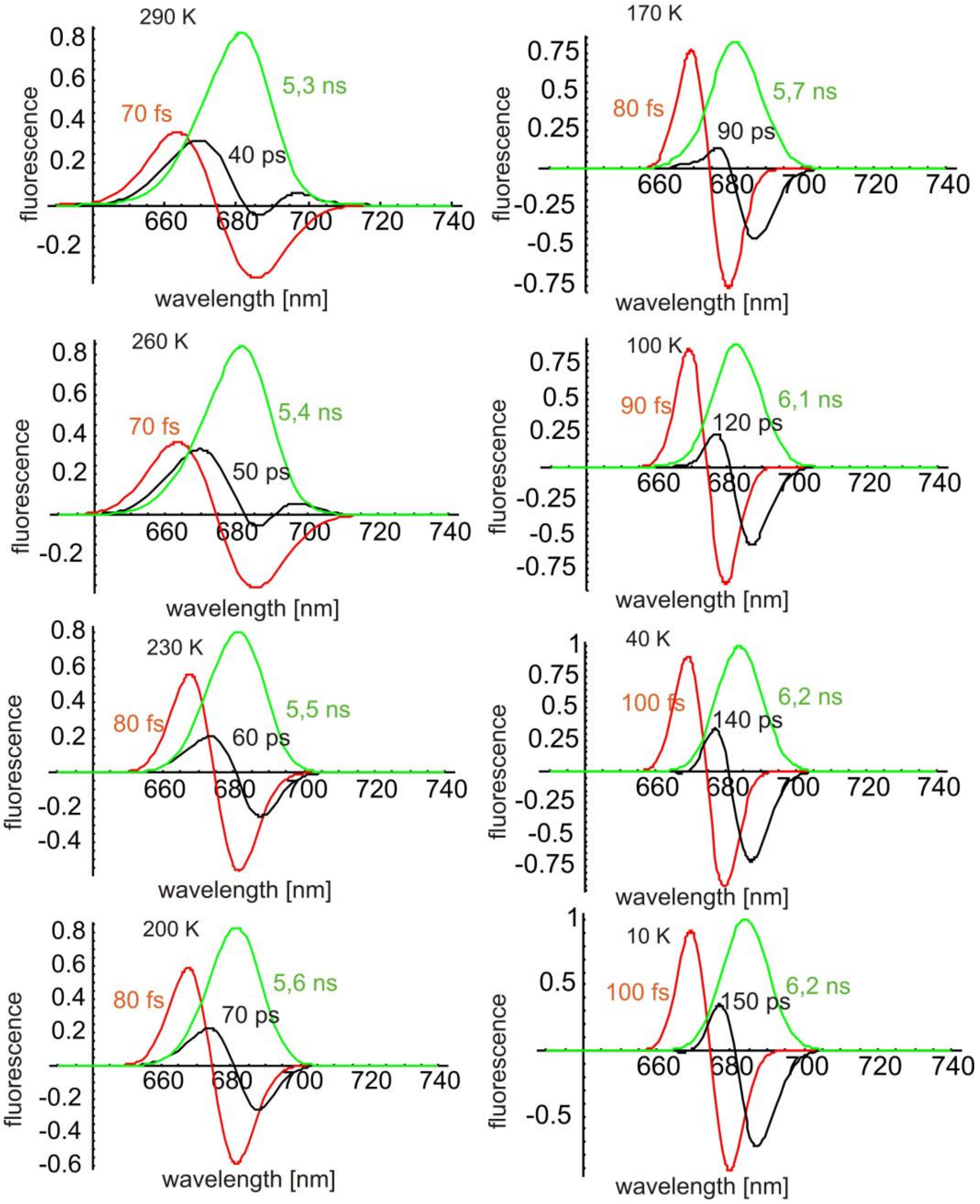

Figure 70: Simulated temperature dependent DAS of the fluorescence of Chl *a* homodimers bound to WSCP according to the extended scheme presented in Figure 68 assuming an exclusive population of the higher excitonic level during excitation. The simulation was performed to describe the measurement data shown in Figure 65. The red curve describes the resulting (summed) amplitude of two very fast time constants with nearly equal values of 65 fs - 70 fs at room temperature and 100 fs at 10 K.

The spectral shape of the simulated DAS shown in Figure 70 deviate from the measured DAS shown in Figure 65 because the vibrational sidebands of the Chl molecules bound to WSCP are neglected in the simulation. On the other hand the measured DAS exhibit a rather high uncertainty in the spectral resolution which is limited to 12.5 nm due to the measurement setup as described in chap. 2.

In the measurement data presented in Figure 65 one marked characteristics of the rise term (black curve) is the shift from a component with mainly decay kinetics (positive amplitude) at 290 K and 260 K to a component with mainly rise kinetics at temperatures below 230 K. One suggestion for such a behavior of this component with only small positive amplitude at short wavelengths (685 nm, see Figure 65) and marked negative amplitude at longer wavelengths was the suggestion that from the energetically higher configuration state the emission of fluorescence exhibits only a small probability (see Figure 67). However it is difficult to understand how this leads to the opposite behavior at temperatures above 230 K.

Instead of this in the simulations that are presented in Figure 70 it was assumed that the states at $\lambda_{left\ parabola}^{+} = 670\,nm$ and $\lambda_{left\ parabola}^{-} = 679\,nm$ are spectrally broader than the states $\lambda_{right\,parabola}^{+} = 674\,nm$ and $\lambda_{right\,parabola}^{-} = 683\,nm$ while the opposite is the case at temperatures below 230 K (here the states in the higher left parabola of the double well potential $\lambda_{left\ parabola}^{+}$ and $\lambda_{left\ parabola}^{-}$ are assumed to be more narrow than the states in the lower right parabola at $\lambda_{right\,parabola}^{+}$ and $\lambda_{right\,parabola}^{-}$). This lead to a qualitative change of the amplitude of the positive contribution of the rise term in comparison to the negative amplitude of the rise term (see Figure 70)

The comparison of Figure 70 and Figure 65 shows that in spite of this modification of the width of the excited states the amplitude distribution of the rise term and its temperature dependency is only qualitatively described. So it has to be pointed out again that the exact amplitude distribution of the fluorescence rise term is yet not fully understood.The qualitative agreement of the simulations shown in Figure 70 and the measurement shown in Figure 65 might be enough to support the suggested model as presented in Figure 67 and Figure 68. The temperature dependency of the time constants of the rise term (black curves) and of the dominating decay term (green curves) are well described for all temperatures employing the proposed model without the need to change any parameters in dependency of the temperatures (except the spectral width of the different states which leads to spectral changes but not to a change of the calculated lifetimes).

In addition to the rise term with 40 – 150 ps time constant (black curves) and the fluorescence decay with 5.3-6.2 ns time constant (green curves) the simulation shows ultrafast components with time constants of 60 fs at room temperature and 100 fs at 10 K (red curves). As mentioned above the red curves shown in Figure 70 is a sum of two ultrafast components with comparable time constants.

These components result from the excitonic relaxation from the upper to the lower exciton level in mainly the upper protein configurations. However these very fast time constants can not be resolved with TWCSPC.

It can not be ruled out that the biphasic relaxation observed by Theiss in WSCP containing Chl *a* and Chl *b* heterodimers is caused by the relaxation of one strongly coupled exciton only that exhibits a biphasic behaviuour due to the accompanying protein dynamics.

In the measurement data an additional component with kinetics of typically 0.5-1 ns is found (red curves in Figure 65). This component can not be described by the model presented here.

The simulations of Figure 70 exhibit three time constants:

i) < 100 fs determined by the excitonic relaxation (red curve, qualitatively proven by C.Theiss with fs-absorption as mentioned above, measured by C.Theiss for Chl a/ Chl b containing heterodimers).

ii) 40–150 ps determined by the strongly temperature dependent protein relaxation (black curve).

iii) 5.3-6.2 ns which is determined by the electronic relaxation of the excited state ensemble to the ground state. This latter component is also slightly temperature dependent. An effect that can is described by pigment-pigment coupling according to eq. 113 as done in the following chapter.

The 0.5 - 1 ns kinetics shown in the measurement (Figure 65, red curve) has a very small amplitude. It might be possible that this component is caused by sample heterogeneity but alternative explanations cannot be ruled out (e.g. a very slow conformational change of the protein environment with a time constant of about 1 ns). Since the extent of this component is very small and therefore its properties are difficult to resolve, we will refrain from any speculation on its nature.

Despite the results presented here it is not possible to draw unambigious considerations on the pigment-protein coupling in WSCP with time resolved fluorescence measurement data only. As outlined in the introduction, complementary methods have to be used to underline the results of one technique.

For the analysis of dynamics that is related to pigment-protein coupling site-selective spectroscopy has to be used like fluorescence line narrowing (FLN) and hole burning. The results obtained with recent FLN and hole burning studies are in well agreement with the presented findings and deliver additional results like e.g. the electron-phonon coupling (Huang-Rhys-factors) in dependency on the excitation wavelength. The results are published in [48] and [49].

4.3.3 Pigment-pigment coupling in WSCP

The dominating fluorescence decay components with time constants between 5.2 ns (room temperature) and 6.2 ns (10 K) for Chl *a* only WSCP (green curves in Figure 65) and 4.8 ns (room temperature) and 7.2 ns (10 K) for Chl *b* only WSCP (green curves in Figure 64 d)) are ascribed to the resulting emission from strongly coupled Chl dimers embedded into the protein matrix. At 10 K only the lower exciton state of these dimers is populated because the energy gap between both states is of the order of 150 cm^{-1} in the homo-dimers and even larger by nearly a factor of three in Chl *a*/Chl *b* hetero-dimers (see ref. [37, 38, 46, 47]); i.e. the population probability of the upper exciton state is < 10^{-5} in a Boltzmann equilibrium. The emission at 10 K with lifetimes of 6-7 ns for Chl *a* only WSCP and Chl *b* only WSCP, respectively, originates exclusively from the lower exciton state because the exciton relaxation was shown to take place in < 100 fs (see previous chapter and [38, 46]). The fluorescence measurements show that the 6-7 ns lifetime at 10 K of the dominating decay component decreases with increasing temperature for both Chl *a* only and Chl *b* only WSCP (see Figure 71, upper panel). A similar behaviour is also observed for WSCP containing Chl *a*/ Chl *b* heterodimers (Data not shown).

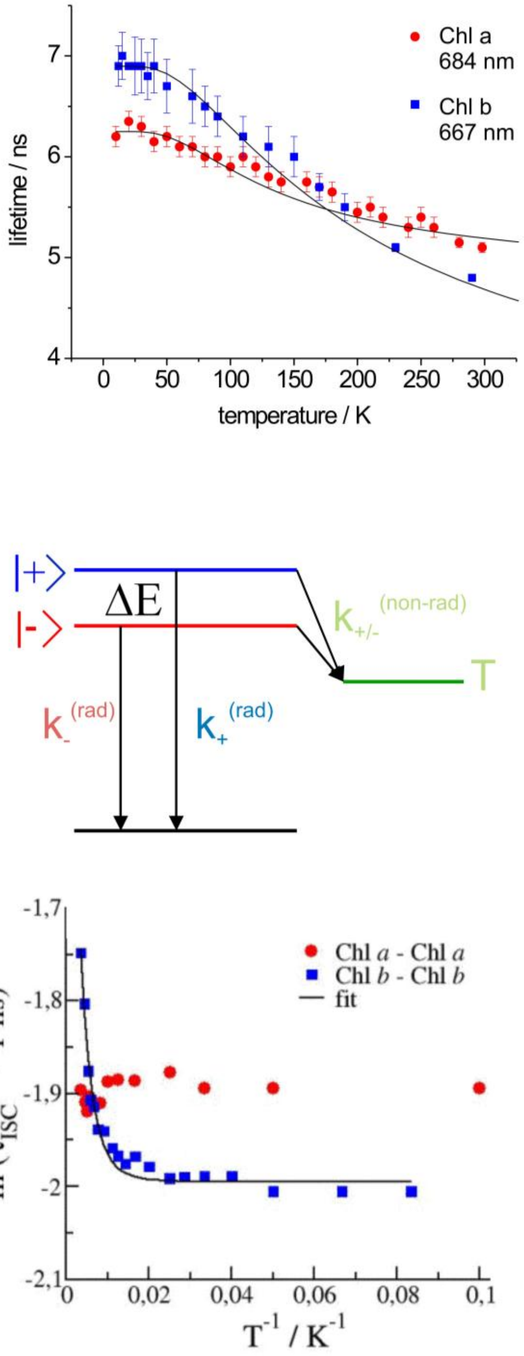

Figure 71: Lifetime of the dominant decay component as a function of temperature of WSCP containing Chl *a* only (blue squares) and Chl *b* only (red circles) in buffer containing 50 % glycerol (top panel), scheme of the radiative $k_{+/-}^{(rad)}$ and nonradiative ($k_{+/-}^{(non-rad)}$) decay of exciton states $|+\rangle$ and $|-\rangle$, respectively (middle panel) and natural logarithm of the calculated intersystem crossing rate constant (see [37]) as a function of inverse temperature of Chl *a* (red dots) and Chl *b* (filled squares) (see [37]). The solid lines represent fit curves. The graph is redrawn from ref. [48].

A consistent explanation of this behaviour is achieved when the systems of Chl *a*/Chl *a* and Chl *b*/Chl *b* homo-dimers satisfy three conditions: i) thermal equilibration is much faster than the decay of the excited state populations, ii) the rate constants of decay differ for the upper and the lower exciton states, and iii) the rate of intersystem crossing (ISC) is invariant to temperature in Chl *a* but not in Chl *b*. Our studies revealed that the conditions i) and ii) are fulfilled in WSCP.

A simplified kinetic scheme of the excited singlet state dynamics in strongly coupled dimers is shown in the middle panel of Figure 71 [37] as it was already proposed in eq. 113. Neglecting the different protein configuration states the inverse lifetime $1/\tau$ of this system is obtained by the relation

114.
$$\frac{1}{\tau}=k=\frac{k_{-g}+k_{+g}\exp\left(-\Delta E/k_BT\right)}{1+\exp\left(-\Delta E/k_BT\right)}$$

The rate constants k_{+g} and k_{-g} comprise the sum of the radiative and non-radiative decay rates of the two exciton levels, i.e.

115.
$$k_{+/-g}=k_{+/-}{}^{(rad)}+k_{+/-}{}^{(non-rad)}$$

Inspection of the Einstein coefficients reveals that the radiative rate constant $k_{+/-}{}^{(rad)}$ is proportional to the oscillator strength of the optical transition from excited state i to the ground state. Hence, in WSCP complexes with a strongly coupled open sandwich dimer arrangement of the two Chl molecules, the radiative lifetimes $k_{+/-}{}^{(rad)}$ of the exciton states $\left|+\right\rangle$ and $\left|-\right\rangle$, respectively, differ strongly due to their different oscillator strengths. Calculations reveal that the oscillator strength of the upper exciton state $\left|+\right\rangle$ is larger by factors of 8-10 (for Chl *a*/Chl *a* homo-dimers, see Figure 56, right side) than that of the lower exciton state $\left|-\right\rangle$. When using the value of $k^{(rad)}$=6.8 10^7 s^{-1} for monomeric Chl *a* in solution [245] the values of $k_-{}^{(rad)}$ and $k_+{}^{(rad)}$ are estimated to be 1.8 10^7 s^{-1} and 1.4 10^8 s^{-1}, respectively. In solutions of monomeric Chl *a* the rate constant $k^{(non-rad)}$ corresponds to $k^{(ISC)}$ for ISC with a value of 1.3 10^8 s^{-1} [245]. Based on the idea that $k^{(ISC)}$ is independent of temperature and not affected by binding to the protein matrix, values of k_{-g}= 1.4 10^8 s^{-1} and k_{+g}=2.7 10^8 $s^{-1}$are obtained. These values are very close to the values of k_{-g}= 1.6 10^8 s^{-1} and k_{+g}=2.6 10^8 s^{-1} as determined by T. Renger et al. [37] and used for the fit of the measured DAS of Chl *a* only WSCP (see chap. 4.2.3, Figure 65) with the model described in chap. 4.3.2 (resulting simulated DAS, see Figure 70). When using the calculated values k_{-g}= 1.4 10^8 s^{-1} and k_{+g}=2.7 10^8 s^{-1}, decay times of 7.2 ns at 10 K and 5.5 ns at 300 K are obtained for Chl *a* only WSCP, which differ slightly from the experimental decrease from 6.2 ns at 10 K to 5.2 ns at 300 K (see Figure 71, top panel) that is in good agreement with k_{-g}= 1.6 10^8 s^{-1} and k_{+g}=2.6 10^8 s^{-1}.
If these parameters and eq. 114 are used to fit the measured dominating fluorescence time constant of Chl *a* containing WSCP one gets the black curve as shown in the upper panel of Figure 71.

The model calculations performed by T. Renger et al. [37] show that the lifetime of the dominating "6-7 ns kinetics" at 10 K is larger for Chl *a* homodimers than for Chl *a*/Chl *b* hetero-dimers because the oscillator strength of the lower exciton state in the latter dimer is larger by a factor of about four than that of the homo-dimer (see Figure 56). This effect is really observed, i.e. the lifetimes at 10 K are 6.2 ns for Chl *a* only WSCP and 6.0 ns for the sample containing Chl *a* and Chl b at a ratio of 2.6:1, which form an ensemble with both WSCP complexes of Chl *a*/Chl *a* homo-dimers and Chl *a*/Chl *b* hetero-dimers (see Figure 64, c)).

Effect of temperature on intersystem crossing of Chl *a* and Chl *b*

A somewhat surprising result, however, is the marked difference in the slope of the temperature dependence of the $^1\mathrm{Chl}^*$ lifetime in Chl *a* only and Chl *b* only WSCP (see Figure 71, top panel). It turns out that the observed fluorescence lifetime of Chl *b* only WSCP can not be described by eq. 114 with parameter values that are in agreement with the theoretical expectation if $k_{+/-g}$ are assumed to be temperature independent.

The following considerations about that effect are calculated by T. Renger and published in [37] and [48].

The markedly different temperature dependency of the excited state lifetime observed in Chl *a* only and Chl *b* only WSCP indicates that besides the exciton oscillator strength/population effect described above, other factors have to be considered as well. One possibility could be a different temperature dependence of the non-radiative decay rate constants $k^{\text{(non-rad)}}$ in Chl *a* and Chl *b* homo-dimers. The temperature dependency of the excited singlet state lifetime of Chl *a* only WSCP is well described with a temperature independent rate constant of intersystem crossing ISC. Contrary a reasonable explanation of the data of Chl *b* only WSCP can be only achieved by the assumption that the corresponding rate constant of Chl *b* is temperature dependent, i.e. $k_{\text{Chlb}}{}^{\text{(ISC)}} = k_{\text{Chlb}}{}^{\text{(ISC)}}(T)$. This idea raises questions on the origin of the phenomenon and the reason for the difference between Chl *a* and Chl *b* only WSCP. A temperature dependent $k_{\text{Chlb}}{}^{\text{(ISC)}}$ can be rationalized on the basis of early quantum chemical calculations of Petke et al. [246] suggesting that ISC from the first excited singlet state S_1 of Chl *a* involves not only the lowest triplet state T_1 but also excited triplet states T_2 and T_3. where the states S_1 and T_3 were reported to be nearly degenerate. This finding implies the possibility that a thermally activated ISC can take place via a higher excited triplet state in Chl *b* only WSCP which is not possible in Chl *a* only WSCP. In order to check for this possibility T. Renger and coworkers performed theoretical studies on the energetics of the $S_0 \rightarrow S_1$ and $T_1 \rightarrow T_n$ (n = 2-4) transitions. The calculations were performed by using time dependent density functional theory with different exchange functionals as outlined in T. Renger et al. [37]. In line with the results of Petke et al. [246] and Knox et al. [247] the excited triplet state T_3 of Chl *a* was found to be energetically slightly below or degenerate with the lowest excited singlet state S_1. The energy gap between S_1 and T_3 was significantly larger for Chl *b*. Therefore state T_3 can be excluded as the candidate for a thermally activated ISC on this pigment. On the other hand, the calculations revealed that the excited triplet state T_4 is energetically either slightly below or above S_1 in Chl *b*. Depending on the method used, the S_1 state in Chl *b* can even be energetically higher than T_4 while the T_4 state in Chl *a* is always markedly above S_1 [37]. Accordingly it is most reasonable to assume that the contribution of T_4 in the ISC process is responsible for the temperature dependency of $k_{\mathrm{Chlb}}^{(\mathrm{ISC})}$ (T). On the basis of this assumption the experimental data could be fitted with a mean energy gap between T_4 and S_1 of 320 cm^{-1} for Chl *b* homodimers as proposed by T.Renger (for details, see [37]). The black curve in the upper panel of Figure 71 represents a fit of the $^1S^*$ lifetime in Chl *b* with values for k_{-g}= 1.4 10^8 s^{-1} and k_{+g}=2.6 10^8 s^{-1} and an additional thermally activated $k_{\mathrm{Chlb}}^{(\mathrm{ISC})}$ separated by an energy gap of 320 cm^{-1}.

"Radiative" lifetime and transition dipole moment orientation in Chl

In addition to the interpretation of the temperature dependent excited singlet state lifetime and the simulation of CD spectra, the theoretical calculations also address two problems of fundamental relevance for the photophysical properties of Chl: i) the "radiative" (natural) lifetime τ_0 and ii) the orientation of the transition dipole moment of the Q_y transition within the coordination system of the pigment (see ref. [48]).

A theoretical simulation of the excited singlet state dynamics with τ_0 as a fit parameter led to a value of 17 ns when using the structural array of the strongly coupled open sandwich dimer of the structure of Horigome et al. [70] for class IIa WSCP [37]. This number is larger than the widely used value of 15 ns reported in ref. [248]. The difference could originate either from a slightly larger tilt angle of the open sandwich dimer (an angle of about 9° larger in the reconstituted class IIa compared to class IIb WSCP would be consistent with τ_0 = 15 ns) or it would indicate that the number of 15 ns has to be revised. The analyses showed that a straightforward solution of this problem can be achieved either by corresponding life time measurements on class IIb WSCP from *Lepidum virginicum* or by structure determination of the reconstituted recombinant class IIa WSCP.

The orientation of the transition dipole moments with respect to the x- and y-axes of Chls (and bacteriochorophylls) is a matter of long lasting discussions and markedly different values have been reported [249-252]. When using the values for the rotational strength of CD spectra determined by Hughes et al. [69] for Chl a in class IIa WSCP a clockwise Q_y deviation of 6-8° from the y-axis was obtained with best fit on the basis of the structure data of Horigome et al. [70]. The only uncertainty of this analysis is the evaluation of spectral data from class IIa with structure data of class IIb WSCP.

In summary, the studies revealed that - in case of suitable spectroscopic data becoming available - the *Lepidium virginicum* WSCP represents an ideal system for the determination of both the "radiative" lifetime τ_0 and especially of the angle between the Q_y transition and the y-axis because the molecular y-axes of the pigments in the strongly coupled dimer are parallel and the rotational strength of parallel dipole moments vanishes [37]. This promising topic will be addressed in future studies.

Likewise, a high resolution X ray crystallographic structure of the recombinant reconstituted class IIa WSCP from cauliflower would offer the same basis for straightforward analyses.

4.4 Concluding remarks to WSCP and future perspectives

The fluorescence and absorption dynamics and especially the complex temperature dependency of the observed fluorescence dynamics are well explained by strong pigment-pigment coupling of the chlorophyll dimer in the open sandwich geometry which is modulated by a strongly temperature dependent protein environment.

The conclusions of our analysis show that reconstituted recombinant class IIa WSCP from cauliflower offers a most suitable sample material for detailed studies on pigment-pigment and pigment-protein interactions.

Moreover, the shielding towards interaction of O_2 with Chls bound to the WSCP protein matrix is a very attractive feature that opens a way for systematic studies on tunable barriers for oxygen diffusion. WSCP can be expected to become a most interesting system for future research.

The reconstituted WSCP is formed from the recombinant apoprotein and chlorophyll molecules in solution and therefore modification of the protein or the chromophores is thinkable. The diffusion barrier could be selectively modified aiming in achieving tunable interaction between O_2 and Chls or other pigments.

The high stability of WSCP is only observed in its tetrameric form where the protein protects the bound Chl from photodegradation.

Switch-able changes of the structural integrity might be used to destabilize the protein tetramers and to enhance the photodynamic activity of WSCP (see Figure 72). One possibility to achieve this goal might be the assembly of WSCP with photoactive groups that trigger light induced structural changes (e.g. cis/trans isomeric forms) thus changing the diffusion barrier to O_2 in a controlled manner. A combined mutagenesis with a selection process might be used to develop such introduced modifications by an evolutionary process. Alternatively structural changes could lead to the release of Chl thereby stimulating enhanced singlet oxygen formation.

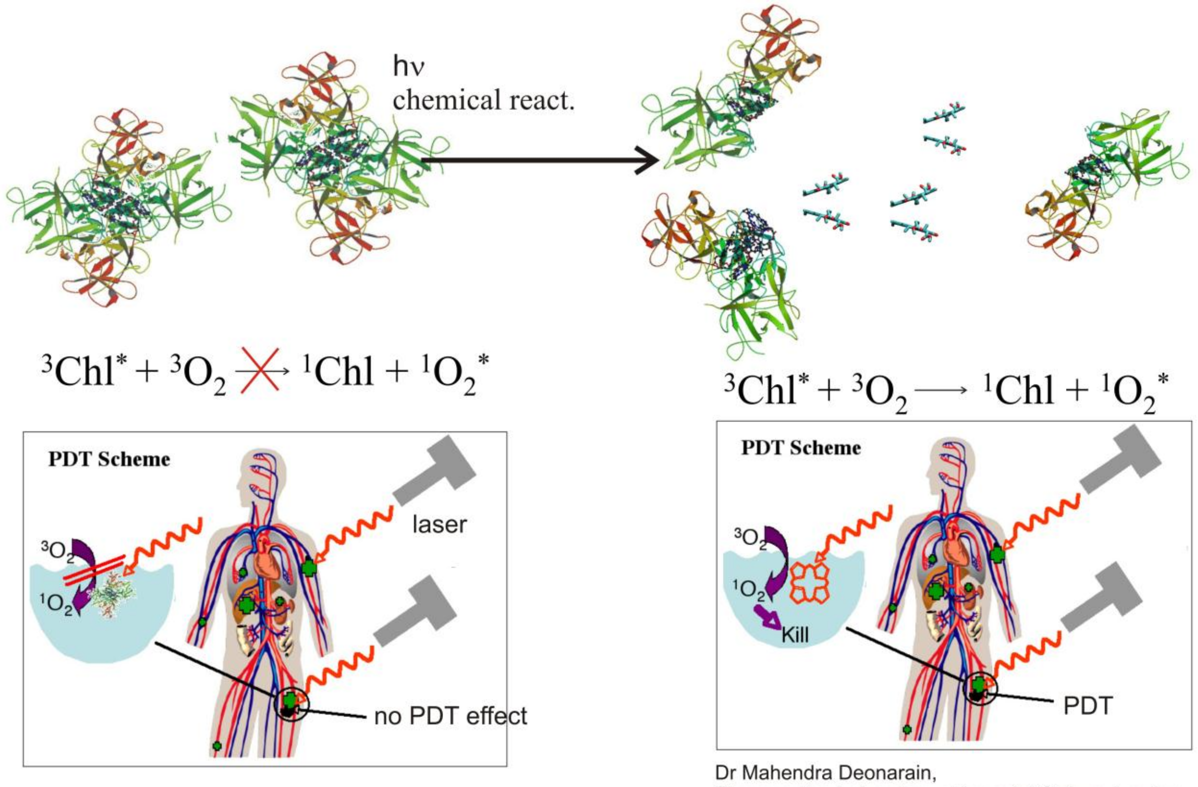

Dr Mahendra Deonarain,
Therapeutics Laboratory at Imperial College London

Figure 72: Scheme for the release of the photodynamically active Chl from WSCP after the application of an external light stimulus. The reaction of photosensibilisation is given by Chl triplets $^3Chl^*$ that interact with surrounding oxygen $^3O_2$ to highly reactive singlet oxygen $^1O_2^*$. This reaction is suppressed by the protein matrix that shields the Chl molecules in WSCP (left side). If this protein matrix can be destabilised by an extern stimulus the photosensibilisation can take place (right side).

Such optical or chemical switch-able destabilisation of the protein tetramer is schematically illustrated in Figure 72. The photosensibilisation process after light absorption as described by chemical equation 4 occurs spontaneously if excited Chl is available and in contact to surrounding oxygen.

Therefore the photosensibilisation by a systemicly applied PDT drug that is not photo switch-able does not occur localized at the therapeutic region but happens anywhere in the body if the cells are exposed to light (e.g. sunlight). A switch-able photosensibilisation would surpress the singlet oxygen generation as long as the switching stimulus is not applied. Therefore such switch-able PDT drugs would enable the use of high potent sensibilisators, because the activity is selectively switched on in the therapeutic region (see Figure 72).

5 PHYCOBILIPROTEIN ANTENNA RODS AND WHOLE CELLS OF *A.MARINA*

In the previous chapter (chap. 4) we discussed the results gathered on Water soluble chlorophyll binding protein (WSCP) binding a well defined Chl dimer in a tetrameric protein structure.

A far more complex system than WSCP is given by the phycobiliprotein (PBP) antenna of *A.marina* consisting of 69 chromophores bound to an ensemble of hierarchically organised protein subunits as described in chap. 1.3.5. In the following sections we present the results gathered from whole cells of *A.marina* and the PBP antenna of *A.marina* that was isolated from whole cells in the Max-Vollmer-Laboratory of the TU Berlin (see refs. [43, 44, 52, 54-56]). Reference measurements were performed on whole cells and phycobilisome (PBS) preparations of *Synechocystis* to demonstrate that the experimental DAS and the results obtained from the simulation of the DAS according to the formalism presented in chap. 3 are in well agreement with literature.

5.1 Excitation energy transfer and electron transfer in whole cells of *Synechocystis* and *A.marina*

The DAS of whole cells of *Synechocystis* are shown in Figure 73, left side. The energy transfer form PC to APC is associated with a characteristic fluorescence time constant of 60 ps (red curve in Figure 73). The fluorescence exhibits an additional 150 ps component (black curve) associated with an EET from the pigments around 640-660 nm (PC and APC) to Chl *a* of PS II (685 nm). The Chl *a* fluorescence decays with time constants of 300 ps (green curve) and 1 ns (blue curve).

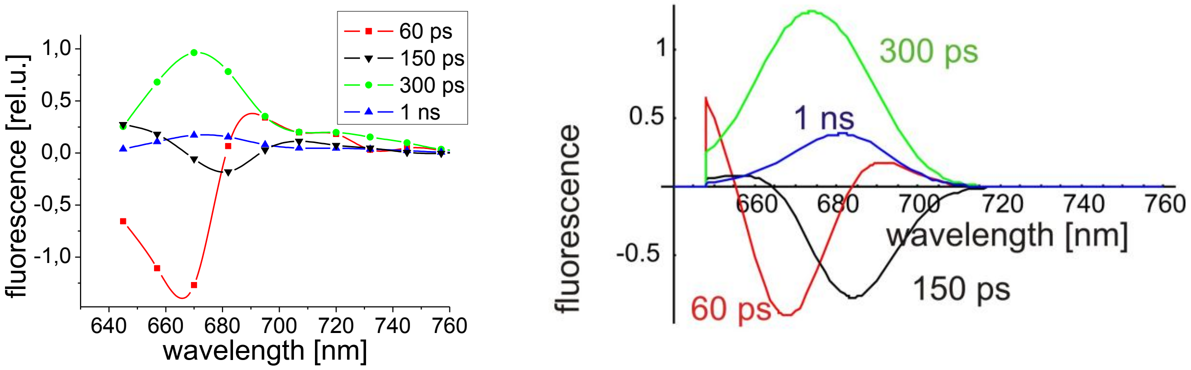

Figure 73 left side: DAS of a measurement obtained on Synechocystis at room temperature after excitation with 632 nm laser light. The time constants of the components exhibit values of 60 ps with a minimum in the fluorescence regime of APC (670 nm, red curve), 150 ps with a minimum in the fluorescence regime of Chl *a* (680 nm, black curve) and additional positive time constants in the Chl *a* regime with 300 ps (green curve) and 1 ns (blue curve). Right side: Simulation of the DAS according to the scheme given in Figure 74, assuming a temperature of 300 K and a spectral bandwidth of the Gaussian emitter states of 25 nm. An edge filter width a cut off wavelength at 648 nm is simulated comparable to the edge filter used in the measurement data (DAS of the measurement is given at the left side)

Figure 73, right side shows the result of a simulation that is performed according to the scheme given in Figure 74. The scheme comprises the photochemical light reaction in the PS II according to chemical equation 2 with an additional PC and APC containing PBS antenna.

In common Chl *a* dominated cyanobacteria such as *Synechococcus* 6301 (which exhibits a similar phycobilisom antenna like *Synechocysti*) the energy transfer from the PBS to PS II occurs on an at least 3 times slower time scale in comparison to *A.marina* [54, 56]. In these cyanobacteria the fluorescence decay of the PBS is characterized by multiphasic kinetics [60, 255] with lifetimes of typically 120 ps for the energy transfer from the PC-containing rods to the APC-core, 70 ps for the energy transfer from the APC-core to the terminal emitters and 200 ps for the energy transfer from the terminal emitter to Chl *a* of PS II [61, 256].

Based on experimental results from ps-studies Holzwarth et al. calculated a time constant of 102 ps to 124 ps for the overall EET from a PC rod containing 4 hexamers to the APC core [60, 226]. Comparable rate constants found in literature are $(80 - 120\ \text{ps})^{-1}$ [257] and $(90 – 120\ \text{ps})^{-1}$ [61].

The simulation and the experimental results (compare Figure 73, right side and left side, respectively) are in agreement if the EET time constant is set to 70 ps for the transfer from PC to APC which is slightly faster than the values given in literature, as mentioned above (see Figure 74). The time constant for the APC to Chl *a* transfer is simulated with 280 ps which resembles the sum of 70 ps for the energy transfer from the APC-core to the terminal emitters and 200 ps for the energy transfer from the terminal emitter to Chl *a* of PS II [61, 256].

In addition a time constant of 230 ps is found for the primary charge separation and ΔG of the relaxed primary radical pair in comparison to the excited Chl state in the antenna system is found to be about 50 meV. The charge stabilisation (see also chemical equation 2) appears to be quite slow with 800 ps. Especially the time constant of the 1 ns component (see Figure 73) depends critically on this ET step. The reason for the high amplitude of the 1 ns component and the concomitant slow 800 ps charge separation may be the existence of partially closed reaction centers during the measurement.

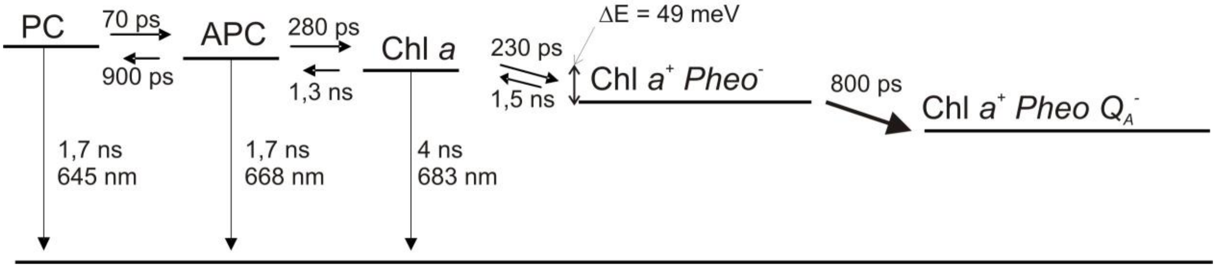

Figure 74: Scheme for the simulation of the DAS shown in Figure 73, right side.

The main difference of the simulated DAS (Figure 73, right side) and the measurement (Figure 73, left side) is the apparent amplitude deviation of the rise kinetics of the fast 60 ps term (red curve in Figure 73). The determination of the amplitude of the rise kinetics is very difficult and exhibits confidential intervals that are of comparable size to the amplitude itself. This situation is even more critical for the measurements presented in Figure 73, as there are two overlapping rise terms with time constants of 60 ps and 150 ps that are resolved in the DAS. Therefore the agreement between the experiment, Figure 73, left side and the simulation Figure 73, right side is sufficient within the confidence interval of the experimental results. The time constants determined as given in Figure 74 show that there is an agreement between the results obtained with our setup and the concomitant analysis via rate equations and literature values. Therefore our experiments and the theoretical approach is supported by the successful determination of the EET steps in the PBS of *Synechocystis*.

In the study presented in this chapter we will carefully analyse the EET dynamics in *A.marina* and compare the results with the EET in PBS of *Synechocystis* and *Synechococcus 6301* in detail. The PBS of *Synechocystis* and *Synechococcus 6301* are of comparable architecture and therefore expected to exhibit similar EET time constants.

For that purpose we shortly refer to chapter 2.2 where the main results obtained on whole cells of *A.marina* as published in [54, 56] are summarized in Figure 33.

Figure 33 (see page 57) shows the results of a measurement of the fluorescence dynamics in whole cells of *A.marina* upon excitation at 632 nm. Figure 33 a) depicts a color intensity plot (CIP) of the fluorescence emission $F(t,\lambda)$ that exhibits two intense fluorescence bands assigned to emissions from the PBPs (650-670 nm) and Chl *d* (725nm) (see [54] for details).

Figure 33 b) shows that the PBP-fluorescence at 660 nm decays much faster than the Chl *d* emission at 725 nm. The PBP emission (640 – 690 nm) is dominated strongly by a 70 ps decay component. Additionally, the DAS of the 70 ps-fluorescence contains a rise term of the Chl *d*-fluorescence at 725 nm (Figure 33 d)). Therefore we ascribe the 70 ps component to an excitation energy transfer from the PBP antenna to the Chl *d* containing membrane integral antenna complex of *A.marina* [54]. The slower decay components with very small amplitude (τ = 350 ps and 1.2 ns) in the 640 – 690 nm range most probably result from PBP antenna complexes that are not coupled to the Chl *d* antenna and from conformationally distorted PBP antenna complexes [43].

The rise kinetics representing the population of Chl *d* via energy transfer from the PBP complexes exhibits a time constant of 70 ps (see Figure 33 d)). Additionally there exist two dominating decay components with 130 ps and 630 ps with nearly equal amplitudes in the Chl *d* emission as shown in Figure 33 d). According to our previous findings (see chap. 2.2 and [54]) the 630 ps-component is ascribed to PS II with open reaction centers. The slow decay component with a lifetime of 1.2 ns has only a very small amplitude. It originates from a small fraction of PS II with closed reaction centers as shown by the increase of its initial amplitude upon closure of the RC of PS II (data not shown, for details see [54]).

The lifetimes of the 725 nm fluorescence band observed in our study are largely consistent with those reported by Mimuro et al. [190]. However, they found a much higher relative contribution of the slow component ($\tau > 1$ ns, about 25% at room temperature) than in our measurements ($\leq 5\%$). This difference could be due to a relatively large fraction of closed reaction centers in the measurements reported in [190]. The fast 130 ps-decay component of the 725 nm fluorescence is shown to originate predominantly from Chl *d* of PS I [54, 161, 190] and our studies revealed that a part of this fast 130 ps component originates from the PS II because it is partially affected by closing the reaction centers of PS II [43, 54, 161].

The DAS of the 70 ps component exhibits a maximum at 650 nm and a shoulder at about 670 nm after excitation with 632 nm in the PBP range (640 – 690 nm) (Figure 33 c) and Figure 33 d), see also Figure 76 and Figure 77). In agreement with [183] and [186] we ascribe the 650 nm emission to PC and the 670 nm shoulder to APC. A Gaussian fit of the PBP emission shows that the PC emission peaks at 650 nm while the APC peak is found at 666 nm [43, 161].

5.2 Excited state dynamics inside the PBP antenna of *A.marina*

The emission spectra of the chromophores of the PBP antenna of *A.marina* containing phycocyanine (PC) (emission wavelength: 650 nm) and allophycocyanine (APC) (emssion wavelength: 666 nm) and of the Chl antenna (emission wavelength of Chl *d*: 725 nm) are spectrally clearly separated. This purpose makes the light harvesting complex in living cells of *A.marina* to an excellent model system for the *in vivo* analyse of energy transfer processes with the technique of TWCSPC.

As described in chap. 1.3.4 and chap. 1.3.5., the rod-shaped PBP antenna of *A.marina* was suggested to consist of three hexamers containing only PC and one hetero-hexamer with both PC and APC. This unique structure, and the fast overall EET from the PBP antenna to the Chl *d* containing core complex reported in the previous section, raise questions about the mechanism and kinetics of EET within the PBP-antenna.

Therefore we studied the EET in isolated PBP-complexes using transient sub-ps absorption spectroscopy, site selective spectroscopy (hole burning and fluorescence line narrowing spectroscopy), and time- and wavelength-resolved fluorescence spectroscopy and compared the results with time- and wavelength- resolved fluorescence spectra obtained on living cells. A part of the results presented here had already been published in ref. [56].

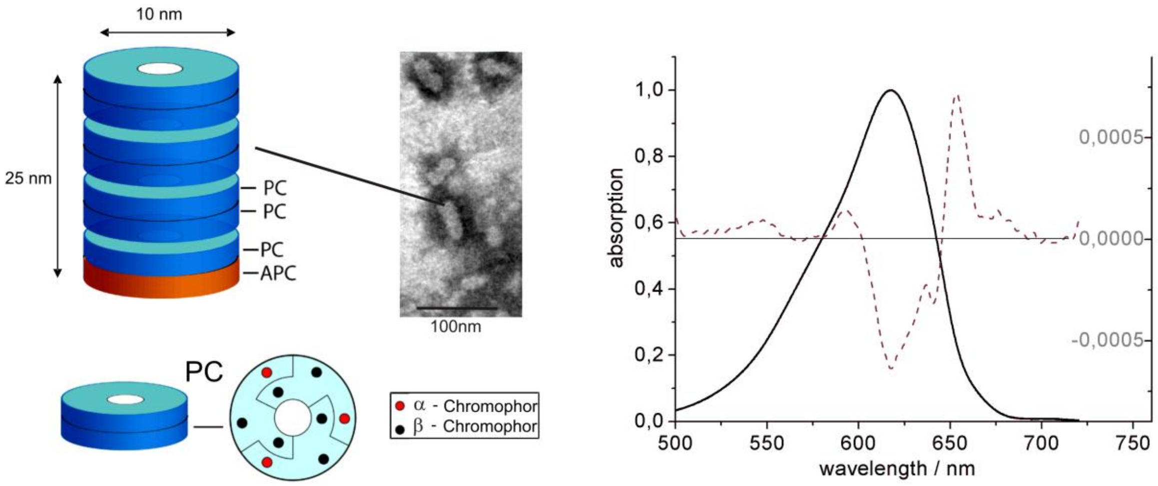

Figure 75 left side: Electron microscopic study of PBP preparations of *A.marina* in buffer containing phosphate after negative staining with $Na_4[W_{12}SiO_{40}]$. Due to the process of negative staining the PBP antenna complexes appear grey while the staining salt leads to a dark black contrast. Right side: Ground state absorption spectra of the isolated PBP antenna of *A.marina* (black, straight line) and the second derivative (grey, dashed line) at room temperature. The graphic had already been published in [56].

The PBP complexes from *A.marina* were isolated as described by Marquardt et al. [183]. In agreement with Marquardt et al. the electron micrographs (see Figure 23 and Figure 75, middle) of the obtained PBPs show the previously reported rod-shaped structure. The absorption spectrum of the PBPs exhibits a maximum at 618 nm (Figure 75, right) and its second derivative has minima at 617 nm and 641 nm. This shows that the obtained PBP complexes contain also a small amount of APC (641 nm) besides PC (618 nm).

In respect to shape and spectral position, the spectrum of PC from *A.marina*, reported in [183], closely resembles that of PC from common cyanobacteria. In contrast to this, the absorption spectrum of APC in the isolated PBP antenna from *A.marina* (λ_{max} = 641 nm) is blue shifted by about 10 nm in comparison to APC from cyanobacteria with PBS (see e.g. [180, 258]).

As in detail described in chapter 1.3.4 monomeric APC is known to consist of two subunits (α and β) each containing one phycocyanobilin pigment (α-84 and β-84). Therefore the trimeric APC contains altogether 6 chromophores. Monomeric PC is also composed of two subunits. Whereas the α-unit contains one chromophore (α-84), the β-unit has two pigments (β-84, β-155) leading to 9 pigments per disk shaped PC trimer arranged in a C3 symmetry configuration (see Figure 75) (for a review on phycobiliproteins see e.g. [64]). The hexameric structure is formed by two of the disk shaped trimers in a head to head configuration. Assuming that the antenna rods of *A.marina* consist of 3 homohexamers PC and 1 heterohexamer PC/APC [183, 186] a total number of 69 pigments are involved in the spectral properties of the antenna rods. However, a considerable number of pigments can be expected to show similar spectral characteristics because of the C3 symmetry of the trimers and the identical structure of several of the subunits.

The differences in arrangement and orientation of phycocyanobilin pigments in PC and APC, respectively, the pigment-pigment as well as the pigment-protein interaction result in the very different spectral characteristics of these pigment-protein complexes. Especially the excitonic interaction between very close pigments (typically d< 2 nm) could give rise to an excitonic split, leading to significant changes in the spectra (see chapter 3.4 and Figure 52).

5.2.1 Fluorescence measurements

In order to characterize the isolated PBP complexes more thoroughly the fluorescence emission was used as a monitor of the functional coupling between the PC- and APC-containing subunits. It is known that the functional coupling between PC and APC is interrupted in the absence of PO_4^{2-} [260-262]. A comparison of the fluorescence spectra of the PBP antenna obtained in the absence and presence of PO_4^{2-} in the buffer can therefore be used to investigate the efficiency of the EET between PC and APC.

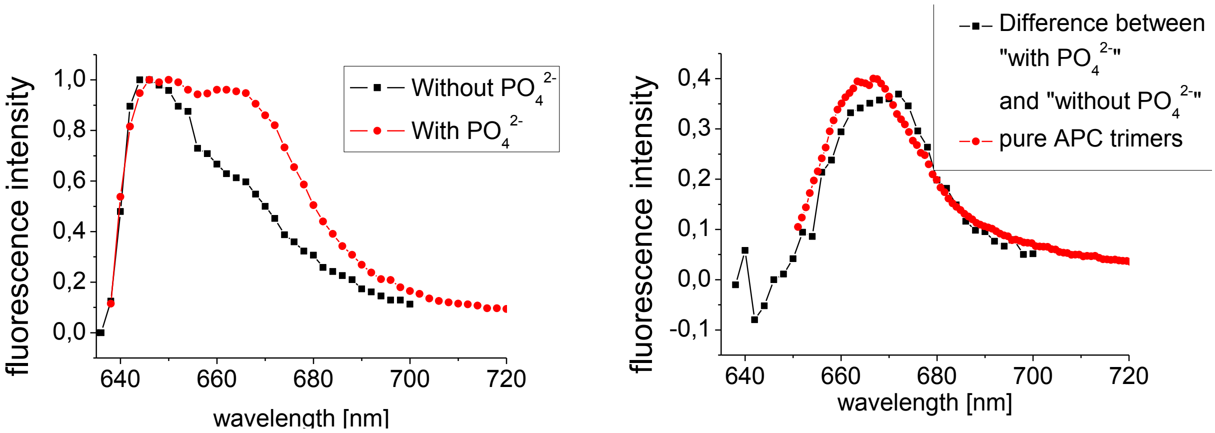

Figure 76 left side: fluorescence spectra of isolated PBP antenna complexes from *A.marina* excited at 632 nm (20°C) in buffer containing 0.75 M PO_4^{2-} (red circles) and in buffer without PO_4^{2-} (black squares). Right side: difference between both spectra (with and without PO_4^{2-}) (black squares) and emission spectrum of pure APC trimers in the same solubilisation medium (including PO_4^{2-}) (red circles). The fluorescence below 645 nm (left side) is cut off by a long-pass filter. The graphics is redrawn from the data published in [48].

Figure 76 (left) shows the fluorescence spectra of isolated PBP complexes of *A.marina* after excitation at 632 nm. In the presence of phosphate the spectrum is characterized by two bands at 650 nm and 670 nm which are assigned to emissions from PC and APC, respectively. In the absence of phosphate the intensity of the 670 nm band is largely reduced. The difference (with and without PO_4^{2-}) between both spectra (Figure 76, right) closely resembles the fluorescence spectrum of isolated APC. This indicates an efficient EET in the presence of phosphate and an uncoupling of the EET in the absence of it. An uncoupling of the EET was also observed in the presence of 70% glycerol (data not shown). In samples with intact EET the temperature dependent population probability of excited PC and APC chromophores is expected to be described by the Boltzmann distribution. Therefore the population of excited PC in comparison to APC is expected to be highly temperature dependent. Temperature dependent emission spectra were performed in the range between 10 K and room temperature as shown in Figure 77, left side to check the functional coupling between PC and APC.

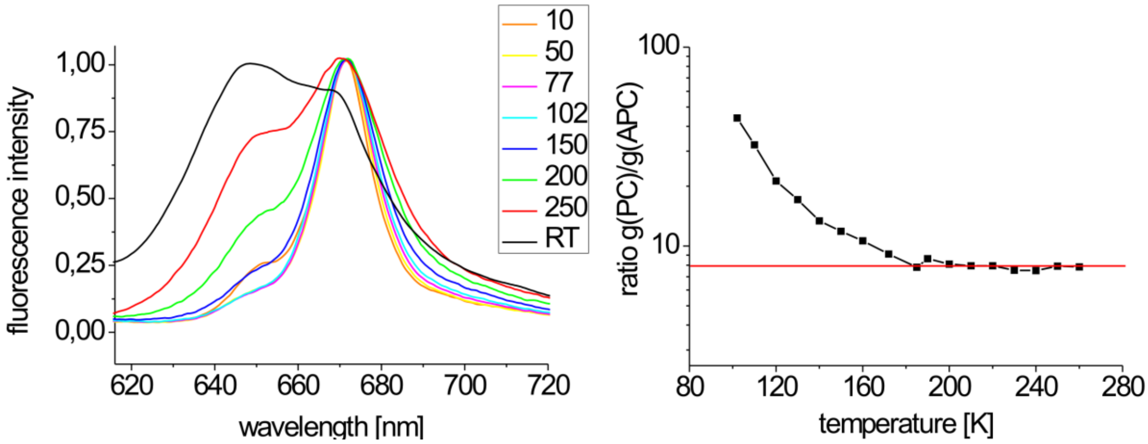

Figure 77 left side: Normalised fluorescence spectra of isolated PBP complexes from *A.marina* at different temperatures between room temperature (RT, black curve) and 10 K (orange curve) upon excitation at 593 nm. Right side: The value g_{PC}/g_{APC} as calculated from the relative intensities of the fluorescence at 650 nm and 670 nm. The red lines mark the position $g_{PC}/g_{APC}=8$. The graphics is redrawn from the data published in [48].

Figure 77, left side shows the fluorescence spectra of isolated PBP antenna complexes in a buffer containing phosphate at different temperatures upon excitation at 593 nm. At room temperature the emission spectrum (black curve) has a maximum at 650 nm (PC) and a pronounced shoulder at 670 nm (APC). With decreasing temperature the PC emission peak (650 nm) shrinks relative to the APC emission. This is observed down to 77 K (magenta curve). At lower temperatures the amplitude of the 650 nm fluorescence rises slightly again and reaches an amplitude at 650 nm at 10 K (orange curve) that is comparable to the PC emission at 150 K (dark blue curve).

To analyse the relative distribution of the PC and APC emission, Gaussian fits of the spectra shown in Figure 77, left side, were performed in the frequency domain with two Gaussian emission bands only that were found to be located at 645 nm (room temperature) to 650 nm (10 K) for the PC emission and at 666 nm (room temperature) to 671 nm (10 K) for the APC emission. Interestingly the PC emission band shifts gradually to longer wavelengths with lower temperature while the APC emission shifts from 666 nm to 670 nm between room temperature and 200 K and stays constant at lower temperatures (see Figure 77, left side). The effect is reproducible, but further details of this analysis are not shown here. This feature indicates that there is a low energy state in the APC emission regime (670 nm) which is spectrally clearly separated and therefore exclusively populated at comperatively high temperatures of 200 K while the excited states are spectrally more dense in the PC emission regime between 645 nm and 650 nm.

In samples with intact EET the ratio between the integrated fluorescence bands of a gaussian fit to the PC emission, $F(PC)$, at 645-650 nm and to the APC emission, $F(APC)$, at 666-671 nm is expected to follow Boltzmann statistics according to:

116. $$\frac{F(PC)}{F(APC)} = \frac{\Phi_{PC}}{\Phi_{APC}} \frac{g_{PC}}{g_{APC}} e^{-\frac{\Delta E}{k_B T}} \approx \frac{g_{PC}}{g_{APC}} e^{-\frac{\Delta E}{k_B T}}$$

Where ΔE is the energy difference between the excited states of PC and APC, $k_B T$ is the thermal energy, and Φ_{PC} and Φ_{APC} are the fluorescence quantum yields of PC and APC, respectively. In the case of PBP complexes with intact EET the degeneracy factors g_{PC} and g_{APC} represent the total number of the respective bilin chromophores in the PC and APC proteins of one PBP antenna rod: $g_{PC/APC} = N_{PC/APC}$.

The right side of Figure 77 depicts the values of g_{PC} / g_{APC} which were obtained assuming, that the fluorescence quantum yields of PC and APC are the same, i.e. Φ_{PC} = Φ_{APC}. According to this calculation the ratio g_{PC} / g_{APC} has a constant value of $g_{PC} / g_{APC} \approx 8$ between 180 K and 260 K. However, since Φ_{PC} is slightly larger than the quantum yield of APC ($\Phi_{PC} > \Phi_{APC}$ = 0.68) [208] the value $g_{PC} / g_{APC} = 8$ is rather an upper limit, i.e. $g_{PC} / g_{APC} < 8$. This value is smaller than what one would expect from a PBP antenna suggested by Marquardt et al. [183] with three PC homohexamers and one heterohexamer containing one PC- and one APC-trimer. In this model the 7 PC trimers would bind 63 chromophores and the APC trimer would contain 6 chromophores (see above) which results in a ratio of $N_{PC} / N_{APC} = 63/6 = 10.5$ The increase of g_{PC} / g_{APC}, which is observed when the temperature decreases below 170 K, might be the result of an interruption of the EET from PC to APC. This could be caused by a glass-liquid-transition of the surrounding medium or by a dynamical transition of the protein backbone itself.

These considerations suggest that the isolated PBP complex used for our measurements might contain at least two additional APC chromophores in addition to the 6 chromophores of the PC/APC heterohexamer. This could indicate that some of the PBP-complexes contain linker proteins with additional APC bilins.

In an attempt to monitor the kinetics of the EET between PC and APC under *in vivo* conditions, the fluorescence kinetics in the PBP antenna of living cells of *A.marina* were studied at higher time resolution than that used for Figure 33 employing the McPherson Monochromator (see chap. 2.1.). As shown by the DAS depicted in Figure 78, the fluorescence dynamics in the PBP antenna of living cells is characterized by four exponential decay components with lifetimes of <20 ps, 80ps (+/- 10 ps) , 180 ps (+/- 100 ps) and 0.9 ns (+/- 0.1 ns).

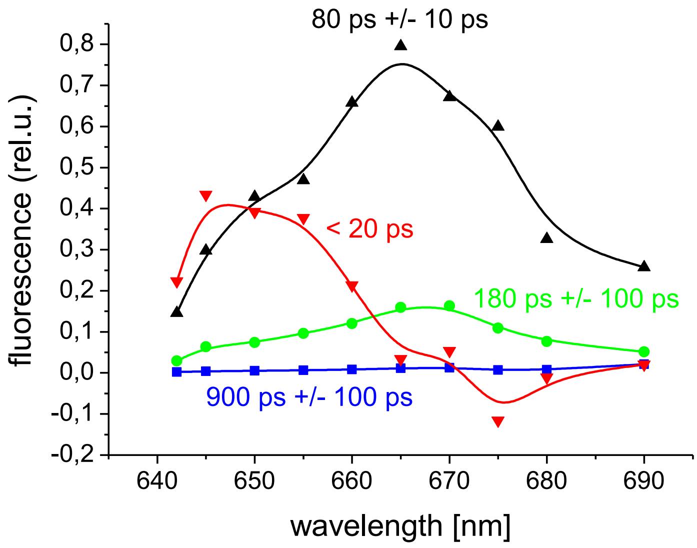

Figure 78: Decay associated spectra (DAS) of a global fit (4 exponential components) of the fluorescence emission at 20 °C of whole cells of *A.marina* in the 640 nm – 690 nm range after excitation at 632 nm. The fluorescence below 645 nm is cut off by a long-pass filter. The graphics is redrawn from the data published in [48].

The DAS of the <20 ps component has a positive amplitude in the PC and APC emission band (645 - 660 nm) and a negative amplitude at 675 nm that is red shifted in comparison to the APC emission. This suggests that in living cells of *A.marina* the EET from PC to the most red chromophore of the PBP antenna occurs with a time constant of less than 20 ps. The 80 ps decay component reflects the EET from the PBP antenna to PS II (see above) and the slower components (180 ps, 0.9 ns) are probably due to conformationally distorted and/or functionally decoupled PBP complexes in *A.marina* [16].

As mentioned above the relative amplitude of the 650 nm fluorescence (PC) in comparison to the 670 nm fluorescence (APC) rises again at temperatures below 77 K and reaches an amplitude at 650 nm at 10 K (orange curve in Figure 77) that is comparable to the PC emission at 150 K (dark blue curve in Figure 77). This phenomenon is inconsistent with the assumption of a Boltzmann distribution describing the g_{PC} / g_{APC} ratio as mentioned above. Therefore g_{PC} / g_{APC} rises below 170 K (see Figure 77, right side), a feature that was confirmed with different preparations and in different fractions of PBP from *A.marina*.

An independent measurement of the emission spectra of isolated PBP complexes at different temperatures is shown in Figure 79.

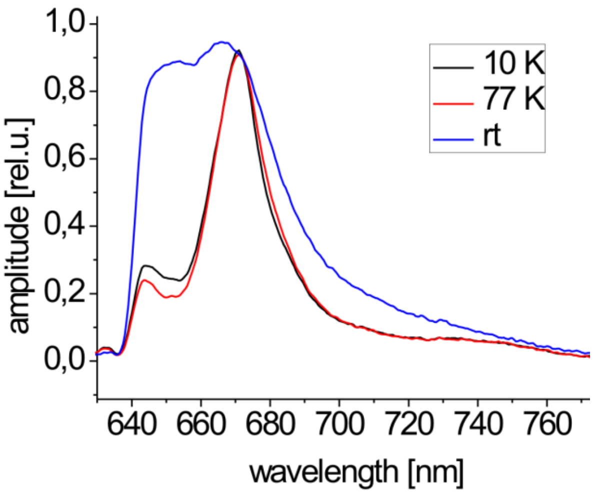

Figure 79: Fluorescence spectra of isolated PBP complexes from *A.marina* at room temperature (RT, blue curves), 77 K (red curve) and 10 K (black curve) upon excitation at 632 nm.

Figure 79 shows the emission spectra of isolated PBP complexes at three different temperatures. The data shows that the deep temperature shoulder in the PBP emission (650 nm) is more pronounced at 10 K (black curves) than at 77 K (red curves). That means, as indicated above (see Figure 77, right side), that there is not a pure temperature dependent distribution between all PC and APC molecules according to the Boltzmann statistics for all temperatures but the probability for an excited state located on the PC molecules (650 nm) is higher at 10 K than at 77 K.

The amplitude of the population in the PC emission band seems to rise at temperatures below 70 K inverse to the expectation from the Boltzmann statistics.

As mentioned above the physical reason of this effect is not solved in detail yet but it indicates that the EET from PC to APC is disturbed at temperatures below 150 K (see Figure 77, right side). It might be explained by a distance change and/or orientational change between the terminal emitter in the PC trimer of the PBP heterohexamer and the primary acceptor pigment in the APC trimer. A quantitative discussion of such conformational changes of protein complexes in dependency on the temperature is found in chapter 6 for the artificial system of CdSe/ZnS quantum dots and the PBP antenna of *A.marina*.

5.2.2 Transient absorption measurements

Due to the limited time resolution of the fluorescence setup, further EET steps faster than the < 20 ps equilibration between all molecules in the PBP antenna that was found in the previous section can not be resolved with TWCSP. In isolated PC- and APC- trimers of the phycobilisomes in Chl *a* containing cyanobacteria very fast excitation energy transfer processes with time constants of less than 1 ps were observed (see e.g.[263], [180]). Therefore the excited state dynamics in the isolated PBP antenna rods of *A.marina* were analysed using transient absorption spectroscopy with femtosecond time resolution at room temperature. These measurements were done by C.Theiss as published in ref. [56].

The home built multicolour pump- probe setup with time resolution of about 200 fs is described in detail in ref. [2]. The setup is based on a spectra physics fs-lasersystem at a repetition rate of 1 kHz. For the pump beam an excitation wavelength of 618 nm in the center of the absorption profile of the PBP antennas was chosen. At this wavelength mainly PC is excited while the absorption of APC is comparatively small.

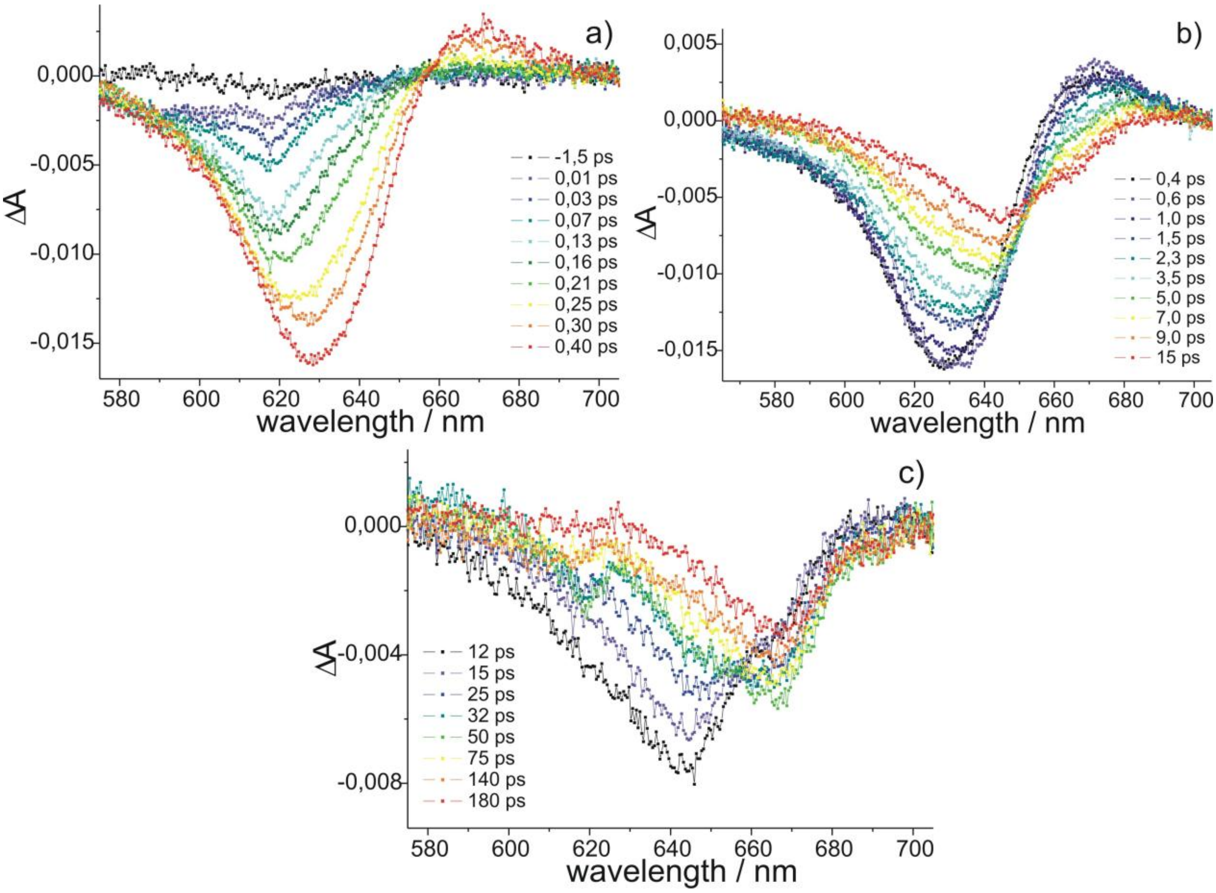

Figure 80: Transient absorption difference spectra induced by 618 nm excitation ($\tau \approx$ 70 fs, E=65 nJ), in the isolated PBP antenna of *A.marina* at a) 0-0.4 ps, b) 0.4-15 ps and c) 12-180 ps delay time between pump and probe pulses (see [44]). Graphics taken from [56].

Figure 80 a-c show time-resolved absorption difference spectra of the intact PBP antenna systems between 580 nm and 700 nm after excitation with 65 nJ pump pulses [44]. The changes of the absorption spectra were monitored at various delay times between the pump and probe pulses in a time window of 0-180 ps. For reasons of clarity Figure 80 is separated in three graphs containing the transient spectra of different time delay intervals. The transient spectra at very early delay times of t<0.25 ps reflect the state initially formed by the excitation pulses. They exhibit a negative maximum around 620 nm (see Figure 80 a) which is assigned to a bleaching of PC. This is followed by a very fast spectral shift to longer wavelengths up to a peak wavelength centred at 630 nm while the amplitude of the bleaching further increases up to a time delay of 0.4 ps. This feature indicates a very fast EET between “blue” and “red” absorbing PC-pigments which occurs with a time constant similar or faster than the time resolution of our equipment (≈ 200 fs). Such fast relaxation processes are typical for excitonically coupled pigments (calculations for excitonic relaxation in WSCP are found in [37, 38]). While negative values of ΔA correspond to ground state bleaching and stimulated emission, positive values in the transient absorption spectra are indicative for excited state absorption (ESA). For this reason it can be assumed that the small positive band observed between λ=660 nm and 690 nm in Figure 80 b,c at these short delay times is associated with an ESA of PC because it arises concomitantly with the bleaching of the PC-band.

The very fast spectral shift of the bleaching from 620 nm to 630 nm during the first 400 fs is in agreement with model calculations by Sauer and Scheer [175], suggesting a fast 370 fs kinetics that was attributed to a relaxation between two excitonic states formed as the result of the excitonic interaction between pigments in adjacent subunits of the PC trimers while EET within the single monomers occurs on a longer timescale, caused by the comparatively larger distance between adjacent chromophores (for arrangement and distances of pigments in PC see e.g. [264]. Similar subpicosecond recovery kinetics with t<500 fs were also found in trimeric PC [263] and APC [179] and assigned to a very fast EET between neighbouring chromophores of different monomeric subunits: α-84 and β-84 (PC).

Increasing the time delay between the pump and the probe pulse the bleaching decreases and the center peak wavelength shifts further to “red”, however, at a significantly slower time scale (Figure 80 b). This continuous spectral red shift is observed approximately until delay times of t=20 ps where the bleaching shows its maximum at 648 nm. This feature reflects another slower energy transfer process to pigments absorbing further in the red spectral range.

This spectral shift is assigned to an EET from PC to APC molecules absorbing in the spectral range between 640 nm and 650 nm. As in the case of the subpicosecond energy transfer steps the observed absorption changes cannot be attributed to specific pigments because the detected signal consists of a superposition of different spectrally closely related chromophores. At even longer delay times a new bleaching arises (Figure 80 c). It exhibits a pronounced band at around 670 nm and approaches its maximum value within a time interval of about 50 ps. This result is in agreement with the acceptor state of the 20 ps fluorescence component located at 675 nm (in fluorescence) as discussed above (see Figure 78) which is ascribed to the “red”-APC. In the spectral range of the PC absorption λ<640 nm only a small residual bleaching can be observed at these long time delays, indicating an efficient EET within the PBP-antenna as wells as the sample contains a high fraction of complete and intact antenna rods. At delay times t> 50 ps up to the limit of the detectable time window of 180 ps of the multi colour setup this 670 nm-bleaching decays without a further shift of its spectral position.

A global fit of the transient absorption data between 610 nm and 670 nm was performed using a multi-exponential decay model analogous to the one described in chap. 2.

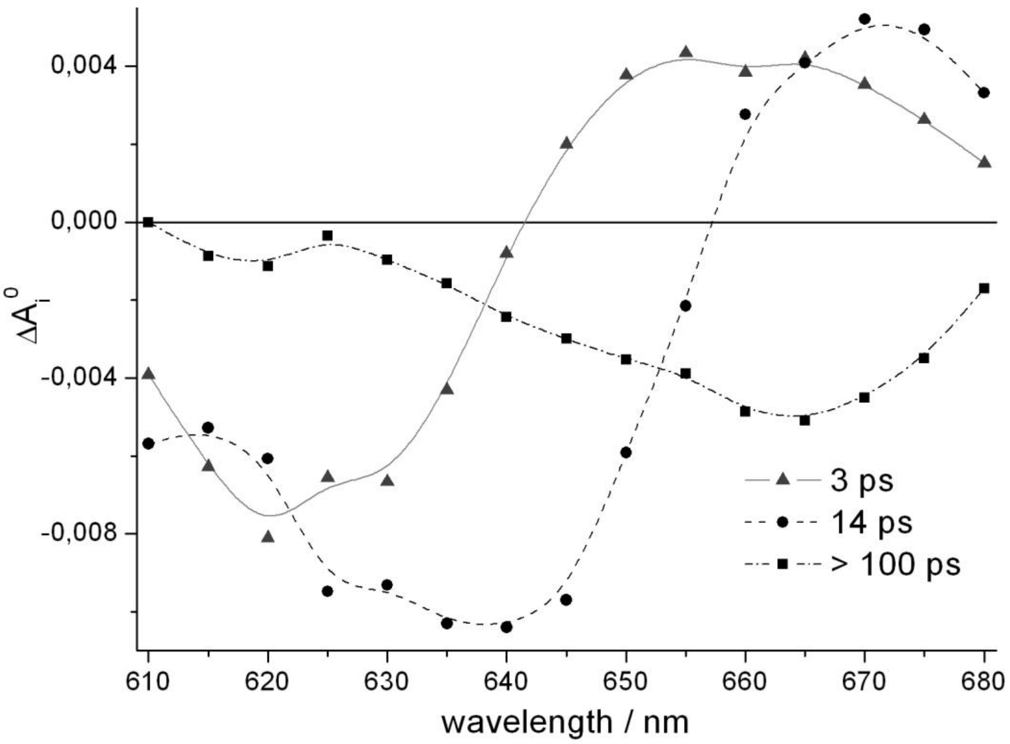

Figure 81 Decay associated spectra (DAS) gathered from the data analysis of the transient absorption spectra in Figure 80.

A reasonable global fit of the decays required three components with lifetimes of τ_1=3 ps, τ_2=14 ps, and τ_3>100 ps. The resulting decay associated spectra (DAS) are shown in Figure 81. The very fast (< 400 fs) EET component observed in Figure 80 by the very fast 620 nm to 630 nm shift of the bleaching is not included in this fit.

The DAS of the 3 ps component is characterized by a negative band around 620 nm and positive values above 642 nm. The negative band at 620 nm reflects the decay of the excited state of PC. The broad positive band above 642 nm has two different causes as can be seen by comparison with Figure 80. Between 642 nm and 655 nm the positive amplitude can be ascribed to an increase of the ground state bleaching, probably that of APC. Above 655 nm, however, this positive component is mainly due to the decay of the excited state absorption (ESA) of PC. Because the ESA decays mainly with the 3 ps component we assign the ESA to pigments in PC. The spectral distribution of the 3 ps component supports the conclusion that the excitation energy is equilibrated between all the PC-hexamers and also between the majority of the APC-molecules of the PC/APC heterohexamers with a time constant of about 3 ps.

This time constant is drastically shorter than the EET from the PC-containing rods to the APC-core in the phycobilisomes of typical cyanobacteria which has been reported to occur with a lifetime of 120 ps (see i.e. [61] and Figure 84). In a recent report Krumova et al. [265] found a transfer time of 20 ps within phycocyanin disks and an overall EET in isolated phycobilisomes of *Synechocystis sp.* that occurs with a time constant of 84 ps.

Mimuro et al. suggested, that the direction of the energy flow inside PC disks is from the outside to the inside and that the EET between the PC trimers occurs almost exclusively through the β-84 chromophores [264]. The presence of APC inside the antenna rods leading to a higher energy gradient can explain the much faster PC-APC EET in *A.marina*.

The DAS of the 14 ps decay component shows a similar course as the 3 ps component but it is shifted by about 20 nm to the red. It exhibits a broad negative band ranging from <610 nm to 657 nm with a maximum around 640 nm where the absorption of APC has its center wavelength and a positive band for $\lambda > 655$ nm with a maximum at 670 nm. These characteristics suggest that the 14 ps decay component reflects an EET from APC in the PC/APC-heterohexamer to a pigment absorbing at 670 nm. In analogy to the terminal emitters in the phycobilisomes of other cyanobacteria [256, 266, 267], we assume that this 670 nm pigment could be an APC containing linker protein that connects the rod antenna of *A.marina* with the thylakoid membrane and transfers the excitation energy to the Chl *d* of PS II. The assignment of this linker to APC is in line with the statistical consideration in chapter 5.2.1, where it was found, that the total amount of APC is somewhat higher than the ratio of 63:6 (PC:APC chromophores), i.e. 8:1 (PC:APC) or smaller, that results from the assumption that the antenna rods consist of 3 homohexamers (PC) and 1 heterohexamer APC. Interestingly the second derivative of the absorption spectra in Figure 75 has also a shoulder in the 665-675 nm range which is also present in the second derivative of the PBP absorption spectrum of [186]. This feature might be an indication for the presence of a red-shifted APC.

The results obtained on *A.marina* with the sensitive technique of TWCSPC show that the time-constants that are determined for different EET processes inside the whole cells are in agreement with the spectroscopic measurements of isolated PBP antenna complexes to demonstrate that the preparation process did not harm the molecular configuration of the PBP.

The ultrafast dynamics inside the PBP antenna on the fs-timescale resolved by using fs-absorption spectroscopy with high excitation energies requires samples of highest optical quality with low scattering coefficients to achieve a sufficient signal-to-noise ratio.

The ps fluorescence spectroscopic studies performed on isolated PBP complexes and living cells are in good agreement with the time-constants that are found with fs-absorption spectroscopy (see [2, 44]) and therefore ensure that the high excitation intensity of the fs laser flashes does not disturb the natural pathways of EET or even destroy the sample.

5.3 Simulation of the excited state dynamics in *A.marina*

Figure 82a) shows a typical DAS gathered from TWCSPC spectroscopy on whole cells of *A.marina*. The values of the long decay components in the Chl *d* regime are given by time constants of 400 ps (blue triangles) and 900 ps (black circles) that differ slightly from the statistically evaluated data exhibiting time constants of 630 ps (+/- 30 ps) and 1.2 ns (+/- 0.1 ns) measured in 2005 (see [54] and chap. 2.2). It has to be pointed out that these values differ between different cells and different illumination conditions. The main focus of the simulated exciton dynamics is the fast fluorescence decay with time constants of 20 ps (green triangles) and 80 ps (red squares). These values are found to be widely invariant between all investigated cells of *A.marina*. Therefore the mentioned deviations in the Chl *d* dynamics are not relevant for the following conclusions.

The simulation shown in Figure 82 b) is based on the assumption, that the EET between the PC trimers occurs almost exclusively through the β-84 chromophores [264]. In addition about 3-6 chromophores of the trimeric PC disk should be involved into the EET inside the PC disc which occurs from outside to inside of the PC trimer [264]. Therefore the excitation energy is trapped at the β-84 chromophore inside of a trimer first and subsequently funneled to the APC chromophores and the terminal emitter (TE). The pathway of EET is guided by "fluorescing" chromophores in accordance with calculations of Suter and Holzwarth that were done for PBS [226]. The scheme that was used for the simulation shown in Figure 82 b) is presented in Figure 83.

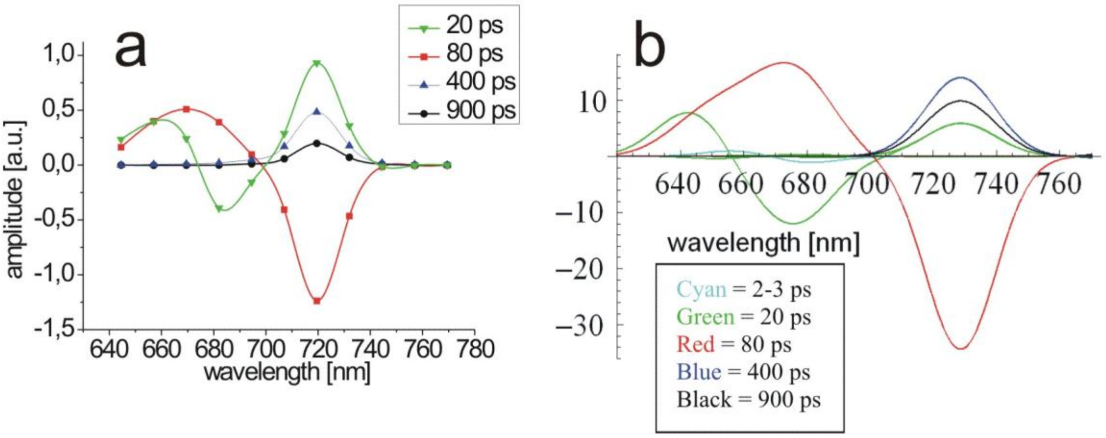

Figure 82 a) measured DAS of *A.marina* after excitation with 632 nm at room temperature. The simulated DAS is shown in panel b). The graphics was published in [52].

The results presented in Figure 82 a) show the fluorescence decay of the PBP (640 – 700 nm) with the dominating 80 ps kinetics (red squares) and the additional fast fluorescence decay component with a time constant of 20 ps (green triangles) found in the region between 640 and 660 nm while a pronounced rise kinetics of the 20 ps time constant is found around 680 nm and the rise kinetics of the 80 ps component is found at 720 nm. We simulated a situation where 22 out of the 69 chromophores found in the PBP antenna of *A.marina* were involved in EET. The simulations presented in this paper were performed by a simplified model of the PBP antenna containing 17 PC chromophores with emission wavelengths between 638 nm and 654 nm, 5 APC chromophores with emission wavelengths between 660 nm and 680 nm, 5 Chl *d* pigments with emission wavelengths between 723 nm and 732 nm and two radical pairs similar.

For the simulation the EET between different PC and APC molecules in the PBP antenna is set to 400 fs as found by Theiss [2, 44, 56]. The EET from the “red” APC molecule (TE) to Chl *d* is set to 30 ps and the EET between the Chl *d* molecules in the Chl containing core antenna is set to 100 fs. (see Figure 83). For the sake of simplicity only four PC, two different APC molecules and four acceptor states of Chl *d* are explicitly shown in this scheme (Figure 83). In addition it has to be clearly pointed out that the EET in the Chl antenna of the PS II also exhibits rate limting steps in the range of 5 ps to 50 ps for EET between CP 43/ CP 47 and the reaction center [6, 125]. The charge separation and stabilization in the core complex was simulated as found for *Synechocystis* shown in Figure 74 (see chap. 5.1). However it was not the aim of this simulation to analyse the Chl *d* dynamics but the EET from the PC and APC containing PBP antenna via the terminal emitter to the core complex. This EET is independent from the coupling scheme of the Chl *d* containing subunits und ET processes in the core complex.

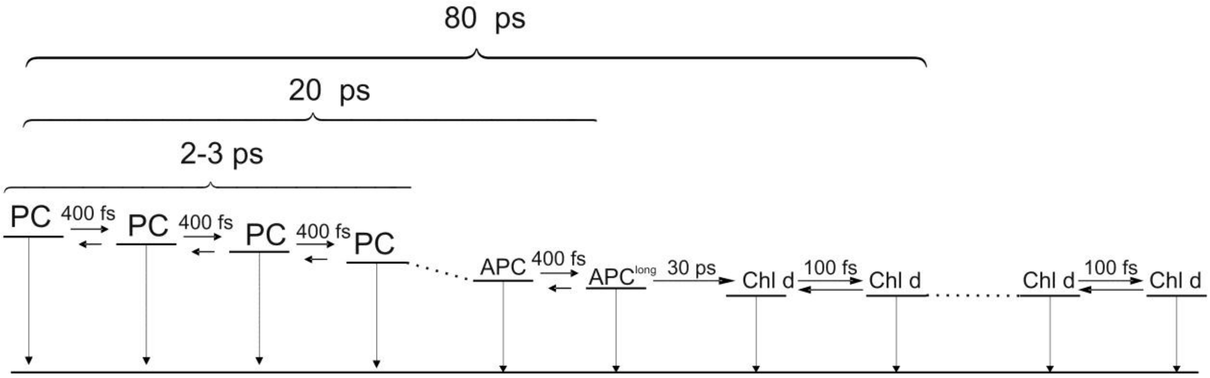

Figure 83: Scheme for simulating the data presented in Figure 82 a). The simulated DAS are shown in Figure 82 b)

The simulation results presented in Figure 82 b) show that the experimental data can be simulated by assuming equally coupled PC and APC molecules in the PBP antenna as shown in Figure 83. It turned out that all values found in the fluorescence decay kinetics should be understood as “effective” transfer times which can not necessarily be identified with rate constants for single EET steps. The 2-3 ps kinetics most probably describe the overall relaxation between several PC pigments while the 20 ps component describes the overall relaxation from PC, APC and red APC (TE) in the linker protein. The exact value of the EET transfer step from the TE to Chl *d* depends on the number of chromophores involved in the EET. If only 8 instead of 17 PC molecules are used in the simulation, this value prolongates to 40 ps instead of 30 ps, respectively (data not shown). The TE, which most probably is the long wavelength APC around 680 nm (APC^{long}) found by Theiss et al. gives rise to the negative amplitude (rise kinetics) of the 20 ps component at 680 nm. Variations of the time constants in the model of Figure 83 reveal that the 20 ps component of the experimental data (Figure 82 a)) can be explained by EET along equally coupled PC/APC molecules. A rate limiting step between PC and APC or APC and APC^{long} can also explain the 20 ps component (data not shown). But in all cases the overall EET time from the PBP to the Chl *d* is found to be 80 ps in the model only if a transfer time of max. 30 - 40 ps is set for the inverse transition probability between APC^{long} and Chl *d*.

The decay time constants of the Chl *d* (400 ps and 900 ps at 725 nm) are explained by the electron transfer processes in the PS II (see [43, 54, 161]). The diffusion along the PC molecules leads to additional fast components of 2-3 ps with very small amplitude (cyan curve in Figure 82 a)) which can not be resolved in our experiment.

The simulation presented in Figure 82 b) fits the data presented in Figure 82 a), except of the large amplitude of the 20 ps component (green curve) dominating in the measurement at 725 nm. This effect probably originates from PS I fluorescence at 725 nm as investigated in [54, 161]. The simulations are performed for the dynamics of the PS II only and therefore can not reproduce the large fraction of the 20 ps component which mainly results from fast PS I fluorescence.

The simulation exhibits that in fluorescence spectroscopy the measurement data reflects apparent time constants for EET processes. If an ensemble of several energetic states couples to an acceptor then the fluorescence dynamics summarizes the diffusion of excitation in the donor states and the EET process. The 10-20 ps EET component (green curve of Figure 82) is also found in the fluorescence emission of isolated PBP. Therefore the fluorescence spectroscopic data reveals that the EET along the whole PBP antenna takes place within a time of about 20 ps.

There exist two alternative explanations for this 10-20 ps component: i) after very fast equilibration of the excitation energy transfer the overall process is limited by a single EET step between two molecules, e.g. APC and TE or ii) the 10-20 ps component results from the equilibration among all equally coupled molecules within the PBP antenna. The latter model was evaluated in the study presented here and the results show that the simulated DAS fits the experimental data (compare Figure 82 a) and Figure 82 b)). But in fact the experimental data can not be used to distinguish accurately between these both options. For a detailed experimental study of rate limiting steps in photosynthetic complex systems complementary techniques (e.g. chemical dissociation of bthe complexes or mutants with PBS of different size) have to be used to draw unambiguous conclusions.

In both cases (i) and ii)) the overall EET from the PBP to the Chl *d* is found to appear as a 70-80 ps component in the fluorescence data if the inverse transition probability between APC^{long} (the TE) and Chl *d* is about 30 ps. The reason for this prolongated “apparent” decay time are the entropy effects of the degenerated PC states found in the PBP antenna structure.

Based on a Förster type EET the distance for the PBP/Chl *d* system calculates to be 2.7 nm if a time constant of 30 ps for the EET between the TE and the primary acceptor in the Chl *d* antenna is taken into account.

5.4 Summary excitation energy transfer

According to the results presented in the previous sections the excitation energy transfer in the antenna complexes of *A.marina* can be summarized as shown in Figure 84, left side. In this scheme it is assumed that the PBP antenna of *A.marina* resembles the rods of the phycobilisomes in common cyanobacteria with the main exception, that the hexamer closest to the thylakoid membrane is a heterohexamer consisting of one PC- and one APC-trimer as suggested by Marquardt et al. [183]. The EET from PC to Chl *d* is characterized by four kinetic components with lifetimes of < 400 fs, 3ps, 14 ps and 70 ps. The red arrows in Figure 84 exhibit our own evaluation results while literature values are marked black. According to the simulation presented in chap. 5.3 we ascribe an EET step of 30-40 ps for the EET from the TE (linker APC) to Chl *d*.

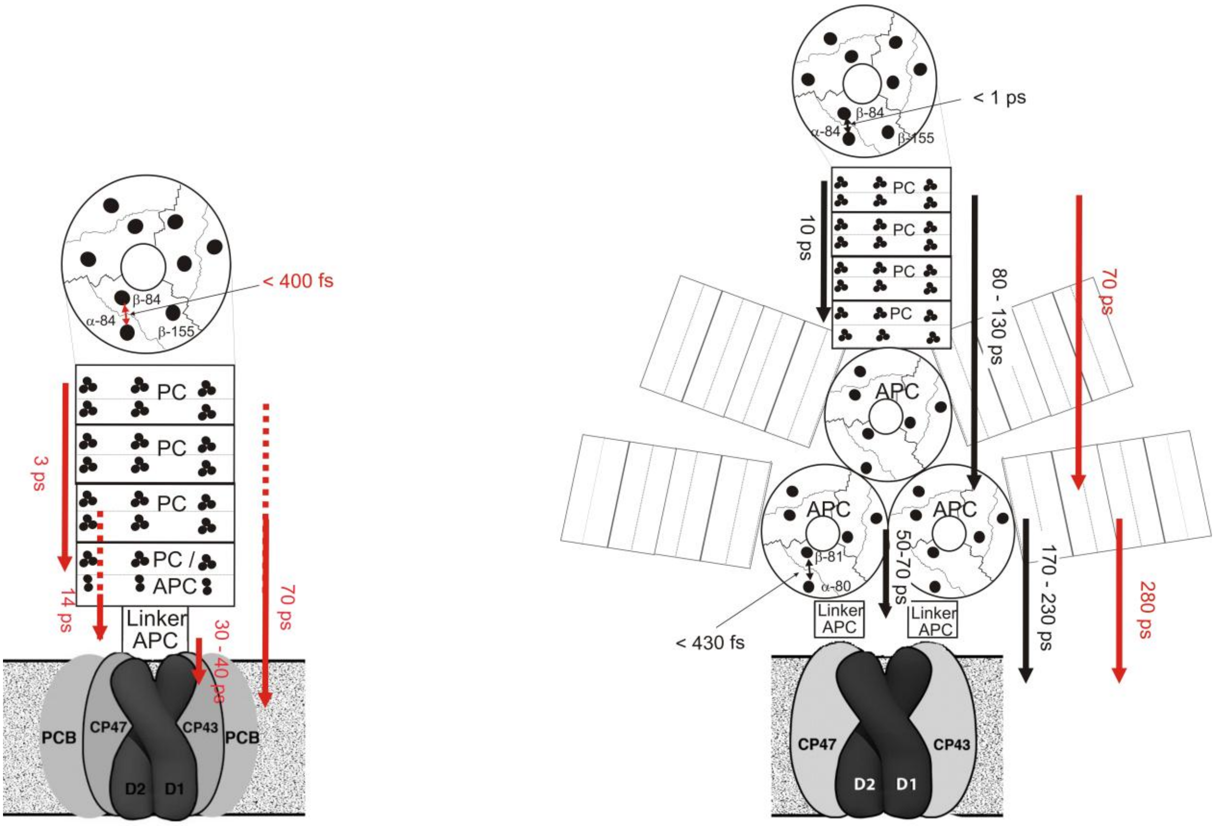

Figure 84: Kinetics of excitation energy transfer (EET) processes in *A.marina* and in the cyanobacterium *Synechococcus* 6301 as published in [56]. left panel: Model Scheme for of the excitation energy processes (EET) inside the PBP antenna rod and between the PBP antenna and Chl d in a A. marina. At the top the model scheme of the PC trimer with its bilin chromophores is shown. Right panel: Model Scheme and time constants for the EET inside the phycobilisomes of Synechococcus 6301 and from there to the RC giving a resúmé of the literature [60, 61, 177, 178, 180, 226, 257].

The < 400 fs process is observed upon excitation of PC at 618 nm in the transient absorption spectra as a very fast shift of the maximum of the initial bleaching from 620 nm to 630 nm in less than 400 fs (see Figure 80). In agreement with observations in PC trimers from other cyanobacteria [177, 263], and model calculations based on Förster theory [175], we assign this component to an EET from the α–84 to the β–84 chromophore in different monomeric subunits of PC trimers of the PBP antenna. From the transient absorption data presented in chapter 5.2.2 we cannot decide, whether this process reflects an EET between localized states of the α–84 and β–84 chromophores [178] or a relaxation between two excitonic states formed by the excitonic interaction between these two pigments [268].

Figure 84, right side, shows a scheme with the range of time constants for EET processes in *Synechococcus 6301* as reported in literature (black arrows) in comparison to our own findings obtained on Synechocystis (red arrows, compare Figure 73 and Figure 74). The equilibration along the trimeric PC disks in the PC containing rod appears with a typical rate of about (10 ps)$^{-1}$ [257]. Based on experimental results from ps-studies [226] presented a random walk model for the EET in the PC rods of Synechococcus 6301 and calculated rates of (10 ps)$^{-1}$ to (3.3 ps)$^{-1}$ for single step EET between trimeric PC disks and about (25 ps)$^{-1}$ - (40 ps)$^{-1}$ for the EET from the innermost PC trimer to the APC core. For the overall EET from a PC rod containing 4 hexamers to the APC core the literature reports rate constants of (80 ps)$^{-1}$ to (120 ps)$^{-1}$ ([60] and ref. therein, [226], [257], [61]) (Figure 84, right side). Our own findings obtained at a slightly different organism, *Synechocystis*, did not resolve the involvement of an APC bound to the linker molecule but was sufficiently simulated with time constants of 70 ps for the EET from PC to APC and 280 ps from APC to the Chl *a* containing membrane integral antenna complex (Figure 73 and Figure 74).

In contrast, in *A.marina* where APC and PC share the same hexamer, the PC to APC EET occurs with a rate constant of only (3 ps)$^{-1}$ (Figure 84, left panel). This is at least 8 times faster than the fastest EET rate reported from the innermost PC trimer to the APC core in phycobilisomes as reported in [226] and even faster than the single step EET between adjacent trimers in pure PC rods of other cyanobacteria. The 14 ps component is observed in the DAS of the transient absorption spectra as a decay of a bleaching at 640 nm and a rise of a bleaching at 670 nm. We assign this component tentatively to an EET from APC (absorbing at 640 nm) to a low energy APC (bound to a linker protein) that transfers it´s energy to Chl d with a time constant of 30-40 ps and therefore facilitates an efficient overall EET from the PBP antenna to Chl *d* which occurs with a rate constant of (70 ps)$^{-1}$. This is more than three times faster than the EET transfer from the APC core to Chl *a* in *Synechococcus 6301* which occurs typically with (170 - 120 ps)$^{-1}$ [61].

The very fast EET in *A.marina* from PC to APC then to Chl *d* reflects the unique feature of *A. marina* due to its tiny rod shaped PBP antenna where PC and APC share the same heterohexamer instead of huge phycobilisomes with rods containing PC only and an additional APC core.

6 HYBRID COMPLEXES OF PBP ANTENNA COMPLEXES AND CDSE/ZNS NANOPARTICLES

The targeted design of the optical properties of artificial and particularly biomimetic systems will lead to innovative units with high efficiency of light absorption and directed EET. Such systems are the first step into a new research field: Hybrid systems for artificial photosynthesis, consisting for example of highly absorbent nanostructures and photosynthetic reaction centers or formed by biological light harvesting systems functionally coupled to solar cells.

The external power conversion efficiency after immobilization of photosynthetic reaction centers (RCs) on electrodes is low mainly for two reasons:

a) electron transfer (ET) between RC and electrode is hampered due to localization of ET cofactors inside the protein matrix, thus giving rise to a rather long electron tunneling distance and

b) the optical density of the monolayer of RCs immobilised on the electrode surface is very low (about 0.01) and therefore the light capture is negligibly small.

In addition hybrid complexes of photosynthetic subunits and artificial nanostructures are unstable due to degradation processes of pigment-protein complexes.

These problems have to be solved for using pigment-protein-complexes as parts of electronic devices.

We have started investigations on the mechanisms of interaction between various chromophor-protein complexes and semiconducting CdSe/ZnS and CdTe nanocrystals denoted as quantum dots (QDs) in the following. It was shown that QDs can form hybrid structures with fluorescent proteins and phycobiliproteins from cyanobacteria. The efficiency of EET can reach values of up to 90 % [51, 53].

QDs that were functionalized at the surface with acidic groups interact electrostatically with proteins and can serve as efficient artificial donors and acceptors in hybrid systems consisting of QDs and proteins. EET, ET reactions and protein reorganization in these hybrid systems were studied experimentally and analyzed within the framework of theoretical models of rate equations.

In this chapter hybrid systems will be described that are formed from quantum dots (CdSe/ZnS, CdTe and InAs) as donors of electronic excitation energy and PBP complexes as acceptors. Absorption and time integrated fluorescence spectroscopy was applied to characterize the steady state optical properties of these hybrid systems. Kinetics and efficiency of EET from QDs to photosynthetic pigment-protein-complexes are monitored by using time-resolved fluorescence spectroscopy.

Figure 85 presents a schematic view of the PBP antenna of *A.marina* and the structure of the QDs used in this study. For the detailed structure and electronic properties of these QDs see also [269] and [270] and references therein. The description of EET processes inside QDs modelled by rate equations is found in ref. [270].

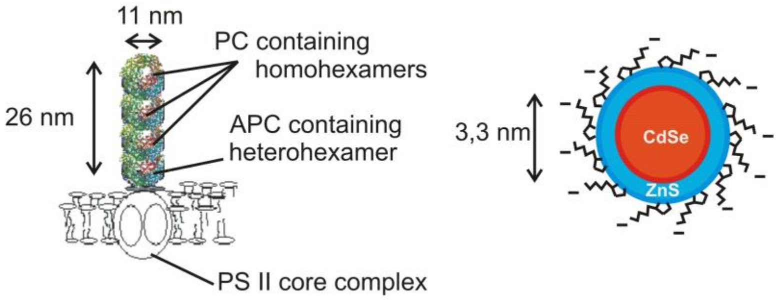

Figure 85: Scheme of the organisation of the PBP antenna in *A.marina* (left side) and structure of the CdSe/ZnS-530-QDs with fluorescence maximum at 530 nm (right side) used in this study as published in [51].

The PBPs of *A. marina* are thoroughly described in chapter 5. For the coupled quantum dots we used the water soluble CdSe/ZnS QDs exhibiting a 530 nm fluorescence maximum (Green530) from NanoFluorescent Materials LTD, Ukraine. The schematic overall structure of the QDs used in this study is shown on the right side of Figure 85. The QDs consist of a Cd/Se core of 3.3 nm diameter and a ZnS shell which is functionalised at the surface by dihydrolipoic acid ligands that are negatively charged in pH=7 solution. The chemical composition of these QDs is thoroughly described in ref. [269].

6.1 Time integrated Fluorescence emission of CdSe/ZnS-530-QD - PBP hybrid complexes

Hybrid structures of QDs-PBPs can be formed by mixing CdSe/ZnS-530-QDs and PBP at different stoichiometric rations [271, 272].

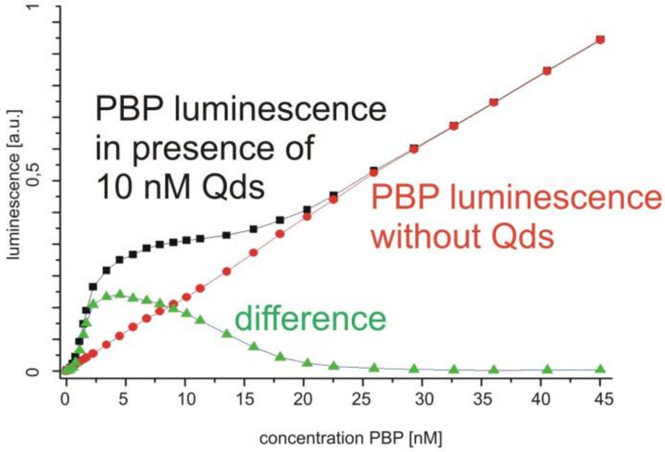

Figure 86: Overall integrated luminescence of PBP as a function of concentration without (red curve) and with 5 nM QDs added (black curve). The green curve shows the difference of the PBP luminescence with QDs in the solution and without QDs. Data is redrawn from ref. [272].

Figure 86 presents the fluorescence that is emitted by PBP complexes. Without QDs in the solution the PBP luminescence is proportional to the PBP concentration (red circles). In the presence of 5 nM QDs the PBP luminescence is enhanced (black squares). As shown by the difference between the emission with and without QDs (green triangels) this fluorescence enhancement is maximal for 5 nM PBP concentration which corresponds to a 1:1 stoichiometry of PBP and QDs.

Immediately after the addition of PBP of *A.marina* to the CdSe/ZnS-530-QDs solution at a stoichiometric ratio of 1:1 the fluorescence of the sample visible under blue excitation (405 nm) is green with a maximum at 530 nm. This green fluorescence turned into red within few seconds after combining QDs and PBP thus indicating the assembly of a functional coupling via EET from the QDs as donor to the PBPs as acceptor. After few minutes the red luminescence remains stable (data not shown).

Temperature dependency of the CdSe/ZnS-530-QD – PBP hybrid complex emission

Time integrated fluorescence measurements at different temperatures were performed in the cryostatic system as described in chap 2.1 (see Figure 32) to analyse the time constants of EET between PBP complexes and the QDs in the hybrid complexes as a function of the temperature.

For these measurements a commercial USB-connected fluorometer system with CCD array (EPP2000, Scientific Instruments, Berlin, Germany) was used with a spectral resolution of 3 nm. Excitation was performed with a pulsed 405 nm Laser diode (LDH-405, Picoquant, Berlin, Germany) delivering 60 ps FWHM pulses, driven at a repetition rate of 8 MHz.

Figure 87 shows time integrated emission spectra at different temperatures of the hybrid system containing QDs and PBP and the absorption spectrum of the PBPs which remains virtually invariant to temperature in the investigated range.

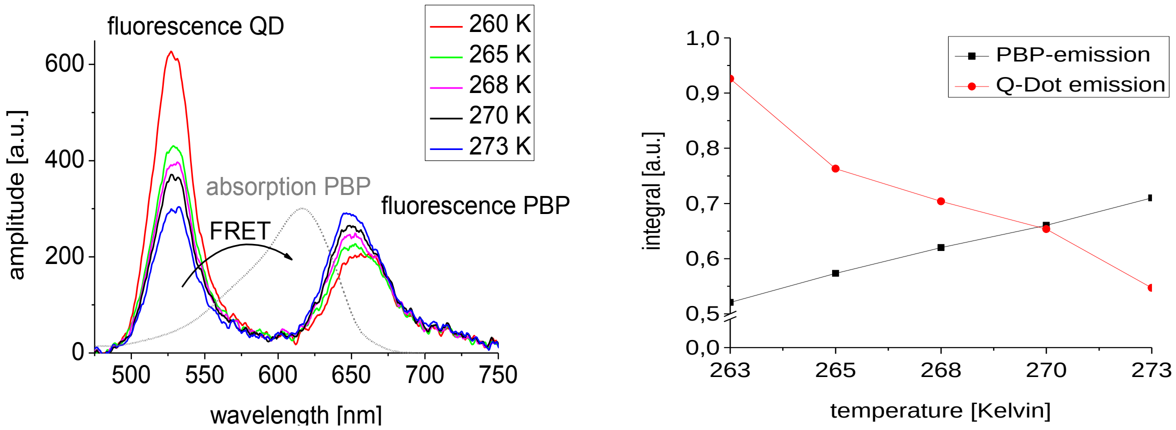

Figure 87: Left side: Time integrated fluorescence spectrum of the hybrid systems containing CdSe/ZnS-QDs and PBP antenna complexes at different temperatures after excitation with 405 nm laser pulses and absorption spectrum of the PBPs at room temperature (grey, dashed line). Right side: integral of the fluorescence spectrum of CdSe QDs (500-560 nm, red curve) and PBP antenna complexes (600-710 nm, black curve) at different temperatures. Graphics is published in [51].

At 273 K the intensity of the integrated red PBP luminescence exceeds the integrated green QD luminescence (see right side of Figure 87). In samples cooled down below 273 K (the freezing point of the solution containing QD-PBP hybrid complexes is about 270 K) the integrated fluorescence of the QDs continously increases at the expense of the PBP luminescence with decreasing temperatures (see right side of Figure 87). This effect is fully reversible, i.e. during warming up to 273 K the pronounced peak at 530 nm of the fluorescence spectrum decreases down to the original level.

6.2 Time resolved fluorescence of CdSe/ZnS QD - PBP hybrid complexes

To investigate the temperature dependent functional coupling via EET from the QDs to the PBPs in more detail, time- and wavelength correlated single photon counting as described in chap 2.1 (see Figure 32) was performed. The same excitation laser system was used as for the time integrated measurements shown in Figure 87 (405 nm laser pulses at a repetition rate of 8 MHz, 60 ps FWHM). Time resolved fluorescence measurements were performed by time- and wavelength-correlated single photon counting in the cryostatic system. The presented time resolved spectra were monitored with a photomultiplier system with a Hamamatsu R5900 16 channel multi-anode photomultiplier tube consisting of 16 separate output (anode) elements and a common cathode and dynode system (PML-16, Becker&Hickl, Germany) as described in chap. 2.1 (see Figure 30, right side). The polychromator was equipped with a 300 grooves/mm grating resulting in a spectral bandwith of the PML-16 of about 12.5 nm /channel.

The left panel of Figure 88 shows the decay curves of the 530 nm emission from the QDs at room temperature in the absence (black curve) and presence (red curve) of isolated PBP antenna rods from *A.marina* (see Figure 88, left side). The right panel shows the fluorescence decay at 660 nm from PBP antenna complexes in the absence (black curve) and presence (red curve) of CdSe- QDs.

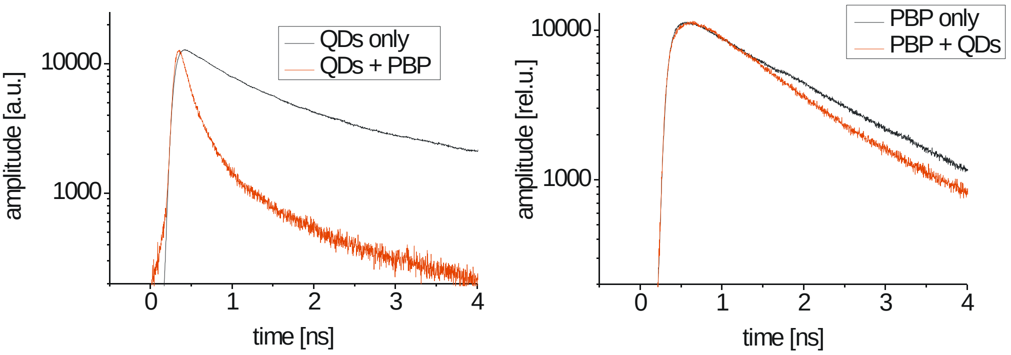

Figure 88 left side: Time course of the fluorescence emission at 530 nm from CdSe-530 QDs after excitation with 405 nm laser pulses (60 ps FWHM) at room temperature in buffer solution in the absence (black curve) and presence (red curve) of isolated PBP antenna rods of *A.marina*. Right side: Time course of the fluorescence emission at 660 nm from isolated PBP antenna rods of *A.marina* after excitation with 405 nm laser pulses (60 ps FWHM) at room temperature in the absence (black curve) and presence (red curve) of CdSe-530 QDs. All decay curves are normalized as published in [51].

The drastically accelerated decay of the 530 nm emission from the QDs is concomitant with the decrease and increase of the 530 nm and 660 nm emission, respectively, of the integrated fluorescence from QDs and PBPs (see Figure 87). This is indicative of a strong quenching of the QD fluorescence by coupled PBPs from *A.marina*. This pronounced effect reflects a highly efficient EET from the QDs to the PBPs.

The PBP fluorescence decay also slightly accelerates in the presence of QDs (compare red and black curves in the right panel of Figure 88). This effect can be explained by a change in the vibrational coupling of the PBP chromophores to the protein matrix in the QD-PBP hybrids in comparison to pure PBP that leads to dissipative relaxation channels. A careful comparison of the PBP decay curves of samples in the absence (Figure 88, right side black curve) and presence (Figure 88, right side, red curve) of QDs shows that the PBP luminescence maximum after excitation is slightly shifted towards longer times in presence of QDs (red curve) in comparison to the emission of pure PBP (black curve). The effect is very small due to the direct acceptor excitation when laser pulses of 405 nm are used.

Information on the EET time constant with best resolution from measurements of fluorescence decay curves in the whole spectral range between 500 – 700 nm can be gathered by analysing the decay associated spectra (DAS).

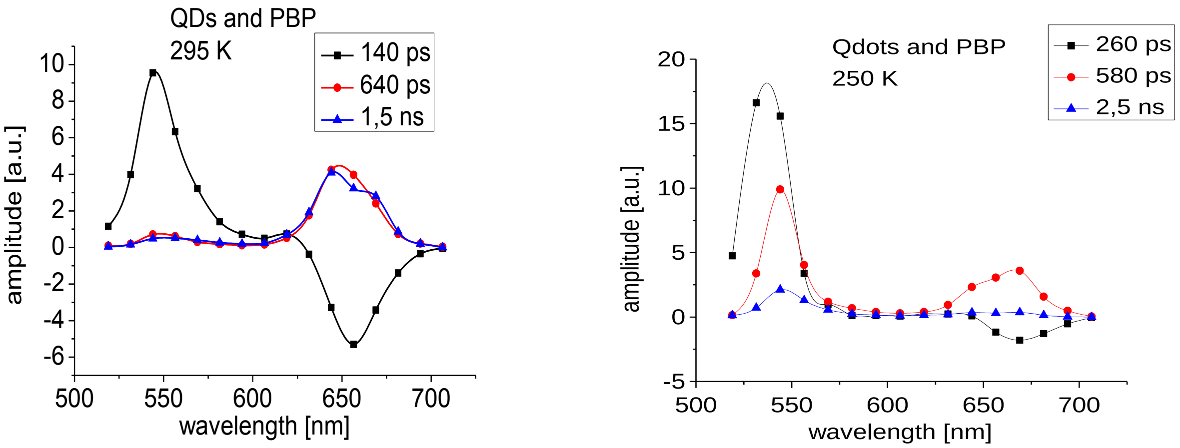

Figure 89: Decay associated spectra of CdSe-530 QDs mixed with PBP from *A.marina* after excitation with 405 nm at room temperature (295 K, left side) and 250 K, right side. Data is redrawn from [51].

Figure 89 shows the DAS of the QD-PBP hybrid complexes after excitation with 405 nm laser pulses at 295 K (left panel of Figure 89) and 250 K (right panel of Figure 89). In both cases a suitable fit of the data was achieved with three exponential components. The DAS of the measurements at 273 K is characterized by components with time constants of 140 ps (black curve), 640 ps (red curve) and 1.5 ns (blue curve) at room temperature. The spectrum of the 140 ps time constant exhibits a positive band at 530 nm and a pronounced negative peak in the region of 660 nm emission from the PBPs. This feature indicates that an EET from QDs to the PBP takes place with a time constant of 140 ps and that more than 90 % of the QDs are involved. Only small contributions with an extent of less than 10 % and time constants longer than 140 ps are found in the green region. In the spectral region of the PBP luminescence near 660 nm a pronounced rise kinetics (negative amplitude) is obtained with a time constant of 140 ps. In addition a characetristic 1,5 ns decay of the PBP luminescence was resolved which is typical for isolated PBP antenna rods and an additional 640 ps component of comparable amplitude. This 640 ps component emerges most probably from conformationally distorted PBP complexes (see ref. [43]).

A markedly different DAS pattern was found at 250 K. A suitable fit of the data was achieved with three exponential components exhibiting time constants of 250 ps (black curve), 580 ps (red curve) and 2.5 ns (blue curve). The negative amplitude in the PBP emission (670 nm) is strongly reduced in comparison to the results obtained at 295 K thus indicating that the EET from CdSe Qdots to PBP is interrupted at low temperatures below the freezing point of water. The pronounced amplitude of the 580 ps component (red curve) in the PBP emission (670 nm) indicates that a larger fraction of PBP antenna complexes is conformationally distorted in comparison to 295 K.

The results of the present study reveal that the CdSe QDs functionally couple via EET with the isolated PBP antenna from *A.marina.* This coupling is reversibly distorted at temperatures below 273 K. It seems reasonable to assume that a conformational distortion due to the freezing process is responsible for the decoupling effect.

6.3 EET between CdSe/ZnS-530-QDs and the primary acceptor in the PBP antenna

The coupling efficiency between CdSe/Zns-530-QDots and the PBP antenna of *A.marina* at room temperature was evaluated within the framework of Förster Resonance Energy Transfer (FRET) as described in chap. 3.3.2. The efficiency η_{FRET} of this EET can be calculated comparing the fluorescence intensity of the donor in the absence (I_D) and the presence (I_{DA}) of the acceptor according to eq. 95: $\eta_{FRET} = 1 - \frac{I_{DA}}{I_D}$. After equilibration of the hybrid system of QDs and PBPs at room temperature it was found that the fluorescence of the QDs diminuishes by about 75 %. A comparable result is gathered from a comparison of the average lifetime of the fluorescence decay curves of the QDs in the presence and absence of PBP. The average lifetime of the QDs in absence of PBP $\bar{\tau}_D$ was found to be about 1.1 ns at 530 nm. After addition of PBPs this value decreased to $\bar{\tau}_{DA}$ = 230 ps. In this consideration an average lifetime is taken into account instead of the multiphasic decay visible in the DAS (Figure 89). Therefore the value for the efficiency η is not the efficiency of the coupled QDs but an average efficiency that also takes into consideration the fraction of uncoupled QDs, which is estimated to be about 10 % according to the amplitude ratio of the different DAS cmponents as shown in Figure 89 (left panel). The total average leads to a value of $\eta_{FRET} = 1 - \frac{\bar{\tau}_{DA}}{\bar{\tau}_{D}} \approx 0.78$ which is in good agreement with the value of η_{FRET} = 0.75 gathered from the time integrated fluorescence.

A more accurate evaluation of the DAS shown in Figure 89 (left panel) indicates that the lifetime $\bar{\tau}_{DA}$ = 140 ps reflects only the coupled QDs, i.e. that the EET in the coupled QDs is more efficient than suggested by the average value. The time resolved results for the coupled fraction of QDs results in a value of $\eta_{FRET} = 1 - \frac{\bar{\tau}_{DA}}{\bar{\tau}_{D}} \approx 0.87$. Therefore the DAS show not only an average efficiency for FRET as found by time integrated fluorescence measurements but also allow to distinguish between the coupled and uncoupled species and therefore provides a suitable tool for the selective evaluation of the efficiency of the coupled species.

From the measured time integrated spectra of the PBP absorption and QD fluorescence (see Figure 87) one can calculate the Förster radius R_0 for the QD-PBP hybrid system as given by eq. 89:

$$R_0 = \left(A\Phi_F \frac{\kappa^2}{n^4} J(\lambda) \right)^{\frac{1}{6}}$$

where *A* is a constant (see eq. 89 for further details), Φ_F denotes the quantum yield of the QDs which is about 0.3 according to [269]. κ^2 denotes the orientation factor which is $\kappa^2 \approx 2/3$ for randomly organized QD/PBP hybrid complexes [208].

The real part of the complex refraction index of the surrounding medium is given by $n \approx 1.33$ for buffer solution.

$$J := \frac{\int_0^\infty F_D(\lambda)\varepsilon(\lambda)\lambda^4 d\lambda}{\int_0^\infty F_D(\lambda) d\lambda}$$

determines the normalized overlap integral between the normalized donor fluorescence $F_D(\lambda)$ and the acceptor extinction $\varepsilon(\lambda)$. For the QD/PBP hybrid system presented in this study a value of $J = 1{,}23 \cdot 10^{15} \frac{nm^4}{Mol \cdot cm}$ is obtained and the Förster radius is calculated to be $R_0 \approx 4.4\, nm.$

From the time resolved spectra the value of $\eta_{FRET} = 0.87$ was found for the QDs coupled to PBP and therefore the average distance between the center of a QD and the next neighbouring chromophore of PBP calculates to

$R_{12} = \left(\frac{1 - \eta_{FRET}}{\eta_{FRET}} \right)^{\frac{1}{6}} R_0 \approx 3.2\, nm$ and the rate constant fro FRET $k_{FRET}\left(R_{12}\right) = \frac{1}{\bar{\tau}_D} \left(\frac{R_0}{R_{12}} \right)^6 \approx \left(140\, ps\right)^{-1}$ according to eq. 90.

These findings are schematically summarized in Figure 90 including earlier data on the EET inside the PBP as shown in chap. 4 (see also ref. [43, 44, 51, 52, 53, 56]).

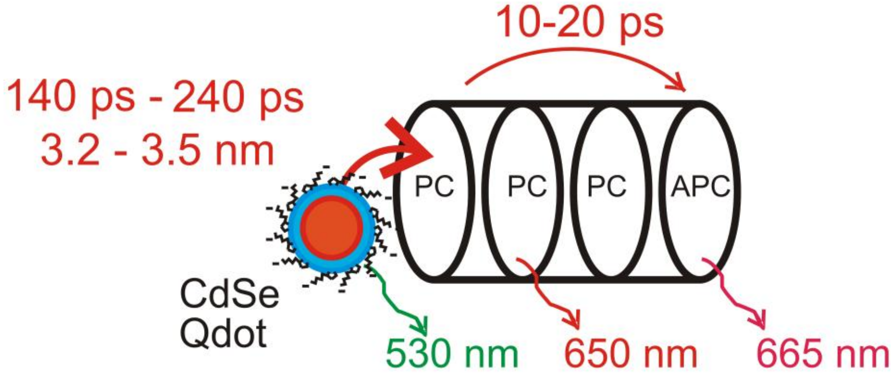

Figure 90 left side: schematic view of the CdSe/ZnS-QDs bound electrostatically to the PBP antenna of *A.marina*. The CdSeQDs exhibit fluorescence emission at 530 nm and transfer the excitation energy to the PBP antenna within 140 ps – 240 ps (red arrow) at room temperature. The luminescence of the PBP antenna occurs with maxima at 650 nm (PC) and 665 nm (APC).

Figure 90 presents a schematic view of the CdSe/ZnS-QDs bound electrostatically to the PBP antenna of *A.marina*. The CdSeQDs with fluorescence emission at 530 nm transfer the excitation energy to the PBP antenna within 140 ps (red arrow), other studies revealed time constants up to 240 ps which would correspond to a distance of 3.5 nm between the QDs and the primary acceptor pigment in the PBP antenna. Former studies showed that the equilibration along the PBP antenna (PC/APC molecules) occurs within <20 ps (see chap. 5). The luminescence of the PBP antenna is characterized by maxima at 650 nm (PC) and 665 nm (APC).

It was found that a significant improvement of the fit of the QD luminescence can be achieved when the decay curves are fit with n=3 decay components (χ_r^2 = 1.3 – 1.4) instead of n=2 decay components (χ_r^2 > 2), while no significant improvement was obtained with n=4 decay components. This finding is in line with literature data on a multiphasic fluorescence decay of the CdSe/ZnS quantum dots due to distinguishable internal and surface localized states in single QDs [270] and sample heterogeinities always found in QD ensembles [273].

The investigation of the FRET efficiency between CdSe/ZnS nanocrystals and PBP complexes revealed that the temperature dependent value of the spectral overlap integral J can be described by a Boltzmann distribution at low temperatures but in addition marked configurational changes must occur around 0°C. This transition leads to an interruption of the EET at low temperatures that can not be explained by spectral narrowing at lower temperatures. Further details of these findings are described in refs. [51] and [53].

6.4 Applications of hybrid structures containing photosynthetic light harvesting complexes.

Hybrid systems consisting of artificial nanostructures and complexes of biological origin offer a wide variety of applications in photovoltaics, optoelectronics, sensing, molecular imaging and medical applications. Complexes isolated from the photosynthetic apparatus provide functionally optimized nanoscale devices for the construction of light driven operational units.

In photovoltaics thin film solar cells are widely used to save costs and to achieve high efficiency for charge separation after light absorption. Thick donor layers in solar cells exhibit the advantage of high absorption coefficients but the disadvantage of high recombination probabilities after exciton generation due to long diffusion pathways of the excitons to the p-n-junction. We have recently shown that the size of biological light harvesting complexes is limited to a functional domain size of about 200 LHCII trimers (see chap. 1.3.1) due to limited excitation diffusion range, recombination and dissipative reaction pathways that are unavoidable in all materials [45].

Losses due to recombination are reduced in thin film solar cells but the thickness of such cells is restricted to be at least 1 µm for amorphous silicon to achieve high absorption coefficients. In that case recombination occurs because the free diffusion length of the excitons is only 200-300 nm. One could consider the possibility of thinner layers width reduced absorption in the Si layer. These structures would have the advantage of a high yield of charge separation using highly absorbing pigment-protein complexes as additional units in hybrid structures suitable for photovoltaics as schematically shown in Figure 91. If excitons can be transferred into the semiconducting material with high efficiency, one could introduce ultra thin donor layers with a thickness of < 10 µm exhibiting a highly efficient charge separation.

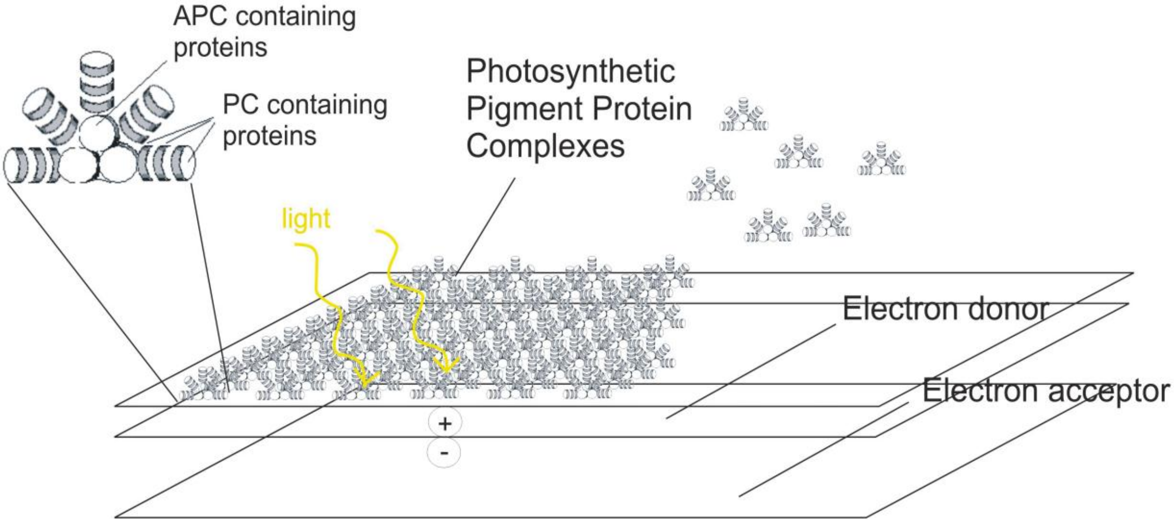

Figure 91: Schematic view of possible hybrid solar cells containing two semiconductor layers with p-n-transition and additional PBS light harvesting complexes (for details see chap. 1.3.4).

The most promising approach of artificial photosynthesis might be the use of hydrogen generating organisms like photosynthetic bacteria or modified green algae that produce hydrogen during illumination in their natural habitat. Possibly one could also think about using plant structures or biomimetic artificial structures as advanced biomimetic fuel cells. The example of a visionary setup is depicted in Figure 92.

The principle of the spatial separation to generate a directed flux of charge has been developed by nature in form of the thylakoid membrane in photosynthetic organisms. In plants the thylakoid membrane separates the interior of chloroplasts into lumen and stroma. In principe such system could be connected to represent the two electrodes of a light driven current source as schematically shown in Figure 92. It seems attractive to speculate about a realization that is artifiacially constructued in a biomimetic way and functions similar to the chloroplast fuel cell shown in Figure 92. Usually biomimetic devices for artificial photosynthesis are assembled in the laboratory exhibiting nanometer-scale dimension and mimicing stable light-induced charge separation of photosynthetic reaction centers (RCs). The chloroplast fuel cell shown in Figure 92 illustrates the necessity of electrodes that are in contact to the different sides of the thylakoid membrane. Usually such devices would be realized by stacking natural and/or artificial thylakoids onto conductive layers. For an overview on concepts of artificial reaction centers, light harvesting complexes and antenna–reaction center systems see chap. 1.5, ref. [73] and references therein.

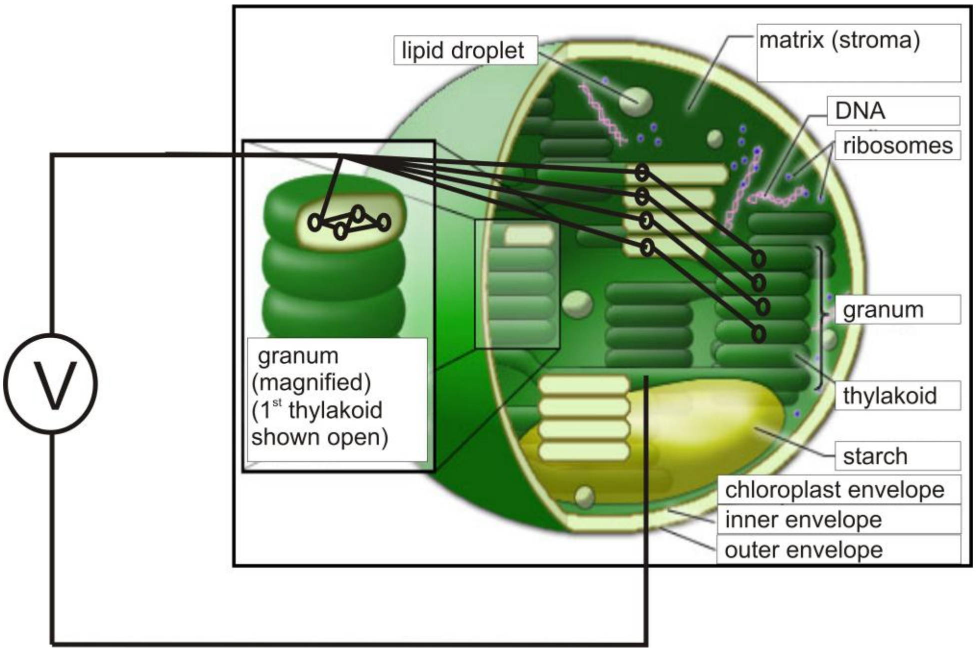

Figure 92: Artificial photosynthetic solar cell.
Inside the intact chloroplasts the thylakoid lumen is connected to a bundle of nanotube electrodes.

As shown in Figure 92 the thylakoid lumen inside the chloroplast is connected to an electrode bundle formed by conductive nanotubes that are all connected outside the chloroplast. During the light reaction a proton gardient is generated between the thylakoid lumen and the stroma due to the transport of electrons from the lumenal side to the stroma side of the thylakoid membrane and coupled protolytic reactions. The stroma is connected with the complementary electrode. To rise the efficiency of the cell one could inhibit or genetically knock out or modify the ATP synthetase which is driven by the proton gradient inside the thylakoid membrane and funnel the charges through the artificial circuit.

In both cases, for biological fuel cells or hydrogen generating organisms, it is a promising task to introduce artificial evolution into such systems. Organisms expressing or coupling to self assembled nanostructures like the electrode nanotubes shown in Figure 92 might be optimized for the desired challenges. Evolution of such organisms that is coupled with an artificial selection process could be used to select and grow enhanced species after genetic modification or active genetic engineering of the cells.

The use of directed genetic evolution of biological systems turns out to be a powerful tool in manipulating efficiently the interaction between molecular structures and metallic/ semiconductor surfaces, because the adhesion between the proteins of the evolving species and metallic structures can be used to select the optimised organisms with help of a kind of “metal filter” . Such an approach was recently shown for bacteriophages expressing metal adhesive peptides in contact to gold nanoparticles. For a review see [274] and references therein.

Suitable bacterial photovoltaic systems could be produced through continuous mutation and selection routines of the “best match” as shown in Figure 93.

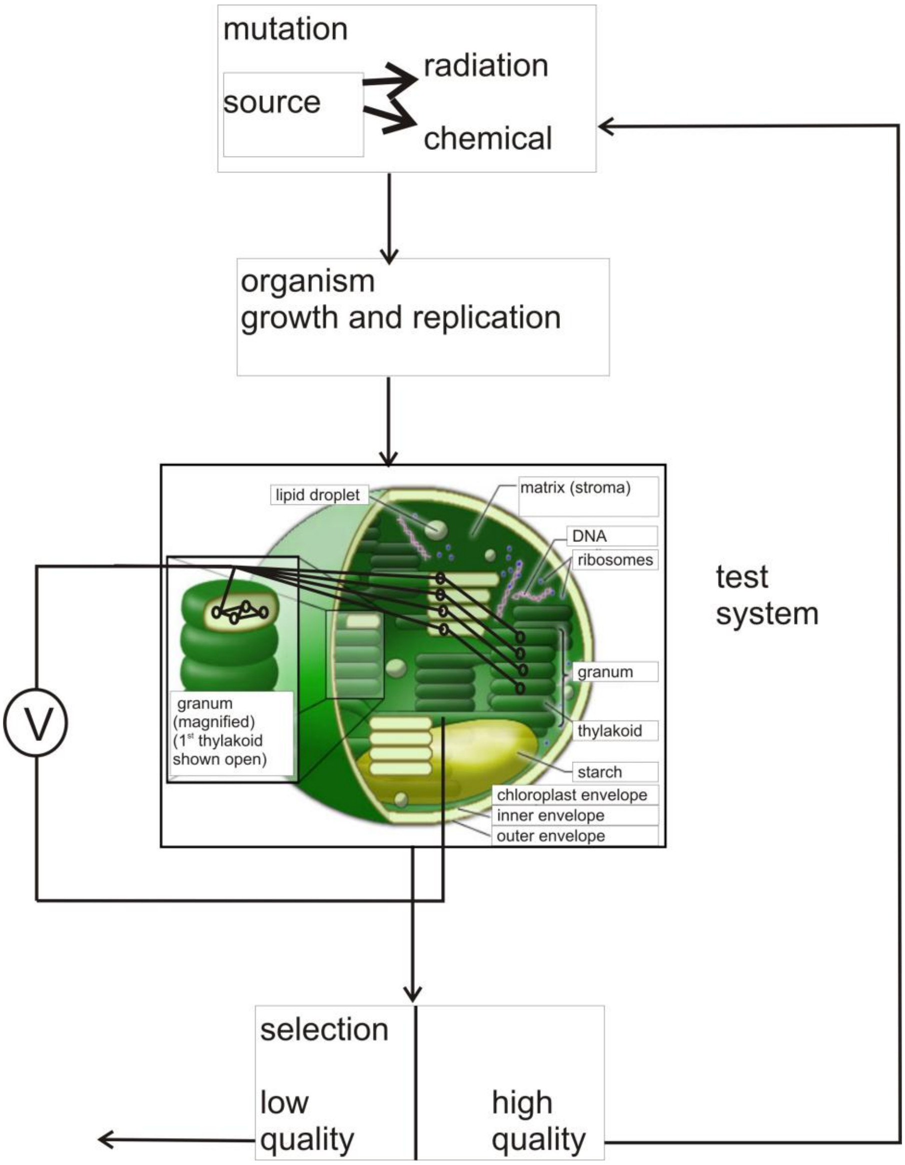

Figure 93: Scheme for an evolutionary strategy for improving the desired properties of living organisms. After passive or active mutation (spontaneous, introduced by irradiation or chemicals, actively by genetic engineering) the organisms are grown in a vessel. These modified organisms are subjected to a test system that is coupled with a selection process. This process selects the most suitable species that undergo the next step of mutation.

The growth and replication of the genetic pool is established in solution in a growth vessel. After accomplishing the growth phase the organisms are divided into several groups by a selection mechanism. After a check for suitability the “best mach” is used for further replication (see Figure 93). Fast mutation rates assure various surface modifications and are realized through exposition of the genetic pool to radiation, chemical substances or are introduced by active genetic engineering.

A more efficient evolutionary algorithm would mutate the whole growth pool during replication by radiation or mutagenetic chemical compounds.

From that pool the "best" mutations have to be identified and selected by a targeted selection mechanism (e.g. by automatically grabbing out the cells with the highest photovoltaic activity, i.e. the cells that deliver the highest current in a fuel cell like system as shown in Figure 92 are actively selected). One criterion might be the achieved photocurrent, another criterion could be the adhesion of the organisms to semiconducting surfaces. The organisms could be brought to contact with the semiconductors and afterwards the less sticky ones are washed away. The selected ones are mutated and replicated again. Very promising seems the approach to use light induced stress as selection criterion. One could shine in a light spectrum and light intensity that leads to photooxidation of the biological structures if the organism does not develop into the desired direction. Such and similar evolutionary approaches are topic of our future research.

7 THE PS II OF WHOLE LEAVES OF *A.THALIANA*

R. Steffen et al. developed a compact fluorescence spectroscopic setup suitable to monitor single (laser) flash induced transient changes of the fluorescence quantum yield (SFITFY) in cell suspensions and whole leaves in the time domain from 100 ns to 10 s [81, 118, 119].

In former studies we used data gathered by this setup to describe the PS II dynamics in whole cells of *Chlorella pyrenoidosa Chick* according to a reaction pattern based on the formalism of rate equations as described in chap. 3.2 [57]. Later it was shown that the intensity dependent pattern of SFITFY traces measured in whole leaves of *Arabidopsis Thaliana* at four different intensities of the actinic laser flash can be described with one set of model parameters [58]. These findings are shortly outlined in this chapter. Details regarding the measurement setup [81, 119], the sample condition [57, 119, 120] and the discussion of the metabolic relevance of the gathered results [57, 58] are described in the cited references. The following results are already published in [58].

The PS II model presented by Belyaeva et al. [57] was improved in order to permit consistent simulation of SFITFY curves that were measured by Steffen and coworkers [119] on whole leaves of *Arabidopsis (A.) thaliana* at four different energies of the actinic flash.

7.1 Single Flash induced transient fluorescence yield measurement data

Dark adapted leaves of *Arabidopsis thaliana* wild type plants (ecotype Columbia-2 (Col-2)) were excited with a single actinic flash (λ=532 nm and fwhm = 10 ns) from a frequency-doubled Nd-YAG laser. The maximum energy of the actinic flash was 28 mJ/(cm^2·flash) which is equivalent to $7.5 \cdot 10^{16}$ photons/(cm^2·flash). The time-course of flash-induced changes of the relative fluorescence quantum yield was obtained by monitoring the fluorescence emission due to excitation by a train of weak measuring light pulses supplied by an array containing a set of LEDs (λ_{max} = 660 nm). The dark time inbetween two measuring light pulses was varied in a wide range from 2 µs (first measuring pulse at 100 ns, second measuring pulse at 2 µs after the actinic flash) up to 0.5 s (in the time domain > 1 s after the actinic flash).

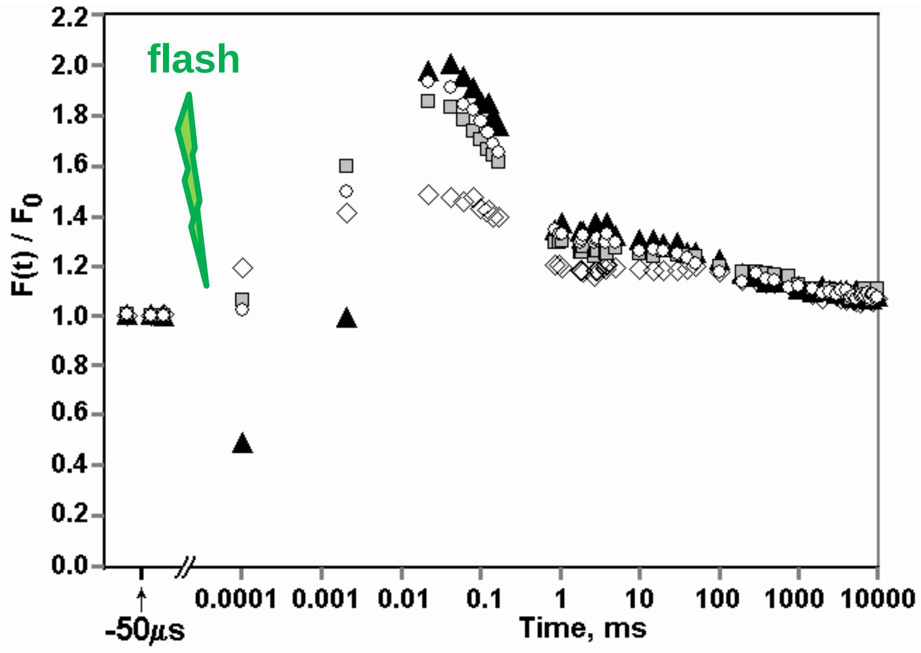

Figure 94: Experimental data of fluorescence yield changes (SFITFY curves) induced in whole leaves of *Arabidopsis thaliana* wild type plants by excitation with a single actinic 10 ns laser flash of different energy: $7.5{\cdot}10^{16}$ photons/ ($cm^2{\cdot}$flash) (triangles), $6.2{\cdot}10^{15}$ photons/ ($cm^2{\cdot}$flash) (circles), $3.0{\cdot}10^{15}$ photons/ ($cm^2{\cdot}$flash) (squares) and $5.4{\cdot}10^{14}$ photons/ ($cm^2{\cdot}$flash) (diamonds). The data are redrawn from ref. [119]. The green arrow symbolizes the excitation by the actinic laser flash.

Figure **94** shows experimental SFITFY data of Steffen and coworkers [119] obtained by excitation of dark adapted whole leaves of *Arabidopsis thaliana* wild type with single actinic laser flashes of different energy. The signal F_0 (–50 µs) before the actinic flash monitors the fluorescence induced by the weak measuring pulses. It reflects the normalized fluorescence quantum yield of dark adapted PS II complexes and is used to normalize the time dependent SFITFY curve monitored by a sequence of weak measuring light pulses in the range from 100 ns to 10 s after the actinic flash (which is symbolized by the green arrow in Figure 94). The photon densities per flash and unit area of the actinic laser flash of the four different SFITFY data sets were: $5.4{\cdot}10^{14}$ (diamonds), $3{\cdot}10^{15}$(squares), $6.2{\cdot}10^{15}$ (circles) and $7.5{\cdot}10^{16}$ (triangles) photons/($cm^2{\cdot}$flash) (0.7 %, 4 %, 8 % and 100 % of reference).

The SFITFY patterns exhibit an “instantaneous” change of the fluorescence yield within 100 ns that strongly depends on the energy of the actinic flash (see Figure 94). This instantaneous change is a rise at low energies and turns into a drop below F_0 at high energies of the laser flash. This drop is explained by the population of ^{3}Car states that act as highly efficient quenchers of the fluorescence [118]. A normalized maximum value $F_{max}(t)/F_0$ of about two is reached about 50 µs after the actinic flash. In the subsequent time domain the normalized fluorescence yield declines to a level slightly above its original value F_0.

7.2 PS II model based on rate equations

Simulations based on a model of the PS II reaction pattern presented in Figure 95 can provide information on the time courses of population probabilities of different PSII states. The appropriate application of the formalism of rate equations provides a flexible basis for comparative analyses of time dependent fluorescence signals observed on different photosynthetic samples under various conditions (e.g. presence of herbicides, other stress conditions, excitation with actinic pulses of different intensity and duration). The general formalism is principally suitable to describe any system that can be reduced to states and transitions between these states.

The kinetic scheme of Figure 95 allows the calculation of the transient PS II redox state populations ranging from the dark adapted state, via excitation energy and electron transfer steps induced by pulse excitation, followed by final relaxation into the stationary state eventually attained under the measuring light. The shape of the actinic flash was taken into account by assuming that an exponentially decaying rate constant simulates the time dependent excitation of the PS II by the 10 ns actinic flash. The maximum amplitude of this excitation exceeds that of the measuring light by 9 orders of magnitude.

The aim of this study was the evaluation of rate constants of dissipative processes at different intensities of the actinic flash by means of fitting the calculated model curves to experimental data, keeping all known rate constants within the range of values reported in the literature and to compare the results with the “3-quencher” model that was previously used by Steffen et al. to analyze SFITFY signals (see Figure 94) of whole leaves of *Arabidopsis thaliana* plants [118, 119, 120]. Dissipative processes are mainly the fluorescence quenching by ^{3}Car and further dissipative processes shown in Figure 95 b).

Figure 95 shows the whole scheme of redox states and their transitions as described in detail in [57]. Each box in Figure 95 represents the redox state of the corresponding component (compare chap. 1.2) : antenna and RC chlorophyll – $\left\langle \begin{matrix} \text{Chl} \\ \text{P680} \end{matrix} \right\rangle$, pheophytin – Phe, primary quinone acceptor – Q_A, secondary quinone acceptor – Q_B. The model comprises the processes of light induced charge separation (reaction numbers: 2,9,16,29), charge stabilization by $Q_A^{-\bullet}$ formation (reaction numbers 3,10,17,30), electron transfer from $Q_A^{-\bullet}$ to Q_B (reaction number 7) and from $Q_A^{-\bullet}Q_B^{-\bullet}$ to Q_BH^- (reaction number 14), protonation of Q_BH^- under PQH_2 release (reaction numbers 21-27) and refilling of the empty Q_B-site with oxidized plastoquinones (PQ) (reaction numbers 34-40). For the sake of simplicity we assume that for each electron, transferred from the water oxidizing complex (WOC) via tyrosine Y_Z to the oxidized RC chlorophyll $P680^{+\bullet}$ (reaction numbers 4,11,18,31), one proton is released into the lumen.

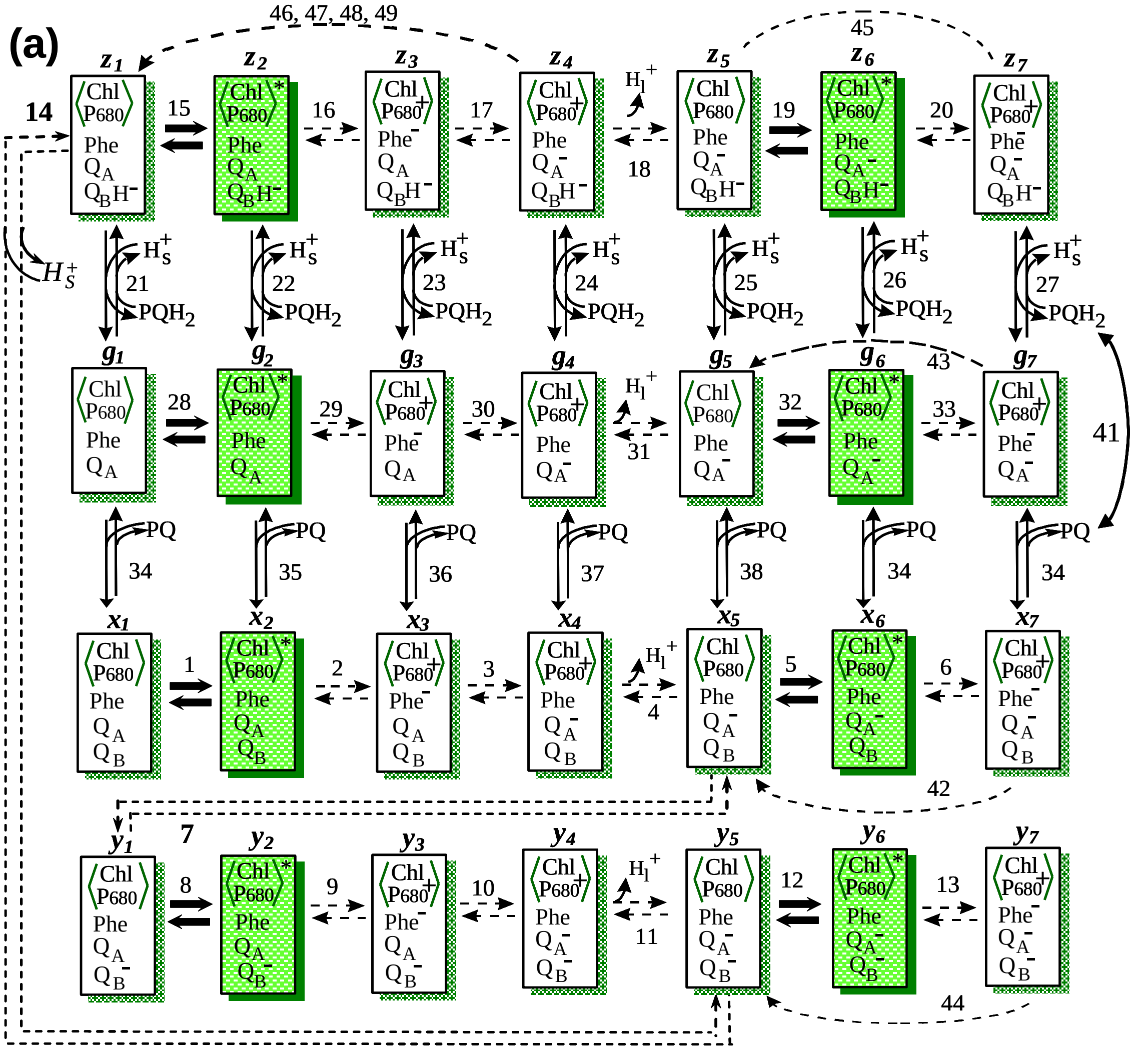

Figure 95: a) Kinetic scheme of Photosystem II as presented in refs. [57], [58]. Each rectangle refers to one of the states. $\left\langle \begin{matrix}\text{Chl}\\ \text{P680}\end{matrix} \right\rangle$ denotes the total PS II chlorophyll including the antenna and the P680 pigments and $\left\langle \begin{matrix}\text{Chl}\\ \text{P680}\end{matrix} \right\rangle^{*}$ is used to determine singlet excited states ^{1}Chl* delocalized over all pigments in antenna and RC. Further components are P680 - photochemically active pigment, Phe – the primary electron acceptor pheophytin. Q_A and Q_B – the primary and secondary quinone acceptors. PQ – plastoquinone, PQH_2 – plastoquinol; H_L^+ – protons, which are released into lumen, H_S^+ – protons in stroma. The letters above rectangles (x_i , y_i , z_i , g_i, i=1,...,7) correspond to the model variables. Shaded areas symbolize the excited states that are capable of emitting fluorescence quanta. Dashed arrows designate fast steps (characteristic time values less than 1 ms). Bold arrows mark the light induced steps. Numbers at the arrows correspond to the step numbers. Dashed arcs designate two types of irreversible reactions of the processes of non-radiative recombination: $Phe^{-\bullet}$ with $P680^{+\bullet}$ (42-45:= k_{Phe}) and $Q_A^{-\bullet}$ with $P680^{+\bullet}$ (46-49).

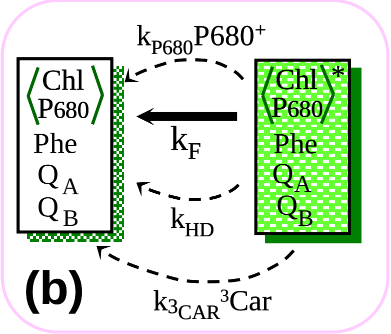

Figure 95 b) The decay into ground state occurs via i) radiative fluorescence emission (k_F), ii) nonradiative dissipation of excited chlorophyll singlets by quenching due to cation radical $P680^{+\bullet}$ and/or by the triplet states of carotenoids with rate constants k_{P680+} and $k_{3_{Car}}$, respectively and iii) radiationless dissipation of excitation to heat (k_{HD}).

The model scheme of Figure 95 a) comprises 28 redox states of the PS II RC together with two states of the PQ pool. Therefore 30 variables (metabolites $N_\mathrm{i}(t)$, i = 1…30) and a set of 30 differential equations describe the rate of production and consumption of $N_\mathrm{i}(t)$ which is a function of the variables $N_\mathrm{j}(t)$ involved into population and deactivation of $N_\mathrm{i}(t)$ (i, j = 1…30) and of the rate constants, i.e. probabilities for each transition per time unit k_n, $k_{-\mathrm{n}}$ (n = 1…49) for forward and backward transfer steps, respectively (see chapter 3.2).

Some of the reactions in the model scheme (Figure 95 a) involve protons in lumen and stroma ($[H_l^+]$ and $[H_S^+]$) as model parameters.

The exact mathematical structure of the set of ordinary differential equations and the method of data variation and fitting is outlined in ref. [57, 58]. The dissipative reactions (including inter-system crossing), given by the rate constants k_{P680^+}, k_{3_Car} and k_HD, quench the fluorescence from PS II in addition to the photochemical quenching via electron transfer to the acceptor quinone molecule Q_A (see Figure 95 b). The fluorescence emission is symbolized in Figure 95 b) by the radiative rate constant k_F. Actinic flash induced formation and decay of non-photochemical quenching states $P680^{+\bullet}$, ^{3}Car and radiation-less dissipation as heat was the main focus of this work. Therefore the experimental data at all laser flash excitation intensities was fit with rate constants fixed to values given in literature (see table 2) except the dissipative relaxation processes which were kept variable.

These deactivation processes are strongly dependent on the energy of the actinic laser flash. The sum of all deactivation processes of $^1\mathrm{Chl}^*$ except of photochemical quenching are given by the relation:

117. $k_A = k_F + k_{P680} \cdot [P680^+] + k_{3Car} \cdot [^3Car] + k_{HD}$.

where $k_\mathrm{A} = k_{-n}$, n=1, 5, 8, 12, 15, 19, 28, 32 (Figure 95 a).

Eq. 117 introduces a nonlinearity into the rate equatio system because the rate constant k_A depends on the concentration of $[P680^+]$ which is determined by the excitation light intensity and $[^3Car]$ which is a light intensity dependent model parameter (see Eq. 119).

The time course of the excitation light constant $k_\mathrm{L}(t)$ is simulated by an exponential decay of the form

118. $k_\mathrm{L}(t) = k_\mathrm{L\text{-}Max} \cdot \exp(-t / \tau_\mathrm{L}) + k_\mathrm{L\text{-}Min}$.

where $k_\mathrm{L\text{-}Max}$ and τ_L describe the maximum photon density of the actinic laser pulses hitting the sample and pulse duration, respectively. The very small value of $k_\mathrm{L\text{-}Min} = 0.2\ \mathrm{s}^{-1}$ corresponds to the photon density of the weak measuring light pulses from LEDs.

Data of Schödel et al. [275, 276] and Steffen et al. [119] were used as the basis for the description of dissipative $^1\mathrm{Chl}^*$ quenching by carotenoid triplets (^{3}Chl). This effect is described by the rate constant k_{3_Car} which depends on the time dependent population ^{3}Car(t). According to [119] the time dependency of ^{3}Car (t) is described by:

119. $[^3\mathrm{Car}(t)] = a_{\mathrm{Car}} \cdot \exp(-t / \tau_{3_{\mathrm{Car}}})$.

where a_{Car} is the population of the ^{3}Car states generated by the actinic flash normalized to the total population of PSII complexes and $\tau_{3_{\mathrm{Car}}}$ the lifetime of the radiationless decay for this ^{3}Car state population.

7.3 Results for energy- and electron transfer processes in *A.thaliana*

The numerical fits of SFITFY data presented as colored solid lines on Figure 96 are seen to describe with high precision the SFITFY patterns at the four different values of the actinic flash energy.

The energies of the actinic flashes and the corresponding relative values are compiled in columns 1 and 2 of Table 1. The maximal light constant values ($k_{\mathrm{L\text{-}Max}}$) in column 3 imitate the rate of light quanta exciting the Chl molecules in the PS II model (Figure 95). The time course of $k_{\mathrm{L\text{-}Max}}$(t) calculated by eq. 118 for the excitation rate is presented in Figure 96 by dashed purple lines corresponding to the values shown in table 1. The $k_{\mathrm{L\text{-}Min}}$ value of eq. 118, reflecting the measuring light beam of the LED pulses, is not visible in Figure 96 because this value is smaller by several orders of magnitude compared to $k_{\mathrm{L\text{-}Max}}$.

Table 2 shows the results gathered from the fit procedure for the values of PS II electron transfer parameters. The parameter values for processes of charge separation, stabilization and Q_B -site reactions could be kept invariant to actinic flash energy without deviations between experimental data and the numerical fit using values from the literature (see column 5 of table 2). In marked contrast the parameters of dissipative reactions in the antenna and PS II and the rate constant for charge recombination (a_{Car}, k_{HD}, Figure 95 b, k_{Phe}, Figure 95 a) had to be changed when varying the relative actinic flash energy (see columns 4, 5, 6 of table 1).

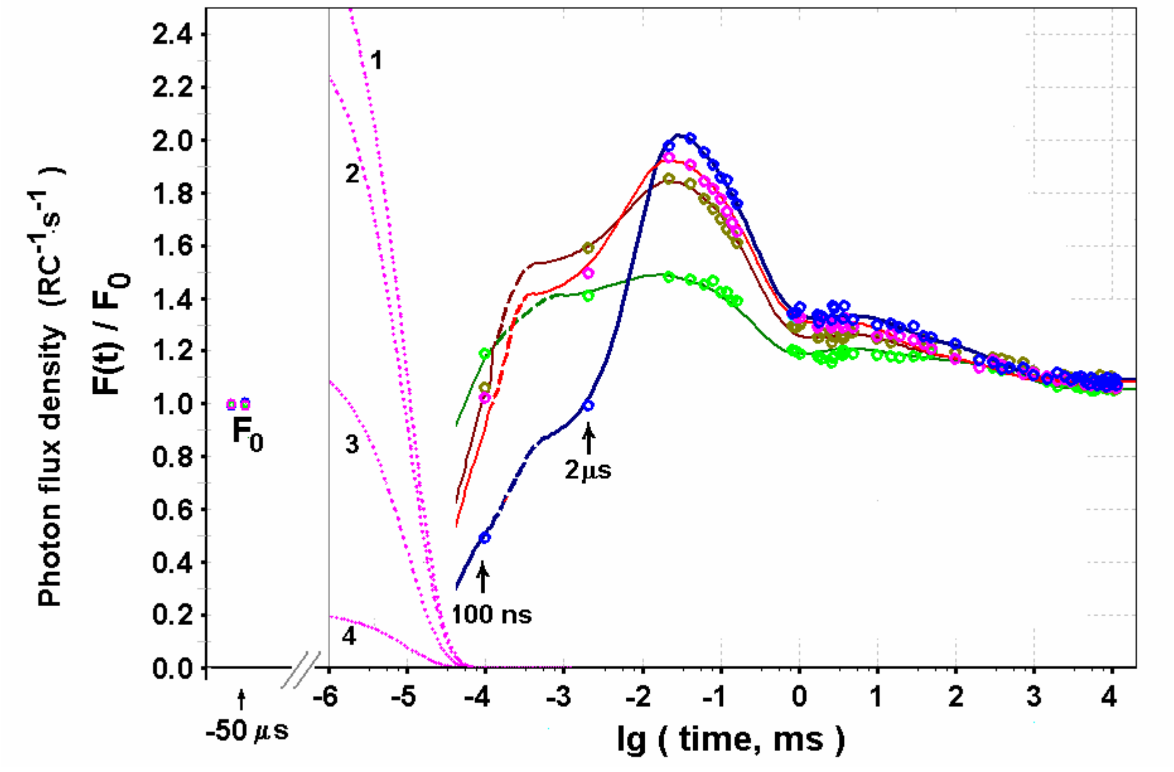

Figure 96: Simulation of the experimental SFITFY data of Figure 94 by the PS II model presented in Figure 95 (a,b) (redrawn from ref. [58]). SFITFY curves in whole leaves of wild type plants of *Arabidopsis thaliana* are shown by symbols at the different laser flash energies: $7.5{\cdot}10^{16}$ photons/cm^2·flash (dark-blue), $6.2{\cdot}10^{15}$ photons/cm^2·flash (magenta), $3.0{\cdot}10^{15}$ photons/cm^2·flash (beige) and $5.4{\cdot}10^{14}$ photons/cm^2·flash (light-green). The numerical fits are shown accordingly by lines calculated with the rate constant $k_{\text{L-Max}}$ values (see table 1): $7.2{\cdot}10^9$ s^{-1} (dark-blue), $6.0{\cdot}10^8$ s^{-1} (red), $2.9{\cdot}10^8$ s^{-1} (brown), $5.2{\cdot}10^7$ s^{-1} (green) and the parameters as shown in table 2. The dotted magenta lines represent the time courses of $k_L(t)$ calculated according to eq. 118. The measuring light of low intensity was simulated with $k_{\text{L-Min}}$ =0.2 s^{-1} (see table 1)

To simulate the fluorescence decay the values of ΔΨ (transmembrane electrical potential difference) and pH$_S$ (pH of the stroma) had to be varied lightly according to the values given in table 1. The pH on the luminal side was set pH$_L$=6.5 for all energies of the actinic flash.

Table 1: Values of parameters used for the fitting of SFITFY data (see Figure 96) according to the model of PS II shown in Figure 95 as published in ref. [58]. (PPFD stands for photosynthetic photon flux density, all other variables are described in the text).

curve number	λ=532 nm; fwhm=10 ns		k_n (s^{-1})			a_{Car} $\tau_{3\text{Car}}$= 5.5 µs	pH$_{\text{Stroma}}$	ΔΨ$_0$, mV (τ$_Ψ$, ms)
	photons/ (cm^2·flash)	%	$k_{\text{L-Max}}$	k_{HD}	k_{Phe}			
1	**$7.5{\cdot}10^{16}$**	100	$7.225{\cdot}10^9$	$1.95{\cdot}10^8$	$8{\cdot}10^8$	$2.08{\cdot}10^9$ 1	7.5	20(800)
2	$6.2{\cdot}10^{15}$	8.27	$5.975{\cdot}10^8$	$1.95{\cdot}10^8$	$7{\cdot}10^8$	$5.6{\cdot}10^8$ 0.27	7.5	15 (500)
3	$3.0{\cdot}10^{15}$	4	$2.89{\cdot}10^8$	$1.95{\cdot}10^8$	$6.4{\cdot}10^8$	$3.5{\cdot}10^8$ 0.17	7.5	14 (500)
4	$5.4{\cdot}10^{14}$	0.72	$5.202{\cdot}10^7$	$1.65{\cdot}10^8$	$3{\cdot}10^8$	$1.2{\cdot}10^8$ 0.06	7.3	14(400)
Measuaring. light PPFD 0.8 µmol photons m^{-2} s^{-1}			0.2					
	1	**2**	**3**	**4**	**5**	**6**	**7**	**8**

Table 2: Values of parameters used for quantitative fits with the PS II model (Figure 95) simulations of SFITFY curves for whole leaves of *Arabidopsis thaliana* plants (see Figure 96).

Figure 95 reaction number, *n*	k_n (s^{-1})	$\boldsymbol{K_{eq}}$	k_{-n} (s^{-1})	Processes References
2,9,16,29	$3.2 \cdot 10^{11}/125$	40	$6.4\ 10^7$	Charge separation (open RC) Charge separation (closed RC) [83, 107, 109]
6,13,20,33	$2.56 \cdot 10^9$ / 2.25	40 / 4	$1.14\ 10^8$	
3,10,17,30	$3 \cdot 10^9$	10^8	30	Charge stabilization on $Q_A^{-\bullet}$ [83, 107, 109, 101]
4,11,18,31	$(3.3 \div 1.5) \cdot 10^7$	80		Electron donation from tyrosine Z to P680$^{+\bullet}$ [277]
7	5000	16	312.5	ET from $Q_A^{-\bullet}$ to Q_B
14	1750	10	1750	ET from $Q_A^{-\bullet}$ to $Q_B^{-\bullet}$ [103, 278]

The SFITFY curves monitored in the range from 100 ns to 10 s after excitation of dark adapted samples with a single actinic flash of a definite energy can be explained by time courses of the PS II redox states that are illustrated in Figure 97 a) and Figure 97 b) for 100 % light intensity and 4 % light intensity, respectively. In closed RCs with redcued Q_A^- the states P680$^{+\bullet}$ Phe$^{-\bullet}$ $Q_A^{-\bullet}$ are populated as a nonlinear process of two photon absorption during the actinic flash followed by a decrease due to the exponential decay of $k_L(t)$. Figure 97 a) (100 % light intensity) shows full saturation (100%) of the closed RC and reduced overall Q_A^- population ($\sum Q_A^-$). The value of 100 % light intensity refers to the value $k_{LMAX}=7.5 \cdot 10^9$ s^{-1}. $\sum Q_A^-$ stays near 100 % until the maximum of the SFITFY curve is reached at about 50 µs.

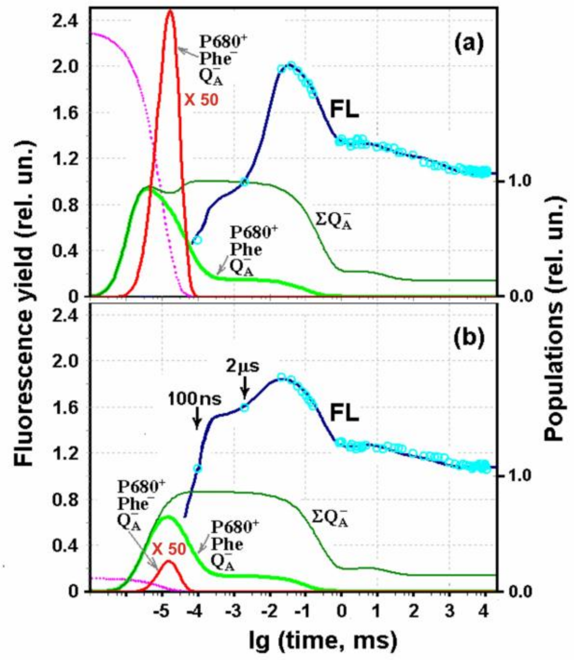

Figure 97: Calculated time course of normalized populations of different redox states in the PS II to simulate the SFITFY data of Figure 94 (circles) in whole leaves of *A. thaliana* wild type plants after illumination with an actinic laser flash (fwhm=10 ns) at two different energies described by $k_{L\text{-}Max}$ values of $7.225 \cdot 10^9$ s^{-1} (panel a) and $2.9 \cdot 10^8$ s^{-1} (panel b) (redrawn from ref. [58]). The measuring light is described by $k_{L\text{-}Min}$ =0.2 s^{-1}. The PS II model parameters used are presented in tables 1, 2. The time courses of $k_L(t)$ are shown as dotted purple lines for $k_{L\text{-}Max}$=$7.225 \cdot 10^9$ s^{-1} (panel a) and $k_{L\text{-}Max}$=$2.9 \cdot 10^8$ s^{-1}(panel b). $\Sigma Q_A^{-\bullet}$ represents the sum of the closed RC states (x_4+g_4+y_4+z_4+x_5+g_5+y_5+z_5) (dark green curve, see nomenclature in the scheme of Figure 95). All states including oxidized Chl *a* in the RC (P680$^{+\bullet}$) are presented in the Fig.: P680$^{+\bullet}$ Phe$Q_A^{-\bullet}$ denoting the sum of the closed RC states (x_4+g_4+y_4+z_4) (light green curve), P680$^{+\bullet}$ Phe$^{-\bullet}$$Q_A^{-\bullet}$ – the sum of the closed RC states with reduced pheophytin (x_7+g_7+y_7+z_7) multiplied with a factor 50 for better visibility (red curve).

Using k_{LMAX}=6.2·10^8 s^{-1} (corresponding to 8%·light intensity) the level of $\sum Q_A^-$ is still very close to saturation (95%) (data not shown). The calculations with k_{LMAX}=3·10^8 s^{-1} (4% light intensity) give rise to redox state population kinetics for $\sum Q_A^-$ as shown in Figure 97 b). Here the levels of maximal $\sum Q_A^-$ are diminished to about 88%.

7.4 Conclusion on dissipative processes in whole leaves of *A.thaliana*

The results as presented in Figure 96 and Figure 97 (see summary in table 2 and ref. [58]) show that a consistent description of the experimental SFITFY data obtained at different excitation intensities can be achieved with invariant rate constants of electron transfer steps for all excitation pulse energies. In marked contrast, an increase of the actinic flash energy by more than two orders of magnitude from 5.4·10^{14} photons/ (cm^2·flash) to 7.5·10^{16} photons/ (cm^2·flash), leads to an increase of the extent of fluorescence quenching due to carotenoid triplet (^{3}Car) formation with factor 14 and of the recombination reaction between reduced primary pheophetin (Phe^-) and $P680^+$ with factor 3 while the probability for heat dissipation in the antenna complex remains virtually constant.

Steffen et al. had shown that saturation of photosynthesis is achieved with actinic laser pulses of 10 ns FWHM and an energy of about 10^{15} photons/ (cm2 ·flash) [118]. In our studies such saturation was observed to be about 88 % at an excitation intensity of 3·10^{15} photons/ (cm^2·flash) (see $\sum Q_A^-$ in Figure 97 b)). At higher excitation intensity the saturation is virtually 100 %. Therefore the PS II model scheme developed for the analyses presented here leads to comparable results regarding the population probability of PS II redox states as the analysis within the “3 quencher model” presented in [81, 118, 119].

The parameter a_{Car} in Eq. 119 designates the amplitude of the ^{3}Car quencher, normalized to the whole PS II complex concentration.

As shown in table 1, at light intensities above around 10^{15} photons/ (cm^2·flash) the yield of ^{3}Car triplet formation is high and exhibits a strong nonlinear relation between the amplitude of ^{3}Car quenching a_{Car} and light intensity. Surprisingly, this relation is not a square dependency of the ^{3}Car quenching amplitude a_{Car} on the light intensity as one would expect from the simple equation $^3\mathrm{Car} + {}^1\mathrm{Chl}^* \rightarrow {}^3\mathrm{Car} + {}^1\mathrm{Chl} + \hbar\omega$, i.e. the annihilation of a carotenoid triplet (formed by light excitation) with an excited Chl singlet state excited within the same LHC.

When using the values of $\tau_{3\mathrm{Car}}$= 5.5 μs and $k_{3\mathrm{Car}}$ = 2.8·10^8 s^{-1} as given by [118, 119] and [275, 276], the simulation of the SFITFY curves based on the generalized model (Figure 95) offers an equivalent but more basic description as the analysis within the framework of the ‘‘3-quencher’’ model. The simulation of the SFITFY curve provides information on the time course of the population probabilities of all different PS II states as shown in Figure 97.

The simulations also reveal that within the time domain from 100 ns to 10 s the measuring light does not produce any significant actinic effect on the control sample (data not shown).

Our evaluation of the rate constant of dissipative processes due to quenching by carotenoid triplets in antennae and $P680^{+\bullet}Q_A^{-\bullet}$ recombination leads to values that close to that outlined in [119].

It turned out that some of the parameters used to reproduce the measurements can be varied in a broad range without a significant change of the simulated SFITFY trace. Parameters describing fast processes (like e.g. k_{HD}) do not influence the shape of the SFITFY decay on a longer timescale (and vice versa). This phenomenon offers the opportunity to analyze a wide range of processes occurring on different time scales simultaneously by precise evaluation of different time domains of the measured SFITFY data or TCSPC traces.

On the other hand, the analysis of processes taking place on similar timescales requires complementary information gathered from independent experiments if there is not a well defined parameter different for these processes (for example wavelength, polarization).

Thus, taking into account these properties, the PS II model offers new opportunities to compare electron transfer and dissipative parameters for different species (e.g. for the green algae and the higher plant) under varying illumination or growth conditions.

8 Summary

The huge potential of fluorescence microscopy below the Abbe diffraction limit are the reasons why these methods advanced to a highly powerful technique in nanobiophotonics. Fluorescence methods seem to be most appealing for investigations on pigment-protein complexes and other chromophores in vitro and in vivo or living cells. These techniques are suitable to resolve weakly illuminated sub-nanometer structures inside living cells without the need of using unphysiological conditions like vacuum, cryostatic temperatures or destructive radiation. In addition fluorescence studies can be combined with several other high resolution techniques. New approaches were developed to combine atomic force microscopy (AFM) with Foerster Resonance Energy Transfer (FRET) [22, 23]. Stimulated Emission Depletion (STED) microscopy has overcome the diffraction limit of conventional far field methods [12]. The resolution of STED and similar techniques like Photo Activation Localisation Microscopy (PALM) suggest that unlimited resolution could be achieved by employing infinite excitation intensity [13-17]. Although experimental limitations and absolute barriers exist for the resolution, an optical resolution of structures down to the picometer scale might be possible [19, 30]. The resolution rises with the square root of the energy used for the measurement. This law holds independently of the variables for resolution in both the spatial and the time domain.

It should therefore be possible to gather information on fluorescence decay components with sub-ps dynamics from time-correlated single photon counting (TCSPC).

In marked contrast to the optimistic interpretation, the investigations and simulations performed for complex systems like the phycobiliprotein (PBP) antenna of *Acaryochloris marina* (chap. 5), hybrid complexes composed by PBP antenna complexes and CdSe nanocrystals (chap. 6) and whole leaves of *Arabidopsis thaliana* (chap. 7) showed that a strightforward analysis of ultrafast individual energy transfer steps is not possible if the system is composed by many two-level systems that are coupled via EET. In this case it is intrinsically impossible to extract information on the accurate values of individual energy transfer steps if the dynamics of several coupled states take place in the same time domain [57]. An improvement can be achieved by decomposition of the sample into subsystems. This separation might lead to a loss of emergent phenomena due to the reduction of the system [1]. If a reduction is not reasonable, complementary experiments must be performed up to a level of methodical statistics of the experimental techniques. To a certain extent the scientist can shift systematic aberrations to statistical uncertainties employing different experimental techniques. The desired goal would be to extract all information from a system which is experimentally accessible.

The time resolution of TCSPC is mainly limited by the quality of the instrumental response function (IRF, see chap. 2) [279]. In analogy to spatial resolution the temporal resolution is not limited by the temporal width of the IRF but by the noise and reproducibility of this function. Detailed numerical simulations revealed that the time resolution of TCSPC of the setup shown in chap. 2 is limited to about 10 % of the IRF when 10.000 counts of signal and IRF are collected in the temporal maximum of these functions [161]. The achievable resolution is therefore about 10 ps.

This thesis described the results of ps-fluorescence spectroscopic studies performed on different structures exhibiting different levels of hierarchic complexity. The most simple model system is represented by the water soluble chlorophyll binding protein (WSCP) genetically expressed in *E.coli* and reconstituted with Chl *a*, Chl *b* or mixtures of Chl *a* and Chl *b* [46-49]. The experimental spectra can be well explained by a strongly coupled Chl dimer inside a tetrameric protein structure that is modulated by the protein environment. Higher complexity is found in the PBP antenna of the unusual cyanobacterium *A.marina* [43, 44,56], which contains 69 chromophores. In vivo measurements were done on whole cells of *A.marina* [43, 54, 55, 56] and on whole cells of the green algae *Chlorella pyrenodoisa chick* and the higher plant *Arabidopis thaliana* [57, 58].

All data were simulated within the framework of rate equations and it was shown that the underlying models are suitable to explain the time resolved fluorescence spectra giving rise to a parameter adaption that delivers new information within a given model. For Chl bound to WSCP the energy landscape of a double well potential and the temperature dependency of the ISC rate constant were determined.

WSCP exhibits an unusual high photostability of bound chlorophyll dimers. The reason for this photostability is not yet clearified in full detail [66, 68]. In literature it is speculated that the protein environment forms a diffusive barrier for oxygen and therefore prevents the reaction between Chl triplet states and oxygen triplets to highly reactive singlet oxygen [69] which is the most probable explanation taking the results of TWCSPC into account as presented in chap. 4. Based on the proposal of an “open sandwich” dimer motif for the pigment array of recombinant class IIa WSCP from *cauliflower* [69] T. Renger et al. used a microscopic theory of the spectra and available data of linear absorption at 77 K and 298 K and circular dichroism at 298 K to characterize the pigment-pigment interaction [38]. They calculated that the angle between the planes of the two Chl molecules in this configuration is about 30° in contrast to the value of about 60° gathered from the original calculations [69]. T. Renger et al. calculated the center-to-center distance of the transition dipole moments of the two coupled Chl molecules to be 0.74 nm [38] from the optical spectra and were able to predict the exciton relaxation time gathered from femtosecond absorption spectroscopy [46, 48]. The 30° angle between the transition dipoles of the Chl molecules was later confirmed by X-ray diffraction microscopy for class IIb WSCP [70]. The fluorescence dynamics of WSCP occurs with three time constants at low temperatures (10 K) and can be explained by pigment-pigment- interactions and pigment-protein interactions [37, 38, 47, 48, 49]. It was shown that there exists a modulation of the energetic states of the coupled Chl dimer by the protein environment that occurs with a typical time constant of 100 ps. Smaller and bigger time constants of 7-8 ps and 1 ns, respectively, might also be caused by protein oscillations. These values would explain heterogeneities as observed in the fs absorption spectroscopy [46] and TWCSPC [47].

Protein dynamics can lead to resonant modulation of the excited state (i.e. the modulation occurs on a similar time scale like the fluorescence decay) which leads to dynamical localisation of the electrons. Therefore such resonant protein oscillations can not be treated easily quasi statically or dynamically, i.e. much slower or much faster, respectively, than the excited state lifetime.

The cyanobacterium *A. marina* was discovered in 1996 and is the only known organism which mainly contains Chl *d* instead of Chl *a* in the membrane intrinsic Chl antenna [59]. Additionally, *A. marina* contains rod shaped PBP antenna complexes that exhibit faster excitation energy transfer (EET) to the reaction center than the phycobilisomes (PBS) found in other cyanbacteria like *Synechococcus 6301* or *Synechocystis*.

The experimental results show that in the PBP antenna of *A.marina* ultrafast EET occurs between different phycocyanine (PC) units (< 1 ps). This relaxation process is followed by the equilibration of energy between the phycocyanin and the allophycocyanin (APC) containing hexamers with a time constant of 3-5 ps [56]. A subsequent EET from PC and APC to spectrally red shifted APC which is most probable located in the linker protein was resolved to 20 (+/- 10) ps in the work presented here [43, 44, 52, 56]. The TWCSPC of living cells contained this 20 ps component as well as preparations of isolated PBP complexes. The findings are in good agreement with the fs absorption spectroscopic results [56]. In whole cells of *A.marina* the EET between the PBP antenna and the Chl *d* containing membrane intrinsic antenna complexes was found to occur within an additional transfer step of about 30-40 ps. The time constant of this EET step critically depends on the number of phycocyanobilin chromophores that are involved in the EET and it describes an "effective" energy transfer from the PBP antenna to Chl *d*. The excitons reach the reaction centre inside the membrane intrinsic Chl *d* complexes within 70 ps in *A.marina*. This value is 3 times faster than in typical cyanobacteria with PBS and Chl *a* containing antenna complexes [44, 52, 56]. The distance of the terminal emitter of the PBP antenna in *A.marina* and the nearest Chl *d* molecule was determined to be 2.7 (+/- 0.3) nm according to the theory of FRET. This distance changes at 0°C leading to a decoupling of the PBP antenna from the membrane intrinsic Chl *d* antenna [43].

Similar effects were also observed in coupled hybrid structures containing the PBP antenna of *A.marina* and additional CdSe/ZnS nanocrystals (QDs) with an average distance of 3.2-3.5 nm between the transition dipole moment of the QDs and the first acceptor chromophore in the PBP antenna [51, 53]. The mechanism could help to construct temperature switch-able light harvesting systems.

The most complex system that was analysed is represented by whole cells of the green alga *Chlorella pyrenoidosa Chick* and whole leaves of the higher plant *Arabidopsis thaliana*.

It turned out that in such systems many parameters used to reproduce the measurement data can be varied in a broad range. But parameters describing fast processes do not influence the distribution of measurement data that occurs on a longer timescale. This phenomenon offers the opportunity to analyze a wide range of processes occurring on different time scales simultaneously by precise evaluation of different time domains. The scientist has the opportunity to separate the time scales of the dynamics of the system. These temporally quasi-separated subsystems are coupled by intermediate processes that can be treated in the frame of rate equation models.

The photophysical and biochemical properties of chlorophyll molecules in photosynthetic complexes are tuned by binding to specific protein environments. This principle has evolutionary developed in the biosphere and lead to amazing structures with highest efficiency in light harvesting, transfer of electronically excited states and transformation of light into electrochemical free energy.

Up until today it is not possible to copy this principle and construct a nanomachine of comparable complexity and stability. The full understanding of the relevance and function of molecular interaction processes in photosynthetic pigment-protein-complexes (PPC) might help us in many areas of application.

One possible industrial relevant application for artificially designed PPC are e.g. nanoscaled organic antenna systems for photovoltaics which could act as innovative light harvesting complexes rising and/ or regulating the absorption cross section of photovoltaic cells. Other applications are switch-able PPC which undergo state transitions from an inactive to an active state when illuminated or when in contact to certain environments. Such PPC could be applicable in the photodynamic therapy of skin cancer and reduce the toxicology of the applied photodynamic dyes. These two applications were suggested in the framework of the thesis presented here. They have the most innovative potential on industry (solar technology and medical/pharmaceutical industry) rising from basic research performed in the field of time correlated fluorescence spectroscopy.

ABBREVIATIONS

ADC	Analog to Digital Converter
AFM	Atomic Force Microscopy
APC	Allophycocyanin
A. marina	Acaryochloris marina
A. thaliana	Arabidopsis thaliana
ATP	Adenosine Triphosphate
BChl	Bacterio-Chlorophyll
Cars	Carotenoids
CBP	Chlorophyll Binding Proteins
CC	Core Complex
CCD	Charged Coupled Device
CD	Circular Dichroism
CdSe	Cadmium selenide
CFD	Constant Fraction Discriminator
Chl	Chlorophyll
CIP	Color Intensity Plot
CP	Core Protein
Cyt	Cytochrome
DAS	Decay Associated Spectra
DF	Delayed Fluorescence
DGL	Differential Equation
DNA	Deoxyribonucleic Acid
E. coli	Escherichia Coli
EET	Excitation Energy Transfer
ESA	Excited State Absorption
ET	Electron Transfer
FLIN	Fluorescence Lifetime Nanoscopy
FLN	Fluorescence Line Narrowing
FMO	Fenna-Matthews-Olson
FRET	Förster Resonance Energy Transfer
FWHM	Full width at half maximum
IC	Internal Conversion
IRF	Instrumental Response Function
ISC	Inter System Crossing
LD	Linear Dichroism

LED	Light Emitting Device
LHC	Light Harvesting Complex (eukaryotes)
LH	Light Harvesting (antenna) (bacteria)
MCP	Microchannel Plate
NADP	Nicotinamide adenine dinucleotide phosphate
NIR	Near Infrared
PALM	Photoactivation Localisation Microscopy
PBP	Phycobiliproteins
PBS	Phycobilisomes
PC	Phycocyanin
PCB	Phycocyanobilin
PDT	Photodynamic Therapy
PE	Phycoerythrin
PID	Proportional-Integral-Differential
PMT	Photomultiplier Tube
PPC	Pigment-Protein Complex
PQ	Plastoquinone
PS I	Photosystem I
PS II	Photosystem II
QD	Quantum Dot
RC	Reaction Center
RNA	Ribonucleic Acid
SFITFY	Single Flash Induced Transient Fluorescence Yield
SPC	Single Photon Counting
STED	Stimulated Excited State Depletion
TAC	Time-to-amplitude Converter
TCSPC	Time-correlated Single Photon Counting
TE	Terminal Emitter
TEM	Transmission Electron Microscopy
Ti:Sa	Titan-Saphire
TWCSPC	Time- and Wavelength-Correlated Single Photon Counting
WOC	Water Oxidising Complex
WSCP	Water-Soluble Chlorophyll binding Protein
ZnS	Zinc Sulfide

REFERENCES

1. W. Heisenberg "Der Teil und das Ganze", Gespräche im Umkreis der Atomphysik, Piper, München, 6. Auflage (1986)
2. C. Theiss, "Transiente femtosekunden-absorptionsspektroskopie des Anregungs-Energietransfers in isolierten Pigment-Proteinkomplexen des Photosyntehseapparates", PhD thesis, Technische Universität Berlin, Mensch & Buch Verlag, Berlin, ISBN: 3-86664-188-5 (2006)
3. J. Shah, "Ultrafast luminescence spectroscopy using sum frequency generation" IEEE J. Quantum Electron. 24, 276 (1988).
4. W. Becker, A. Bergmann, M.A. Hink, K. König, K. Benndorf and C. Biskup "Fluorescence Lifetime Imaging by Time-Correlated Single-Photon Counting" MICROSCOPY RESEARCH AND TECHNIQUE 63:58 (2004)
5. L.Young, W.T. Hill, S.J. Sibener, S.D. Price, C.E. Tanner, C.E. Wieman, S.R. Leone "Precision lifetime measurements of Cs 6p $^2P_{1/2}$ and 6p $^2P_{3/2}$ levels by single photon counting", Phys. Rev. A, 50, 3: 2174 (1994)
6. M. Szczepaniak, M. Sugiura, A.R. Holzwarth "The role of TyrD in the electron transfer kinetics in Photosystem II", Biochimica et Biophysica Acta - Bioenergetics. 1777, 12:1510 (2008)
7. J. Yano, J. Kern, K. Sauer, M. J. Latimer,Y. Pushkar, J. Biesiadka, B. Loll, W. Saenger, J. Messinger, A. Zouni, V. K. Yachandra, "Where Water Is Oxidized to Dioxygen: Structure of the Photosynthetic Mn4Ca Cluster", Science, 314, 5800: 821 (2006)
8. M. Krikunova, B. Voigt, H. Lokstein "Direct evidence for excitonically coupled chlorophylls *a* and *b* in LHCII of higher plants by non-linear polarization spectroscopy in the frequency domain" Biochim. Biophys. Acta 1556:1 (2002)
9. R. Agarwal, B. P. Krueger, G. D. Scholes, M. Yang, J. Yom, L. Mets, G. R. Fleming, "Ultrafast Energy Transfer in LHC-II Revealed by Three-Pulse Photon Echo Peak Shift Measurements" J. Phys. Chem. B, 104, 13:2908 (2000).
10. J. Pieper, K.-D. Irrgang, M. Rätsep, J. Voigt, G. Renger, G. Small "Assignment of the lowes Qy- State and spectral dynamics of the CP 29 chlorophyll *a*/*b* antenna complex of green plants: A hole burning study". Photochem. And Photobiol., 71: 574 (2000)
11. H.-J. Eckert, Z. Petrášek and K. Kemnitz "Application of novel low-intensity non-scanning fluorescence lifetime imaging microscopy for monitoring excited state dynamics in individual chloroplasts and living cells of photosynthetic organisms", Proc. SPIE Vol. 6372, 637207:1 (2006)
12. T.A. Klar, S. Jakobs, M. Dyba, A. Egner and S. W. Hell " Fluorescence microscopy with diffraction resolution limit broken by stimulated emission", Proc. Natl. Acad. Sci. USA 97(15): 8206 (2000)
13. S.W. Hell, "Strategy for far-field optical imaging and writing without diffraction limit", Phys.Lett.A 326 (1-2): 140 (2004)
14. J. V. Westphal, and S. W. Hell "Nanoscale Resolution in the Focal Plane of an Optical Microscope", Phys. Rev. Lett. 94: 143903 (2005)
15. V. Westphal, J. Seeger, T. Salditt, and S. W. Hell "Stimulated Emission Depletion Microscopy on Lithographic Nanostructures", J.Phys.B: At.Mol.Opt.Phys., 38: 695 (2005)

16. A. Egner, C. Geisler, C. v. Middendorff, H. Bock, D. Wenzel, R. Medda, M. Andresen, A. C. Stiel, S. Jakobs, C. Eggeling, A. Schönle and S. W. Hell “Fluorescence Nanoscopy in Whole Cells by Asynchronous Localization of Photoswitching Emitters”, Biophysical Journal, 93: 3285 (2007)
17. J. Fölling, V. Belov, D. Riedel, A. Schönle, A. Egner, C. Eggeling, M. Bossi, and S. W. Hell “Fluorescence Nanoscopy with Optical Sectioning by Two-Photon Induced Molecular Switching using Continuous-Wave Lasers”, ChemPhysChem, 9: 321 (2008)
18. Z. Zalevsky “Superresolution effects in classical microscopy”, lecture during the ICO phtonics conference, 6.-9. Oct. 2009, Delphi. Greece (2009)
19. F.-J. Schmitt “resolution limits of time- and space-correlated single photon counting”, In: Proceedings of the 2008 international conference on information theory and statistical learning ITSL, editors: M.Dehmer, M.Drmota, F. Emmert-Streib, ISBN: 1-60132-079-5, S. 91-97 (2008)
20. S. Hell, “superresolution microscopy”, lecture during the PicoQuant workshop on fluorescence microscopy, Berlin Adlershof, 16.9.2009
21. L. Gross, F. Mohn, N. Moll, P. Liljeroth, G. Meyer “The Chemical Structure of a Molecule Resolved by Atomic Force Microscopy, Science, 325: 1110 (2009)
22. S.A. Vickery and S.U. Dunn, “Combining AFM and FRET for high resolution fluorescence microscopy”, Journal of Microscopy, 202, 2: 408 (2000)
23. A. Sarkar, R.B. Robertson and J.M. Fernandez, “Simultaneous atomic force microscope and fluorescence measurements of protein unfolding using a calibrated evanescent wave”, Proc. Natl. Acad. Sci. USA 101 , 35: 12882 (2004)
24. F-J. Schmitt, A. Matschulat, M. Schoengen and H. J. Eichler “Combination of fluorescence spectroscopy with various microscopic techniques for biotechnological applications”, Seeing on the Nanoscale V, 24. – 27.6.2007, poster with 3rd place of poster award, Santa Barbara, CA (2007)
25. A. Matschulat “Mikroskopische Visualisierung von Gold-Nanopartikeln für die Medizin“, Diplomarbeit, TU Berlin (2007)
26. M. Schoengen “Rasterkraftmikroskopie & Fluoreszenzspektroskopie zur nichtinvasiven und hochaufgelösten Untersuchung von Nanostrukturen“, Diplomarbeit, TU Berlin (2008)
27. M. Müller “A lower bound on the uncertainty of probability measurements in closed systems”, arXiv:0712.4090v1 [hep-th], Dec. 2007
28. P. C. W. Davies, “The implications of a cosmological information bound for complexity, quantum information and the nature of physical law”, http://cosmos.asu.edu/publications/chapters/chaitin_book.pdf
29. J. D. Bekenstein “A universal upper bound on the entropy to energy ratio for bounded systems”, Phys. Rev. D 23: 287 (1981)
30. F.-J. Schmitt “The lower bound on the energy for bounded systems is equivalent to the Bekenstein upper bound on the entropy to energy ratio for bounded systems”, arXiv:0901.3686v1 [hep-th], Jan. 2009
31. S. Wolfram “new kind of science”, Wolfram Media Inc., 1st edition, Champaign, IL (2002)
32. E. Schroedinger „Was ist Leben?: Die lebende Zelle mit den Augen des Physikers betrachtet“, Serie Piper; Auflage: 10., München (1989)
33. J. Barrett “Information processing in generalized probabilistic theories”, Physical Review A 75, 032304, (2007)

34. J. Barrett, N. Linden, S. Massar, S. Pironio, S. Popescu and D. Roberts “Nonlocal correlations as an information-theoretic resource”, Physical review A 71: 022101 (2005)
35. H. Barnum, J. Barrett, L. Orloff Clark, M. Leifer, R. Spekkens, N. Stepanik, A. Wilce and R. Wilke “Entropy and information causality in general probabilistic theories”, New Journal of Physics 12, 033024 (2010)
36. L. Masanes, M. P. Müller “A derivation of quantum theory from physical requirements”, arXiv:1004.1483v2 (2010)
37. T. Renger, M. E. Madjet, F. Müh, I. Trostmann, F.-J. Schmitt, C. Theiss, H. Paulsen, H. J. Eichler, A. Knorr and G. Renger “Thermally Activated Superradiance and Intersystem Crossing in the Water-Soluble Chlorophyll Binding Protein “, J. Phys. Chem. B, 113: 9948 (2009)
38. T. Renger, I. Trostmann, C. Theiss, M.E. Madjet, M. Richter, H. Paulsen, H.J. Eichler, A. Knorr, G. Renger “Refinement of a structural model of a pigment-protein complex by accurate optical line shape theory and experiments” J. Phys. Chem. B, 111: 10487 (2007)
39. M. Richter, K. J. Ahn, A. Knorr, A. Schliwa, D. Bimberg, T. Renger “Theory of excitation energy transfer in coupled nanostructures – from quantum dots to light harvesting systems”, Phys. Stat. Sol. (b), 243 : 2302 (2006).
40. M. Richter, T. Renger, G. Renger, A. Knorr “Theory of non-perturbative optical response of a light harvesting system: Application to the intensity dependence of the fluorescence quantum yield of the LHC-II”, J. Chem. Phys. 127, 075105 (2007)
41. T. Renger and A. R. Holzwarth “Theory of excitation energy transfer and optical spectra of photosynthetic systems”, in Biophysical Techniques in Photosynthesis, Volume 2 (Eds. J. Matysik, T. Aartsma), Springer Dodrecht (2007)
42. A. Carmele, A. Knorr and M. Richter “Photon statistics as a probe for exciton correlations in coupled nanostructures”, Physical Review B 79, 035316 (2009)
43. F.-J. Schmitt, C. Theiss, K. Wache, J. Fuesers, S. Andree, A. Handojo, A. Karradt, D. Kiekebusch, H. J. Eichler, H.-J. Eckert “Investigation of the excited states dynamics in the Chl *d*- containing cyanobacterium *Acaryochloris marina* by time- and wavelength correlated single-photon counting”, Proc. SPIE Vol. 6386, 638607/1 (2006)
44. C. Theiss, F.-J. Schmitt, S. Andree, C. Cardenas-Chavez, K. Wache, J. Fuesers, M. Vitali, M. Wess, S. Kussin, H. J. Eichler, and H.-J. Eckert, “Excitation Energy Transfer in the Phycobiliprotein Antenna of Acaryochloris marina Studied by Transient fs Absorption and Fluorescence Spectroscopy” In: Photosynthesis. Energy from the Sun, editor: J.F. Allen, E. Gantt, J. H. Golbeck, B. Osmond, Dordrecht Springer, Netherlands, ISBN 978-1-4020-6707-5: 339 (2008)
45. P. H. Lambrev, F.-J. Schmitt, S. Kussin, M. Schoengen, Z. Várkonyi, H. J. Eichler, G. Garab, G. Renger, “Functional domain size in isolated aggregates of light-harvesting complex II and thylakoid membranes”, Biochim. Biophys. Acta, 1807: 1022–1031 (2011)
46. C. Theiss, S. Andree, F.-J. Schmitt, T. Renger, I. Trostmann, H.J. Eichler, H. Paulsen, G. Renger (2007), Pigment-pigment and pigment-protein interactions in recombinant water-soluble chlorophyll proteins (WSCP) from cauliflower, J. Phys. Chem. B, 111, 46: 13325-13335 (2007).
47. F.-J. Schmitt, I. Trostmann, C. Theiss, J. Pieper, T. Renger, J. Fuesers, E. H. Hubrich, H. Paulsen, H. J. Eichler, G. Renger, “Excited State Dynamics in Recombinant Water-Soluble Chlorophyll Proteins (WSCP)

from Cauliflower Investigated by Transient Fluorescence Spectroscopy", J. Phys. Chem. B, 112: 13951 (2008)

48. G. Renger, J. Pieper, C. Theiss, I. Trostmann, H. Paulsen, T. Renger, H. J. Eichler, F.-J. Schmitt, „Water soluble chlorophyll binding protein of higher plants: a most suitable model system for basic analyses of pigment-pigment and pigment-protein interactions in chlorophyll protein complexes", J Plant Physiol., 168, 12: 1462-1472 (2011)
49. J. Pieper, M. Ratsep, I. Trostmann, F.-J. Schmitt, C. Theiss, H. Paulsen, A. Freiberg, G. Renger, H.J. Eichler "Excitonic Energy Level Structure and Pigment-Protein Interactions in the Recombinant Water-Soluble Chlorophyll Protein (WSCP), Part II: Spectral Hole-Burning Experiments ", J Phys Chem B., 115, 14:4053-4065 (2011)
50. A. V. Barinov, N. S. Goryachev, F.-J. Schmitt, G. Renger, and A. I. Kotel'nikov, "Luminescent Analysis of Microsecond Relaxation Dynamics of Viscous Media", Optics and Spectroscopy (Condensed matter spectroscopy), 107, 1: 95 (2009)
51. F.-J. Schmitt, E. G. Maksimov, H. Suedmeyer, V. Jeyasangar, C. Theiss, V. Z. Paschenko, H. J. Eichler and G. Renger "Time resolved temperature switchable excitation energy transfer processes between CdSe/ZnS nanocrystals and phycobiliprotein antenna from Acaryochloris marina", Photon Nanostruct: Fundam Appl, 9, 2: 190-195 (2011)
52. F.-J. Schmitt, J. Fuesers, H. Südmeyer, J. Börner, V. Jeyasangar, R. Olliges, E.G. Maksimov, M. Grehn, C. Theiss, V.Z. Paschenko, H.J. Eichler and G.Renger "Simulations of energy transfer processes along the rod shaped PBP antenna and Chl d antenna of *A.marina*", in AIP conference proceedings, 1288, editors: Nikolaos A. Vainos, Stavros Pissadakis, Stelios Couris, Emmanuel Paspalakis, Ioannis Koutselas, emerging trands and novel materials in photonics, International Commission for Optics Topical Meeting, ICO photonics Delphi 2009, Delphi, Greece, 7-9 Okt. 2009, ISBN 978-0-7354-*0843*-2, ISSN: 0094234X (2010)
53. F.-J. Schmitt "Temperature induced conformational changes in hybrid complexes formed from CdSe/ZnS nanocrystals and the phycobiliprotein antenna of *Acaryochloris marina*", J. Opt. 12 084008, doi: 10.1088/2040-8978/12/8/084008 (2010)
54. Z. Petrášek, F.-J. Schmitt, C. Theiss, J. Huyer, M. Chen. A. Larkum, H. J. Eichler, K. Kemnitz and H.-J. Eckert "Excitation energy transfer from Phycobiliprotein to Chlorophyll *d* in intact cells of *Acaryochloris marina* studied by time- and wavelength resolved fluorescence spectroscopy", Photochem. Photobiol. Sci., 4: 1016 (2005)
55. E. Schlodder, M. Çetin, H.-J. Eckert, F.-J. Schmitt, J. Barber and A. Telfer "Both Chlorophylls *a* and *d* are essential for the photochemistry in photosystem II of the cyanobacterium, *Acaryochloris marina*" Biochim. Biophys. Acta, 1767, 589 (2007)
56. C. Theiss, F.-J. Schmitt, J. Pieper, C. Nganou, M. Grehn, M. Vitali, R. Olliges, H.J. Eichler, H.-J. Eckert "Excitation energy transfer in intact cells and in the phycobiliprotein antennae of the chlorophyll *d* containing cyanobacterium *Acaryochloris marina*", J Plant Physiol., 168, 12: 1473– 1487 (2011)
57. N. E. Belyaeva, F.-J. Schmitt, R. Steffen, V. Z. Paschenko, G. Yu. Riznichenko, Yu. K. Chemeris, G. Renger, A. B. Rubin "PS II model-based simulations of single turnover flash-induced transients of fluorescence yield monitored within the time domain of 100 ns–10 s on dark-adapted Chlorella pyrenoidosa cells", Photosynth Res., 98:105 (2008)

58. N. E. Belyaeva, F.-J. Schmitt, V. Z. Paschenko, G. Y. Riznichenko, A. B. Rubin, G. Renger, "PS II model based analysis of transient fluorescence yield measured on whole leaves of Arabidopsis thaliana after excitation with light flashes of different energies", BioSystems, 103, 2-3: 188-195 (2011)
59. H. Miyashita, H. Ikemoto, N. Kurano, K. Adachi, M. Chihara and S. Miyachi, "Chlorophyll *d* as a major pigment" Nature (London), 383: 402 (1996)
60. A. R. Holtzwarth "Structure-function relationships and energy transfer in phycobiliprotein antennae", physiologia plantarum 83: 518 (1991)
61. C.W. Mullineaux, A.R. Holzwarth "Kinetics of excitation energy transfer in the cyanobacterial phycobilisome-Photosystem II complex", Biochim Biophys. Acta 1098: 68 (1991)
62. A. R. Holtzwarth, "Energy transfer kinetics" In: Antennas and reaction centers of photosynthetic bacteria ed: M.E. Michel-Beyerle, Springer Verlag, Berlin, S.45-52 (1985)
63. H.-W. Trissl, "Modeling the Excitation Capture in Thylakoid Membranes", In: Photosynthesis in Algae, ed: T.W. Larkum, S.E.Douglas and J.A. Raven, Kluwer Academic Publishers, S. 245-276 (2003)
64. A.N. Glazer, "Light harvesting by phycobilisomes", Ann. Rev. Biophys. Chem., 14: 47 (1985)
65. M. Mimuro "Photon capture, exciton migration and fluorescence emission in cyanobacteria and red algae", in: G.C. Papageorgiou and Govindjee (eds) Chlorophyll a Fluorescence: A Signature of Photosynthesis, Springer: Dordrecht, The Netherlands , S. 173-195 (2004)
66. H. Satoh, A. Uchida, K. Nakayama, M. Okada, "Water soluble Chlorophyll Protein in *Brassicaceae* Plants is a Stress-Induced Chlorophyll-Binding Protein" Plant Cell Physiol., 42: 906 (2001)
67. H. Satoh, K. Nakayama, M. Okada, "Molecular cloning and functional expression of a water-soluble chlorophyll protein, a putative carrier of chlorophyll molecules in cauliflower", J. Biol. Chem. 46: 30568 (1998).
68. K. Schmidt, C. Fufezan, A. Krieger-Liszkay, H. Satoh, H. Paulsen "Recombinant water-soluble chlorophyll protein from *Brassica oleracea Var. botrys* binds various chlorophyll derivatives", Biochemistry, 42: 7427 (2003)
69. J.L. Hughes, R. Razeghifard, M. Logue, A. Oakley, T. Wydrzynski, E. Krausz, "Magneto-Optic Spectroscopy of a Protein Tetramer Binding Two Exciton-Coupled Chlorophylls" J. Am. Chem. Soc., 12: 3649 (2006)
70. D. Horigome, H. Satoh, N. Itoh, K. Mitsunaga, I. Oonishi, A. Nakagawa, A. Uchida "Structural mechanism and photoprotective function of water-soluble chlorophyll-binding protein" J. Biol. Chem., 282, 9: 6525 (2007).
71. D.S. Talaga "Information Theoretical Approach to Single-Molecule Experimental Design and Interpretation", J. Phys Chem A, 110, 31: 9743 (2006)
72. H. Yang, X.S. Xie "Statistical approaches for probing single-molecule dynamics photon-by-photon", Chemical Physics, 284: 423 (2002)
73. G. Renger, in: Primary processes of photosynthesis, Vol. I: Basic principles and apparatus; G. Renger, Ed.; RSC Publ.: Cambridge, U.K. (2008)
74. D. W. Lawlor, D.-P. Häder „Photosynthese“, Thieme Verlag Stuttgart (1990)
75. O. V. S. Heath „Physiologie der Photosynthese“, Thieme Verlag Stuttgart (1972)
76. D.-P. Häder „Photosynthese“, Thieme Verlag Stuttgart (1999)
77. B. Ke "Photosynthesis", Kluwer Academic: Dordrecht, The Netherlands, Vol. 10 (2001)

78. B. Green, W.W. Parson (editors.) Light Harvesting Antennas. Advances in Photosynthesis and Respiration, Vol. 13, Springer, Dordrecht (2003)
79. G. Renger “The light reactions of photosynthesis”. Curr Sci., 98, 10: 1305 (2010)
80. M. Byrdin „Messungen und Modellierungen zur Dynamik angeregter Zustände in Photosystem I“ , PhD thesis, Freie Universität Berlin (1999)
81. R. Steffen “Time-resolved spectroscopic investigations of photosystem II”, PhD thesis, TU Berlin (2003)
82. P.-A. Albertsson, E. Andreasson, A. Persson, P. Svensson “Organization of the thylakoid membrane with respect to the four photosystems, PSIα, PSIβ, PSllα, PSIIβ.” In: 'Current Research in Photosynthesis'. (Ed. M Baltschefsky), Kluwer Academic Publishers: Dordrecht: 923-926 (1990)
83. G. Schatz, H. Brock, A.R. Holtzwarth „Kinetic and energetic model for the primary processes in photosystem II“, Biophys Journal, 54: 397 (1988)
84. G. Renger, T. Renger "Photosystem II: The machinery of photosynthetic water splitting " Photosynthesis research, 98, 1-3:53 (2008)
85. C. Law, R. Cogdell In: Primary processes of photosynthesis: Basic principles and apparatus, Vol. I, ed. Renger, G., RSC Publ.: Cambridge, U.K., p 205 (2008)
86. M. Mimuro, M. Kobayashi, A. Murakami, T. Tsuchiya, H. Miyashita, In: Primary processes of photosynthesis: Basic principles and apparatus, Vol. I, ed. Renger, G., RSC Publ.: Cambridge, U.K., p 261 (2008)
87. H. van Amerongen, R. Croce, In: Primary processes of photosynthesis: Basic principles and apparatus, Vol. I, ed. Renger, G., RSC Publ.: Cambridge, U.K., p 329 (2008)
88. W. Parson, In: Primary processes of photosynthesis: Basic principles and apparatus, Vol. II, ed. Renger, G., RSC Publ.: Cambridge, U.K., p 57 (2008)
89. P. Setif, W. Leibl, In: Primary processes of photosynthesis: Basic principles and apparatus, Vol. II, ed. Renger, G., RSC Publ.: Cambridge, U.K., p 147 (2008)
90. G. Renger, in: Primary processes of photosynthesis: Basic principles and apparatus, Vol. II, G. Renger, Ed., RSC Publ.: Cambridge, U.K. (2008)
91. J. Kern, G. Renger, "Photosystem II: structure and mechanism of the water:plastoquinone oxidoreductase", Photosynthesis research, 94, 2-3:183 (2007)
92. G. Renger, "Oxidative photosynthetic water splitting: energetics, kinetics and mechanism " Photosynthesis research, 92, 3:407 (2007)
93. T. Polivka, V. Sundstrom “Ultrafast dynamics of carotenoid excited states - from solution to natural and artificial systems” Chem. Rev. 104: 2021 (2004)
94. J. Barber, J. Nield, E.P. Morris, D. Zheleva, B. Hankamer “The structure, function and dynamics of photosystem two“, Physiol. Plantarum 100: 817 (1997)
95. A. Bergmann, „Picosekunden-Fluoreszenzspektroskopie mithilfe doppeltkorrelierter Einzelphotonendetektion zur Untersuchung der Primärprozesse im Photosystem II“, PhD thesis, Mensch und Buch Verlag, Berlin (1999)
96. G. Renger, “Energy transfer and trapping in photosystem II”, in: The photosystems: Structure, Function and Molecular Biology, edited by J. Barber, Elsevier Science Publishers B.V. (1992)
97. J. Barber „Photosystem II: The engine of life”, Biophys. Quart. Revs. 36: 71 (2003)

98. T. S. Bibby, J. Nield, M. Chen, A.W.D. Larkum, J. Barber, „Structure of a photosystem II supercomplex isolated from Prochloron didemni retaining it´s chlorophyll a/b light-harvesting system“, PNAS, 100, 15: 9050 (2003)

99. M. Chen, T. S. Bibby, J. Nield, A.W.D. Larkum, J. Barber, „Structure of a large Photosystem II supercomplex from acaryochloris marina“, FEBS Letters 579: 1306 (2005)

100. H.-J. Eckert, G. Renger, J. Bernarding, P. Faust, H. J. Eichler, J. Salk, „Examination of fluorescence lifetime and radical-pair decay in Photosystem II membrane fragments from spinach” Biochim. Biophys. Acta 893: 208 (1987)

101. G. Renger, A.R. Holzwarth, “Primary electron transfer.” In: Wydrzynski, T., Satoh, K. (Eds.), Photosystem II: The Water:Plastoquinone Oxido-Reductase in Photosynthesis. Springer, Dordrecht, pp. 139–175 (2005)

102. C. R. Ireland, S. P. Long, N. R. Baker “The relationship between carbon dioxide fixation and chlorophyll *a* fluorescence during induction of photosynthesis in maize leaves at different temperatures and carbon dioxide concentration.” Planta 160:550 (1984)

103. G. Renger G, A. Schulze A “Quantitative analysis of fluorescence induction curves in isolated spinach chloroplasts.” Photobiochem Photobiophys 9:79 (1985)

104. U. Schreiber, U. Schliwa, W. Bilger ”Continuous recording of photochemical and nonphotochemical fluorescence quenching with a new type of modulation fluorometre.” Photosynth Res 10:51 (1986)

105. A.A. Bulychev, M.M. Niyazova, A.B. Rubin “Fluorescence changes of chloroplasts caused by the shifts of membranepotential and their dependence on the redox state of the acceptor of photosystem II”. Biolog Membr 4:262 (1987)

106. C. Neubauer, U. Schreiber “The polyphasic rise of chlorophyll fluorescence upon onset of strong continuous illumination: I. Saturation characteristics and partial control by the photosystem II acceptor side.” Z Naturforsch C 42:1246 (1987)

107. T.A. Roelofs, C.H. Lee, A.R. Holzwarth “Global target analysis of picosecond chlorophyll fluorescence kinetic from pea chloroplasts.” Biophys J 61:1147 (1992)

108. H. Dau “Short-term adaptation of plants to changing light intensities and its relation to photosystem II photochemistry and fluorescence emission.” J Photochem Photobiol B Biol 26:3 (1994)

109. G. Renger, H. J. Eckert, A. Bergmann, J. Bernarding, B. Liu, A. Napiwotzki, F. Reifarth, H. J. Eichler “Fluorescence and spectroscopic studies on exciton trapping and electron transfer in photosystem II of higher plants.” Aust J Plant Physiol 22:167 (1995)

110. G. V. Lebedeva, N. E. Belyaeva, O. V. Demin, G. Y. Riznichenko, A. B. Rubin “Kinetic model of primary photosynthetic processes inchloroplasts. Description of the fast phase of chlorophyll fluorescence induction under different light intensities.” Biophysics 47:968 (2002)

111. D. Lazar “Chlorophyll *a* fluorescence rise induced by high light illumination of dark-adapted plant tissue studied by means of a model of photosystem II and considering photosystem II heterogeneity.” J Theor Biol 220:469 (2003)

112. D. Lazar “The polyphasic chlorophyll *a* fluorescence rise measured under high intensity of exciting light.” Funct Plant Biol 33:9 (2006)

113. R.J. Strasser, A. Srivastava, Govindgee “Polyphasic chlorophyll *a* fluorescence transient in plants and cyanobacteria.” Photochem Photobiol 61:32 (1995)

114. R.J. Strasser, M. Tsimilli-Michael, A. Srivastava “Analysis of the chlorophyll *a* fluorescence transient.” In: G.C. Papageorgiou, Govindjee (eds) Chlorophyll fluorescence: a signature of photosynthesis. Advances in photosynthesis and respiration, vol 19. Kluwer Academic Publishers, The Netherlands, pp 321–362 (2004)

115. Govindjee, “Sixty-three years since Kautsky: Chlorophyll *a* fluorescence” , AustJ Plant Physiol. 22: 131 (1995)

116. K. Sauer, M. Debreczeny *“*Fluorescence*”* in: J. Auresz and A. Hoff (eds), Biophysical Techniques in Photosynthesis, Kluwer Academic Publishers, London (1996)

117. A. A. Bulychev, W. J. Vredenberg “Modulation of photosystem II chlorophyll fluorescence by electrogenic events generated by photosystem I.” Bioelectrochemistry 54:157 (2001)

118. R. Steffen, G. Christen, G. Renger “Time-resolved monitoring of flash-induced changes of fluorescence quantum yield and decay of delayed light emission in oxygen-evolving photosynthetic organisms.” Biochemistry 40:173 (2001)

119. R. Steffen, H. J. Eckert, A. A. Kelly, P. Dormann, G. Renger G “Investigations on the reaction pattern of photosystem II in leaves from Arabidopsis thaliana by time-resolved fluorometric analysis.” Biochemistry 44:3123 (2005)

120. R. Steffen, A. A. Kelly, J. Huyer, P. Doermann, G. Renger “Investigations on the reaction pattern of photosystem II in leaves from Arabidopsis thaliana wild type plants and mutants with genetically modified lipid content.” Biochemistry 44:3134 (2005)

121. O. van Kooten O, J. F. H. Snel, W. J. Vredenberg “Free energy transduction related to the electric potential changes across the thylakoid membrane.” Photosynth Res 9:211 (1986)

122. N.E. Belyaeva “Generalized model of primary photosynthetic processes in chloroplasts.” PhD thesis, Lomonosov State University, Moscow (2004)

123. N. E. Belyaeva, G. V. Lebedeva, G. Y. Riznichenko “Kinetic model of primary photosynthetic processes in chloroplasts. Modeling of thylakoid membranes electric potential.” In: Riznichenko Gyu (ed) Mathematics computer education, vol 10. Progress-Traditsiya, Moscow, pp 263–276 (2003)

124. N. E. Belyaeva, V. Z. Paschenko, G. Renger, G. Y. Riznichenko, A. B. Rubin “Application of a photosystem II model for analysis of fluorescence induction curves in the 100 ns to 10 s time domain after excitationwith a saturating light pulse.” Biophysics 51:860 (2006)

125. G. Raszewski and T. Renger “Light-Harvesting in Photosystem II Core Complexes Is Limited by the Transfer to the Trap: Can the Core Complex Turn into a Photoprotective Mode?” J. Am. Chem. Soc., 130, 13: 4431 (2008)

126. M. Sarovar, A. Ishizaki, G. R. Fleming and K. B. Whaley, “Quantum entanglement in photosynthetic light harvesting complexes.” arXiv:0905.3787v1 [quant-ph] 23 May 2009

127. T. R. Calhoun, N. S. Ginsberg, G. S. Schlau-Cohen, Y.-C. Cheng, M. Ballottari, R. Bassi, G. R. Fleming, "Quantum Coherence Enabled Determination of the Energy Landscape in Light-Harvesting Complex II", J. Phys. Chem. B, 113, 51: 16291 (2009)

128. G. F. Peter, J. P. Thornber, “Biochemical composition and organization of higher plant photosystem II light -harvesting pigment-proteins”, J. Biol. Chem. 266, 16745 (1991)

129. E. J. Boekema, J. F. L. van Breemen, H. van Roon, J.P. Dekker, “Arrangement of photosystem II supercomplexes in crystalline macrodomains within the thylakoid membrane of green plant chloroplasts”, J. Mol. Biol. 301: 1123 (2000)

130. V. Barzda, L. Mustárdy, G. Garab "Size dependency of circular dichroism in macroaggregates of photosynthetic pigment-protein complexes", Biochemistry 33: 10837 (1994)
131. G. Garab, L. Mustárdy, "Role of LHCII-containing macrodomains in the structure, function and dynamics of grana", Aust. J. Plant Physiol. 26: 649 (1999).
132. J. Lavorel, P. Joliot, "A connected model of the photosynthetic unit", Biophys. J. 12: 815 (1972)
133. J. Lavergne, H.-W. Trissl, "Theory of fluorescence induction in Photosystem II: Derivation of analytical expressions in a model including exciton-radical- pair equilibrium and restricted energy transfer between photosynthetic units", Biophys. J. 68: 2474 (1995)
134. W. L. Butler, "Energy transfer between photosystem II units in a connected package model of the photochemical apparatus of photosynthesis", Proc. Natl. Acad. Sci. USA 77: 4697 (1980)
135. W. T. F. den Hollander, J. G. C. Bakker, R. van Grondelle, "Trapping, loss and annihilation of excitations in a photosynthetic system. I. Theoretical aspects", Biochim. Biophys. Acta 725: 492 (1983)
136. G. Paillotin, C. E. Swenberg, J. Breton, N. E. Geacintov, "Analysis of picosecond laserinduced fluorescence phenomena in photosynthetic membranes utilizing a master equation approach", Biophys. J. 25: 513 (1979)
137. T. Kolubayev, N. E. Geacintov, G. Paillotin, J. Breton, "Domain sizes in chloroplasts and chlorophyll-protein complexes probed by fluorescence yield quenching induced by singlet-triplet exciton annihilation", Biochim. Biophys. Acta 808: 66 (1985)
138. T. Gillbro, A. Sandström, M. Spangfort, V. Sundström, R. van Grondelle, "Excitation energy annihilation in aggregates of chlorophyll *a*/*b* complexes", Biochim. Biophys. Acta 93: 369 (1988)
139. V. Barzda, G. Garab, V. Gulbinas, L. Valkunas, "Evidence for long-range excitation energy migration in macroaggregates of the chlorophyll a/b light-harvesting antenna complexes", Biochim. Biophys. Acta 1273: 231 (1996)
140. V. Barzda, V. Gulbinas, R. Kananavicius, V. Cervinskas, H. van Amerongen, R. van Grondelle, L. Valkunas, "Singlet-singlet annihilation kinetics in aggregates and trimers of LHCII", Biophys. J. 80: 2409 (2001)
141. R. Schödel „Zur Kinetik von Singulett- und Triplett-Anregungen im Lichtsammelkomplex des Photosystems II höherer Pflanzen (LHCII)." PhD thesis, Humboldt-Universität zu Berlin, http://edoc.hu-berlin.de/dissertationen/physik/schoedel-rene/ (1999)
142. R. Schödel, F. Hillmann, T. Schrötter, J. Voigt, K.D. Irrgang, G. Renger G "Kinetics of excited states of pigment clusters in solubilized light-harvesting complex II: photon density-dependent fluorescence yield and transmittance." Biophys J, 71:3370 (1996)
143. M. Richter, T. Renger, A. Knorr, "A Bloch equation approach to intensity dependent optical spectra of light harvesting complex II: excitation dependence of light harvesting complex II pump-probe spectra." Photosynth Res. 95:119 (2008)
144. P. Horton, "Nonphotochemical Quenching of Chlorophyll Fluorescence", in: R.C. Jennings (Ed.), Light as an Energy Source and Information Carrier in Plant Physiology, New York, Plenum Press, pp. 99-111 (1996)
145. G. H. Krause, P. Jahns, "Non-Photochemical Energy Dissipation Determined by Chlorophyll Fluorescence Quenching: Characterization and Function", in: G.C. Papageorgiou, Govindjee (Eds.), Chlorophyll *a* Fluorescence: A Signature of Photosynthesis, Advances in Photosynthesis and Respiration Vol.19, Springer, Dordrecht, pp. 463-495 (2004).

146. C. W. Mullineaux, A. A. Pascal, P. Horton, A. R. Holzwarth, “Excitation energy quenching in aggregates of the LHCII chlorophyll-protein complex: A time-resolved fluorescence study”, Biochim. Biophys. Acta 1141: 23 (1993)
147. S. Vasil'ev, K.-D. Irrgang, T. Schrötter, A. Bergmann, H.-J. Eichler, G. Renger, “Quenching of chlorophyll *a* fluorescence in the aggregates of LHCII: Steady state fluorescence and picosecond relaxation kinetics”, Biochemistry 36: 7503 (1997)
148. P. Horton, A. V. Ruban, D. Rees, A. A. Pascal, G. Noctor, A. J. Young, “Control of the light-harvesting function of chloroplast membranes by aggregation of the LHCII chlorophyll-protein complex”, FEBS Lett. 292 (1991)
149. A. V. Ruban, R. Berera, C. Ilioaia, I.H.M. van Stokkum, J. T. M. Kennis, A. A. Pascal, H. van Amerongen, B. Robert, P. Horton, R. van Grondelle, “Identification of a mechanism of photoprotective energy dissipation in higher plants”, Nature 450: 575 (2007)
150. Y. Miloslavina, A. Wehner, E. Wientjes, M. Reus, P. Lambrev, G. Garab, R. Croce, A. R. Holzwarth, “Far-red fluorescence: A direct spectroscopic marker for LHCII oligomers forming in non photochemical quenching”, FEBS Lett. 582: 3625 (2008)
151. B. van Oort, A. van Hoek, A.V. Ruban, H. van Amerongen, “Equilibrium between quenched and nonquenched conformations of the major plant light-harvesting complex studied with high-pressure time-resolved fluorescence”, J. Phys. Chem. B 111: 7631 (2007)
152. L. Valkunas, I. von Stokkum, R. Berera, R. van Grondelle, “Exciton migration and fluorescence quenching in LHCII aggregates: Target analysis using a simple nonlinear annihilation scheme”, Chemical Physics 357(1-3):17 (2008) .
153. B. van Oort, A. van Hoek, A.V. Ruban, H. van Amerongen, “Aggregation of light-harvesting complex II leads to formation of efficient excitation energy traps in monomeric and trimeric complexes”, FEBS Lett. 581: 3528 (2007)
154. J. Standfuss, A. C. Terwisscha van Scheltinga, M. Lamborghini and W. Kühlbrandt: “Mechanisms of photoprotection and nonphotochemical quenching in pea light-harvesting complex at 2.5 Å resolution”, The EMBO Journal 24: 919 (2005)
155. Z. Liu, H. Yan, K. Wang, T. Kuang, J. Zhang, L. Gui, X. An, W. Chang ”Crystal structure of spinach major light-harvesting complex at 2.72 Å resolution” Nature 428 : 287 (2004)
156. P. Jahns, A. Wehner, W. Paulsen, S. Hobe, „De-epoxidation of violaxanthin after reconstitution into different carotenoid binding sites of light-harvesting complex II.“, Biol. Chem. 276: 22154 (2001)
157. T. Morosinotto, R. Baronio, R. Bassi, “Dynamics of chromophore binding to Lhc proteins in vivo and in vitro during operation of the xantophyll cycle.”, Biol.Chem. 277: 36913 (2002)
158. P. Nieuwenburg, R.J. Clarke, Z.L. Cai, M. Chen, A. W. Larkum, N.M. Cabral, K.P. Ghiggino, J.R. Reimers, „examination of the photophysical processes of chlorophyll d leading to a clarification of proposed uphill energy transfer processes in Cells of Acaryochloris marina“, Photochem Photobiol.,77 (6):628 (2003)
159. V. Sivakumar, R. Wang and G. Hastings, „Photo-Oxidation of P740, the Primary Electron Donor in Photosystem I from Acaryochloris marina“, Biophysical Journal 85:3162 (2003)
160. H. Miyashita, K. Adachi, N. Kurano, H. Ikemoto, M. Chihara and S. Miyachi “Pigment composition of a novel oxygenic photosynthetic prokaryote containing chlorophyll *d* as the major chlorophyll”, Plant Cell Physiol., 38: 274 (1997)

161. F.-J. Schmitt, “Untersuchung der Fluoreszenzdynamik im Antennensystem des Chlorophyll *d*-haltigen Cyanobakteriums *Acaryochloris marina*.“ Diplomarbeit (2005), TU Berlin, Grin Verlag, München (2010)

162. P. I. Harris and D. Chapman, „Analysis of polypeptide and protein structures using Fourier transform infrared spectroscopy“. In Methods in Molecular Biology, Vol. 22, Humana Press Inc., Totowa, NJ (1994)

163. T. Renger, V. May, O. Kühn, „Ultrafast Excitation Energy Transfer Dynamics in Photosynthetic Pigment-Protein Complexes“, Physics Reports 343: 137 (2001)

164. M. Ketelaars, A. M. van Oijen, M. Matsushita, J. Köhler, J. Schmidt, and T. J. Aartsma, “Spectroscopy on the B850 Band of Individual Light-Harvesting 2 Complexes of Rhodopseudomonas acidophila I. Experiments and Monte Carlo simulations”, Biophysical Journal, 80:1591 (2001)

165. T. S. Park, K. Schulten. „Kinetics of excitation migration and trapping in the photosynthetic unit of purple bacteria”. Journal of Physical Chemistry B, 105:8259 (2001)

166. A. Freer, S. Prince, K. Sauer, M. Papiz, A. H. Lawless, G. McDermott, R. Cogdell, N. W. Isaacs “Pigment–pigment interactions and energy transfer in the antenna complex of the photosynthetic bacterium Rhodopseudomonasacidophila” Structure, 4, 4: 449 (1996)

167. K. Schulten. “From simplicity to complexity and back: Function, architecture and mechanism of light harvesting systems in photosynthetic bacteria” In H. Frauenfelder, J. Deisenhofer, and P. G. Wolynes (ed.), Simplicity and Complexity in Proteins and Nucleic Acids, pp. 227-253. Dahlem University Press , Berlin, 1999.

168. S. Scheuring, F. Reiss-Husson, A. Engel, J.-L. Rigaud and J.-L. Ranck, “High-resolution AFM topographs of Rubrivivax gelatinosus light-harvesting complex LH2”, The EMBO Journal, 20, 12: 3029 (2001)

169. T.Renger and Kühn, “Molekulare Energietrichter”, wissenschaftsmagazin fundiert, Energie, 1/2007, FU Berlin ISSN: 1616-524 (2007)

170. J. Adolphs, T.Renger, “How Proteins Trigger Excitation Energy Transfer in the FMO Complex of Green Sulfur Bacteria”, Biophysical Journal, 91, 8 (2006)

171. F. Müh, M. El-Amine Madjet, J. Adolphs, A. Abdurahman, B. Rabenstein, H. Ishikita, E.-W. Knapp and T. Renger, "α-Helices direct excitation energy flow in the Fenna–Matthews–Olson protein", PNAS, 104,43: 16862 (2007)

172. J. Wen, H. Zhang, M.L. Gross, R. Blankenship “Native electrospray mass spectrometry reveals the nature and stoichiometry of pigments in the FMO photosynthetic antenna protein”, Biochemistry, dx.doi.org/10.1021/bi200239k (2011)

173. J. Nield, P.J. Rizkallah,J. Barber,N.E. Chayen "The 1.45A three-dimensional structure of C-phycocyanin from the thermophilic cyanobacterium Synechococcus elongatus" J. Struct. Biol. 141: 149 (2003)

174. J. W. Murray, K. Maghlaoui, J. Barber, “The structure of allophycocyanin from Thermosynechococcus elongatus at 3.5 A resolution.” Acta Crystallogr., Sect.F, 63: 998 (2007)

175. K. Sauer, H. Scheer, ”Excitation transfer in C-phycocyanin. Förster transfer rate and exciton calculations based on new crystal struture data for C-phycocyanins from A gmenellum quadruplicatum and Mastigocladus laminosus”, Biochimica et Biophysica Acta, 936: 157 (1988)

176. M. P. Debreczeny, K. Sauer, J. Zhou, D. A. Bryant, “Monomeric C-Phycocyanin at Room Temperature and 77K: Resolution of the Absorption and Fluorescence Spectra of the Individual Chromophores and the Energy- Transfer Rate Constants”, J. Phys. Chem., 97: 9852 (1993)

177. M. P. Debreczeny, K. Sauer, J. Zhou, D. A. Bryant, “Comparison of Calculated and Experimentally Resolved Rate Constants for Excitation Energy Transfer in C-Phycocyanin 1. Monomers”, J. Phys. Chem., 99: 8412-8419 (1995)

178. M. P. Debreczeny, K. Sauer, J. Zhou, D. A. Bryant, “Comparison of Calculated and Experimentally Resolved Rate Constants for Excitation Energy Transfer in C-Phycocyanin 2. Trimers”, J. Phys. Chem., 99 : 8420 (1995)

179. A.V. Sharkov, I. Kryukov, E.V. Khoroshilov, P.G. Kryukov,R. Fischer, H. Scheer, T. Gillbro, “Femtosecond energy transfer between chromophores in allophycocyanin trimers”, Chemical Physics Letters 191, 6 : 633 (1992)

180. A.V. Sharkov, I. Kryukov, E.V. Khoroshilov, P.G. Kryukov,R. Fischer, H. Scheer, T. Gillbro, “Femtosecond spectral and anisotropy study of excitation energy transfer between neighbouring α-80 and β-81 chromophores of allophycocyanin trimers”, Biochimica et Biophysica Acta 1188: 349 (1994)

181. A. V. Sharkov, V. Gulbinas, L. Gottschalk, H. Scheer, T. Gillbro, “Dipole-Dipole Interaction in Phycobiliprotein Trimers. Femtosecond Dynamics of Allophycocyanian. Excited State Absorption.” Brazilian Journal of Physics, 26, 2 (1996)

182. J. Minagawa, “Live-cell imaging of photosystem II antenna dissociation during state transitions”, seminar talk in the seminar for optics and photonics, 14.5.2010, Institute of Optics and Atomic Physics, TU Berlin (2010)

183. J. Marquardt, H. Senger, H. Miyashita, S. Miyachi and E. Mörschel, “Isolation and characterization of biliprotein aggregates from *Acaryochloris marina*, a Prochloron-like prokaryote containing mainly chlorophyll *d”* FEBS Lett., 410: 428 (1997)

184. M. Mimuro, S. Akimoto, T. Gotoh, M. Yokono, M. Akiyama, T. Tsuchiya, H. Miyashita, M. Kobayashi, I. Yamazaki, „Identification of the primary electron donor in PS II of the Chl *d*-dominated cyanobacterium *Acaryochloris marina*“, FEBS letters 556: 95 (2004)

185. K. Olliges, “Fluoreszenzspektroskopie zur Photoinhibition von photosynthetischen Organismen“ Diplomarbeit, TU Berlin (2007)

186. Q. Hu, J. Marquardt, I. Iwasaki, H. Miyashita, N. Kurano, E. Mörschel, S. Miyachi „Molecular structure, localization and function of phycobiliproteins in the chlorophyll *a/d* containing oxygenic photosynthetic prokaryote Acaryochloris marina“, Biochim. Biophys. Acta 1412: 250 (1999)

187. H. Schiller, H. Senger, H. Miyashita, S. Miyachi, H. Dau, “Light-harvesting in *Acaryochloris marina* - spectroscopic characterization of a chlorophyll *d*-dominated photosynthetic antenna system.” FEBS Lett., 410: 433 (1997)

188. M. Mimuro, K. Hirayama, K. Uezono, H. Miyashita, S. Miyachi, “Uphill energy transfer in a chlorophyll *d*-dominating oxygenic photosynthetic prokaryote, *Acaryochloris marina*,” Biochim. Biohys. Acta, 1456: 27 (2000)

189. Q. Hu, H. Miyashita, I. Iwasaki, N. Kurano, S. Miyachi, M. Iwaki, S. Itoh, “A photosystem I reaction center driven by chlorophyll d in oxygenic photosynthesis”, Proc. Natl. Acad. Sci. USA, 95: 13319 (1998)

190. M. Mimuro, S. Akimoto, I. Yamazaki, H. Miyashita, S. Miyachi, “Fluorescence properties of Chlorophyll *d*-dominating prokaryotic alga, *A. marina* : studies using time-resolved fluorescence spectroscopy on intact cells”, Biochim. Biohys. Acta, 1412: 37 (1999)

191. S. Itoh, M. Iwaki, T. Noguti, A. Kawamori, H. Mino, Q. Hu, I. Iwasaki, H. Miyashita, K. N. Kurano, S. Miyachi, R. Shen, "Photosystem I and Photosystem II reaction centres of a new oxygenic organism *Acaryochloris marina* that use chlorophyll *d"*, in: Proceedings of 12th Int. Congress on Photosynthesis 2001, S6-028, CSIRO Publ. (2001)

192. S. Itoh, K. Sugiura, Fluorescence of photosystem I, in: G.C. Papageorgiou and Govindjee (eds) Chlorophyll a Fluorescence: A Signature of Photosynthesis, pp. 231-250. Springer: Dordrecht, The Netherlands (2004)

193. W.L. Downing, F. Mauxion, M.O. Fauvarque, M.P. Reviron, D. de Vienne, N. Vartanian, J. Giraudat, "A Brassica napus transcript encoding a protein related to the Künitz protease inhibitor family accumulates upon water stress in leaves, not in seeds" Plant J. 2, 5: 685 (1992)

194. M.-P. Reviron, N. Vartanian, M. Sallantin, J. Huet, J. Pernollet, D. de Vienne "Characterization of a Novel Protein Induced by Progressive or Rapid Drought and Salinity in Brassica napus Leaves", Plant Physiol.**,** 100, 3 : 1486 (1992)

195. P. Annamalai, S. Yanagihara "Identification and characterization of a heat-stress induced gene in cabbage encodes a Kunitz type protease inhibitor. " Plant Physiol., 155, 2 : 226 (1999)

196. N. Nishio, H. Satoh, "water-soluble chlorophyll protein in cauliflower may be identical to BnD22, a drought-induced, 22-kilodalton protein in rapeseed. " Plant Physiol., 115 : 841 (1997)

197. G. Beddard, G. Porter "Concentration quenching in chlorophyll" Nature, 26*0*, 5549 : 366 (1976)

198. W.Cramer, H. Zhang, H., J. Yan, G. Kurisu, E. Yamashita, N. Dashdorj, H. Kim, S. Savikhin, in "Primary processes of photosynthesis:Basic principles and apparatus", Vol. II, Renger, G., Ed.; RSC Publ.: Cambridge, U.K., p.417-446 (2008)

199. N. Dashdorj, H. Zhang, H. Kim, J. Yan, W. Cramer, S. Savikhin, "The Single Chlorophyll a Molecule in the Cytochrome b6f Complex: Unusual Optical Properties Protect the Complex against Singlet Oxygen" Biophys. J., 88: 4178 (2005)

200. S. Vasil'ev, T. Schrötter, A. Bergmann, K. Irrgang, H.J. Eichler, G. Renger, G. "Cryoprotectant-induced quenching of chlorophyll a fluorescence from light-harvesting complex 2 in vitro: time-resolved fluorescence and steady state spectroscopic studies" Photosynthetica, 33, 3-4 : 553 (1997)

201. K. Henning, Anti-Chaos. "Der Pfeil der Zeit in der Selbstorganisation des Lebens. Mit einem Vorw. von Illya Prigogine", Rowohlt Taschenbuch Verlag, Reinbek (1994)

202. I. Prigogine, "Introduction To Thermodynamics of Irreversible Processes", Charles C Thomas, Springfield, IL (1955)

203. J. Cohen, I. Stuart "Chaos, Antichaos", Ein Ausblick auf die Wissenschaft des 21. Jahrhunderts, Byblos Verlag, Berlin, (1997)

204. A. Bergmann, H.J. Eichler, H.-J. Eckert and G. Renger "Picosecond laser-fluorometer with simultaneous time and wavelength resolution for monitoring decay spectra of photoinhibited Photosystem II particles at 277 K and 10 K", Photosynthesis research 58: 303 (1998)

205. Becker & Hickl GmbH, PML-16-C 16 "Channel Detector Head for Time-Correlated Single Photon Counting User Handbook", http://www.becker-hickl.de/pdf/pml16c21_.pdf, Berlin (2006)

206. D. Kim, P.T.C. So, "Photon counting by large-area detection with multianode photomultiplier tube in high-throughput multiphoton microscopy", SPIE Proc., 6372-12 (2006)

207. A. Bergmann, Diplomarbeit, TU Berlin (1994)

208. J. R. Lakowicz "principles of fluorescence spectroscopy", Springer, New York (2006)

209. J. Fuesers, Diplomarbeit zum Thema „Fluoreszenzspektroskopische Untersuchung mit hoher Zeitauflösung zur Anregungszustandsdynamik bei photosynthetischen Organismen“, TU Berlin (2007)

210. J. Eichler, H.J. Eichler, “Laser, Grundlagen, systeme, Anwendungen“, 2. Auflage, Springer Verlag, Berlin (1991)

211. S. Mukamel, „principles of nonlinear optical spectroscopy“, Oxford University press, New York (1995)

212. L. Bergmann, C. Schäfer, H.Niedrig “Optik“, Lehrbuch der Experimentalphysik Band 3, 9. Auflage, de Gruyter, Berlin (2004)

213. M. Planck "On the Law of Distribution of Energy in the Normal Spectrum". Annalen der Physik, 4: 553 (1901)

214. J. D. Jackson “Klassische Elektrodynamik”, 2. Auflage, de Gruyter, Berlin (1994)

215. O. Schoeps, “Optical Spectroscopy on SemiconductorNanocrystals: Emission Dynamics on a Nanoscale“, PhD thesis, TU Dortmund (2009)

216. C. Cohen-Tannouji, B. Diu, F. Laloe “Quantenmechanik, Teil 1“, 2. Auflage, de Gruyter, Berlin (1999)

217. C. Cohen-Tannouji, B. Diu, F. Laloe “Quantenmechanik, Teil 2“, 2. Auflage, de Gruyter, Berlin (1999)

218. F. Schwabl “Quantenmechanik (QM I) : Eine Einführung“, Springer, Berlin (2007)

219. F. Schwabl “Quantenmechanik für Fortgeschrittene (QM II) “, Springer, Berlin (2008)

220. A. Messiah “Quantenmechanik I “, 2. Auflage, de Gruyter, Berlin (1991)

221. A. Messiah “Quantenmechanik II “, 2. Auflage, de Gruyter, Berlin (1991)

222. W. Demtröder "Molekülphysik: Theoretische Grundlagen und experimentelle Methoden",Oldenbourg, München (2003)

223. H. Haken, “Synergetik. Eine Einführung”, Springer, Berlin (1990)

224. T. Renger, E. Schlodder, „Modeling of optical spectra and light harvesting in photosystem I“, in Photosystem I: The Plastocyanin Ferredoxin Oxidoreductase in Photosynthesis, Series: Advances in Photosynthesis and Respiration, Kluwer Academic Publishers (2005)

225. R. P. Hemenger „The effects of band shapes on circular dichroism spectra of chromophore aggregates”, J. Chem. Phys. 68: 1722 (1978)

226. A.R. Holzwarth, G. W. Suter, „A kinetic model for the energy transfer in phycobilisomes“, Biophys., 52: 673 (1987)

227. B. Stec, R. F. Troxler, M. M. Teeter, „Crystal- Structure of C- Phycocyanin from Cyanidium caldarium provides a new perspective on phycobilisome Assembly“, Biophysical Journal, 76: 2912 (1999)

228. T. Förster, „Intramolecular energy transfer and fluorescene“. Ann. Phys. , 2: 55 (1948)

229. T. Förster “Fluoreszenz organischer Verbindungen”, Vandenhoeck & Ruprecht, Göttingen (1982)

230. T. Förster, „Delocalized excitation and excitation transfer“. Modern Quantum Chemistry, O. Sinanoglu (Ed.) academic press, New York, IIIB: 93 (1965)

231. T.Renger, personal communication, TU Berlin (2008)

232. R. C. Jennings, E. Engelmann, F. Garlaschi, A. P. Casazza, G. Zucchelli “Photosynthesis and negative entropy production“ Biochimica et Biophysica Acta, 1709:251 (2005).

233. R.C. Jennings, A.P. Casazza, E. Belgio, F.M. Garlaschi, G. Zucchelli, “Reply to “Commentary on: “Photosynthesis and Negative Entropy Production”, Biochimica et Biophysica Acta 1757: 1460 (2006)

234. R.C. Jennings, E. Belgio, A.P. Casazza, F.M. Garlaschi, G. Zucchelli, “Entropy consumption in primary photosynthesis”, Biochimica et Biophysica Acta 1767: 1194 (2007)

235. I. Müller, „Entropy and Energy“, Springer, Berlin (2005)

236. N. A. Campbell, J. B. Reece “Biologie”, 8. Auflage, Pearson Studium, München (2009)

237. J. Lavergne. “Commentary on: “photosynthesis and negative entropy production“ by Jennings and coworkers”. Biochimica et Biophysica Acta, 1757:1453 (2006).

238. A.D. Kirwan ” Intrinsic photon entropy? The darkside of light”, International Journal of Engineering Science, 42: 725 (2004)

239. N.D. Gudkov “Some thermodynamics of chemiluminescence”, Journal of Luminescence**,** 79: 85 (1998)

240. G. Crooks, "Nonequilibrium Measurements of Free Energy Differences for Microscopically Reversible Markovian Systems", Journal of Statistical Physics, 90: 1481 (1998)

241. J. Pieper, R. Schödel, K. Irrgang, J. Voigt, G. Renger „Electron-Phonon Coupling in Solubilized LHCII Complexes of Green Plants Investigated by Line-Narrowing and Temperature-Dependent Fluorescence Spectroscopy” J. Phys. Chem. B, 105: 7115 (2001)

242. J. Pieper, M. Rätsep, R. Jankowiak, K.D. Irrgang, J. Voigt, G. Renger, G.J. Small “Q_y-Level Structure and Dynamics of Solubilized LHCII Antenna Complexes: Pressure and Hole Burning Studies” Phys. Chem. A, 103: 2412 (1999)

243. C. Tietz C, F. Jelezko, U. Gerken, S. Schuler, A. Schubert, H. Rogl, J. Wrachtrup “Single Molecule Spectroscopy on the Light-Harvesting Complex II of Higher Plants “ Biophys. J., 81: 556 (2001)

244. J. Pieper, T. Hauß, A. Buchsteiner, K. Baczynski, K. Adamiak, R.E. Lechner, G. Renger “Temperature- and hydration-dependent protein dynamics in photosystem II of green plants studied by quasielastic neutron scattering” Biochemistry, 46: 11398 (2007)

245. C. Parker, T. Joyce “Delayed fluorescence and some properties of the chlorophyll” Photochem. Photobiol., 6: 395 (1967)

246. J.D. Petke, G.M. Maggiora, L. Shipma, R.E. Christoffersen “Stereoelectronic properties of photosynthetic and related systems — v. *ab initio* configuration interaction calculations on the ground and lower excited singlet and triplet states of ethyl chlorophyllide *a* and ethyl pheophorbide *a*” Photochem. Photobiol., 30:203 (1979)

247. R.S. Knox “Dipole and Oscillator Strengths of Chromophores in Solution.” Photochem. Photobiol., 77: 492 (2003)

248. S.S. Brody, E. Rabinowitch E “Excitation lifetimes of photosynthetic pigments in vivo and in vitro.” Science 125: 555 (1957)

249. M. Fragata, B. Nordén, T. Kurucsev ”Linear dichroism (250–700 nm) of chlorophyll a and pheophytin a oriented in a lamellar phase of glycerylmonooctanoate/h2o. characterization of electronic transitions”. Photochem. Photobiol., 47: 133 (1995)

250. M. A. M. J. van Zandvoort, D. Wróbel, P. Lettinga, G. van Ginkel, Y.K. Levine ”The orientation of the transition dipole moments of chlorophyll a and pheophytin a in their molecular frame. Photochem. Photobiol., 62: 299 (1995)

251. M. Linke, A. Lauer, T. von Haimberger, A. Zacarias, K. Heyne “Three-dimensional orientation of the Qy electronic transition dipole moment within the chlorophyll a molecule determined by femtosecond polarization resolved VIS Pump−IR probe spectroscopy” J. Am. Chem. Soc., 130: 14904 (2008)

252. Y. Shibata, S. Tateishi, S. Nakabayashi, S. Itoh, H. Tamiaki "Intensity borrowing via excitonic couplings among Soret and Qy transitions of bacteriochlorophylls in the pigment aggregates of chlorosomes, the light-harvesting antennae of green sulfur bacteria" Biochemistry, 49: 7504 (2010)
253. M. Rätsep, A. Freiberg "Resonant emission from the B870 exciton state and lectron–phonon coupling in the LH2 antenna chromoprotein" Chem. Phys. Lett., 377: 371 (2003)
254. M. Rätsep, A. Freiberg "Electron–phonon and vibronic couplings in the FMO bacteriochlorophyll a antenna complex studied by difference fluorescence line narrowing" J. Lumin., 127: 251 (2007)
255. H. Scheer H, S. Schneider "Photosynthetic light harvesting systems. organization and function." ,de Gruyter, Berlin (1988)
256. M. Mimuro, C. Lipschultz, E. Gantt "Energy flow in the phycobilisome core of Nostoc sp. (MAC):Two independent terminal pigments" Biochimica et Biophysica Acta, 852:126 (1986)
257. T. Gillbro, A. Sandström, V. Sundström, J. Wendler, A.R. Holzwarth "Picosecond Study of energy transfer kinetics in phycobilisomes of Synechococcus 6301 and the Mutant AN 112" Biochimica et Biophysica Acta, 808:52 (1985)
258. K. Csatorday, R. MacColl, V. Csizmadia, J. Grabowski, C. Bagyinka "Exciton Interaction in Allophycocyanin" Biochemistry, 23:6466 (1984)
259. R. MacColl "Cyanobacterial phycobilisomes" Journal Of Structural Biology, 124:311 (1988)
260. M. Sarcina, M.J. Tobin, C.W. Mullineaux "Diffusion of phycobilisomes on the thylakoid membranes of the cyanobacterium Synechococcus 7942 - Effects of phycobilisome size, temperature, and membrane lipid composition" Journal of Biological Chemistry, 276:46830 (2001)
261. E. Gantt, C. Lipschultz, J. Grabowski, B. Zimmerman "Phycobilisomes From Blue-green and Red Algae - Isolation Criteria and Dissociation Characteristics." Plant Physiology, 63:615 (1959)
262. H. Lokstein, C. Steglich, W.R. Hess "Light-harvesting antenna function of phycoerythrin in Prochlorococcus; marinus." Biochimica et Biophysica Acta-bioenergetics, 1410:97 (1999)
263. T. Gillbro, A. Sharkov, I. Kryukov, E. Khoroshilov, P. Kryukov, R. Fischer "Förster Energytransfer Between Neighboring Chromophores In C-phycocyanin Trimers." Biochimica Et Biophysica Acta, 1140:321 (1993)
264. M. Mimuro, P. Füglistaller, R. Rümbeli, H. Zuber "Functional assignment of chromophores and energy transfer in C phycocyanin isolated from the thermophilic cyanobacterium Mastigocladus laminosus." Biochimica et Biophysica Acta, 848:155 (1986)
265. S.B. Krumova, S.P. Laptenok, J.W. Borst, B. Ughy, Z. Gombos, G. Ajlani "Monitoring Photosynthesis in Individual Cells of Synechocystis sp. PCC 6803 on a Picosecond Timescale." Biophysical Journal ,99:2006 (2010)
266. D. Lundell, A. Glazer "Molecular Architecture Of A Light-harvesting Antenna - Structure Of The 18-S Core-rod Subassembly Of The Synechococcus-6301 Phycobilisome." Journal of Biological Chemistry, 258:894-901 (1983)
267. M. Mimuro, I. Yamazaki, N. Tamai, T. Katoh "Excitation energy transfer in phycobilisomes at -196°C isolated from the cyanobacterium Anabaena variabilis (M-3): evidence for the plural transfer pathways to the terminal emitters." Biochimica et Biophysica Acta, 973:153 (1989)

268. X. Xie, M. Du, L. Mets, G. Fleming “Femtosecond fluorescence depolarization study of photosynthetic antenna proteins: observation of ultrafast energy transfer in trimeric C-phycocyanin and allophycocyanin. Time-resolved laser spectroscopy in biochemistry III: SPIE 1992: 690

269. I.L. Medintz, H. Mattoussi, “Quantum dot-based resonance energy transfer and its growing application in biology”, Phys. Chem. Chem. Phys. 11:17 (2009)

270. M.G. Bawendi, P.J. Carroll, W.L. Wilson, L.E. Brus, “Luminescence properties of CdSe quantum crystallites: Resonance between interior and surface localized states’’, J. Chem. Phys. 96, 2: 946 (1992)

271. E.G. Maksimov, T.S. Gostev, F.I. Kuzminov, N.N. Sluchanko, F.-J. Schmitt, G. Renger, V.Z. Paschenko, A.B. Rubin. “Photophysical properties of hybrid systems consisting of nanocrystals and photosynthetic pigment-protein complexes.” Conference “Photochemistry of chlorophyll in model and native systems”. Abstract, p. 40. Pushchino 2009

272. E.G. Maksimov, T.S. Gostev, F.I. Kuzminov, N.N. Sluchanko, F.-J. Schmitt, G. Renger, V.Z. Paschenko, A.B. Rubin, “Research of photophysical properties of hybrid systems consisting of nanocrystals connected with phycobiliproteins.” 1st Int. summer school “Nanomaterials and Nanotechnologies in Living Systems”. June 29 – July 4, 2009. P. 78. Moscow Region, Stupinsky Area.

273. S.A. Empedocles, D.J. Norris, M.G. Bawendi, “Photoluminescence spectroscopy of single CdSe nanocrystallite quantum dots”, Phys. Rev. Lett. 77, 18: 3873 (1996)

274. U. Ozgur, S. Seker, H. V. Demir, “Material Binding Peptides for Nanotechnology”, Molecules, 16: 1426 (2011)

275. R. Schödel, K.D. Irrgang, J. Voigt, G. Renger, „Rate of carotenoid triplet formation in solubilized light-harvesting complex II (LHCII) from spinach.” Biophys. J. 75: 3143 (1998)

276. R. Schödel, K.D. Irrgang, J. Voigt, G. Renger, “Quenching of chlorophyll fluorescence by triplets in solubilized light-harvesting complex II (LHCII).” Biophys. J. 76: 2238 (1999)

277. G. Renger, “Photosynthetic water oxidation to molecular oxygen: apparatus and mechanism.” Biochim. Biophys. Acta 1503: 210 (2001)

278. A.R. Crofts, C.A. Wraight “The electrochemical domain of photosynthesis.” Biochim. Biophys. Acta 726: 149 (1983)

279. A.Spinelli, M.A. Ghioni, S.D.Cova and L.M. Davis “Avalanche detector with Ultraclean Response for Time-Resolved Photon Counting”, IEEE Quant. Elec., 34, 5 (1998)

ACKNOWLEDGMENTS

My gratitude belongs to Prof. Hans Joachim Eichler and Prof. Gernot Renger who supervised my research. The interdisciplinary environment in the framework of SfB 429 inspired me on my way from being a student to becoming a scientist in such a way that I found my place in the wide field of research: it is located between laserphysics as brought to me by Prof. Eichler and biophysical chemistry represented by Prof. Renger.

The collaborations in the field of biophysical research were various and fruitful. The physics theory group Prof. Thomas Renger and Prof. Andreas Knorr as well as Dr. Marten Richter helped us to understand various spectral properties of our samples. Dr. Heiko Lokstein from the university Potsdam, Prof. Vladimir Paschenko from the Lomonosov university Moscow, Prof. Harald Paulsen and Dr. Inga Trostmann from the university Mainz delivered us new and interesting samples as WSCP and various quantum dots. Prof. Mario Dähne and Dr. Kai Hodeck gave us the opportunity to measure with a SNOM and Prof. Mario Dähne is now the chairman of the referees during my defense. I thank him for all this support.

I acknowledge the help of the whole lasergroup with slight preference to Dr. Christoph Theiss who complemented my research with his accurate studies of fs absorption changes in biological pigment-protein complexes. Special thanks also belong to Moritz Grehn, Chris Scharfenorth, Jenny Schawdtke and Georg Krieg who supported me in many areas. In the department of biophysical chemistry I was assisted by Dr. Hann-Jörg Eckert, Dr. Marco Vitali and Prof. Thomas Friedrich and I thank them for long discussions and helpful comments. The technical assistance of Monika Weß and Sabine Kussin and also Steffen Saarstedt also deserve recognition.

I appreciate the help, support and collegiality of many people from the lasergroup and the bioenergetics group in the biophysical chemistry, who are too numerous to list individually. I do not mention them all by name because I would just forget someone and therefore I suggest to check the “about us” pages of these groups in the internet. I especially refer to the acknowledgements of the thesis of Marco Vitali who mentioned all of the lasergroup and bioenergetics group.

Furthermore, we had fruitful cooperations and financial support by Prof. Michael Lehmann and the ZELMI represented by Dr. Dirk Berger and Irene Preuss. The group of Prof. Ulrike Woggon, especially Dr. Oliver Schöps contributed to my research with discussions and equipment.

In particular all students I supervised during their diploma thesis, Bachelor thesis or PhD thesis shall be honoured at this point as they contributed to my research, generated data and helped to deliver the scientific results that led to many publications. They are Dr. Andrea Matschulat, Justus Fuesers, Max Schöngen, Karin Olliges, Elmar Hassan Hubrich, Heinrich Südmeyer, Fulya Bagci, Rachel Olliges, Jannis Hessel, Joachim Börner, Vithiya Jeyasangar, Patrick Hätti, Jörn Weißenborn, Collins Nganou and, supervised by Marco Vitali also Cornelia Junghans and Matthias Reis.

We worked together on different topics: photosynthesis, environmental spectroscopy and biomedical research.
I thank all additional people who worked in these projects like Imke Salhofen, Miran Alic, Insa Kahlen, Kai Reineke, Jakob Löber who also gave me lots of advice regarding the theoretical part of this thesis and Hans-Joachim Cappius who is head scientist of LMTB.

All people mentioned should not only feel as colleagues but also as my friends. Dr. Markus Müller and Adam Tetzlaff, who proof-read my thesis. I remember the long scientific discussions with Markus Müller during our student and PhD times at TU Berlin and thank him, Adam Tetzlaff and all my friends like Dr. Nikolas Pomplun, Arash Azhand, Aljoscha Hahn, Torsten Lüdge, Jan Geißendörfer and many other people, especially from our philosophic “Berliner Zirkel” with hope that we soon renew that iniative. The connection of physics and philosophy, the big question of life and the interesting field of nonequilibrium thermodynamics brought me to my final decision to step into biophysics. The discussions on mathematical concepts, evolution theory, quantum information and optics inspired me and hopefully also you to look at physics from a broader view. My students know that I sometimes tend to inject these aspects into my teaching and I thank them for their patience and interest. I thank everyone who was ever involved in such a discussion with me during the long nights between our usual daily business.

I would like to acknowledge Prof. Eichler again, who gave me the chance to proceed with these discussions on a broader, more scientific basis during all meetings I attended in Berlin, Potsdam, Munich, Dresden, Frankfurt, Hannover, Münster, Düsseldorf, Regensburg, Ancona, Delphi, Glasgow, Visegrad, Certraro, Ischia, Boston, Santa Barbara, Las Vegas and Moscow. To mention all the scientists I met there would blow the frame of these acknowledgments. But everyone who remembers one of our talks should feel addressed. Last but not least I thank Nancy Graf for her mental support and patience, even if our love did not last.
Financial support by DFG (SfB 429) and by Federal Ministry of Education and Research (BMBF, FKZ 01 RI 0645 A-F) is gratefully acknowledged.

CURRICULUM VITAE AND PUBLICATIONS

24.04.1978	Born in Marburg/ Lahn
1984 – 1998	Basic school Randegg and Münnerstadt Grammar school Münnerstadt and Bad Königshofen Civilian services
March – Sep. 1998	Correspondence course of economics, AKAD, Stuttgart

Studies at Friedrich-Alexander-University Erlangen-Nürnberg

Nov.1998 – Sep.2001	Studying of physics, FAU Erlangen-Nürnberg
Oct. 2000	Pre-diploma in Physics
Nov. 1998 – Sep. 2001	Studies in philosophy, chemistry, astronomy and informatics

Studies and teaching at Technical University Berlin

Oct. 2001 – July 2005	Studying of physics, TU Berlin
Oct. 2001 – Sep. 2004	Minor subjects: astronomy, general relativity, laser & quantum optics, quantum information theory and atomic physics & elementary particles
April 2002 – Sep.2005	Tutor (working student) for the student lab internship in physics
April 2004 – July 2005	Working student in the DFG project “Molecular Physiology, Energetics, and Regulation of Primary Metabolism in Plants” with Prof. Hans Joachim Eichler, TU Berlin
July 2005	Diploma in physics, mark: “very good”
Jan. 2006 – 2010	Supervision of 10 diploma and Bachelor students during their diploma thesis (8 of them finished with “very good”, 2 of them won awards)
Oct. 2006 – 2010	Lectures of thermodynamics and supervision of the advanced student lab internship in physics
Since Apr. 2011	Student lab internship in chemistry and exercises “mathematics for chemists”
Since Apr. 2006	Supervision of 10 diploma and bachelor students, 2 of them won awards.

Research at TU Berlin

Oct. 2005 - 2010	Employment in the DFG project “Molecular Physiology, Energetics, and Regulation of Primary Metabolism in Plants” Main research: time- and space correlated single photon counting for fluorescence-spectroscopy in photosynthesis research, nanobiophotonics and environmental spectroscopy. Further research fields: energy transfer and conversion in organic systems. Medical physics, information processing in complex networks
Since Jan. 2011	Employment in the group Bioenergetics of Prof. Friedrich
Feb. 2006	“Erhard Höpfner Studienpreis”, award for an excellent diploma thesis
June 2007	Third place in the poster award of the VEECO conference “Seeing on the Nanoscale V”, Santa Barbara, CA
October 2009	Chorafas award for extraordinary scientific results during the PhD
Since Oct. 2005	16 publications in scientific journals, 1 book article
Since Oct. 2005	11 online publications and conference proceedings
Since March 2004	more than 50 contributions (talks and/or posters) at international congresses and exhibitions, 1 invited talk

Publications in scientific journals and books

1. Z. Petrášek, F.-J. Schmitt, C. Theiss, J. Huyer, M. Chen. A. Larkum, H. J. Eichler, K. Kemnitz and H.-J. Eckert, “Excitation energy transfer from Phycobiliprotein to Chlorophyll *d* in intact cells of Acaryochloris marina studied by time- and wavelength resolved fluorescence spectroscopy”, *Photochem. Photobiol. Sci.*, 4: 1016-1022 (2005)

2. E. Schlodder, M. Çetin, H.-J. Eckert, F.-J. Schmitt, J. Barber and A. Telfer, “Both Chlorophylls *a* and *d* are essential for the photochemistry in photosystem II of the cyanobacterium *Acaryochloris marina*”, *Biochim. Biophys. Acta*, 1767: 589-595 (2007)

3. C. Theiss, S. Andree, F.-J. Schmitt, T. Renger, I. Trostmann, H.J. Eichler, H. Paulsen and G. Renger, “Pigment-pigment and pigment-protein interactions in recombinant water-soluble chlorophyll proteins (WSCP) from cauliflower”, *J. Phys. Chem. B*, 111, 46: 13325-13335 (2007)

4. C. Theiss, F.-J. Schmitt, S. Andree, C. Cardenas-Chavez, K. Wache, J. Fuesers, M. Vitali, M. Wess, S. Kussin, H. J. Eichler, and H.-J. Ecker “ Excitation energy transfer in the phycobiliprotein antenna of *Acaryochloris marina* studied by transient sub-ps absorption and fluorescence spectroscopy”, *Photosynthesis Research*, 91:2 (2007)

5. C. Theiss, F.-J. Schmitt, S. Andree, C. Cardenas-Chavez, K. Wache, J. Fuesers, M. Vitali, M. Wess, S. Kussin, H. J. Eichler, and H.-J. Eckert, “Excitation Energy Transfer in the Phycobiliprotein Antenna of *Acaryochloris marina* Studied by Transient fs Absorption and Fluorescence Spectroscopy” In: Photosynthesis. Energy from the Sun, editor: J.F. Allen, E. Gantt, J. H. Golbeck, B. Osmond, ISBN 978-1-4020-6707-5: 339-342 (2008)

6. F.-J. Schmitt, I. Trostmann, C. Theiss, J. Pieper, T. Renger, J. Fuesers, E. H. Hubrich, H. Paulsen, H. J. Eichler, G. Renger “Excited State Dynamics in Recombinant Water-Soluble Chlorophyll Proteins (WSCP) from Cauliflower Investigated by Transient Fluorescence Spectroscopy”, *J. Phys. Chem. B* 112: 13951–13961 (2008)

7. N. E. Belyaeva, F.-J. Schmitt, R. Steffen, V. Z. Paschenko, G. Yu. Riznichenko, Yu. K. Chemeris, G. Renger, A. B. Rubin “PS II model-based simulations of single turnover flash-induced transients of fluorescence yield monitored within the time domain of 100 ns–10 s on dark-adapted *Chlorella pyrenoidosa* cells”, *Photosynth Res.*, 98:105–119 (2008)

8. T. Renger, M. Madjet, F. Mũh, I. Trostmann, F.-J. Schmitt, C. Theiss, H. Paulsen, H. J. Eichler, A. Knorr, G. Renger “Theory of optical spectra and intersystem crossing in the water soluble chlorophyll binding protein“, *J. Phys. Chem. B*, 113: 9948–9957 (2009)

9. A. V. Barinov, N. S. Goryachev, F.-J. Schmitt, G. Renger, and A. I. Kotel’nikov “Luminescent Analysis of Microsecond Relaxation Dynamics of Viscous Media”, ISSN 0030_400X, *Optics and Spectroscopy* (Condensed matter spectroscopy), 107, 1: 95–100 (2009)

10. F.-J. Schmitt, E.G. Maksimov, H.Suedmeyer, V. Jeyasangar, C. Theiss, V.Z. Paschenko, H.J. Eichler and G.Renger “Time resolved temperature switchable excitation energy transfer processes between CdSe/ZnS nanocrystals and phycobiliprotein antenna from *Acaryochloris marina*”. *Photon Nanostruct: Fundam Appl*, 9, 2: 190-195 (2011)

11. F.-J. Schmitt, "Temperature induced conformational changes in hybrid complexes formed from CdSe/ZnS nanocrystals and the phycobiliprotein antenna of *Acaryochloris marina* ", *Journal of Optics*, J. Opt. 12 084008, doi: 10.1088/2040-8978/12/8/084008 (2010)

12. G. Renger, J. Pieper, C. Theiss, I. Trostmann, H. Paulsen, T. Renger, H. J. Eichler, F.-J. Schmitt, „Water soluble chlorophyll binding protein of higher plants: a most suitable model system for basic analyses of pigment-pigment and pigment-protein interactions in chlorophyll protein complexes”, *J Plant Physiol.*, 168, 12: 1462-1472 (2011)

13. N. E. Belyaeva, F.-J. Schmitt, V. Z. Paschenko, G. Y. Riznichenko, A. B. Rubin, G. Renger, "PS II model based analysis of transient fluorescence yield measured on whole leaves of *Arabidopsis thaliana* after excitation with light flashes of different energies", *BioSystems,* 103, 2-3: 188-195 (2011)

14. J. Pieper, M. Ratsep, I. Trostmann, F.-J. Schmitt, C. Theiss, H. Paulsen, A. Freiberg, G. Renger, H.J. Eichler "Excitonic Energy Level Structure and Pigment-Protein Interactions in the Recombinant Water-Soluble Chlorophyll Protein (WSCP), Part II: Spectral Hole-Burning Experiments ", *J Phys Chem B.,* 115, 14:4053-4065 (2011)

15. C. Theiss, F.-J. Schmitt; J. Pieper, C. Nganou, M. Grehn, M. Vitali, R. Olliges, H.J. Eichler, H.-J. Eckert "Excitation energy transfer in intact cells and in the phycobiliprotein antennae of the chlorophyll *d* containing cyanobacterium *Acaryochloris marina*", *J Plant Physiol.* 168, 12: 1473– 1487 (2011)

16. P. H. Lambrev, F.-J. Schmitt, S. Kussin, M. Schoengen, Z. Várkonyi, H. J. Eichler, G. Garab, G. Renger, "Functional domain size in isolated aggregates of light-harvesting complex II and thylakoid membranes", *Biochim. Biophys. Acta*, 1807: 1022–1031 (2011)

17. F.-J. Schmitt, H. Südmeyer, J. Börner, J. Löber, K. Olliges, K. Reineke, I. Kahlen, P. Hätti, H. J. Eichler and H.-J. Cappius, "Handheld measurement device for fast and non-contact optical measurement of protein films on surfaces", *Optics and Lasers in engineering* (2011), in press

Conference proceedings and online publications

18. F.-J. Schmitt, H.-J. Eckert, H.J. Eichler "analytical methods based on fluorescence spectroscopy", in: Bornimer Agrartechnische Berichte, COST Action 924, Working Group Meeting, ATB 54, ISSN 0947-7314: 17-25 (2005)

19. F.-J. Schmitt, C. Theiss, K. Wache, J. Fuesers, S. Andree, A. Handojo, A. Karradt, D. Kiekebusch, H.J. Eichler and H.-J Eckert "Investigation of the excited states dynamics in the Chl *d*- containing cyanobacterium *Acaryochloris marina* by time- and wavelength correlated single-photon counting", Proc. SPIE, Vol. 6386, 638607/1-12 (2006)

20. F.-J. Schmitt, C. Theiss, K. Wache, J. Fuesers, S. Andree, H.J. Eichler and H.-J. Eckert "Investigation of metabolic changes in living cells of the Chl *d*- containing cyanobacterium *Acaryochloris marina* by time- and wavelength correlated single-photon counting", ZiG-Print, Zentrum für innovative Gesundheitstechnologien der TU Berlin, 02, ISSN 1862-4871 (2007)

21. F.-J. Schmitt, "Magnetismus A-Z", www.supermagnete.de/magnetism_terms.php, Webcraft GmbH, Uster, Schweiz (2008)

22. F.-J. Schmitt, "resolution limits of time- and space-correlated single photon counting", In: Proceedings of the 2008 international conference on information theory and statistical learning ITSL, editors: M.Dehmer, M.Drmota, F. Emmert-Streib, ISBN: 1-60132-079-5, pp.91-97 (2008)

23. F.-J. Schmitt "The lower bound on the energy for bounded systems is equivalent to the Bekenstein upper bound on the entropy to energy ratio for bounded systems", *arXiv:0901.3686v1* [hep-th], 2009 Jan 23

24. F.-J. Schmitt, J. Fuesers, H. Südmeyer, J. Börner, V. Jeyasangar, R. Olliges, E.G. Maksimov, M. Grehn, C. Theiss, V.Z. Paschenko, H. J. Eichler and G. Renger "Simulations of energy transfer processes along the rod shaped PBP antenna and Chl *d* antenna of *A.marina"*, in AIP conference proceedings, 1288, editors: Nikolaos A. Vainos, Stavros Pissadakis, Stelios Couris, Emmanuel Paspalakis, Ioannis Koutselas, emerging trands and novel materials in photonics, International Commission for Optics Topical Meeting, ICO photonics Delphi 2009, Delphi, Greece, 7-9 Okt. 2009, ISBN 978-0-7354-0843-2, ISSN: 0094234X (2010)

25. F.-J. Schmitt „Untersuchung der Fluoreszenzdynamik im Antennensystem des Chlorophyll d-haltigen Cyanobakteriums Acaryochloris marin", Diplomarbeit, TU Berlin, 2005, ISBN-13: 978-3640729951, Grin Verlag, München (2010)

26. F.-J. Schmitt „A universal resolution limit“, ISBN-13: 978-3640761920, Grin Verlag, München (2010)

27. F.-J. Schmitt „The ultimate resolution limit in the universe“, ISBN-13: 978-3640773374, Grin Verlag, München (2010)

28. H.-J. Cappius, F.-J.Schmitt, J. Börner, H. Südmeyer, K. Olliges, K. Reinicke, I. Kahlen „gemeinsamer Sach- und Schlussbericht zum BMBF-Verbundprojekt "Optische Methoden zur Reinigungs- und Kontaminationskontrolle", TIB Hannover, submitted (2011)

Participation in international congresses and exhibitions

1. COST action 924 meeting “Non-destructive sensing of health-promoting compounds”, Postdam, Germany (7.-8.12.2005), talk

2. “Signals, Sensing and Plant Primary Metabolism”, colloquium of the Collaborative Research Center SfB 429, Potsdam, Germany (26.-29.4.2006), poster

3. Optics East 2006, Boston, MA, USA (1.-5.10.2006), talk

4. German Ukrainian Symposium on Nanobiotechnology, Kiew, Ukraine (14.-16.12.2006), poster

5. European Workshop on movement science, Amsterdam (31.5.2007 – 2.6.2007), talk

6. “Seeing at the Nanoscale V”, Santa Barbara, CA, USA (24. – 27.6.2007), poster, third place of poster award

7. 14th International congress of Photosynthesis, Glasgow (22.7.2007 – 27.7.2007), poster

8. COST action MP0604 meeting “Optical Micro-Manipulation by Nonlinear Nanophotonics”, Ancona, Italy (25.-26.10.2007), talk

9. Exhibition Biotechnica Hannover „Internationale Fachmesse für Biotechnologie“ (9.10.2007-11.10.2007), Hannover, Germany, poster

10. COST action MP0604 meeting “Optical Micro-Manipulation by Nonlinear Nanophotonics”, Münster, Germany (21.-22.02.2008), talk

11. Exhibition Laser Optics Berlin (17.3.2008- 19.3.2008), talk and poster

12. Worldcomp 2008 “international conference on information theory and statistical learning” (14.7.2008-17.7.2008), Las Vegas, NV, USA, talk

13. COST action MP0604 meeting “Optical Micro-Manipulation by Nonlinear Nanophotonics”, Ischia, Italy (2.-5.9.2008), talk

14. Nanomed 2009 “6th International Conference on Biomedical Applications of Nanotechnology”, Berlin, Germany (4.3.2009-6.3.2009), poster

15. Exhibition “World of Photonics”, Shanghai, China (17.3.2009-19.3.2009)

16. Exhibition “World of Photonics”, Munich, Germany (14.-19.6.2009)

17. COST action MP0604 meeting “Optical Micro-Manipulation by Nonlinear Nanophotonics”, Glasgow, Scotland (6.-9.5.2009), talk

18. “Photochemistry of chlorophyll in model and native systems”, Pushchino (2009), talk

19. Summer school “Nanomaterials and Nanotechnologies in Living Systems”, Moscow Region, Stupinsky Area, Russia (29.6.2009-4.7.2009), talk

20. 18. Photosynthese Nord-West Workshop 2009, Berlin, Germany (20.-21.8.2009), 5 contributions (2 talks, 3 posters in collaboration with students of TU Berlin)

21. ICO Photonics Conference and COST action MP0604, Delphi, Greece (7.-9.10.2009), talk and poster

22. Exhibition Laser Optics Berlin, (22.3.2010- 24.3.2010), talk and poster

23. COST meeting & training school “Optical Micromanipulation ba nonlinear nanophotonics”, MP 0604 COST Action and the European network of excellence for biophotonics, Photonics 4 Life, Visegrad, Ungarn, (5.-8.10.2010), Talk

24. 4. Internationales Symposium des SfB429, Potsdam, (6.-9.10.2010), 4 posters

25. “From science fiction to fact (and vice versa)”, 12th International EMBL PhD Student Symposium, (21 - 23 October 2010), Heidelberg (Germany), talk

26. NOMA conference and COST meeting “Optical Micromanipulation ba nonlinear nanophotonics”, MP 0604, Certraro, Italy, 8.6.2011-10.06.2011, talk

Regular participation on the spring meeting of German physical Society in

27. Munich (2004), talk
28. Berlin (2005), talk
29. Frankfurt (2006), 2 talks
30. Düsseldorf (2007), 3 talks
31. Berlin (2008), 3 talks
32. Dresden (2009), 4 talks
33. Regensburg (2010), 4 talks
34. Dresden (2011), 2 talks

Invited talks

“Energy transfer processes inside hybrid structures formed from CdSe/ZnS nanoparticles and the PBP antenna of *A.marina*”, “photosynthesis research for sustainability”, Baku, Azerbaijan, July 24-30, 2011

Patent request

„Radial fokussiert emittierende und detektierende Mikrolichtwellenleiteroptiken“,
DE 10 2010 056 408.7 (request: 27.12.2010)

Awards

1) Support of Haereus foundation: DPG 2007, 2008, 2009
2) Travel stipendia of “Freunde der TU Berlin e.V.: Santa Barbara (2007), Las Vegas (2008)
3) Feb 2006: Anerkennungsprämie in framework of Erhard Höpfner Studienpreises for diploma thesis.
4) June 2007: 3rd Place of poster award during the conference „Seeing at the Nanoscale V“ in Santa Barbara, CA, USA
5) Oct 2009: Chorafas award of the Chorafas foundation, 4000 US-$

Academic Policy

1. Chairman of the education council (2004 – 2006), since 2006 member of the education council
2. Member in the council of physics (2006 – 2008)
3. Member of the council of the institute of optics and atomic physics (2007 – 2010)
4. Member of the faculty council (since 2007)
5. Chairman of the extended Academic Senate (since 2007)
6. Member of the Academic Senate (since 2010)
7. Member in the board of examiners in physics (2007-2011)
8. Member in different boards of examiners of different study courses in chemistry (since 2011)
9. Member in 8 appointment committees since 2005

Approved Projects (as coworker during proposal proposal and work)

1. DFG, SfB 429, TPA1 (2004 – 2007)
2. DFG, SfB 429, TPA1 (2008 – 2010)
3. BMBF, „Optische Methoden zur Reinigungs-und Kontaminationskontrolle“, FKZ 01 RI 0645 B (337.632 €) (2007 – 2010)
4. BMBF / DLR, Förderung der internationalen Zusammenarbeit mit Russland, RUS 06/003 (2007 – 2010)
5. BMBF / DLR, Förderung der internationalen Zusammenarbeit mit Russland, RUS 10/026 (18.280 €) (since 2010)
6. EU, COST Programm „Optical Micro-Manipulation by Nonlinear Nanophotonics, MP0604 (2007 – 2011)

Submitted proposals and projects in preparation

1. BMBF, Bilateral cooperation in education and research (with Russia), “Generation and monitoring of reactive oxygen species in photosynthesis and other biologically relevant systems” (31.884,- €), submitted
2. BMBF, “Optisch-molekularbiologische mobile Detektoren zur spezifischen (Keim- und) Schädlingserkennung“, in preparation
3. DFG, SfB: “Biomimetic synthesis and directed evolution of chromophore targets (BioDirECT)”, in preparation